Nonlinear optical signals and spectroscopy with quantum light

Konstantin E. Dorfman,[*] Frank Schlawin,[†] and Shaul Mukamel[‡]

Department of Chemistry and Department of Physics and Astronomy, University of California, Irvine, California 92697, USA

(published 28 December 2016)

Conventional nonlinear spectroscopy uses classical light to detect matter properties through the variation of its response with frequencies or time delays. Quantum light opens up new avenues for spectroscopy by utilizing parameters of the quantum state of light as novel control knobs and through the variation of photon statistics by coupling to matter. An intuitive diagrammatic approach is presented for calculating ultrafast spectroscopy signals induced by quantum light, focusing on applications involving entangled photons with nonclassical bandwidth properties—known as "time-energy entanglement." Nonlinear optical signals induced by quantized light fields are expressed using time-ordered multipoint correlation functions of superoperators in the joint field plus matter phase space. These are distinct from Glauber's photon counting formalism which uses normally ordered products of ordinary operators in the field space. One notable advantage for spectroscopy applications is that entangled-photon pairs are not subjected to the classical Fourier limitations on the joint temporal and spectral resolution. After a brief survey of properties of entangled-photon pairs relevant to their spectroscopic applications, different optical signals, and photon counting setups are discussed and illustrated for simple multilevel model systems.

DOI: 10.1103/RevModPhys.88.045008

CONTENTS

[*]dorfmank@gmail.com
[†]Also at Physikalisches Institut, Albert-Ludwigs-Universität Freiburg Hermann-Herder-Straße 3, 79104 Freiburg, Germany. Present address: Clarendon Laboratory, University of Oxford, Parks Road, Oxford OX1 3PU, United Kingdom. frank.schlawin@physics.ox.ac.uk
[‡]smukamel@uci.edu

I. INTRODUCTION

Nonlinear optics is most commonly and successfully formulated using a semiclassical approach whereby the matter degrees of freedom are treated quantum mechanically, but the radiation field is classical (Scully and Zubairy, 1997; Boyd, 2003). Spectroscopic signals are then obtained by computing the polarization induced in the medium and expanding it perturbatively in the impinging field(s) (Mukamel, 1995; Hamm and Zanni, 2011). This level of theory is well justified in many applications, owing to the typically large intensities required to generate a nonlinear response from the optical medium, which can be reached only with lasers. Incidentally, it was shortly after Maiman's development of the ruby laser that the first nonlinear optical effect was observed (Franken *et al.*, 1961).

Recent advances in quantum optics extend nonlinear signals down to the few-photon level where the quantum nature of the field is manifested and must be taken into account: The enhanced light-matter coupling in cavities (Raimond, Brune, and Haroche, 2001; Walther *et al.*, 2006; Schwartz *et al.*, 2011), the enhancement of the medium's nonlinearity by additional driving fields (Peyronel *et al.*, 2012; Chen *et al.*, 2013), large dipoles in highly excited Rydberg states (Gorniaczyk *et al.*, 2014; He *et al.*, 2014), molecular design (Loo *et al.*, 2012; Castet *et al.*, 2013), or strong focusing (Pototschnig *et al.*, 2011; Rezus *et al.*, 2012; Faez *et al.*, 2014) all provide possible means to observe and control nonlinear optical processes on a fundamental quantum level. Besides possible technological applications such as all-optical transistors (Shomroni *et al.*, 2014) or photonic quantum information processing (Franson, 1989; Braunstein and Kimble, 2000; Jennewein *et al.*, 2000; Knill, Laflamme, and Milburn, 2001; O'Brien *et al.*, 2003; U'Ren, Banaszek, and Walmsley, 2003; Kok *et al.*, 2007), these also show great promise as novel spectroscopic tools. Parameters of the photon field wave function can serve as control knobs that supplement classical parameters such as frequencies and time delays. This review surveys these emerging applications and introduces a systematic diagrammatic perturbative approach to their theoretical description.

One of the striking features of quantum light is photon entanglement. This occurs between two beams of light [field amplitudes (Van Enk, 2005)] when the quantum state of each field cannot be described in the individual parameter space of that field. Different degrees of freedom of light can become entangled. The most common types of entanglement are their spin (Dolde *et al.*, 2013), polarization (Shih and Alley, 1988), position and momentum (Howell *et al.*, 2004), time and energy (Tittel *et al.*, 1999). Entangled-photon pairs constitute an invaluable tool in fundamental tests of quantum mechanics—most famously in the violation of Bell's inequalities (Aspect, Grangier, and Roger, 1981, 1982; Aspect, Dalibard, and Roger, 1982) or in Hong, Ou, and Mandel's photon correlation experiments (Hong, Ou, and Mandel, 1987; Ou and Mandel, 1988; Shih and Alley, 1988). Besides, their nonclassical bandwidth properties have long been recognized as a potential resource in various "quantum-enhanced" applications, where the quantum correlations shared between the photon pairs may offer an advantage. For example, when one photon from an entangled pair is sent through a dispersive medium, the leading-order dispersion is compensated in photon coincidence measurements—an effect called *dispersion cancellation* (Franson, 1992; Steinberg, Kwiat, and Chiao, 1992a, 1992b; Larchuk, Teich, and Saleh, 1995; Abouraddy *et al.*, 2002; Minaeva *et al.*, 2009). In the field of quantum-enhanced measurements, entanglement may be employed to enhance the precision of the measurement beyond

the Heisenberg limit (Giovannetti, Lloyd, and Maccone, 2004, 2006; Mitchell, Lundeen, and Steinberg, 2004). Similarly, the spatial resolution may be enhanced in quantum imaging applications (Pittman *et al.*, 1995; Bennink *et al.*, 2004), quantum-optical coherence tomography (Abouraddy *et al.*, 2002; Nasr *et al.*, 2003; Esposito, 2016), as well as in quantum lithographic applications (Boto *et al.*, 2000; D'Angelo, Chekhova, and Shih, 2001).

It is now recognized that many of these applications may also be created in purely classical settings: some two-photon interference effects originally believed to be a hallmark of quantum entanglement can be simulated by postselecting the signal (Kaltenbaek *et al.*, 2008; Kaltenbaek, Lavoie, and Resch, 2009). This had enabled quantum-optical coherence tomography studies with classical light (Lavoie, Kaltenbaek, and Resch, 2009). Similarly, quantum imaging can be carried out with thermal light (Valencia *et al.*, 2005), albeit with reduced signal-to-noise ratio. When proposing applications of quantum light, it is thus imperative to carefully distinguish genuine entanglement from classical correlation effects. The approach developed here offers a unified treatment of both types of correlations.

A clear signature of the quantum nature of light is different scaling of optical signals with light intensities: Classical heterodyne $\chi^{(3)}$ signals such as two-photon absorption scale quadratically with the intensity and therefore require a high intensity to be visible against lower-order linear-scaling processes. With entangled photons, such signals scale linearly (Friberg, Hong, and Mandel, 1985; Javanainen and Gould, 1990; Georgiades *et al.*, 1995; Dayan *et al.*, 2004, 2005). This allows one to carry out microscopy (Teich and Saleh, 1998) and lithography (Boto *et al.*, 2000) applications at much lower photon fluxes. The different intensity scaling with entangled photons was first demonstrated in atomic systems by Georgiades *et al.* (1995) and later by Dayan *et al.* (2004, 2005), as well as in organic molecules (Lee and Goodson, 2006). An entangled two-photon absorption (TPA) experiment performed in a porphyrin dendrimer is shown in Fig. 1(a). The linear scaling can be rationalized as follows: entangled photons come in pairs, as they are generated simultaneously. At low light intensity, the different photon pairs are temporally well separated, and the two-photon absorption process involves two entangled photons of the same pair. The process thus behaves as a linear spectroscopy with respect to the pair. At higher intensities, it becomes statistically more plausible for the two photons to come from different pairs, which are not entangled, and the classical quadratic scaling is recovered [Fig. 1(a)] stemming from the Poisson distribution of photon pairs.

The presence of strong time-and-frequency correlations of entangled photons is a second important feature, which we will utilize extensively in the course of this review. Figure 1(b) shows the two-photon absorption signal of entangled photons in rubidium vapor (Dayan *et al.*, 2004). In the left panel, a delay stage is placed into one of the two photon beams, creating a narrow resonance as if the TPA resonance was created by a 23 fs pulse. However, as the frequency of the pump pulse which creates the photons is varied in the right panel, the resonance is also spectrally narrow, as if it was

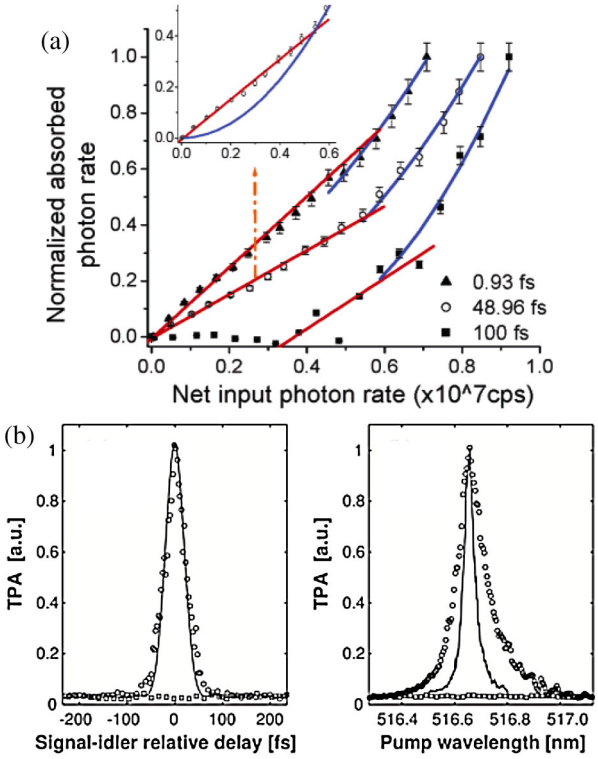

FIG. 1. (a) Linear entangled TPA rate and quadratic nonlinear random TPA rate in a porphyrin dendrimer at different entanglement times. The inset shows the dominant effect of the entangled TPA at low input flux of correlated photons. From Lee and Goodson, 2006. (b) Two-photon absorption $5S_{1/2} \rightarrow 4D_{5/2,3/2}$ in atomic rubidium vs the time delay between the two photons (left panel) and vs the pump frequency (right panel). From Dayan *et al.*, 2004.

created by a ns pulse. This simultaneous time-and-frequency resolution along non-Fourier conjugate axes is a hallmark of the time-energy entanglement, and its exploitation as a spectroscopic tool offers novel control knobs to manipulate the excited-state distribution and thereby enhance or suppress selected features in nonlinear spectroscopic signals.

In a different line of research, the seminal photon coincidence counting experiments were turned into a spectroscopic tool by placing a sample into the beam line of one of the two entangled photons and recording the change of the coincidence count rate (Yabushita and Kobayashi, 2004; Kalachev *et al.*, 2007, 2008; Kalashnikov *et al.*, 2014; Li *et al.*, 2015). We examine related schemes for utilizing entanglement in nonlinear spectroscopy.

This review is structured as follows: In Sec. I.A, we briefly give the background and introduce the superoperator formalism used to describe spectroscopy with quantum light. In Sec. I.B we describe the diagram construction. In Sec. II we discuss properties of entangled photons and present their impact on excited-state distributions upon their absorption in a complex quantum system. In Sec. III we provide general superoperator expressions for nonlinear optical signals and review available setups. Finally, Sec. IV presents a general classification of nonlinear optical processes induced by quantum light, clarifying under which conditions its quantum nature may play a role.

A. Liouville space superoperator notation

The calculation of nonlinear optical signals becomes most transparent and simple by working in Liouville space (Mukamel, 1995; Mukamel and Nagata, 2011), i.e., the space of bounded operators on the combined matter-field Hilbert space. It offers a convenient compact bookkeeping device for matter-light interactions where signals are described as time-ordered products of superoperators.

Here we introduce the basic superoperator notation. With each operator A acting on the Hilbert space, we associate two superoperators (Chernyak, Wang, and Mukamel, 1995; Harbola and Mukamel, 2008; Roslyak and Mukamel, 2009b, 2010)

$$A_L X \equiv AX, \tag{1}$$

which represents the action from the left on another operator X, and

$$A_R X \equiv XA, \tag{2}$$

representing the action from the right. We further introduce their linear combinations, the commutator superoperator

$$A_- \equiv A_L - A_R, \tag{3}$$

and the anticommutator

$$A_+ \equiv \tfrac{1}{2}(A_L + A_R). \tag{4}$$

This notation allows one to derive compact expressions for spectroscopic signals. At the end of the calculation, after the time ordering is taken care of, we can switch back to ordinary Hilbert space operators.

The total Hamiltonian of the field-matter system is given by

$$H_{\rm tot} = H_0 + H_{\rm field} + H_{\rm int}. \tag{5}$$

H_0 describes the matter, and the radiation field Hamiltonian is given by

$$H_{\rm field} = \hbar \sum_s \omega_s a_s^\dagger(\omega_s) a_s(\omega_s). \tag{6}$$

Here we introduced the creation (annihilation) operators for mode s which satisfy bosonic commutation relations $[a_s, a_{s'}^\dagger] = \delta_{s,s'}$ and $[a_s, a_{s'}] = [a_s^\dagger, a_{s'}^\dagger] = 0$. In some applications, we replace the discrete sum over modes by a continuous integral $\sum_s \to [V/(2\pi)^3] \int d\omega_s \tilde{D}(\omega_s)$ with $\tilde{D}(\omega_s)$ being the density of states that we assume to be flat within the relevant bandwidths $\tilde{D}(\omega_s) \simeq \tilde{D}$.

We assume a dipole light-matter interaction Hamiltonian,

$$H_{\rm int} = \epsilon \sum_\nu \mathcal{V}_\nu, \tag{7}$$

where $\mathcal{V}_\nu = V_\nu + V_\nu^\dagger$ is the dipole operator of molecule ν with the summation running over all the molecules contained in the sample. V ($V^\dagger$) is the excitation lowering (raising) part of the dipole. $\epsilon = E + E^\dagger$ denotes the electric field operator and E ($E^\dagger$) are its positive (negative) frequency components which can be written in the interaction picture with respect to the field Hamiltonian (Loudon, 2000) as

$$E(t) = \int \frac{d\omega}{2\pi} e^{-i\omega t} a(\omega) \tag{8}$$

which is written in the slowly varying envelope approximation. Hereafter unless specified otherwise, E denotes the sum of all relevant field modes. Note that the field normalization is absorbed in the dipole matrix element in Eq. (7).

In the following applications, we neglect rapidly oscillating terms, by employing the dipole Hamiltonian in the rotating wave approximation (RWA),

$$H_{\rm int,RWA} = EV^\dagger + E^\dagger V. \tag{9}$$

B. Diagram construction

We adopt the diagram representation of nonlinear spectroscopic signals as summarized, for instance, by Mukamel and Rahav (2010). It bears close similarity to analogous methods in quantum electrodynamics (Cohen-Tannoudji *et al.*, 1992). We employ two types of diagrams for calculating the expectation value of an operator $A(t)$, which are based on either the density matrix or the wave function. For details, see Appendix A. First we evaluate it by propagating the density matrix $\rho(t)$,

$$\langle A(t) \rangle_{\rm DM} \equiv {\rm tr}\{A(t)\varrho(t)\}. \tag{10}$$

Equation (10) can be best analyzed in Liouville space (3): We write the time evolution of the joint matter plus field density matrix using a time-ordered exponential which can be expanded as a Dyson series,

$$\varrho(t) = \mathcal{T} \exp\left[-\frac{i}{\hbar}\int_{t_0}^t d\tau H_{{\rm int},-}(\tau)\right]\varrho(t_0), \tag{11}$$

where $H_{\rm int-}$ is a superoperator (3) that corresponds to the interaction Hamiltonian (7) written in the interaction picture with respect to H_0 plus $H_{\rm field}$. The time-ordering operator $\mathcal{T}$ orders the following products of superoperators so that their time arguments increase from right to left. For example when acting on two arbitrary superoperators $A(t)$ and $B(t)$,

$$\begin{aligned}\mathcal{T}A(t_1)B(t_2) \equiv{}& \theta(t_1 - t_2)A(t_1)B(t_2) \\ &+ \theta(t_2 - t_1)B(t_2)A(t_1).\end{aligned} \tag{12}$$

The perturbative expansion of Eq. (11) to nth order in $H_{\rm int}$ generates a number of pathways—successions of excitations and deexcitations on both the bra or the ket part of the density matrix. These pathways are depicted by double-sided ladder diagrams, which represent convolutions of fully time-ordered superoperator nonequilibrium Green's functions (SNGF) of the form (Roslyak and Mukamel, 2010)

$$\begin{aligned}&\int_0^\infty dt_1 \cdots \int_0^\infty dt_n \mathbb{V}^{(n)}_{\nu_n \cdots \nu_1}(t - t_n \ldots, t - t_n \cdots - t_1) \\ &\quad \times \mathbb{E}^{(n)}_{\nu_n \cdots \nu_1}(t - t_n \ldots, t - t_n \cdots - t_1).\end{aligned} \tag{13}$$

The field SNGF in Eq. (13)

$$\mathbb{E}^{(n)}_{\nu_n\cdots\nu_1}(t-t_n\ldots,t-t_n\cdots-t_1) = \langle \mathcal{T} E_{\nu_n}(t-t_n)\cdots E_{\nu_1}(t-t_n\cdots-t_1)\rangle \tag{14}$$

is evaluated with respect to the initial quantum state of the light. The indices are $\nu_j = L, R$ or $\nu_j = +, -$. When replacing the field operators by classical amplitudes, we recover the standard semiclassical formalism of quantum optics (Mukamel, 1995). Similarly, we may also convert the field operators into classical random variables to describe spectroscopic signals with stochastic light (Asaka *et al.*, 1984; Beach and Hartmann, 1984; Morita and Yajima, 1984; Turner *et al.*, 2013).

The material SNGFs in Eq. (13) are similarly defined:

$$\mathbb{V}^{(n)}_{\nu_n\cdots\nu_1}(t-t_n\ldots,t-t_n\cdots-t_1) = \langle V^{(\dagger)}_{\nu_n}\mathcal{G}(t_n)\cdots\mathcal{G}(t_1)V^{(\dagger)}_{\nu_1}\rangle, \tag{15}$$

where

$$\mathcal{G}(t) = -\frac{i}{\hbar}\theta(t)\exp\left[-\frac{i}{\hbar}H_0 t\right] \tag{16}$$

denotes the propagator of the free evolution of the matter system, and $\nu_j = L, R$. Similarly SNGF may be obtained by replacing $V^\dagger$ by V and E by $E^\dagger$. This representation further allows for reduced descriptions of open systems where bath degrees of freedom are eliminated.

As an example, the set of fourth-order pathways for the population of state f in a three-level scheme shown in Fig. 2(a) are given in Fig. 2(b). We shall repeatedly refer to these pathways in the course of this review. This ladder diagram representation is most suitable for impulsive experiments involving sequences of short, temporally well-separated pulses, as is done from nuclear magnetic resonance (NMR) to the x-ray regimes (Mukamel, 1995; Hamm and Zanni, 2011). In such multidimensional experiments, the time variables used to represent the delays between successive pulses (Abramavicius *et al.*, 2009) $t_1, t_2, t_3, \ldots$ serve as the primary control parameters. Spectra are displayed versus the Fourier conjugates $\tilde{\Omega}_1, \tilde{\Omega}_2, \tilde{\Omega}_3, \ldots$ of these time variables.

As indicated in Fig. 2(b), each interaction with a field also imprints its phase ϕ onto the signal. Filtering the possible phase combinations $\pm\phi_1 \pm \phi_2 \pm \phi_3 \pm \phi_4$ of the signal, known as phase cycling, allows for the selective investigation of specific material properties (Keusters, Tan, and Warren, 1999; Scheurer and Mukamel, 2001; Tian *et al.*, 2003; Tan, 2008; Abramavicius *et al.*, 2009; Zhang, Wells, Hyland, and Tan, 2012; Zhang, Wells, and Tan, 2012; Krčmář, Gelin, and Domcke, 2013). Acousto-optical modulation discussed in Raymer *et al.* (2013) offers the possibility to achieve this selectivity even at the single-photon level. Phase-cycling techniques have been successfully demonstrated as control tools for the selection of fixed-phase components of optical signals generated by multiwave mixing (Keusters, Tan, and Warren, 1999; Tian *et al.*, 2003; Tan, 2008; Zhang, Wells, Hyland, and Tan, 2012; Zhang, Wells, and Tan, 2012). Phase cycling can be easily implemented by varying the relative interpulse phases using a pulse shaper, which is cycled over 2π radians in a number of equally spaced steps (Keusters, Tan, and Warren, 1999; Tian *et al.*, 2003).

Rather than propagating the density matrix Eq. (10), we can alternatively follow the evolution of the wave function by

$$\langle A(t)\rangle_{\mathrm{WF}} \equiv \langle \psi(t)|A(t)|\psi(t)\rangle, \tag{17}$$

with

$$|\psi(t)\rangle = \mathcal{T}\exp\left(-\frac{i}{\hbar}\int_{t_0}^{t} d\tau H'_{\mathrm{int}}(\tau)\right)|\psi(t_0)\rangle. \tag{18}$$

Keeping track of the wave function results in different pathways which can be represented by loop diagrams. Rather than propagating of both the bra and the ket, we can then place the entire burden of the time evolution on the ket and write

$$\langle A(t)\rangle = \langle \psi(t_0)|\tilde{\psi}(t)\rangle, \tag{19}$$

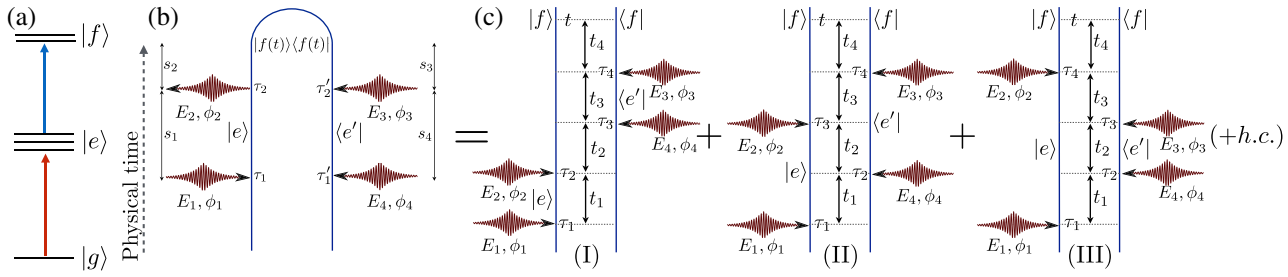

FIG. 2. (a) The three-level scheme which we consider in most of the review consists of a unique ground state $|g\rangle$, and single excited state manifold $|e\rangle$ and doubly excited manifold $|f\rangle$. The vertical arrows indicate dipole-allowed transitions. (b) The single loop diagram representing the evolution of the wave function. On the left-hand side, the vertical line represents the ket and on the right-hand side it corresponds to the bra. The wave function in this closed time path loop diagram propagates forward in a loop from the bottom branch of the diagram along the ket branch to the top of the diagram. It then evolves backward in time from the top to the bottom of the right branch (bra). This forward and backward propagation is similar to the Keldysh contour diagram rules (Keldysh, 1965). Horizontal arrows represent field-matter interactions. (c) The corresponding three ladder diagrams for the evolution of the density matrix. Here the density matrix evolves forward in time upward from the bottom to the top of the diagram. In order to achieve a doubly excited-state population starting from the ground state the density matrix has to undergo four interactions represented by the absorption of two photons represented by four inwardly directed arrows. The three diagrams represent different time orderings of ket vs bra interactions. Together with their mirror reflected diagrams (interchanging left and right sides of the diagram) the total six diagrams are lumped together in the single loop diagram (b).

where

$$|\tilde{\psi}(t)\rangle = \mathcal{T}^{-1}\exp\left(\frac{i}{\hbar}\int_{t_0}^{t} d\tau H'_{\rm int}(\tau)\right)A(t) \times \mathcal{T}\exp\left(-\frac{i}{\hbar}\int_{t_0}^{t} d\tau H'_{\rm int}(\tau)\right)|\psi(t_0)\rangle, \quad (20)$$

and $\mathcal{T}^{-1}$ denotes the anti-time-ordering operator (time increases from left to right). Here the ket first evolves forward and then backward in time, eventually returning to the initial time (Schwinger, 1961; Keldysh, 1965). Back propagation of the ket is equivalent to forward propagation of the bra. The resulting terms are represented by loop diagrams as is commonly done in many-body theory (Rammer, 2007; Mukamel, 2008; Rahav and Mukamel, 2010; Hansen and Pullerits, 2012).

As can be seen from Fig. 2, this representation yields a more compact description (fewer pathways) of the signals than the density matrix, since the relative time ordering of ket and bra interactions is not maintained. In this example, the f-state population is given by a single loop diagram, which can be separated into the sum of the six ladder diagrams (the three shown plus their complex conjugates obtained by interchanging all left and right interactions). It is harder to visualize short pulse fully time ordered experiments in this representation, and due to the backward time propagation the elimination of bath degrees of freedom in an open system is not possible. Nevertheless, this representation proves most useful and compact for frequency-domain techniques involving long pulses where time ordering is not maintained anyhow (Rahav and Mukamel, 2010) and for many-body simulations that are usually carried out in Hilbert space (Dalibard, Castin, and Mølmer, 1992).

The double-sided (ladder) and the loop diagrams constitute two bookkeeping devices for field-matter interactions. The loop diagrams suggest several wave-function-based simulation strategies for signals (Dorfman, Fingerhut, and Mukamel, 2013a). The first is based on the numerical propagation of the wave function, which includes all relevant electronic and nuclear (including bath) degrees of freedom explicitly. A second protocol uses a sum-over-states (SOS) expansion of the signals. In the third, semiclassical approach a small subsystem is treated quantum mechanically and is coupled to a classical bath, which causes a time-dependent modulation of the system Hamiltonian. The third approach for a wave function is equivalent to the stochastic Liouville equation for the density matrix (Tanimura, 2006), which is based on the ladder diagram book keeping.

II. STATES OF QUANTUM LIGHT

In this section, we first discuss classical light which is the basis for the semiclassical approximation of nonlinear spectroscopy. We then briefly describe the main concepts from Glauber's photon counting theory for a single mode of the electromagnetic field. Finally, we discuss in detail the multimode entangled states of light, which will be repeatedly used in this review.

A. Classical versus quantum light

Clearly, our world is governed by quantum mechanics, and so on a fundamental level light is always quantum. Yet, in many situations a classical description of the light field may be sufficient (Scully and Zubairy, 1997; Boyd, 2003). For pedagogical reasons, before we describe properties of quantum light, we first discuss in some detail how the classical description of the field emerges from quantum mechanics, and, more importantly, under which circumstances this approximation may break down.

The coherent state of the field, i.e., the eigenstate of the photon annihilation operator at frequency ω, is generally considered as "classical." In this state the annihilation operator, and hence the electric field operator, has a nonvanishing expectation value $\langle a(\omega)\rangle \neq 0$. In general, we can write a multimode coherent state as

$$|\phi_{\rm coh}(t)\rangle = \int d\omega e^{\alpha_\omega(t)a^\dagger(\omega)-\alpha^*_\omega(t)a(\omega)}|0\rangle, \quad (21)$$

where the mode amplitudes α are given by

$$\alpha_\omega(t) = \alpha_\omega e^{-i\omega t}. \quad (22)$$

In a normally ordered correlation function (all $a^\dagger$ are to the left of all a), we may then simply replace the field operators in the correlation functions by classical amplitudes (Mandel and Wolf, 1995),

$$E_\nu(t) \to \int d\omega \alpha^\nu_\omega e^{\pm i\omega t}. \quad (23)$$

However, a coherent state is not yet sufficient for the field to be classical: As seen in Eq. (13), the light field enters into spectroscopic signals through its multipoint correlation function $\mathbb{E}^{(n)}_{\nu_n\cdots\nu_1}(t-t_n\ldots, t-t_n\cdots-t_1)$. These correlation functions can always be rewritten as the sum of a normally ordered term labeled $\langle:\cdots:\rangle$ and lower-order normal correlation functions multiplied with commutator terms

$$\begin{aligned}\mathbb{E}^{(n)}_{\nu_n\cdots\nu_1}(t-t_n\ldots, t-t_n\cdots-t_1) &= \langle:E_{\nu_n}(t-t_n)\cdots E_{\nu_1}(t-t_n\cdots-t_1):\rangle \\ &+ [E_{\nu_n}(t-t_n), E_{\nu_{n-1}}(t-t_n-t_{n-1})] \\ &\times \mathbb{E}^{(n)}_{\nu_{n-2}\cdots\nu_1}(t-t_n-t_{n-1}-t_{n-2}\ldots, t-t_n\cdots-t_1)+\cdots.\end{aligned} \quad (24)$$

For the semiclassical limit to hold, we must be able to neglect all the terms containing field commutators. This is typically the case when the intensity of the coherent state, i.e., its mean photon number is very large.

More generally, probability distributions of coherent states are classical (Mandel and Wolf, 1995): States, whose density matrix has a diagonal Glauber-Sudarshan P representation, are considered classical. This includes classical stochastic fields, which show nonfactorizing field correlation functions (for instance, for Gaussian statistics with $\langle E\rangle = 0$ and

$\langle E^\dagger E\rangle \neq 0$). Such classical correlations can also be employed in spectroscopy (Turner *et al.*, 2013), but are not the focus of this review.

According to this strict criterion, any other quantum state is considered nonclassical. However, that does not mean that such state will also show nonclassical features, and the elucidation of genuine quantum effects in a given experiment is often very involved; see, e.g., the discussion around dispersion cancellation with entangled photons (Franson, 1992; Steinberg, Kwiat, and Chiao, 1992b), or quantum imaging (Bennink *et al.*, 2004; Valencia *et al.*, 2005).

The interest in quantum light for spectroscopy is twofold: As stated by Walmsley (2015), "the critical features of quantum light […] are exceptionally low noise and strong correlations." In the following section, we first discuss the noise properties of quantum light, i.e., quantum correlations within a single electromagnetic mode. The rest of the section is devoted to strong time-frequency correlations, i.e., quantum correlations between different modes, which are the main focus of this review.

B. Single mode quantum states

In confined geometries, the density of states of the electromagnetic field can be altered dramatically. In a cavity, the mode spacing may be large so that we can describe the field by a single radiation mode with well-defined frequency ω_0, which may be strongly coupled to dipoles inside the cavity. In this section, we study this case, where we can write the cavity field Hamiltonian simply as

$$H_{\mathrm{cav}} = \hbar\omega_0 a^\dagger a, \tag{25}$$

where a ($a^\dagger$) describes the photon annihilation (creation) operator of the cavity mode. We introduce the dimensionless cavity field quadratures

$$x = \frac{1}{\sqrt{2}}(a + a^\dagger), \tag{26}$$

$$p = \frac{1}{\sqrt{2}i}(a - a^\dagger), \tag{27}$$

which represent the real and imaginary parts of the electric field, respectively. A whole family of quadratures $x(\theta)$ and $p(\theta)$ may be obtained by rotating the field operators as $a \to ae^{-i\theta}$.

Quantum mechanics dictates the Heisenberg uncertainty

$$\langle \Delta x^2\rangle\langle \Delta p^2\rangle \geq \tfrac{1}{4} \tag{28}$$

for any quantum state.

Coherent states are minimal uncertainty states, in which the lower bound in Eq. (28) applies

$$\langle \Delta x^2\rangle = \langle \Delta p^2\rangle = \tfrac{1}{2}. \tag{29}$$

This coincides with the quantum fluctuations of the vacuum state. Any quantum state that features fluctuations in one of its quadratures below this fundamental limit $1/2$ is therefore said to be squeezed. Note that due to the Heisenberg uncertainty (28) the conjugate quadrature must show larger fluctuations.

The simplest example thereof is the squeezed vacuum state

$$|\xi\rangle = e^{(1/2)\xi a^2 - (1/2)\xi^* a^{\dagger 2}}|0\rangle, \tag{30}$$

where

$$\langle \Delta x^2\rangle = \tfrac{1}{2}e^{-2|\xi|}, \tag{31}$$

$$\langle \Delta p^2\rangle = \tfrac{1}{2}e^{2|\xi|}. \tag{32}$$

Thus, a squeezed vacuum state is also a minimum uncertainty state.

These fluctuations show up in nonlinear signals, as discussed in Sec. III.A. In the remainder of this section, we focus on multimode analogs of such squeezed states and show how new correlations arise due to the multimode structure of the field. This is known as time-energy entanglement.

C. Photon entanglement in multimode states

Before presenting some specific models for quantum light, we first discuss time-energy entanglement in a more general setting. An exhaustive discussion of continuous variable entanglement theory can be found in a number of reviews (Kok *et al.*, 2007; Lvovsky and Raymer, 2009). Here we briefly introduce some important properties of entangled-photon pairs. These will later be used to distinguish genuine entanglement from other broad bandwidth properties, which could also be encountered with classical light sources.

We are concerned with pairs of distinguishable photons that are described by separate Hilbert spaces $\mathcal{H}^{(1)}_{\mathrm{field}}$ and $\mathcal{H}^{(2)}_{\mathrm{field}}$. They may be distinguished, e.g., by their polarization, their frequencies, or their wave vectors and propagation direction. A two-photon state may be generally expanded as

$$|\psi\rangle = \int d\omega_a \int d\omega_b \tilde{\Phi}(\omega_a,\omega_b) a_1^\dagger(\omega_a) a_2^\dagger(\omega_b)|0\rangle_1|0\rangle_2, \tag{33}$$

where $\tilde{\Phi}(\omega_a,\omega_b)$ is the two-photon amplitude.

To analyze the properties of this state, it is convenient to map it onto a discrete basis. This can be achieved by the singular value decomposition of the two-photon amplitude (Law, Walmsley, and Eberly, 2000; Law and Eberly, 2004; McKinstrie and Karlsson, 2013; McKinstrie, Ott, and Karlsson, 2013)

$$\tilde{\Phi}(\omega_a,\omega_b) = \sum_{k=1}^{\infty} \tilde{r}_k \psi_k^*(\omega_a)\phi_k^*(\omega_b), \tag{34}$$

where $\{\psi_k\}$ and $\{\phi_k\}$ form orthonormal bases, known as the Schmidt modes, and $\tilde{r}_k$ are the mode weights. These are obtained by solving the eigenvalue equations

$$\int d\omega' \kappa_1(\omega,\omega')\psi_k(\omega') \equiv \tilde{r}_k^2 \psi_k(\omega), \tag{35}$$

with

$$\kappa_1(\omega,\omega') = \int d\omega'' \tilde{\Phi}^*(\omega,\omega'')\tilde{\Phi}(\omega',\omega''), \tag{36}$$

and

$$\int d\omega' \kappa_2(\omega,\omega')\phi_k(\omega') \equiv \tilde{r}_k^2 \phi_k(\omega), \tag{37}$$

with

$$\kappa_2(\omega,\omega') = \int d\omega'' \tilde{\Phi}^*(\omega'',\omega)\tilde{\Phi}(\omega'',\omega'). \tag{38}$$

We can then recast Eq. (33) using Eq. (34)

$$|\psi\rangle = \sum_{k=1}^{\infty} \tilde{r}_k \int d\omega_a \int d\omega_b \psi_k^*(\omega_a)\phi_k^*(\omega_b) a_1^\dagger(\omega_a) a_2^\dagger(\omega_b)|0\rangle_1|0\rangle_2. \tag{39}$$

The Schmidt decomposition (34) may be used to quantify the degree of entanglement between photon pairs. Rewriting the singular values as $\tilde{r}_k = \sqrt{B}\lambda_k$, where B denotes the amplification factor of the signal and λ_k the normalized set of singular values of the normalized two-photon state, with $\sum_k \lambda_k^2 = 1$. A useful measure of entanglement is provided by the entanglement entropy (Law, Walmsley, and Eberly, 2000)

$$E(\psi) = -\sum_k \lambda_k^2 \ln(\lambda_k^2). \tag{40}$$

In quantum information applications, $E(\psi)$ represents the effective dimensionality available to store information in the state.

We call the state (33) *separable* if the two-photon amplitude factorizes into the product of single-photon amplitudes $\tilde{\Phi}(\omega_a,\omega_b) = \tilde{\Phi}^{(1)}(\omega_a)\tilde{\Phi}^{(2)}(\omega_b)$. This implies that $\lambda_{k\neq 1} = 0$, so that the entanglement entropy is $E = 0$. In this situation, no correlations exist between the two photons: Measuring the frequency of photon 1 will not alter the wave function of the other photon. Otherwise, the state is entangled. We then have $\lambda_i < 1$, and correspondingly $E > 0$; measuring the frequency of photon 1 now reduces photon 2 to a mixed state described by the density matrix,

$$\varrho_2 \sim \sum_k |\psi_k(\omega_a^{(0)})|^2 \times \int d\omega_b \int d\omega_b' \phi_k^*(\omega_b)\phi_k(\omega_b') a_2^\dagger(\omega_b)|0\rangle\langle 0|a_2(\omega_b'), \tag{41}$$

and the measurement outcome $\omega_a^{(0)}$ thus influences the quantum state of photon 2.

D. Entangled photons generation by parametric downconversion

Entangled-photon pairs are routinely created, manipulated, and detected in a variety of experimental scenarios. These include decay of the doubly excited states in semiconductors (Edamatsu *et al.*, 2004; Stevenson *et al.*, 2007), four-wave mixing in optical fibers (Garay-Palmett *et al.*, 2007, 2008) or cold atomic gases (Balić *et al.*, 2005; Cho *et al.*, 2014). Here we focus on the oldest and most established method for their production—parametric downconversion (PDC) in birefringent crystals (Wu *et al.*, 1986; Kwiat *et al.*, 1995).

We shall introduce the basic Hamiltonian which governs the PDC generation process and discuss the output fields it creates. These will then be applied to calculate spectroscopic signals. We restrict our attention to squeezed vacuum, where the field modes are initially in the vacuum state and become populated only through the PDC process [see also Eqs. (251)–(255)].

In the PDC setup, a photon from a strong pump pulse is converted into an entangled-photon pair by the interaction with the optical nonlinearity in the crystal (as discussed in detail in Sec. IV). A birefringent crystal features two ordinary optical axes (o), and an extraordinary optical axis (e) in which the group velocity of optical light is different. The PDC process can be triggered in different geometries: One distinguishes type-I ($e \to oo$) and type-II ($o \to eo$) downconversion (Shih, 2003), and more recently type 0 (Abolghasem *et al.*, 2010; Lerch *et al.*, 2013). The two photons show strong time-and-frequency correlations stemming from the conservation of energy and momentum: Since they are created simultaneously, the two photons are strongly correlated in their arrival time at the sample or detector, such that each individual photon wave packet has a very broad bandwidth. At the same time, the sum of the two photon frequencies has to match the energy of the annihilated pump photon, which may be more sharply defined than the individual photons (the pump photon bandwidth is typically below 100 MHz in the visible regime).

The created photon pairs are entangled in their frequency, position, and momentum degree of freedom (Walborn *et al.*, 2010). The setup may be exploited to control the central frequencies of the involved fields (Grice and Walmsley, 1997). For simplicity, we consider a collinear geometry of all fields. This simplifies the notation, while retaining the time-frequency correlations, which are most relevant in spectroscopic applications. After passing through the nonlinear crystal, the state of the light field is given by (Christ *et al.*, 2011, 2013)

$$|\psi_{\rm out}\rangle = \exp\left[-\frac{i}{\hbar}H_{\rm PDC}\right]|0\rangle_1|0\rangle_2 \equiv U_{\rm PDC}|0\rangle_1|0\rangle_2. \tag{42}$$

Equation (42) neglects four-, six-, etc., photon processes in which only the total energy is conserved. In PDC, this approximation is shown to work well beyond the single-photon regime [see Fig. 4 in Christ *et al.* (2013), where only minor deviations occur at a mean photon number larger than 1]. The propagator $U_{\rm PDC}$ depends on the effective Hamiltonian

$$H_{\rm PDC} = \int d\omega_a \int d\omega_b \Phi(\omega_a,\omega_b) a_1^\dagger(\omega_a) a_2^\dagger(\omega_b) + \text{H.c.}, \tag{43}$$

which creates or annihilates pairs of photons, whose joint bandwidth properties are determined by the two-photon amplitude

$$\Phi(\omega_a,\omega_b)=\alpha A_p(\omega_a+\omega_b)\mathrm{sinc}\left(\frac{\Delta k(\omega_a,\omega_b)L}{2}\right)e^{i\Delta kL/2}. \tag{44}$$

Here A_p is the normalized pump pulse envelope and $\mathrm{sinc}(\Delta kL/2)$ with $\mathrm{sinc}x=\sin x/x$ denotes the phase-matching function, which originates from wave vector mismatch inside the nonlinear crystal $\Delta k(\omega_a,\omega_b)=k_p(\omega_a+\omega_b)-k_1(\omega_a)-k_2(\omega_b)$. $k_i(\omega)$ denotes the wave vector of either the pump or beams 1 or 2 at frequency ω. The prefactor α which is proportional to the pump amplitude determines the strength of the PDC process (and hence the mean photon number). Hence, in contrast to $\tilde{\Phi}$ in the enangled state (33), the two-photon amplitude Φ is not normalized, but increases with the pump intensity.

Typically, the wave vector mismatch $\Delta k(\omega_a,\omega_b)$ depends very weakly on the frequencies ω_a and ω_b. It is then possible to expand it around the central frequencies ω_1 and ω_2 of the two downconverted beams. For type-I downconversion, the group velocities $dk_1/d\omega_1$ and $dk_2/d\omega_2$ are identical [unless the PDC process is triggered in a strongly nondegenerate regime (Kalachev *et al.*, 2008)], and the expansion around the central frequencies yields (Joobeur, Saleh, and Teich, 1994; Wasilewski *et al.*, 2006)

$$\begin{aligned}\Delta k(\omega_a,\omega_b)L/2=&\left(\frac{dk_p}{d\omega_p}-\frac{dk}{d\omega}\right)L/2(\omega_a+\omega_b-\omega_p)\\&+\frac{1}{2}\frac{d^2k_p}{d\omega_p^2}L/2(\omega_a+\omega_b-\omega_p)^2\\&-\frac{1}{2}\frac{d^2k}{d\omega^2}L/2[(\omega_a-\omega_1)^2+(\omega_b-\omega_2)^2].\end{aligned} \tag{45}$$

The first two terms of Eq. (45) create correlations between the two photon frequencies, while the third determines the bandwidth of the individual photons.

In type-II downconversion, the group velocities of the two beams differ, and the wave vector mismatch may be approximated to linear order in frequency (Rubin *et al.*, 1994; Keller and Rubin, 1997)

$$\Delta k(\omega_a,\omega_b)L/2=(\omega_a-\omega_1)T_1/2+(\omega_b-\omega_2)T_2/2, \tag{46}$$

where the two time scales $T_1=L(dk_p/d\omega_p-dk_1/d\omega_1)$ and $T_2=L(dk_p/d\omega_p-dk_2/d\omega_2)$ denote the maximal time delays the two photon wave packets can acquire with respect to the pump pulse during their propagation through the crystal. Without loss of generality, we assume $T_2>T_1$. In the following applications we consider type-II phase matching (46). The corresponding wave functions may be controlled to maintain frequency correlations, as elaborated on in Sec. II.G.

We will focus on the weak downconversion regime, in which the output light fields are given by entangled-photon pairs,

$$|\psi_{\mathrm{twin}}\rangle\approx-\frac{i}{\hbar}H_{\mathrm{PDC}}|0\rangle_1|0\rangle_2. \tag{47}$$

Equation (47) takes the form of the entangled two-photon state, Eq. (33), discussed earlier, where $\tilde{\Phi}$ denotes the normalized two-photon amplitude. We review the quantum correlations of the created fields upon excitation by a cw pump, which simplifies the discussion, or finite-bandwith pump pulses. The two cases require different theoretical tools.

E. Narrow-band pump

One important class of time-frequency entangled-photon pairs is created by pumping the nonlinear crystal with a narrow bandwidth laser, where the pump spectral envelope in Eq. (44) is given as

$$A_p(\omega_a+\omega_b)\simeq\delta(\omega_a+\omega_b-\omega_p). \tag{48}$$

Using Eqs. (46) and (48), the phase mismatch in Eq. (44) can be expressed as (Peřina, Saleh, and Teich, 1998)

$$\begin{aligned}&\mathrm{sinc}\left(\frac{\Delta k(\omega_a,\omega_b)L}{2}\right)e^{i\Delta kL/2}\\&\quad=\mathrm{sinc}\Big[(\omega_1-\omega_a)T/2\Big]e^{i(\omega_1-\omega_a)T/2},\end{aligned} \tag{49}$$

where $T\equiv T_2-T_1$ is the entanglement time, which represents the maximal time delay between the arrival of the two entangled photons. For a cw pump laser, the first photon arrives at a completely random time, but the second photon necessarily arrives within the entanglement time. This property has been exploited in several proposals to probe ultrafast material processes using a cw photon pair source (Roslyak and Mukamel, 2009a; Raymer *et al.*, 2013).

Entangled photons affect optical signals via their multipoint correlation functions (Roslyak, Marx, and Mukamel, 2009b; Mukamel and Nagata, 2011). The relevant field quantity in most applications discussed later, describing the interaction of pairs of photons with a sample, is the four-point correlation function. Using Eqs. (48) and (49), for the entangled state (47) this correlation function can be factorized as

$$\begin{aligned}&\langle E^\dagger(\omega_a')E^\dagger(\omega_b')E(\omega_b)E(\omega_a)\rangle\\&\quad=\langle\psi_{\mathrm{twin}}|E^\dagger(\omega_a')E^\dagger(\omega_b')|0\rangle\langle 0|E(\omega_b)E(\omega_a)|\psi_{\mathrm{twin}}\rangle.\end{aligned} \tag{50}$$

Here

$$\begin{aligned}\langle 0|E(\omega_b)E(\omega_a)|\psi_{\mathrm{twin}}\rangle=&\,\mathcal{N}\delta(\omega_a+\omega_b-\omega_p)\\&\times\{\mathrm{sinc}[(\omega_1-\omega_a)T/2]e^{i(\omega_1-\omega_a)T/2}\\&+\mathrm{sinc}[(\omega_1-\omega_b)T/2]e^{i(\omega_1-\omega_b)T/2}\}\end{aligned} \tag{51}$$

is known as the two-photon wave function (Rubin *et al.*, 1994).

Upon switching to the time domain, we obtain

$$\begin{aligned}&\int d\omega_a\int d\omega_b e^{-i(\omega_a t_1+\omega_b t_2)}\langle 0|E(\omega_b)E(\omega_a)|\psi_{\mathrm{twin}}\rangle\\&\quad=\mathcal{N}'e^{-i(\omega_1 t_1+\omega_2 t_2)}\mathrm{rect}\left(\frac{t_2-t_1}{T}\right)\\&\qquad+\mathcal{N}'e^{-i(\omega_2 t_1+\omega_1 t_2)}\mathrm{rect}\left(\frac{t_1-t_2}{T}\right),\end{aligned} \tag{52}$$

where $\mathrm{rect}(x) = 1$ for $0 \le x \le 1$ and zero otherwise, and $\mathcal{N}$, $\mathcal{N}'$ denote the normalization of the two-photon wave function. The physical significance of the entanglement time is now clear: it sets an upper bound for the arrival of the second photon, given the arrival of the first one. Note that Eq. (52) is symmetric with respect to t_1 and t_2 because each interaction occurs with the entire field $E = E_1 + E_2$. In a situation where $\langle 0|E_2(t_2)E_1(t_1)|\psi_{\mathrm{twin}}\rangle$ is measured, the two-photon wave function is not symmetric.

F. Broadband pump

We next consider entangled light created by a pump pulse with a normalized Gaussian envelope,

$$A_p(\omega_a + \omega_b) = \frac{1}{\sqrt{2\pi\sigma_p^2}} \exp\left(-\frac{(\omega_a + \omega_b - \omega_p)^2}{2\sigma_p^2}\right). \tag{53}$$

This is a realistic model in many experimental scenarios.

The analysis of Eq. (42) becomes most transparent by switching to a basis obtained by the Schmidt decomposition (34) of the two-photon wave function. The mode weights r_k are positive and form a monotonically decreasing series, such that in practical applications the sum in Eq. (34) may be terminated after a finite number of modes. (For a cw pump, an infinite number of Schmidt modes is required to represent the delta function.) In Appendix B, we present approximate analytic expressions for the eigenfunctions $\{\psi_k\}$ and $\{\phi_k\}$. The following analysis is restricted to a PDC regime in which six- (and higher) photon processes may be neglected. Such corrections can affect the bandwidth properties at very high photon numbers (Christ *et al.*, 2013). The linear to quadratic intensity crossover of signals is further discussed in Sec. II.J.3.

We next introduce the Schmidt mode operators

$$A_k = \int d\omega_a \psi_k(\omega_a) a_1(\omega_a) \tag{54}$$

and

$$B_k = \int d\omega_b \phi_k(\omega_b) a_2(\omega_b), \tag{55}$$

which inherit the bosonic commutation relations from the orthonormality of the eigenfunctions $\{\psi_k\}$ and $\{\phi_k\}$. The transformation operator U_{PDC} now reads (Christ *et al.*, 2011, 2013)

$$U_{\mathrm{PDC}} = \exp\left(\sum_k r_k A^\dagger B_k^\dagger - \mathrm{H.c.}\right). \tag{56}$$

The output state $|\psi_{\mathrm{out}}\rangle$ is thus a multimode squeezed state with squeezing parameters r_k,

$$|\psi_{\mathrm{out}}\rangle = \prod_{k=1}^{\infty} \frac{1}{\sqrt{\cosh(r_k)}} \sum_{n_k=0}^{\infty} (\tanh(r_k))^{n_k} |n_k\rangle_1 |n_k\rangle_2, \tag{57}$$

in which fluctuations of the collective quadrature of the two states $Y_k = (A_k^\dagger + B_k^\dagger - A_k - B_k)/(2i)$ may be squeezed below the coherent state value ($\langle Y_k^2\rangle = 1/2$),

$$\langle Y_k^2\rangle = \tfrac{1}{2} e^{-2r_k}. \tag{58}$$

The mean photon number in each of the two fields is given by

$$\bar{n} = \left\langle \sum_k A_k^\dagger A_k \right\rangle = \left\langle \sum_k B_k^\dagger B_k \right\rangle = \sum_k \sinh^2(r_k). \tag{59}$$

We are mostly concerned with the time-frequency correlations in the weak downconversion regime, i.e., $\bar{n} \le 1$, when the output state is dominated by temporally well-separated pairs of time-frequency entangled photons.

The multipoint correlation functions of state (57), which are the relevant quantities in nonlinear spectroscopy, may be most conveniently evaluated by switching to the Heisenberg picture, in which the Schmidt mode operators become (Christ *et al.*, 2011, 2013)

$$A_k^{\mathrm{out}} = \cosh(r_k) A_k^{\mathrm{in}} + \sinh(r_k) B_k^{\dagger \mathrm{in}}, \tag{60}$$

$$B_k^{\mathrm{out}} = \cosh(r_k) B_k^{\mathrm{in}} + \sinh(r_k) A_k^{\dagger \mathrm{in}}. \tag{61}$$

The four-point correlation function then reads (Schlawin and Mukamel, 2013)

$$\begin{aligned}\langle E^\dagger(\omega_a') E^\dagger(\omega_b') E(\omega_b) E(\omega_a)\rangle &= [h_{12}^*(\omega_a', \omega_b') + h_{21}^*(\omega_a', \omega_b')][h_{12}(\omega_a, \omega_b) + h_{21}(\omega_a, \omega_b)] \\ &+ [g_1(\omega_a, \omega_a') + g_2(\omega_a, \omega_a')][g_1(\omega_b, \omega_b') + g_2(\omega_b, \omega_b')] \\ &+ [g_1(\omega_a, \omega_b') + g_2(\omega_a, \omega_b')][g_1(\omega_b, \omega_a') + g_2(\omega_b, \omega_a')],\end{aligned} \tag{62}$$

with

$$h_{12}(\omega_a, \omega_b) = \sum_k \cosh(r_k) \sinh(r_k) \psi_k(\omega_a) \phi_k(\omega_b), \tag{63}$$

$$g_1(\omega, \omega') = \sum_k \sinh^2(r_k) \psi_k(\omega) \psi_{k'}^*(\omega'), \tag{64}$$

and

$$g_2(\omega, \omega') = \sum_k \sinh^2(r_k) \phi_k(\omega) \phi_{k'}^*(\omega'). \tag{65}$$

The first line in Eq. (62) shows the same structure as Eq. (50), in that the two absorption events at frequencies ω_a and ω_b (and at ω_a' and ω_b') are correlated. Indeed, in the weak pump regime, when $r_k \ll 1$, Eq. (63) reduces to the two-photon wave function of the pulsed entangled pairs, and $\sinh(r_k)\cosh(r_k) \simeq r_k$ (Schlawin and Mukamel, 2013),

$$\begin{aligned} h_{12}(\omega_a, \omega_b) &\Rightarrow_{r_k \ll 1} \sum_k r_k \psi_k(\omega_a) \phi_k(\omega_b) \\ &= \Phi^*(\omega_a, \omega_b) = \langle 0|E_2(\omega_b) E_1(\omega_a)|\psi_{\mathrm{twin}}\rangle. \end{aligned} \tag{66}$$

h_{12} denotes the two-photon contribution to the correlation function, which should be distinguished from the autocorrelation contributions g_1 and g_2.

The ratio of the inverse entanglement time T^{-1} and the pump bandwidth σ_p determines the frequency correlations in Eq. (63): As shown in Fig. 3(a), for $\sigma_p \ll T_2^{-1}$ we recover the cw regime with strong frequency *anticorrelations*. In the opposite regime, when $\sigma_p \gg T_2^{-1}$ [Fig. 3(c)], the two photons

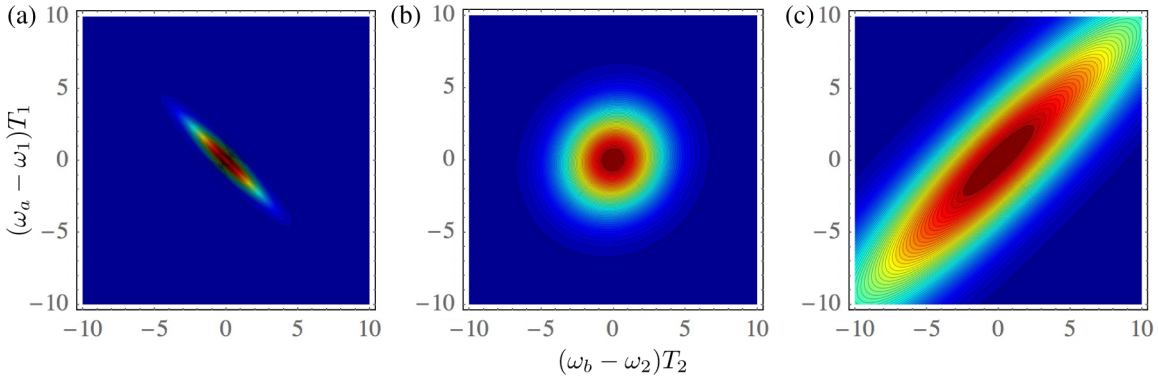

FIG. 3. Absolute value of the two-photon correlation function (63) of entangled-photon pairs with (a) strong frequency anticorrelations $\sigma_p = 0.6/T_2$ [entanglement entropy (40) $E = 1.9$], (b) very weak correlations ($E = 0.018$), $\sigma_p = 3.5/T_2$, and (c) strong positive frequency correlations $\sigma_p = 50/T_2$ ($E = 1.7$).

show *positive* frequency correlations, and in between there is a regime shown in Fig. 3(b), in which the photonic wave function factorizes, and no frequency correlations exist. The field correlation function as depicted in Fig. 3 can be measured experimentally (Kim and Grice, 2005).

In spectroscopic applications, two-photon events involving uncorrelated photons from different pairs become statistically more likely at higher pump intensities. These events are described by the functions g_1 and g_2, which at low intensities scale as $\sim r_k^2$, so that Eq. (63) with $h_{12} \sim r_k$ dominates the signal. As the pump intensity is increased, events involving photons from different pairs must be taken into account as well.

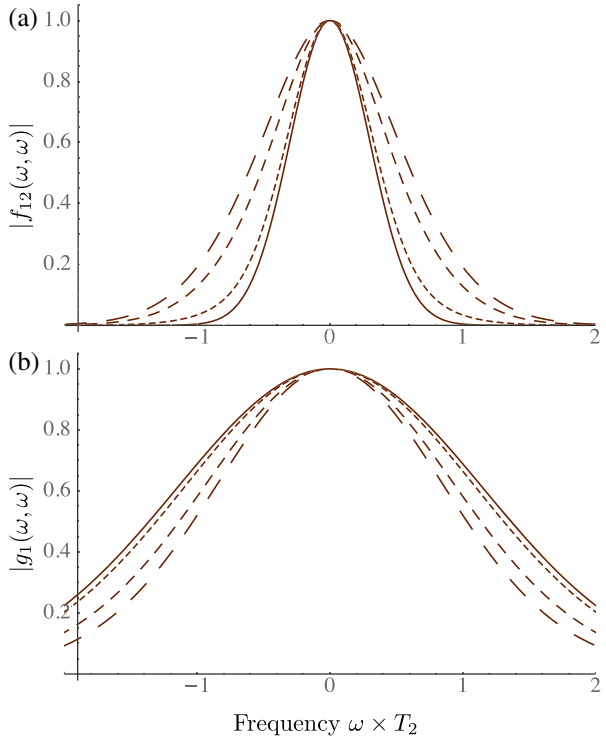

FIG. 4. (a) The two-photon correlation function $h_{12}(\omega,\omega)$, Eq. (63), plotted vs the frequency ω in units of T_2, and for mean photon numbers (with increasing, dashed) $\bar{n} \sim 0.1$, 1, 10, and 100. (b) The same for the autocorrelation function $g_1(\omega,\omega)$, Eq. (64).

The various contributions to the correlation function behave differently with increasing photon number: They depend nonlinearly on the mode weights r_k which in turn depend linearly on the pump amplitude. Thus, with increasing pump amplitude (and photon number) the few largest eigenvalues get enhanced nonlinearly compared to the smaller values, and fewer Schmidt modes contribute to Eqs. (63) and (64). This is shown in Fig. 4 where the two correlation functions are plotted for different mean photon numbers $\bar{n} = 0.1, \ldots, 100$. As the number of participating Schmidt modes is decreased, the frequency correlations encoded in h_{12} are weakened, and h_{12} broadens. Conversely, the bandwidth of the beams g_1 is reduced with increasing $\bar{n}$.

G. Shaping of entangled photons

The ability to manipulate the amplitude and phase of ultrashort pulses allows one to coherently control matter information in chemical reactions and other dynamical processes (Wollenhaupt, Assion, and Baumert, 2007). Pulse shaping can drive a quantum system from an initial state to a desired final state by exploiting constructive quantum-mechanical interferences that build up the state amplitude, while eliminating undesirable final states through destructive interferences (Silberberg, 2009). The most common experimental pulse shaping technique is based on spatial dispersion and often involves a back-to-back optical grating spectrometer which contains two gratings [see the top part of Fig. 5(a)]. The first disperses the spectral components of the pulse in space, and the second packs them back together, following a pixelated spatial light modulator (SLM) which applies a specific transfer function (amplitude, phase, or polarization mask), thereby modifying the amplitudes, phases, or polarization states of the various spectral components. Originally developed for strong laser beams, these pulse shaping techniques have now been extended all the way to the single-photon regime (Bellini *et al.*, 2003; Pe'er *et al.*, 2005; Carrasco *et al.*, 2006; Zäh, Halder, and Feurer, 2008; Defienne *et al.*, 2016) allowing one to control the amplitude and phase modulation of entangled-photon pairs, thereby providing additional spectroscopic knobs.

An example of a pulse shaping setup is shown in Fig. 5(a). A symmetric phase profile in the SLM yields a single

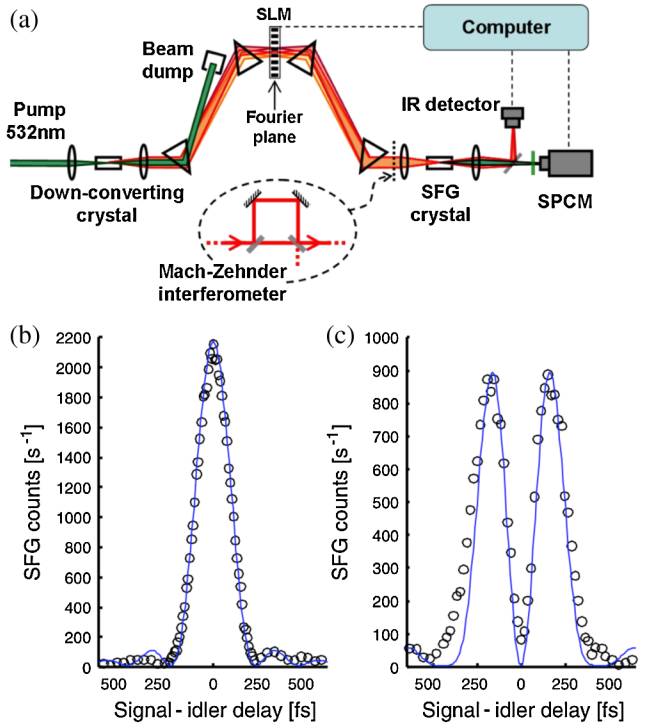

FIG. 5. (a) Experimental layout of the entangled-photon shaper: A computer-controlled spatial light modulator (SLM) is used to manipulate the spectral phase of the entangled photons. The photon pairs are detected in the inverse process of the PDC—sum-frequency generation (SFG). The SFG photons are subsequently counted in a single-photon counting module. In order to demonstrate two-photon interference oscillations, a Mach-Zehnder interferometer is placed between the last prism and the SFG crystal. (b) The SFG counts (circles) and the calculated second-order correlation function (line) of the unperturbed wave function as a function of the signal-idler delay. (c) The same for the shaped wave function. From Pe'er *et al.*, 2005.

unshaped Gaussian pulse [Fig. 5(b)]. The phase step results in a shaped pulse that mimics two pulses with ∼400 fs delay [Fig. 5(c)]. By employing more complex functions in the SLM, one may produce a replica of multiple well-separated pulses or more complex shapes. This may also be achieved using, e.g., the Franson interferometer with variable phases and delays in both arms as proposed by Raymer *et al.* (2013) (see Sec. III.B.4). Beam splitters in the two arms can create four pulses, out of a single entangled-photon pair.

H. Polarization entanglement

So far we have ignored the photon polarization degrees of freedom. In type-II PDC the two photons are created with orthogonal polarizations. Using a suitable setup, this allows for the preparation of Bell states of the form (Pan *et al.*, 2012)

$$|\text{Bell}\rangle = \frac{1}{\sqrt{2}}(|H\rangle_1|V\rangle_2 \pm |V\rangle_1|H\rangle_2), \tag{67}$$

where $(|H\rangle, |V\rangle)$ denote the horizontal (vertical) polarization, respectively. The fidelity for this state preparation is maximal, when the two-photon wave packets factorize. Similarly, type-I PDC allows for the creation of states of the form $(|HH\rangle \pm |VV\rangle)/\sqrt{2}$ (Pan *et al.*, 2012).

The polarization degrees of freedom offer additional control knobs which may be used to suppress or enhance the signal from (anti)parallel or orthogonal dipoles in a sample system—in a quantum-mechanical extension of polarized photon echo techniques (Voronine, Abramavicius, and Mukamel, 2006, 2007).

I. Matter correlations in noninteracting two-level atoms induced by quantum light

The entangled-photon correlation functions may be used to prepare desired distributions of excited states in matter. In an insightful article (Muthukrishnan, Agarwal, and Scully, 2004), which triggered followup work (Akiba, Akamatsu, and Kozuma, 2006; Das and Agarwal, 2008), it was argued that using time-ordered entangled-photon pairs, two-body two-photon resonances, where two noninteracting particles are excited simultaneously, can be observed in two-photon absorption. The surprising consequence is that the nonlinear response is cooperative (nonadditive) and does not scale as the number of atoms N. It was argued that such a cooperative response is not possible with classical or coherent light fields. Arguments were made that the cooperative response is induced in two-photon absorption by the manipulation of the interference among pathways. One possible consequence of the interference in the nonlinear response is that the fluorescence from one atom can be enhanced by the presence of a second atom, even if they do not interact. If true, this effect could be an interesting demonstration of this prediction and has some subtle implications on quantum nonlocality and the Einstein-Podolsky-Rosen (EPR) paradox. In this section, we calculate this two-photon process with quantum light and show that quantum locality is never violated.

1. Collective resonances induced by entangled light

We now use the superoperator formalism to investigate how the two-atom excitation cross section depends on the properties of the photon wave function.

Consider two noninteracting two-level atoms A and B coupled to the radiation field [see Fig. 6(a)]. We assume that the entire field-matter density matrix is initially in a factorizable form:

$$\rho(t_0) = \rho_{A,0} \otimes \rho_{B,0} \otimes \rho_{ph,0}, \tag{68}$$

where the $\rho_{A,0}$ ($\rho_{B,0}$) corresponds to the density matrix of atom A (B) and $\rho_{ph,0}$ is the density matrix of the field. The time-dependent density matrix is given by Eq. (11), which in the present case reads (Richter and Mukamel, 2011)

$$\rho(t) = \mathcal{T}\exp\left(-\frac{i}{\hbar}\int_{t_0}^{t} H^A_{\text{int}-}(\tau)d\tau - \frac{i}{\hbar}\int_{t_0}^{t} H^B_{\text{int}-}(\tau)d\tau\right)\rho(t_0). \tag{69}$$

If the radiation fields were classical then the matter density matrix would factorize so that atoms A and B remain uncorrelated at all times:

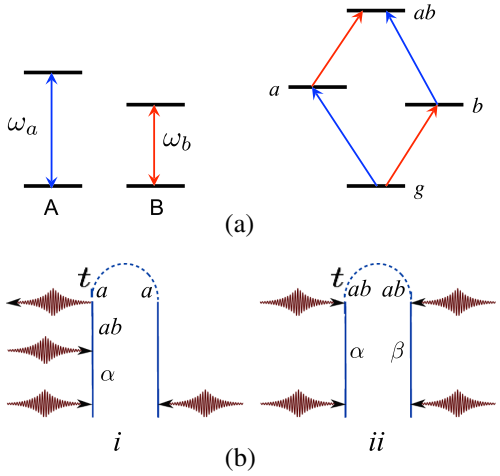

FIG. 6. (a) Scheme of two noninteracting two-level atoms A and B and corresponding many-body state diagram where ground state g corresponds to both atoms in the ground state, a—atom A is excited and B is in the ground state, b—atom B is in the excited state and atom A is in the ground state, and ab—both atoms are in the excited state. The arrows directed upward represent two-photon excitations. (b) Relevant set of diagrams corresponding to atom A being in the excited state to $\sim|\mu_A|^2|\mu_B|^2$ in field-matter interactions. α and β run over a and b to account for all possible permutations in the excitation pathways.

$$\rho(t) = \rho_A(t) \otimes \rho_B(t), \tag{70}$$

with

$$\rho_A(t) = \mathcal{T} \exp\left(-\frac{i}{\hbar}\int_{t_0}^{t} H^A_{\text{int}-}(\tau)d\tau\right)\rho_{A,0}, \tag{71}$$

$$\rho_B(t) = \mathcal{T} \exp\left(-\frac{i}{\hbar}\int_{t_0}^{t} H^A_{\text{int}-}(\tau)d\tau\right)\rho_{B,0}. \tag{72}$$

This result remains valid for quantum fields as long as all relevant normally ordered field modes are in a coherent state, and cooperative spontaneous emission is neglected so that all field modes behave classically (Glauber, 1963; Marx, Harbola, and Mukamel, 2008). However, Eq. (70) does not hold for a general quantum state of light. We define the reduced matter density matrix in the joint space $w = \text{tr}_{ph}(\rho)$. Upon expanding Eq. (69) order by order in the field operators and tracing over the field modes, we obtain for the reduced matter density matrix

$$w(t) = \sum_{\nu}\int_{t_0}^{t} d\tau_1 \cdots \int_{t_0}^{t} d\tau_{n_\nu}\int_{t_0}^{t} d\tau'_1 \cdots \int_{t_0}^{t} d\tau'_{m_\nu} \times \rho^\nu_A(\tau_1,\ldots,\tau_{n_\nu})\rho^\nu_B(\tau'_1,\ldots,\tau'_{m_\nu})F_\nu(\tau_1,\ldots,\tau_{n_\nu},\tau'_1,\ldots,\tau'_{m_\nu}), \tag{73}$$

where ν is summed over all possible pathways. Pathway ν has n_ν $\tilde{V}^A$ interactions and m_ν $\tilde{V}^B$ interactions. ρ^ν_A (ρ^ν_B) are time-ordered products of system A (system B) operators and $F_\nu(\tau_1,\ldots,\tau_{n_\nu},\tau'_1,\ldots,\tau'_{m_\nu})$ are time-ordered field correlation functions. In each order of this perturbative calculation, all the correlation functions are factorized between the three spaces. The factorization (70) no longer holds, and atoms A and B may become correlated or even entangled. Equation (73) will be used in the following. Note that pathways with $n_\nu = 0$ or $m_\nu = 0$ are single-body pathways, where all interactions occur solely with system A or with B. Our interest is in the two-body pathways, where both n_ν and m_ν contribute to the collective response.

2. Excited-state populations generated by nonclassical light

So far we have not discussed the overall excitation probability by entangled light sources compared to classical light with a similar photon flux. This is relevant to a recent demonstration of molecular internal conversion (Oka, 2012) and two-photon absorption with the assistance of plasmonics (Oka, 2015). This is an important practical point, if quantum spectroscopy is to be carried out at very low photon fluxes, in the presence of additional noise sources. We now discuss the correlations on the excitation probability induced by the interaction with nonclassical light for the model of two noninteracting two-level systems.

The doubly excited-state population is given, to leading-order perturbation theory in the interaction Hamiltonian (9), by the loop diagram in Fig. 2(a) which for the present model may be written as a modulus square of the corresponding transition amplitude

$$p_{ab}(t) = \sum_{\psi'}|T_{ab;\psi'}(t)|^2, \tag{74}$$

with the transition amplitude between initial state $|\psi\rangle$ and final state $|\psi'\rangle$,

$$T_{ab;\psi'}(t) = \int_{t_0}^{t} dt_1 \int_{t_0}^{t} dt_2 \mu_A\mu_B e^{-i\epsilon_a t_1 - i\epsilon_b t_2}\langle\psi|E(t_2)E(t_1)|\psi'\rangle. \tag{75}$$

In the following, we consider only a specific final state and will drop the subscript ψ'.

3. Classical versus entangled light

We first evaluate Eq. (74) for a classical field composed of two modes α and β, which is switched on at $t = t_0$:

$$\tilde{E}(t) = \theta(t - t_0)(E_\alpha e^{i\omega_\alpha t} + E_\beta e^{i\omega_\beta t}) + \text{c.c.} \tag{76}$$

$T^{(c)}_{ab}(t)$ is then given by (Muthukrishnan, Agarwal, and Scully, 2004)

$$T^{(c)}_{ab}(t) = T^{(c)}_a(t)T^{(c)}_b(t), \tag{77}$$

where

$$T^{(c)}_m(t) = \sum_{\mu=\alpha,\beta}\frac{iA_{\mu m}(t)}{\epsilon_m - \omega_\mu - i\gamma}, \quad m = a, b, \tag{78}$$

$A_{\nu m} = \mu_m E_\nu(e^{i(\omega_\nu-\epsilon_m)t_0-\gamma t_0} - e^{i(\omega_\nu-\epsilon_m)t-\gamma t})$ and $\gamma \to 0$. A straightforward calculation of Eq. (75) shows several terms, each containing single-particle resonances $\epsilon_{a,b} - \omega_{\alpha,\beta}$ as well as a collective resonance $\epsilon_a + \epsilon_b - (\omega_\alpha + \omega_\beta)$. The collective resonance disappears when these terms are combined due to destructive interference and the final result factorizes as a

product of two amplitudes that contain only single-particle resonances $\epsilon_j = \omega_\mu$, $j = a, b$ and $\mu = \alpha, \beta$ and no two-photon resonances $\epsilon_a + \epsilon_b = \omega_\alpha + \omega_\beta$ (Richter and Mukamel, 2011).

We first describe the properties of the entangled source. Consider a field made of entangled-photon pairs of a cascade state $|\psi_{\rm ent}\rangle$ depicted in Fig. 7 (Muthukrishnan, Agarwal, and Scully, 2004). This state can be prepared when an atom is promoted to the doubly excited state which then decays spontaneously back to the ground state by emitting a cascade of two photons and described by the wave function

$$|\psi_{\rm ent}\rangle = \sum_{p,q} \phi_{p,q} |1_p, 1_q\rangle,$$

$$\phi_{p,q} = \frac{g_{p\alpha} g_{q\beta} e^{i(\mathbf{p}+\mathbf{q})\cdot\mathbf{r}_R}}{(\omega_p + \omega_q - \omega_\alpha - \omega_\beta + i\gamma_\alpha)(\omega_q - \omega_\beta + i\gamma_\beta)}. \quad (79)$$

Here γ_α is the lifetime of the upper level of the three-level cascade and γ_β is the lifetime of the intermediate state. $\mathbf{p}$ and $\mathbf{q}$ are the wave vectors of different modes in the vacuum state and $g_{p\alpha}$ and $g_{q\beta}$ are coupling constants. ω_α is the transition frequency from the highest to the intermediate state and ω_β is the transition frequency from the intermediate state to the ground state. Note that the photon with momentum $\mathbf{p}$ comes first and interacts with the upper transition, whereas the photon with $\mathbf{q}$ comes later and interacts with the lower β transition. The two-photon frequency $\omega_p + \omega_q$ is narrowly distributed around $\omega_\alpha + \omega_\beta$ with a width γ_α, the lifetime of the upper level, whereas the single-photon frequencies ω_p, ω_q are distributed around ω_β (ω_α) with a width of γ_β (γ_α), the lifetime of the intermediate (highest) level. Maximum entanglement occurs for $\gamma_\beta \gg \gamma_\alpha$.

Using Eq. (79), and assuming that atoms A and B have the same distance from the cascade source, so that t_R is the time retardation (with $t_R = |\mathbf{r}_R|/c$) we obtain (Zheng *et al.*, 2013)

$$T^{\rm ent}_{ab}(t) = \sum_{m\neq n=a,b} \frac{A_{m\alpha,n\beta}(t)}{(\epsilon_m - \omega_\alpha - i\gamma_\alpha)(\epsilon_n - \omega_\beta - i\gamma_\beta)} + \sum_{m=a,b} \frac{A_{\rm TPA}(t)}{(\epsilon_a + \epsilon_b - \omega_\alpha - \omega_\beta - i\gamma_\alpha - i\gamma_\beta)(\epsilon_m - \omega_\beta - i\gamma_\beta)}, \quad (80)$$

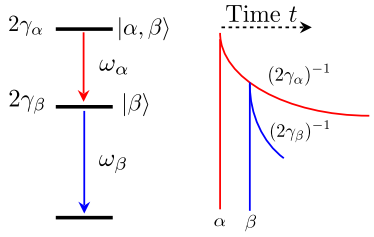

FIG. 7. The temporal profiles of two photons emitted by a cascade source illustrate time-frequency entanglement: the red curve represents the marginal probability $P(\tau_\alpha)$ Eq. (85), and the blue curve corresponds to the conditional probability $P(\tau_\beta|\tau_\alpha)$ Eq. (84). The intrinsic time ordering of the photons, α first, followed by β, suppresses the excitation pathway where β is absorbed first, followed by α, inducing joint two-atom excitation.

where

$$A_{n\nu,m\mu}(t) = \mu_A \mu_B A(e^{i\omega_{n\nu}(t-t_R)-\gamma_\nu(t-t_R)} - e^{-i\epsilon_m t_R - i\epsilon_n t_R}), \quad (81)$$

$$A_{\rm TPA}(t) = \mu_A \mu_B A(e^{-i\epsilon_a t_R - i\epsilon_b t_R} - e^{-i(\epsilon_a+\epsilon_b)t + i(\omega_\alpha - \omega_\beta - \gamma_\alpha - \gamma_\beta)(t-t_R)}). \quad (82)$$

The first term in Eq. (80) contains single-particle resonances, where the two systems are separately excited. The second term represents collective two-photon resonances $\epsilon_a + \epsilon_b - \omega_\alpha - \omega_\beta$. The two can be distinguished only for nonidentical atoms $\epsilon_a \neq \epsilon_b$.

Under the two-photon–two-atom resonance condition $\omega_a + \omega_b = \omega_\alpha + \omega_\beta$ for $\gamma_\alpha t \gg 1$, $\gamma_\beta t \gg 1$ the probability $P^{\rm ent}_{ab}(t)$ reads

$$p^{\rm ent}_{ab} = p_0 \frac{\gamma_\beta}{\gamma_\alpha \Delta^2}, \quad (83)$$

where $\Delta = \epsilon_b - \omega_\beta$ is a single atom detuning and $p_0 = |\mu_A|^2 |\mu_B|^2 \epsilon_a \epsilon_b / \hbar^2 \epsilon_0^2 c^2 S^2$.

Note that the classical amplitude (77) scales quadratically with the field amplitude $A_{\nu m}$, whereas the entangled amplitude (80) scales linearly (Fig. 1). This reflects the fact that at low intensity entangled two-photon absorption can be viewed as a linear absorption of the entangled pair as discussed earlier. A more detailed analysis of the scaling is presented in Sec. II.J.3.

Comparing Eqs. (77) and (80), we see that two-photon resonances require the lack of time ordering between the two photons. To explain this, we calculate the marginal probability

$$P(\tau_\alpha) = 2\gamma_\alpha \theta(\tau_\alpha) e^{-2\gamma_\alpha \tau_\alpha}, \quad (84)$$

and the conditional probability

$$P(\tau_\beta|\tau_\alpha) = 2\gamma_\beta \theta(\tau_\beta - \tau_\alpha) e^{-2\gamma_\beta(\tau_\beta - \tau_\alpha)} \quad (85)$$

for the two-photon absorption process displayed in Fig. 7 (Muthukrishnan, Agarwal, and Scully, 2004). These probabilities have the following meaning: the absorption of α is turned on at $\tau_\alpha = 0$ and decays slowly at the rate γ_α, while the absorption of β turns on at $\tau_\beta = \tau_\alpha$ and decays rapidly at the rate γ_β. Thus, the two photons arrive in strict time ordering, α followed by β, with the time interval between the absorption events vanishing when $\gamma_\beta \gg \gamma_\alpha$, i.e., in the limit of large frequency entanglement. Another related effect, which is discussed later in this section and which eliminates one-particle observables, is based on the lack of time ordering of the absorption of the two systems, while this interference effect originally described by Muthukrishnan, Agarwal, and Scully (2004) is based on a lack of time ordering of the two photons. Only the single-body single-photon resonances remain.

We now turn to the spectroscopy carried out using the model of entangled light given by Eq. (79). We first focus on the excited-state population of atom A, which is given by

$$p_a(t) \equiv {\rm tr}[|a\rangle\langle a|\rho(t)] = p_{a0}(t) + p_{ab}(t), \quad (86)$$

where the two terms differ by the final state of atom B: p_{a0} and p_{ab} represent B events where B ends up in the ground and

excited state, respectively. We calculate only the $\sim\mu_A^2\mu_B^2$ contributions to p_a, which are relevant to collective effects and are represented by the diagrams depicted in Fig. 6(b). Diagram *i* contains three interactions with ket—and one with bra—and represents p_{a0}, whereas diagram *ii* corresponds to p_{ab}. The exact formulas read off from these diagrams are presented in Richter and Mukamel (2011). Unlike the $p_{ab}(t)$ which contains only normally ordered field operators [see Eq. (74)], $p_{a0}(t)$ contains also non-normally ordered contributions. These can be recast as a normally ordered correlation plus a term that includes a field commutator:

$$\langle E^\dagger(t_2)E(t_3)E^\dagger(t_4)E(t_1)\rangle = \langle E^\dagger(t_2)E^\dagger(t_4)E(t_3)E(t_1)\rangle + \langle E^\dagger(t_2)[E(t_3),E^\dagger(t_4)]E(t_1)\rangle. \tag{87}$$

The second term includes a field commutator which is a *c* number. For certain types of states of the field, the commutator remains dependent upon the state of the field and this term has to be evaluated exactly [for instance, in the case of a coherent state this effect is responsible for the revival of damped Rabi oscillations discussed later (Rempe, Walther, and Klein, 1987)]. For other types of states of the field (e.g., the Fock state), the commutator becomes independent of the external field and therefore represents spontaneous emission. The spontaneous emission pathways introduce a coupling between the two systems, since a photon emitted by system *B* can be absorbed by system *A*. This coupling has both real (dipole-dipole) and imaginary (superradiance) parts. These couplings will result in collective signals which involve several atoms.

In the case of a classical field, one can neglect the spontaneous contributions and include only the stimulated ones which results in $p_{a0}(t) = -p_{ab}(t)$. The overall excited-state population of state $p_a(t)$ is unaffected by the collective resonances. We thus do not expect to observe any enhanced fluorescence from *A*; the two-photon absorption signal factorized into a product of individual excitation probabilities for atoms *A* and *B* and shows no collective resonances.

4. Collective two-body resonances generated by illumination with entangled light

The change in the photon number caused by the two-body part Δn_{ph} depends on the following probabilities: the excitation probability of p_{ab}, which means that two photons are absorbed (counts twice), and the excitation probabilities of only system *A* p_a and of only system *B* p_b (we assume that both photons have the same frequency and are resonant with the two-photon absorption):

$$\Delta n_{ph} = -2p_{ab}(t) - p_{a0}(t) - p_{b0}(t). \tag{88}$$

In the stimulated emission and TPA pathway absorption, $p_{ab}(t)$ and $p_{a0}(t)$ cancel as well, and $p_{ab}(t)$ and $p_{b0}(t)$ cancel so that Eq. (88) vanishes. Since the field-matter interaction Hamiltonian connects the photon number with the excitation probability, the photon number itself is a single-particle observable like the population of state $|a\rangle$ or state $|b\rangle$, and therefore vanishes. However, collective resonances in $p_{ab}(t)$ can be revealed in two-photon counting (Hanbury-Brown-Twiss measurements) (Brown, 1956; Richter and Mukamel, 2011). For the entangled-photon state, Eq. (79), the change in the photon-photon correlation $\Delta' n_{ph}$ is attributed to any buildup of probability that either atom *A*, or atom *B* or both atoms are excited, which will cause a reduction of the photon-photon correlation:

$$\Delta' n_{ph} = -p_{ab}(t) - p_{a0}(t) - p_{b0}(t). \tag{89}$$

Since $p_{ab}(t)$ enters twice [unlike Eq. (88)] the stimulated contributions can cancel only with one of the two other contributions $p_{a0}(t)$ or $p_{b0}(t)$, and we finally have

$$\Delta' n_{ph} = p_{ab}(t). \tag{90}$$

The interference mechanism, which caused the cancellation in the stimulated signal and the photon number, does not lead to a full cancellation, and two-photon absorption involving both systems may be observed.

Two-photon two-atom signals with nonentangled quantum states. We now discuss whether entangled light is essential for the creation of collective resonances. This is the subject of current debate. Zheng *et al.* (2013) presented a detailed analysis of the cross section created by entangled pulses and compared it with "correlated-separable" states in which the entanglement is replaced by classical frequency correlations. They concluded that it is the frequency anticorrelations [see Fig. 4(a)], and not the entanglement *per se*, which is responsible for the enhancement of the cross section. The effect of enhanced two-photon absorption probability was later shown to come from the entangled matter or field evolution that occurs with any type of quantum light (not necessarily entangled) (Zheng *et al.*, 2013) which is consistent with earlier demonstrations of Georgiades, Polzik, and Kimble (1997). Starting with an entangled pure quantum state having a density matrix $\rho_0 = |\psi_{\rm ent}\rangle\langle\psi_{\rm ent}|$ of matrix elements $\rho_{kk'qq'} = \langle 1_k, 1_q|\rho_0|1_{k'}1_{q'}\rangle$ one can construct other states that have the same mean energy and the same single-photon spectrum, and hence that would give the same transition probabilities for a single-photon resonance. We now examine a special case of the states that originates from entangled state (79) that will allow a quantitative evaluation of the role of correlations. It is the diagonal part of ρ_0 defined as

$$\rho_1 = \sum_{k,q}\rho_{kkqq}|1_k,1_q\rangle\langle 1_k,1_q|. \tag{91}$$

Equation (91) does not yield any temporal field coherence and is time independent. It is in fact a correlated-separable state (Duan *et al.*, 2000), in which the quantum correlations are replaced by a purely classical frequency distribution. It gives rise, however, to correlations between its two parties. Using the entangled state (79), Eq. (91) reads

$$\rho_1 = \left(\frac{2c}{L}\right)^2\sum_{k,q}\frac{\gamma_\beta}{(\omega_{q\beta}^2+\gamma_\beta^2)}\frac{\gamma_\alpha}{[(\omega_{q\beta}+\omega_{k\alpha})^2+\gamma_\alpha^2]} \times |1_k,1_q\rangle\langle 1_k,1_q|. \tag{92}$$

The state (92) corresponds to an atomic cascade for which the starting time is random, thereby averaging to zero all the

off-diagonal time-dependent terms in the density matrix. It results in the following transition probability:

$$p_1(t) \simeq p_0 \frac{\gamma_\alpha \gamma_\beta}{\delta^2 + \gamma_\alpha^2} \left(\frac{1}{(\omega_1 - \omega_\beta)^2} + \frac{1}{(\omega_2 - \omega_\beta)^2} \right) \frac{t^2}{(L/c)^2}. \tag{93}$$

At exact two-photon two-atom resonance, we have $p_1 \simeq p_0 \gamma_\beta \gamma_\alpha^{-1} c^2 t^2/(\Delta L)^2$. Note that p_1 depends on time, as can be expected in a situation where the detecting atoms, which have an infinite lifetime, are subjected to a stationary quantum state, and therefore to cw light. In order to compare p_1 to the corresponding probability (83) for pulsed entangled light, we need to set the interaction time at $t = L/c$ and be at exact resonance

$$p_1 \simeq p_0 \frac{\gamma_\beta}{\gamma_\alpha \Delta^2} \simeq p_{ab}^{\text{ent}}. \tag{94}$$

We thus found that a correlated-separable state like ρ_1 can induce a two-photon two-atom transition similar to the entangled cascade state. Note that even though ρ_1 is not entangled, it has quantum properties, being a mixture of single-photon Fock states which are highly nonclassical.

In summary, the two-photon absorption probability of noninteracting atoms can be enhanced compared to classical light by using certain types of quantum light. These do not require entanglement, rather it is necessary to have spectral anticorrelations which can be achieved in, e.g., correlated-separable states. This is a consequence of the stationary system of two noninteracting atoms.

In the following section we consider a more complex material system that is subjected to various relaxation channels, e.g., transport between excited states. We show that entanglement may then be used to achieve both high spectral and high temporal correlations which is not possible by classical correlated light.

J. Quantum light induced correlations between two-level particles with dipole-dipole coupling

1. Model system

The standard calculation of the nonlinear response to classical light assumes that the matter is made up of N noninteracting active particles (atoms or molecules), such that the matter Hamiltonian may be written as the sum over the individual particles [see Eq. (7)]

$$H_0 = \sum_\nu H_\nu. \tag{95}$$

The individual nonlinear susceptibilities or response functions of these atoms then add up to give the total response. The nonlinear response then becomes a single-body problem and no cooperative resonances are expected. It is not obvious how to rationalize the $\sim N$ scaling for noninteracting atoms had we chosen to perform the calculation in the many-body space. Massive cancellations of most $\sim N(N-1)$ scaling light-matter pathways recover in the end the final $\sim N$ signal scaling (Spano and Mukamel, 1989).

When the atoms are coupled, the calculation must be carried out in their direct-product many-body space whose size grows exponentially with N ($\sim n^N$ dimensions for n-level atoms). The interatomic coupling is induced by the exchange of virtual photons leading to dipole-dipole and cooperative spontaneous emission, or superradiance (Das, Agarwal, and Scully, 2008; Salam, 2010). In molecular aggregates, the dipole interaction between its constituents creates inherent entanglement on the level of the quasiparticles (Mukamel, 2010). This shifts the doubly excited-state energies and redistributes the dipole moments. The individual Hamiltonians H_ν are (Abramavicius *et al.*, 2009)

$$H_\nu = \hbar \sum_i \varepsilon_m B_{m\nu}^\dagger B_{m\nu} + \hbar \sum_{m \neq n} J_{mn} B_{m\nu}^\dagger B_{n\nu} + \hbar \sum_m \frac{\Delta_m}{2} B_{m\nu}^\dagger B_{m\nu}^\dagger B_{m\nu} B_{m\nu}, \tag{96}$$

where B_m ($B_m^\dagger$) describes an excitation annihilation (creation) operators for chromophore m. These excitations are hard-core bosons with Pauli commutation rules (Lee, Huang, and Yang, 1957):

$$[B_m, B_n^\dagger] = \delta_{mn}(1 - 2B_n^\dagger B_n). \tag{97}$$

To describe two level sites, which cannot be doubly excited according to the Pauli exclusion we set $\Delta_m \to \infty$. In condensed matter physics and molecular aggregates the many particle delocalized states are called excitons. The model Hamiltonian (96) can represent, e.g., Rydberg atoms in optical lattice or Frenkel excitons in molecular aggregates. To describe four-wave-mixing processes, we have truncated the Hamiltonian H_ν in Eq. (96) at the doubly excited level, such that the diagonalization reads

$$H_\nu = \hbar \omega_{g\nu} |g_\nu\rangle\langle g_\nu| + \hbar \sum_e \omega_{e\nu} |e_\nu\rangle\langle e_\nu| + \hbar \sum_f \omega_{f\nu} |f_\nu\rangle\langle f_\nu|, \tag{98}$$

where g indexes the ground state, e the singly, and f the doubly excited states, which are the central concern. We consider processes in which the signals factorize into ones stemming from individual particles, as well as collective signals from two or more particles. We illustrate basic properties of the interaction of entangled photons with complex quantum systems using the simple multilevel model depicted in Fig. 8, which has two excited states e_1 and e_2, and two doubly excited states f_1 and f_2. The higher-energy excited state e_2 decays to e_1 within a few tens of femtoseconds. We focus on the doubly excited states created by the absorption of pairs of photons.

Similarly to the noninteracting case (75), the population in the final state f at time t is given by the loop diagram in Fig. 2, which can be written as the modulus square of a transition amplitude. Tracing out the matter degrees of freedom, the amplitude can be written as a nonlinear field operator,

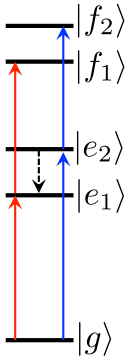

FIG. 8. Level scheme of the multilevel model employed in this review: two singly excited states e_1 and e_2 with energies 11 000 and 11 500 cm^{-1} are coupled to doubly excited states f_1 and f_2, as indicated. Furthermore, e_2 decays to e_1 within $1/k \simeq 30$ fs.

$$T_{fg}(t;\Gamma) = -\frac{1}{\hbar^2}\int_{t_0}^{t} d\tau_2 \int_{t_0}^{\tau_2} d\tau_1 E(\tau_2)E(\tau_1) \times \langle f(t)|V^\dagger(\tau_2)V^\dagger(\tau_1)\rangle|g(t_0)\rangle, \tag{99}$$

which may be evaluated for arbitrary field input states. Using Eq. (52), we obtain

$$T_{fg}^{(\mathrm{ent})}(t;\Gamma) = \frac{1}{\hbar^2 T}\frac{\mu_{ge}\mu_{ef}\mathcal{N}}{\omega_1+\omega_2-\omega_f+i\gamma_f}e^{-i(\omega_1+\omega_2)t} \times\left[\frac{e^{i(\omega_1-\omega_e+i\gamma_e)T}-1}{\omega_1-\omega_e+i\gamma_e}+\frac{e^{i(\omega_2-\omega_e+i\gamma_e)T}-1}{\omega_2-\omega_e+i\gamma_e}\right], \tag{100}$$

where we used $\mathcal{N} = \mathcal{N}'' A_p$ which is linear in the classical pump amplitude. For comparison, the classical probability governed by excitation by two classical fields with amplitudes A_1 and A_2 is given by

$$T_{fg}^{(c)}(t;\Gamma) = \frac{1}{\hbar^2}\frac{\mu_{ge}\mu_{ef}A_1A_2e^{-i(\omega_1+\omega_2)t}}{[\omega_1-\omega_{eg}+i\gamma_{eg}][\omega_2-\omega_{fe}+i\gamma_{fe}]} + (\omega_1 \leftrightarrow \omega_2), \tag{101}$$

which is quadratic in the field amplitudes, unlike Eq. (100). The second term denotes the same quantity, but with the beam frequencies ω_1 and ω_2 interchanged. We shall discuss the intensity scaling later.

Equation (100) reflects the entangled-photon structure described earlier: The pump frequency $\omega_p = \omega_1 + \omega_2$ is sharply defined such that the ω_f resonance is broadened only by the state's lifetime broadening and pure dephasing rate γ_f. The strong time correlations in the arrival time create a resonance of the form $[\exp(i\omega T)-1]/\omega$, which for very short entanglement times is independent of the frequency $[\exp(i\omega T)-1]/\omega \simeq T + \mathcal{O}(T^2)$. This implies that the intermediate e states effectively interact with broadband light, whereas the f states interact with cw light. Put differently, due to their large bandwidth, the entangled photons can induce all possible excitation pathways through the e manifold leading to a specific selected f state (Schlawin *et al.*, 2012). Tuning the pump frequency ω_p allows one to select the excitation of specific wave packets: Fig. 9 depicts the density matrices for doubly excited states induced by the absorption of entangled-photon pairs with different pump frequencies. This behavior remains the same for pulsed excitation in the strong frequency anticorrelations regime (Schlawin, 2016).

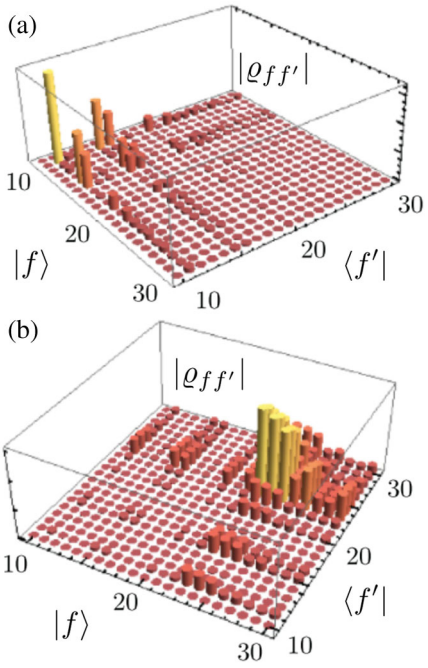

FIG. 9. (a) The density matrix for doubly excited states $\varrho_{ff'}(t) = T^*_{f'g}(t)T_{fg}(t)$, Eq. (100), prepared by the absorption of entangled photons with pump frequency $\omega_p = 22\times 160\,\mathrm{cm}^{-1}$. (b) The same, with $\omega_p = 24\times 200\,\mathrm{cm}^{-1}$. From Schlawin *et al.*, 2012.

2. Control of energy transfer

When the material system is coupled to an environment which causes relaxation among levels, the distributions of excited-state populations may no longer be described by the wave function and transition amplitudes, and the density matrix must be used instead. As shown in Fig. 2, the loop diagram, which represents the transition amplitudes needs to be broken up into three fully time-ordered ladder diagrams (and their complex conjugates). These are given in the time domain (Schlawin *et al.*, 2013),

$$p_{f,(\mathrm{I})}(t;\Gamma) = \left(-\frac{i}{\hbar}\right)^4\int_{-\infty}^{t} d\tau_4\int_{-\infty}^{\tau_4} d\tau_3\int_{-\infty}^{\tau_3} d\tau_2\int_{-\infty}^{\tau_2} d\tau_1 \times\langle V_R(\tau_4)V_R(\tau_3)V_L^\dagger(\tau_2)V_L^\dagger(\tau_1)\rangle \times\langle E^\dagger(\tau_3)E^\dagger(\tau_4)E(\tau_2)E(\tau_1)\rangle, \tag{102}$$

$$p_{f,(\mathrm{II})}(t;\Gamma) = \left(-\frac{i}{\hbar}\right)^4\int_{-\infty}^{t} d\tau_4\int_{-\infty}^{\tau_4} d\tau_3\int_{-\infty}^{\tau_3} d\tau_2\int_{-\infty}^{\tau_2} d\tau_1 \times\langle V_R(\tau_4)V_L^\dagger(\tau_3)V_R(\tau_2)V_L^\dagger(\tau_1)\rangle \times\langle E^\dagger(\tau_2)E^\dagger(\tau_4)E(\tau_2)E(\tau_1)\rangle, \tag{103}$$

$$p_{f,(\mathrm{III})}(t;\Gamma)=\left(-\frac{i}{\hbar}\right)^4\int_{-\infty}^{t}d\tau_4\int_{-\infty}^{\tau_4}d\tau_3\int_{-\infty}^{\tau_3}d\tau_2\int_{-\infty}^{\tau_2}d\tau_1 \times\langle V_L^\dagger(\tau_4)V_R(\tau_3)V_R(\tau_2)V_L^\dagger(\tau_1)\rangle \times\langle E^\dagger(\tau_2)E^\dagger(\tau_3)E(\tau_4)E(\tau_1)\rangle. \quad (104)$$

Here Γ collectively denotes the set of control parameters of the light field. The matter correlation functions in Eqs. (102)–(104) are given by Liouville space superoperator correlation functions, which translate for the integration variables in Eqs. (102)–(104) to the Hilbert space correlation functions

$$\langle V_R(\tau_4)V_R(\tau_3)V_L^\dagger(\tau_2)V_L^\dagger(\tau_1)\rangle = \langle V(\tau_3)V(\tau_4)V^\dagger(\tau_2)V^\dagger(\tau_1)\rangle, \quad (105)$$

$$\langle V_R(\tau_4)V_L^\dagger(\tau_3)V_R(\tau_2)V_L^\dagger(\tau_1)\rangle = \langle V(\tau_2)V(\tau_4)V^\dagger(\tau_3)V^\dagger(\tau_1)\rangle, \quad (106)$$

$$\langle V_L^\dagger(\tau_4)V_R(\tau_3)V_R(\tau_2)V_L^\dagger(\tau_1)\rangle = \langle V(\tau_2)V(\tau_3)V^\dagger(\tau_4)V^\dagger(\tau_1)\rangle. \quad (107)$$

The entangled-photon field correlation functions are given by the Fourier transform of Eq. (62).

We first restrict our attention to the weak downconversion regime $\bar{n}\ll 1$ in which the autocorrelation functions $g_{1,2}$, Eqs. (64) and (65), may be neglected. The essential properties of entangled-photon absorption may be illustrated by using the simple model system introduced in Sec. II.J.1 where the correlation functions (102)–(104) can be written as the sum-over-states expressions given in Appendix C. To excite state f_2 faithfully, one needs to select it spectrally, and the intermediate decay process $e_2\to e_1$ needs to be blocked (see Fig. 8). This can be achieved with entangled photons. Figure 10 shows how the relative population in each final state versus the pump frequency ω_p. At each frequency the total population is normalized to unity, i.e., $p_{f_1}+p_{f_2}=1$. By choosing a spectrally narrow pump bandwidth $\sigma_p=100\ \mathrm{cm}^{-1}$ in combination with a short entanglement time $T=10$ fs, almost 90% of the total f population can be deposited in the state f_2 at $\omega_p=22\,500\ \mathrm{cm}^{-1}$ (and ~95% in f_1 at $\omega_p=21\,800\ \mathrm{cm}^{-1}$).

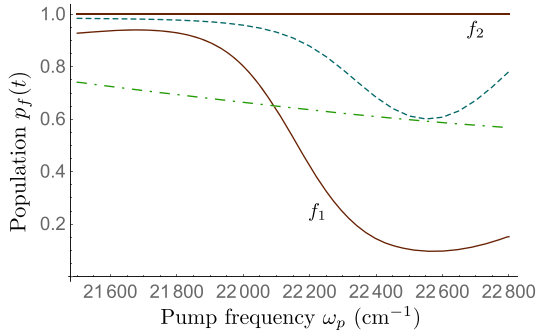

FIG. 10. Variation of the double-excited-state populations $p_f(t)$, Eqs. (102)–(104), with the pump frequency ω_p after excitation by entangled photons with strong frequency anticorrelations (solid, red), by laser pulses matching the pump bandwidth σ_p (dashed, blue), and laser pulses matching the photon bandwidths $\sim 1/T$ (dot-dashed, green). The total f population is normalized to unity at each frequency, i.e., $\sum_f p_f(t)=1$.

Such degree of state selectivity may not be achieved with classical laser pulses: For comparison, the f-manifold populations created by classical laser pulses with bandwidths $\sigma=100\ \mathrm{cm}^{-1}$ (same spectral selectivity) and with $\sigma=1000\ \mathrm{cm}^{-1}$ (same time resolution in the manifold of singly excited states) are shown as well in Fig. 10. In the former case, the intermediate relaxation process limits the maximal yield in f_2 to ~35% (with ca. 65% population in f_1 at $\omega_p=22\,500\ \mathrm{cm}^{-1}$); in the latter case, the lower spectral resolution limits the achievable degree of control over the f populations.

For very short entanglement times, transport between various excited states in the e manifold may be neglected, and the f populations may as well be calculated using transition amplitudes, thus greatly reducing the computational cost (Schlawin, 2016). By varying the entanglement time it becomes possible to probe subsets of transport pathways via the selection of specific f states in the detected optical signal.

The above properties may also be observed in more complex systems such as molecular aggregates (Schlawin *et al.*, 2013), where the number of excited states is much higher, but the described physics is essentially the same: Ultrafast relaxation processes limit the classically achievable degree of selectivity due to the trade-off between spectral and time resolution for each absorption process. With entangled photons, this trade-off limits only the overall two-photon process, but not each individual transition. This may be understood in the following way: in the absorption of entangled photons, the light-matter system becomes entangled in the interval between the two absorption events, but it remains separable at all times for classical pulses so that the energy-time uncertainty applies only to the entire system.

Finally it is worth noting an additional advantage of using entangled photons for two-photon excitation in molecules pointed out by Raymer *et al.* (2013). In many aggregates, the doubly excited state undergoes rapid nonradiative decay to the singly excited states. This may occur on the same time scale of the excited-state transport (Van Amerongen, Valkunas, and Van Grondelle, 2000). For weakly anharmonic aggregates where the transition frequencies $f\to e$ and $e\to g$ are close, it is hard to discriminate between the two-photon-excited and single-photon-excited fluorescence. Entangled light can help isolate the doubly excited-state population by monitoring the transmitted single-photon pathways with a high-quantum-efficiency detector that can partially rule out one-photon absorption.

3. Scaling of two-photon absorption with pump intensity

Equation (101) shows that the TPA probability $|T_{fg}|^2$ scales quadratically with pump intensity $A_1^2A_2^2$ for classical light but Eq. (100) shows linear scaling A_p^2 for weak entangled light. As the pump pulse intensity is increased, the two-photon state (33) does not represent the output state (57), and the autocorrelation contributions $g_{1,2}$ to Eq. (62) must be taken into account. To understand how this affects the excited-state distributions, we first simulate in Fig. 11 the relative

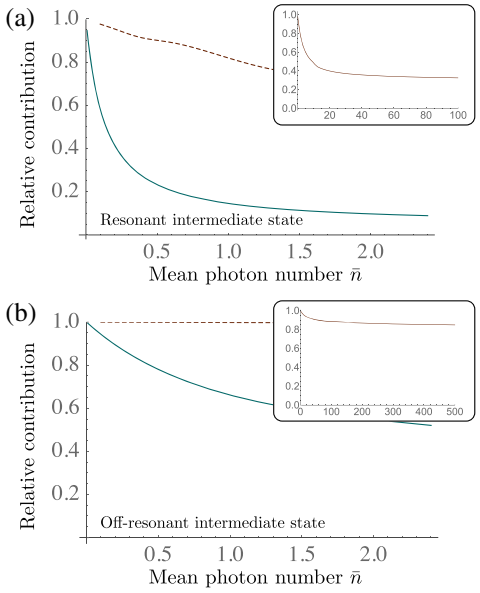

FIG. 11. (a) Relative contribution of the coherent two-photon contribution h_{12}, Eq. (63), to the full time-integrated population of f_2 plotted vs the mean photon number $\bar{n}$, Eq. (59). The dashed line shows strong entanglement with entanglement time $T = 10$ fs, and the solid line shows weaker entanglement with $T = 100$ fs. (b) The same for an intermediate state moved to $\omega_{e_2} = 18\,500\ \mathrm{cm}^{-1}$.

contribution of the two-photon term h_{12} in Eq. (62) to the population in f_2, when the pump frequency is set at resonance $\omega_p = 22\,500\ \mathrm{cm}^{-1}$ and its variation with the mean photon number (59). Clearly, in the weakly entangled case this contribution drops rapidly, and already at $\bar{n} = 0.5$ the autocorrelation contribution (i.e., excitations by uncorrelated photons from different downconversion events) dominates the signal. In contrast, in the strongly entangled case the contribution drops much more slowly, and—as can be seen in the inset—still accounts for roughly one-third of the total absorption events even at very high photon number $\bar{n} \simeq 100$. As described by Dayan *et al.* (2005), this may be attributed to the strong time correlations in the former case: For $T = 10$ fs, one can fit 10 times as many photon pairs into a time period compared to $T = 100$ fs, before different pairs start to overlap temporally. In addition, the strong frequency correlations discussed in the previous section imply that, on resonance with the final state f_2, the coherent contribution is enhanced even further.

The situation becomes more striking in Fig. 11(b) when the intermediate state e is shifted away from the entangled-photon frequencies, where we set it to $\omega_{e_2} = 18\,500\ \mathrm{cm}^{-1}$, and only the two-photon transition $g \to f_2$ is resonant. In the weakly entangled case (solid line), little has changed, and parity between the two-photon and the autocorrelation contribution is reached again for $\bar{n} \sim 2$. In the strongly entangled regime, however, the coherent contribution remains close to unity and dominates the signal even at $\bar{n} \simeq 500$, as seen in the inset.

The strong frequency correlations of entangled-photon pairs lead to the enhancement of the two-photon contribution h_{12} compared to the autocorrelation contributions $g_{1,2}$—even for very high photon fluxes. Consequently, the nonclassical excited-state distributions created by entangled photons can still dominate the optical signal even when the mean photon number in each beam greatly exceeds unity (Schlawin, 2016). The linear to a quadratic crossover of the two-photon absorption rate with the pump intensity [Fig. 1(a)], which is traditionally regarded as a transition from a quantum to a classical regime (Lee and Goodson, 2006), is not necessarily a good indicator for this transition, as pointed out by Georgiades, Polzik, and Kimble (1997). The time-frequency correlations of entangled pairs may be harnessed at much higher photon fluxes as long as the coherent contribution h_{12} dominates the incoherent contributions $g_{1,2}$.

III. NONLINEAR OPTICAL SIGNALS OBTAINED WITH ENTANGLED LIGHT

We now revisit the excited-state populations created in matter following the absorption of entangled-photon pairs in Sec. II and present optical signals associated with these distributions. We first derive compact superoperator expressions for arbitrary field observables, which naturally encompass standard expressions based on a semiclassical treatment of the field (Mukamel, 1995).

Using Eq. (11), the expectation value of an arbitrary field operator $A(t)$ is given by

$$S(t;\Gamma) = \langle A_+(t)\rangle_{\mathrm{final}} \tag{108}$$

$$= \left\langle \mathcal{T} A_+(t) \exp\left[-\frac{i}{\hbar}\int_{t_0}^{t} d\tau H_{\mathrm{int},-}(\tau)\right]\right\rangle \tag{109}$$

$$= S_0 - \frac{i}{\hbar}\int_{t_0}^{t} d\tau \left\langle \mathcal{T} A_+(t) H_{\mathrm{int},-}(\tau) \times \exp\left[-\frac{i}{\hbar}\int_{t_0}^{\tau} d\tau' H_{\mathrm{int},-}(\tau')\right]\right\rangle. \tag{110}$$

Here the first term describes the expectation value in the absence of any interaction with the sample, which we set to zero. The second term describes the influence of the sample on the expectation value. It may be represented more compactly, when the interaction Hamiltonian is not written in the RWA approximation (Schlawin, 2016)

$$S(t;\Gamma) = -\frac{i}{\hbar}\int_{t_0}^{t} d\tau \langle [A(t), \epsilon(\tau)]_+ \mathcal{V}_+(\tau)\rangle_{\mathrm{final}}, \tag{111}$$

where we recall $\epsilon(t) = E(t) + E^\dagger(t)$ and $\mathcal{V}(t) = V(t) + V^\dagger(t)$.

Equation (111) may be used to calculate arbitrary optical signals induced by entangled photons, as demonstrated in the following.

A. Stationary nonlinear signals

We consider the situation described in Sec. II.B, where only a single quantum mode of the light is relevant. This is most prominently the case in the strong coupling regime of cavity quantum electrodynamics (Walther *et al.*, 2006), or when one is interested in steady state solutions, where only a single (or few) frequency(ies) of the field is (are) relevant.

The intricate connection between nonlinear optical signals and photon counting was first made explicit by Mollow

(1968), who connected the two-photon absorption rate of stationary fields with their $G^{(2)}$ function[1]

$$w_2 = 2|g(\omega_0)|^2 \int_{-\infty}^{\infty} dt e^{2i\omega_f t - \gamma_f|t|} G^{(2)}(-t,-t;t,t), \quad (112)$$

where $G^{(2)}(t_1',t_2';t_1,t_2) = \langle E^\dagger(t_1')E^\dagger(t_2')E(t_2)E(t_1)\rangle$ and $g(\omega_0) \sim \mu_{eg}\mu_{eg}/(\omega_0 - \omega_e + i\gamma_e)$ is the coupling element evaluated at the central frequency ω_0 of the stationary light field. The transition rate loosely corresponds to the time-integrated, squared two-photon transition amplitude (99) we derived earlier. If the lifetime broadening of the final state γ_f is much smaller than the field bandwidth $\Delta\omega$, $\gamma_f \ll \Delta\omega$, one may even neglect the time integration and replace $G^{(2)}(-t,-t;t,t) \sim G^{(2)}(0,0,0,0)$.

This implies, as pointed out by Gea-Banacloche (1989), that strongly bunched light can excite two-photon transitions more efficiently than classical light with identical mean photon number. It further implies that the two-photon absorption rate scales linearly in the low gain regime, even though the single mode squeezed state does not show time-energy entanglement in the sense of Sec. II.C. An experimental verification thereof is reported by Georgiades *et al.* (1995) and Georgiades, Polzik, and Kimble (1997).

A more recent proposal (López Carreño *et al.*, 2015) aims at employing nonclassical fluctuations contained in the fluorescence of a strongly driven two-level atom: As is well known, the driven two-level atom's fluorescence develops side peaks—known as the Mollow triplet (Scully and Zubairy, 1997). By driving polaritons—strongly coupled light-matter states in a cavity—with this light, it should allow for precise measurements of weak interactions between polaritons even in strongly dissipative environments.

B. Fluorescence detection of nonlinear signals

The fluorescence signal is given by the (possibly time-integrated) intensity $A(t) = E^\dagger(t)E(t)$, when the detected field mode is initially in the vacuum. It is obtained by expanding Eq. (111) to second order in the interaction Hamiltonian with the vacuum field (Mukamel, 1995),

$$S_{\mathrm{Fluor}} = \frac{1}{\hbar^2}\langle V_L(t)V_R^\dagger(t)\rangle_{\mathrm{final}}. \quad (113)$$

We first investigate the time-integrated $f \to e$ fluorescence signal (113), following excitation by either entangled photons or classical pulses. Using Eqs. (113) and (102)–(104), we may readily evaluate the signal as

$$S_{\mathrm{TPIF}}(\Gamma) = \int dt \sum_{e,f} |\mu_{ef}|^2 p_f(t;\Gamma). \quad (114)$$

In a different scenario, the two-excitation state may rapidly decay nonradiatively, e.g., via internal conversion, and the e-g fluorescence is detected,

$$\tilde{S}_{\mathrm{TPIF}}(\Gamma) \propto \int dt p_f(t;\Gamma). \quad (115)$$

Fluorescence signals are proportional to excited-state populations. Therefore, they are closely related to the excited-state distributions discussed in Secs. II.I–II.J.3. This is not necessarily the case for absorption measurements as shown in Sec. III.D.

1. Two-photon absorption versus two-photon-induced fluorescence (TPIF)

Before reviewing fluorescence signals induced by entangled photons, we comment on some ambiguity in the nomenclature of nonlinear signals such as fluorescence that depend on the doubly excited-state population p_f. Since this population is created by the absorption of two photons, the signal is often termed as *two-photon absorption*. However, it does not pertain to a $\chi^{(3)}$-absorption measurement, discussed in Sec. III.D. We refer to signals measuring p_f as *two-photon-induced fluorescence* and to two-photon resonances in $\chi^{(3)}$ as two-photon absorption.

In Sec. III.C.1, we further show that for off-resonant intermediate state(s) e—as is the case in most experimental studies to date (Dayan *et al.*, 2004, 2005; Lee and Goodson, 2006; Harpham *et al.*, 2009; Guzman *et al.*, 2010; Upton *et al.*, 2013)—the two signals carry the same information.

2. Two-photon-induced transparency and entangled-photon virtual-state spectroscopy

Entangled virtual-state spectroscopy, proposed by Saleh *et al.* (1998), suggests a means to detect far off-resonant intermediate states in the excitation of f states by employing entanglement-induced two-photon transparency (Fei *et al.*, 1997): The transition amplitude (100) of entangled photons created by a cw source oscillates as a function of the entanglement time T. For infinite excited-state lifetimes ($\gamma_e = 0$), the excitation of f is even completely suppressed whenever $(\omega_1 - \omega_e)T = n \times 2\pi \,\forall\, n \in \mathbb{N}$—the medium becomes transparent.

Saleh *et al.* had proposed to turn this counterintuitive effect into a spectroscopic tool by sending one of the two photons through a variable delay stage τ, which simply amounts to evaluating the two-photon wave function (52) $\langle 0|E(\tau_2+\tau)E(\tau_1)|\psi_{\mathrm{twin}}\rangle$. For degenerate downconversion the transition amplitude (100) then reads

$$T_{fg}(\tau,t;\Gamma) = \frac{\mathcal{N}'A_p}{\hbar^2 T}\sum_e \frac{\mu_{ge}\mu_{ef}}{\omega_p - \omega_f + i\gamma_f}\frac{e^{-i\omega_p t}e^{-i\omega_p\tau/2}}{\Delta_e + i\gamma_e} \times [e^{i(\Delta_e+i\gamma_e)(T-\tau)} + e^{i(\Delta_e+i\gamma_e)(T+\tau)} - 2], \quad (116)$$

where we introduced the detuning $\Delta_e = \omega_p/2 - \omega_e$. The Fourier transform of the TPIF signal $\propto |T_{fg}(\tau)|^2$ with respect to τ reveals different groups of resonances shown in Fig. 12 for the TPIF signal in hydrogen: Group A denotes resonances of differences between intermediate states $\Delta_e - \Delta_{e'}$, group B of detunings Δ_e, and group C of the sum of detunings $\Delta_e + \Delta_{e'}$. Such signals were simulated in a molecular system (Kojima and Nguyen, 2004), and similar resonances can be identified in absorption TPA measurements as discussed in Sec. III.C.1.

[1]We change the notation to match the rest of this review.

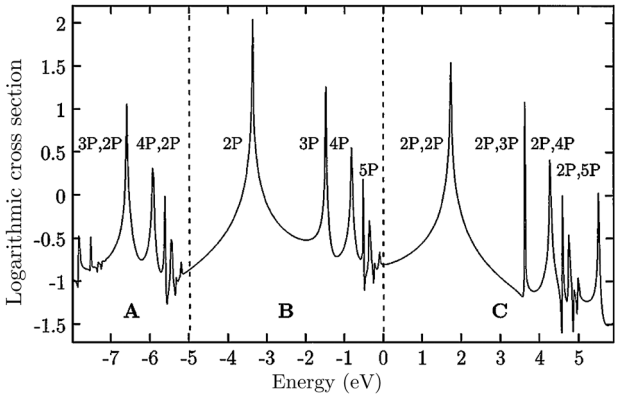

FIG. 12. Entangled virtual-state spectroscopy: the TPIF signal vs the Fourier transform of an additional time delay between the two photons (see text) in hydrogen. From Saleh *et al.*, 1998.

However, it turns out that the effect depends crucially on the tails of the spectral distribution in Eq. (49) (de J Leon-Montiel *et al.*, 2013). The sinc function in the two-photon wave function (51) has a long Lorentzian tail $\sim 1/\omega$, which covers extremely far off-resonant intermediate states. When the sinc is replaced by Gaussian tails, the resonances vanish. The effect is thus caused by the long spectral tails and is not intrinsically connected to entanglement.

3. Fluorescence from multilevel systems

The TPIF signal, Eq. (114), directly reflects the doubly excited-state population distributions created by the absorption of entangled-photon pairs. This may be seen in simulations of the TPIF signal from Frenkel excitons in molecular aggregates (Schlawin *et al.*, 2012). In Fig. 13(a), we present the TPIF signal resulting from the decay of the f-state distributions in Fig. 10. Clearly, the signal peaks whenever a two-excitation state is on resonance with the pump frequency ω_p. The signal from the two f states has approximately the same strength. In contrast, the TPIF signal created by classical pulses shown in Fig. 13(b) has a strong resonance only when the light is on resonance with the state f_1, whereas f_2 can be observed only as a weak shoulder of the main resonance. As discussed in Sec. II.I, the fast decay of the intermediate state e_2 limits the excitation of f_2 with classical light, and therefore the state can hardly be observed, even though it has the same dipole strength as f_1.

These nonclassical bandwidth features of entangled-photon pairs may be further exploited to control vibronic states as reported by Oka (2011a, 2011b). They were also investigated in semiconductor quantum wells. There the absorption of excited states competes with the absorption into a continuum of excited electronic states of free electrons and holes. By interpolating between negative and positive frequency correlations (see Fig. 3), it was shown by Salazar *et al.* (2012) how the absorption of the excited states may be either enhanced or suppressed as shown in Fig. 14.

4. Multidimensional signals

In Fig. 2, we explained how each light-matter interaction event also imprints the light phase ϕ onto the matter response.

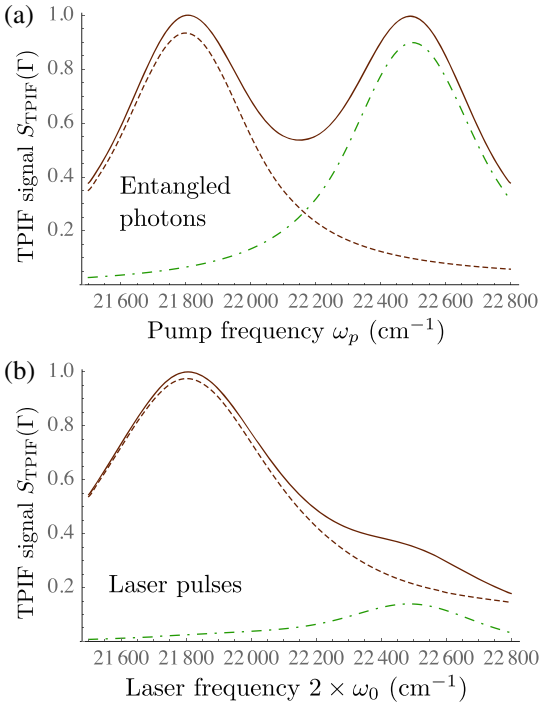

FIG. 13. (a) TPIF action spectrum $S_{\mathrm{TPIF}}(\Gamma)$, Eq. (114), induced by entangled-photon pairs with the same parameters as in Fig. 10. The fluorescence created by the state f_1 is shown separately as a dashed line, and the signal from f_2 as a dot-dashed line. (b) TPIF action spectrum induced by laser pulses with bandwidth $\sigma_0 = 100$ cm^{-1}.

We now exploit this fact to create multidimensional spectroscopic signals. Phase cycling provides a means to postselect signals with a certain phase signature as shown in the next section. Using additional delay stages, as in the entangled-photon virtual-state spectroscopy discussed previously in Sec. III.B.2, these signals can be spread to create multidimensional frequency correlation maps, which carry information about couplings between different resonances or relaxation mechanisms (Ginsberg, Cheng, and Fleming, 2009). Phase cycling is essential for partially noncollinear or collinear geometry 2D spectroscopic experiments (Keusters, Tan, and Warren, 1999; Scheurer and Mukamel,

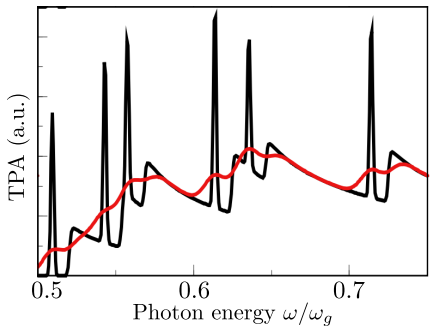

FIG. 14. Two-photon absorption (TPIF in our notation, see Sec. III.B.1) in a semiconductor quantum well: excited-state resonances within a continuum of delocalized states may be enhanced with frequency anticorrelations (black) or suppressed with positive frequency correlations (red). From Salazar *et al.*, 2012.

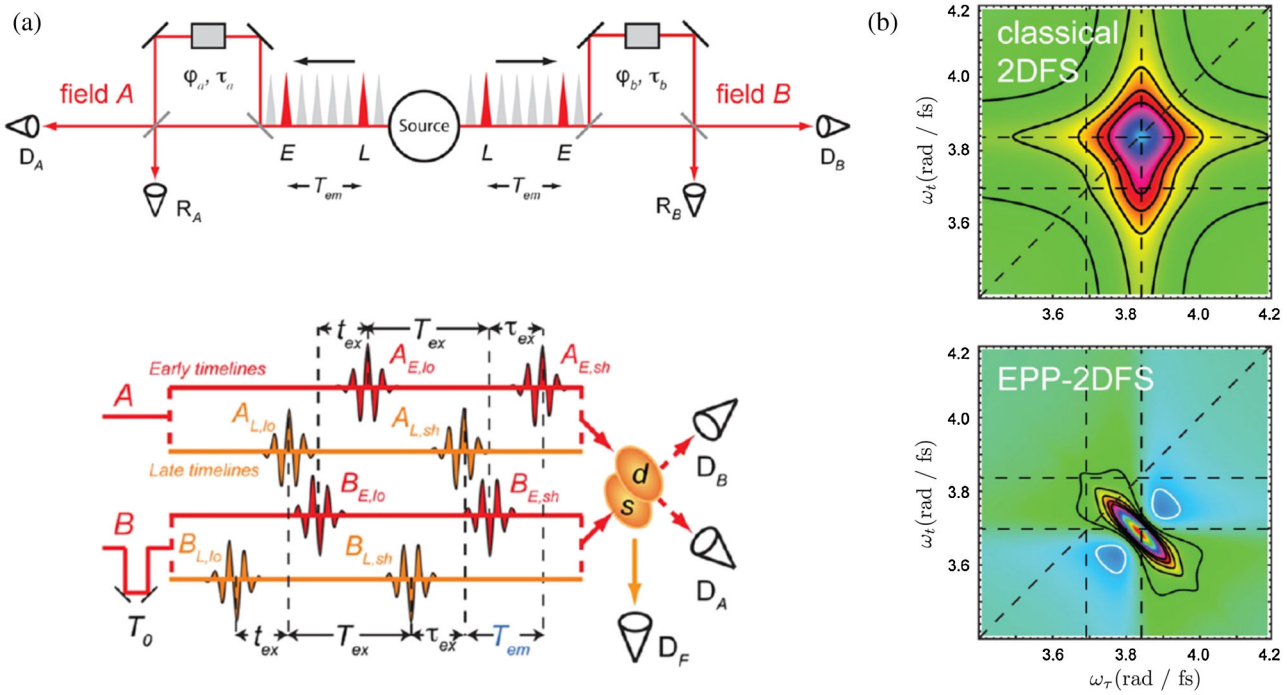

FIG. 15. (a) Experimental setup for the LOP protocol: By sending each beam through a Franson interferometer, the photon excitation may occur via either a delayed or an "early" photon. (b) Top panel: Two-dimensional fluorescence spectrum induced by classical light. Bottom panel: The same spectrum induced by entangled photons. From Raymer *et al.*, 2013.

2001; Tian *et al.*, 2003; Tan, 2008; Yan and Tan, 2009; Zhang, Wells, Hyland, and Tan, 2012; Krčmář, Gelin, and Domcke, 2013). In the phase-cycling protocol, the desired 2D signals are retrieved by the weighted summation of data collected using different interpulse phases ϕ_{21}, which are cycled over 2π radians in a number of equally spaced steps. In the pump-probe configuration, Myers *et al.* (2008) showed that other than the pure absorptive signal, the rephasing and nonrephasing contributions may also be retrieved. This phase difference detection can be defined as a two-step phase-cycling scheme. For the phase difference detection, the Ogilvie group collected signals with interpulse phases of $\phi_{21} = 0, \pi, \pi/2$, and $3\pi/2$. The same signal can be obtained with chopping, but this is only half as intense compared to the phase difference method. In the context of this review, Myers *et al.* (2008) used the technique similar to a four-step phase-cycling scheme, where four sets of data need to be collected and linearly combined.

Raymer *et al.* (2013) exploited the formal similarity between the TPIF and a photon coincidence signal to propose the setup shown in Fig. 15(a). Here the successive absorption events promoting the molecule into the f state are modulated by phase cycling and delay stages in both photon beams, creating interference effects between absorption events in which the photon takes the short path through the interferometer and those in which it takes the long path. The Fourier transform creates two-dimensional signals which are shown in Fig. 15(b). In contrast to the classical signal shown in the upper panel, the proposed scheme shows resonances only at the cross peak between the two electronic states. This could provide a useful tool to study conformations of aggregates. We next discuss this strategy in more detail.

5. Loop (LOP) versus ladder (LAP) delay scanning protocols for multidimensional fluorescence detected signals

Since the loop and the ladder diagrams involve different time variables they suggest different multidimensional signals obtained by scanning the corresponding time delays. We consider the TPIF signal created by a train of four pulses centered at times T_1, T_2, T_3, and T_4 with phases ϕ_1, ϕ_2, ϕ_3, and ϕ_4 (Tekavec, Lott, and Marcus, 2007; Pestov, Lozovoy, and Dantus, 2009). We first analyze signals obtained by the LOP and LAP delay scanning protocols with classical light. The two protocols highlight different resonances and processes. First we demonstrate what type of information can be extracted from each protocol for excited electronic states in a model molecular aggregate. We then show some benefits of LOP protocols for entangled light.

For the model system shown in Fig. 2(a) the signal (114) is given by the single loop diagram in Fig. 2(b). a, b, c, and d denote the pulse sequence *ordered along the loop* (but not in real time); a represents "first" on the loop, etc. Chronologically ordered pulses in real time will be denoted 1, 2, 3, and 4 which are permutations of a, b, c, and d. One can scan various delays $T_\alpha - T_\beta$, $\alpha, \beta = 1, \ldots, 4$ and control the phases $\pm\phi_1 \pm \phi_2 \pm \phi_3 \pm \phi_4$. In standard multidimensional techniques the time variables represent the pulses as they interact with the sample in chronological order (Mukamel, 1995). These are conveniently given by the ladder delays t_i shown in Fig. 16(c). The LAP maintains complete time ordering of all four pulses. The arrival time of the various pulses in chronological order is $T_1 < T_2 < T_3 < T_4$. The ladder delays are defined as $t_1 = T_2 - T_1$, $t_2 = T_3 - T_2$, and $t_3 = T_4 - T_3$. One can then use phase cycling to select the rephasing and

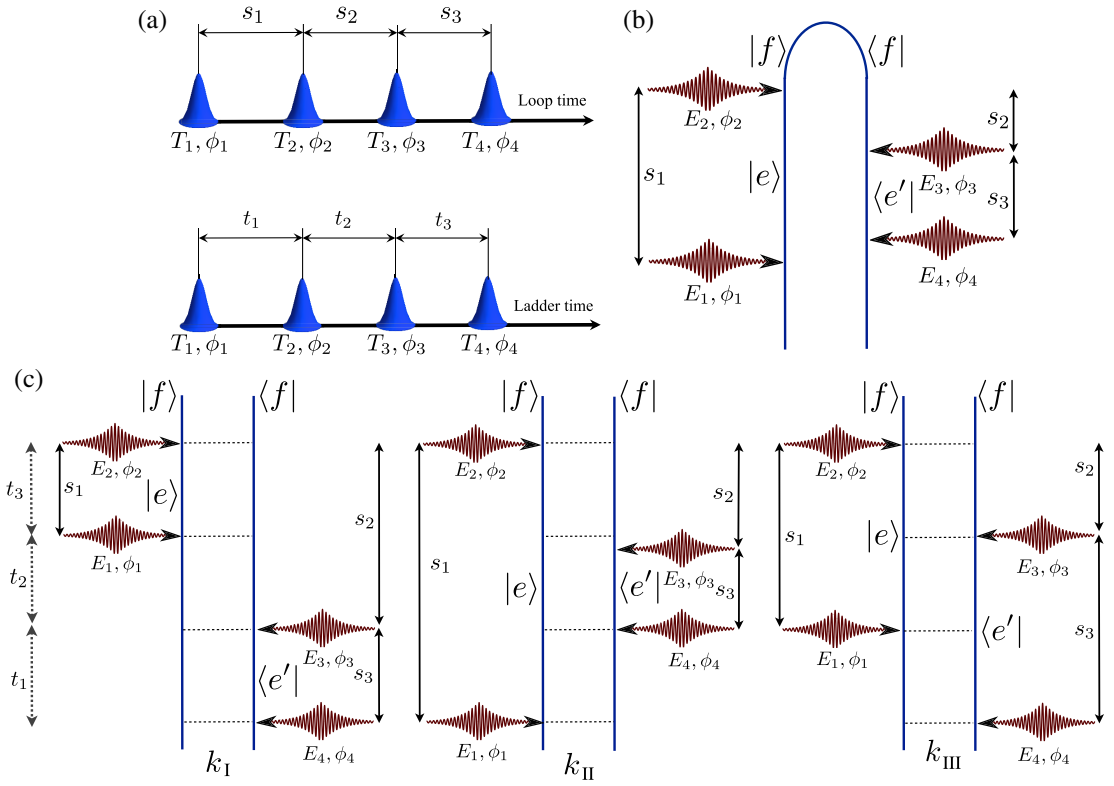

FIG. 16. (a) Pulse sequence for LOP (top panel) and LAP (bottom panel) scanning protocols. (b) Loop diagram for the TPA process with indicated loop delays for the nonspecified phase cycling that depends on chronological time ordering between pulses 1 and 4. (c) Ladder diagrams for the TPA signal with selected phase-cycling components corresponding to the double-quantum-coherence term $\mathbf{k}_{\rm I}$: $-\phi_d-\phi_c+\phi_b+\phi_a$, rephasing $\mathbf{k}_{\rm II}$: $-\phi_4+\phi_2+\phi_1-\phi_3$, and nonrephasing $\mathbf{k}_{\rm III}$: $-\phi_4+\phi_2-\phi_3+\phi_1$. Both loop s_j and ladder t_j delays, $j=1$, 2, and 3 are indicated. The transformation between two is different for each diagram. The time translation invariance implies $\omega_1+\omega_2-\omega_3-\omega_4=0$.

nonrephasing diagrams shown in Fig. 16(c) and read off the signal in a sum-over-states expansion

$$S^{(\mathrm{LAP})}_{\mathbf{k}_{\rm II}}(t_1,t_2,t_3)=\mathcal{I}\mathcal{E}_1^*\mathcal{E}_2^*\mathcal{E}_3\mathcal{E}_4\sum_{e,e',f}\mu_{ge'}\mu_{e'f}\mu^*_{fe}\mu^*_{eg}\times\mathcal{G}_{ef}(t_3)\mathcal{G}_{ee'}(t_2)\mathcal{G}_{eg}(t_1),\tag{117}$$

$$S^{(\mathrm{LAP})}_{\mathbf{k}_{\rm III}}(t_1,t_2,t_3)=\mathcal{I}\mathcal{E}_1^*\mathcal{E}_2^*\mathcal{E}_3\mathcal{E}_4\sum_{e,e',f}\mu_{ge'}\mu_{e'f}\mu^*_{fe}\mu^*_{eg}\times\mathcal{G}_{ef}(t_3)\mathcal{G}_{ee'}(t_2)\mathcal{G}_{ge'}(t_1).\tag{118}$$

The LAP signals (117) and (118) factorize into a product of several Green's functions with uncoupled time arguments. This implies that the corresponding frequency-domain signal will also factorize into a product of individual Green's functions, each depending on a single frequency argument $\tilde{\Omega}_j$, $j=1,2,3$ which yields

$$S^{(\mathrm{LAP})}_{\mathbf{k}_{\rm II}}(\tilde{\Omega}_1,t_2=0,\tilde{\Omega}_3)=\mathcal{R}\sum_{e,e',f}\frac{\mu_{ge'}\mu_{e'f}\mu^*_{fe}\mu^*_{eg}\mathcal{E}_1^*\mathcal{E}_2^*\mathcal{E}_3\mathcal{E}_4}{[\Omega_3-\omega_{ef}+i\gamma_{ef}][\Omega_1-\omega_{eg}+i\gamma_{eg}]},\tag{119}$$

$$S^{(\mathrm{LAP})}_{\mathbf{k}_{\rm III}}(\tilde{\Omega}_1,t_2=0,\tilde{\Omega}_3)=\mathcal{R}\sum_{e,e',f}\frac{\mu_{ge'}\mu_{e'f}\mu^*_{fe}\mu^*_{eg}\mathcal{E}_1^*\mathcal{E}_2^*\mathcal{E}_3\mathcal{E}_4}{[\Omega_3-\omega_{fe}+i\gamma_{fe}][\Omega_1-\omega_{e'g}+i\gamma_{e'g}]}.\tag{120}$$

This factorization holds, only in the absence of additional correlating mechanisms of the frequency variables caused by, e.g., dephasing (bath) or the state of light.

In the LOP the time ordering of pulses is maintained only on each branch of the loop but not between branches. To realize the LOP experimentally the indices 1 to 4 are assigned as follows: first by phase cycling we select a signal with phase $\phi_1+\phi_2-\phi_3-\phi_4$. The two pulses with positive phase detection are thus denoted 1, 2 and with negative phase 3, 4. In the 1, 2 pair pulse 1 comes first. In the 3, 4 pair pulse 4 comes first. The time variables in Fig. 16(b) are $s_1=T_2-T_1$, $s_2=T_3-T_2$, and $s_3=T_3-T_4$. With this choice s_1 and s_3 are positive whereas s_2 can be either positive or negative. This completely defines the LOP experimentally.

When the electronic system is coupled to a bath, it cannot be described by a wave function in the reduced space where the bath is eliminated. As described in Sec. II.J.2, the loop diagram must then be broken into several ladder diagrams shown in Fig. 2(b) which represent the density matrix. The full set of diagrams and corresponding signal expressions are given by Dorfman and Mukamel (2014b). In Fig. 16(c) we

present simplified expressions for the rephasing $\mathbf{k}_{\mathrm{II}}$ and nonrephasing $\mathbf{k}_{\mathrm{III}}$ signals in the limit of well-separated pulses:

$$S^{(\mathrm{LOP})}_{\mathbf{k}_{\mathrm{II}}}(s_1,s_2,s_3) = \mathcal{I}\mathcal{E}_1^*\mathcal{E}_2^*\mathcal{E}_3\mathcal{E}_4\sum_{e,e',f}\mu_{ge'}\mu_{e'f}\mu^*_{fe}\mu^*_{eg} \times \mathcal{G}_{ef}(s_2)\mathcal{G}_{ee'}(s_3)\mathcal{G}_{eg}(s_1-s_2-s_3), \tag{121}$$

$$S^{(\mathrm{LOP})}_{\mathbf{k}_{\mathrm{III}}}(s_1,s_2,s_3) = \mathcal{I}\mathcal{E}_1^*\mathcal{E}_2^*\mathcal{E}_3\mathcal{E}_4\sum_{e,e',f}\mu_{ge'}\mu_{e'f}\mu^*_{fe}\mu^*_{eg} \times \mathcal{G}_{ef}(s_2)\mathcal{G}_{ee'}(s_1-s_2)\mathcal{G}_{ge'}(s_2+s_3-s_1), \tag{122}$$

where $\mathcal{I}$ denotes the imaginary part and $\mathcal{G}_{\alpha\beta}(t) = (-i/\hbar)\theta(t)e^{-[i\omega_{\alpha\beta}+\gamma_{\alpha\beta}]t}$ is the Liouville space Green's function [see Eq. (16)]. Note that the loop delays s_j, $j=1$, 2, and 3 are coupled and enter in the Green's function $\mathcal{G}_{eg}$ in Eq. (121). Because of the Heaviside θ function in this Green's function, the delays s_j are not independent but rather couple the dynamics of the system during these delay times, which eventually result in cross resonances in multidimensional spectra. To see the effect on the mixing of the frequency variables that yield these cross peaks we take a Fourier transform of Eqs. (121) and (122) with respect to loop delay variables s_1 and s_3 keeping $s_2=0$ and obtain the resonant component of the signal analogous to the frequency-domain LAP signals (119) and (120)

$$S^{(\mathrm{LOP})}_{\mathbf{k}_{\mathrm{II}}}(\Omega_1,s_2=0,\Omega_3) = \mathcal{R}\sum_{e,e',f}\frac{\mu_{ge'}\mu_{e'f}\mu^*_{fe}\mu^*_{eg}\mathcal{E}_1^*\mathcal{E}_2^*\mathcal{E}_3\mathcal{E}_4}{[\Omega_1+\Omega_3-\omega_{ee'}+i\gamma_{ee'}][\Omega_1-\omega_{eg}+i\gamma_{eg}]}, \tag{123}$$

$$S^{(\mathrm{LOP})}_{\mathbf{k}_{\mathrm{III}}}(\Omega_1,s_2=0,\Omega_3) = \mathcal{R}\sum_{e,e',f}\frac{\mu_{ge'}\mu_{e'f}\mu^*_{fe}\mu^*_{eg}\mathcal{E}_1^*\mathcal{E}_2^*\mathcal{E}_3\mathcal{E}_4}{[\Omega_1+\Omega_3+\omega_{ee'}+i\gamma_{ee'}][\Omega_3-\omega_{e'g}+i\gamma_{e'g}]}, \tag{124}$$

where $\mathcal{R}$ denotes the real part. Equations (123) and (124) yield cross peaks $\Omega_1+\Omega_3=\omega_{ee'}$. The time correlations therefore result in the frequency mixing of arguments.

Figure 17 compares the LOP and LAP signals for the model dimer parameters of Raymer *et al.* (2013) under two-photon excitation by classical light. The LOP spectra for rephasing $\mathbf{k}_{\mathrm{II}}=-\hat{k}_1+\hat{k}_2+\hat{k}_3$, nonrephasing $\mathbf{k}_{\mathrm{III}}=+\hat{k}_1+\hat{k}_2-\hat{k}_3$, and their sums are shown in Figs. 17(a)–17(c), respectively. The corresponding LAP spectra are shown in Figs. 17(d)–17(f). We see that the scanning protocol makes a significant difference as seen by the two columns. The LOP resonances are narrow and clearly resolve the e_1 and e_2 states whereas the corresponding LAP signals are broad and featureless. This is a consequence of the display variables chosen in each protocol. LOP variables are coupled in a very specific fashion that allows one to extract the intraband dephasing rate $\gamma_{ee'}$ in the (Ω_1,Ω_3) plot with higher precision compared to the LAP case. Of course, one can extract similar information using LAP if displayed using $(\tilde{\Omega}_1,\tilde{\Omega}_2)$ or $(\tilde{\Omega}_2,\tilde{\Omega}_3)$ which is discussed later in the context of entangled light. This difference in two protocols was originally attributed to entanglement by Raymer *et al.* (2013). However, as can be seen from Fig. 17 (Dorfman and Mukamel, 2014b) the difference was unrelated to entanglement and was due to entangled signals being calculated using LOP and classical signals—using LAP.

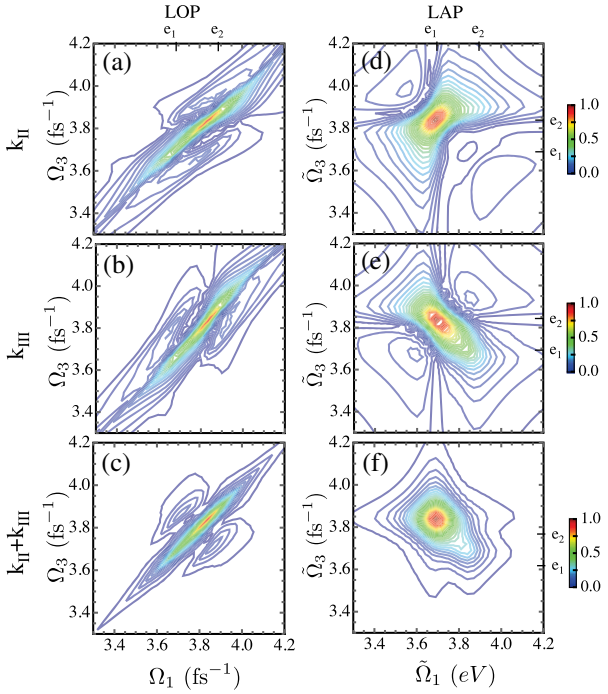

FIG. 17. Left column: $S_{\mathrm{LOP}}(\Omega_1,\tau_2=0,\Omega_3)$ for the molecular dimer model of Raymer *et al.* (2013) calculated using classical light for (a) rephasing $\mathbf{k}_{\mathrm{II}}$ Eq. (123); (b) nonrephasing $\mathbf{k}_{\mathrm{III}}$ Eq. (124); and (c) the sum of the two $\mathbf{k}_{\mathrm{II}}+\mathbf{k}_{\mathrm{III}}$. Right column: The same for $S_{\mathrm{LAP}}(\tilde{\Omega}_1,t_2=0,\tilde{\Omega}_3)$ Eqs. (119) and (120). Note that for the sums of rephasing and nonrephasing components for the LAP signal we flipped the rephasing component to obtain absorptive peaks as is typically done in the standard treatment of photon echo signals. The difference between the two columns stems from the display protocol and is unrelated to entanglement.

Entangled versus classical light: So far we presented the LOP and the LAP delay scanning protocols for classical light. We now turn to the LOP protocol with entangled light. Similarly to Eqs. (121) and (122) we calculate the signals for the cw-pump model (51) discussed earlier and obtain

$$S^{(j)}_{\mathrm{LOP}}(s_1,s_2,s_3) = \mathcal{I}\int_{-\infty}^{\infty}\frac{d\omega_a}{2\pi}\frac{d\omega_b}{2\pi}\frac{d\omega_d}{2\pi} \times R_j(\omega_a,\omega_b,\omega_d)D^{(j)}_{\mathrm{LOP}}(s_1,s_2,s_3;\omega_a,\omega_b,\omega_d) \times\langle E^\dagger(\omega_d)E^\dagger(\omega_a+\omega_b-\omega_d)E(\omega_b)E(\omega_a)\rangle, \tag{125}$$

where $j=\mathbf{k}_{\mathrm{II}}$, $\mathbf{k}_{\mathrm{III}}$, and the display function for both rephasing and nonrephasing contributions reads

$$D^{(j)}_{\mathrm{LOP}}(s_1,s_2,s_3;\omega_a,\omega_b,\omega_d) = \theta(s_1)\theta_j(\pm s_2)\theta(s_3)\times e^{-i\omega_a s_1+i\omega_d s_3-i(\omega_a+\omega_b)s_2}, \tag{126}$$

and matter responses are

$$R_{\mathbf{k}_{\rm II}}(\omega_a,\omega_b,\omega_d)=\sum_{e,e',f}\mu^a_{ge'}\mu^b_{e'f}\mu^{c*}_{fe}\mu^{d*}_{eg}\times\mathcal{G}_{ef}(-\omega_b)\mathcal{G}_{ee'}(\omega_a-\omega_d)\mathcal{G}_{eg}(\omega_a),$$
$$R_{\mathbf{k}_{\rm III}}(\omega_a,\omega_b,\omega_d)=\sum_{e,e',f}\mu^a_{ge'}\mu^b_{e'f}\mu^{c*}_{fe}\mu^{d*}_{eg}\times\mathcal{G}_{ef}(-\omega_b)\mathcal{G}_{ee'}(\omega_a-\omega_d)\mathcal{G}_{ge'}(-\omega_d). \quad (127)$$

Similarly we obtain for LAP signals Eqs. (117) and (118)

$$S^{(j)}_{\rm LAP}(t_1,t_2,t_3)=\mathcal{I}\int_{-\infty}^{\infty}\frac{d\omega_a}{2\pi}\frac{d\omega_b}{2\pi}\frac{d\omega_d}{2\pi}\times R_j(\omega_a,\omega_b,\omega_d)D^{(j)}_{\rm LAP}(t_1,t_2,t_3;\omega_a,\omega_b,\omega_d)\times\langle E^\dagger(\omega_d)E^\dagger(\omega_a+\omega_b-\omega_d)E(\omega_b)E(\omega_a)\rangle, \quad (128)$$

where the display function for the rephasing signal is

$$D^{(\mathbf{k}_{\rm II})}_{\rm LAP}(t_1,t_2,t_3;\omega_a,\omega_b,\omega_d)=\theta(t_1)\theta(t_2)\theta(t_3)\times e^{i\omega_b t_3-i\omega_a t_1+i(\omega_d-\omega_a)t_2}, \quad (129)$$

and for the nonrephasing signal

$$D^{(\mathbf{k}_{\rm III})}_{\rm LAP}(t_1,t_2,t_3;\omega_a,\omega_b,\omega_d)=\theta(t_1)\theta(t_2)\theta(t_3)e^{i\omega_b t_3+i\omega_d t_1+i(\omega_d-\omega_a)t_2}. \quad (130)$$

The complete set of signals along with frequency-domain signals for entangled light can be found in Sec. 2 of Dorfman and Mukamel (2014b).

The Fourier transform of the signal (125) was simulated using the LOP protocol and compared with the standard fully time-ordered LAP protocol given by Eq. (128) for a model trimer with parameters discussed in Sec. 5 of Dorfman and Mukamel (2014b). Figure 18 shows the simulated $S_{\rm LOP}(\Omega_1,\tau_2=0,\Omega_3)$ for a trimer using classical light (top row) and entangled light (bottom row). Figure 18(a) shows classical light which gives a diagonal cross peak $e=e'$ and one pair of weak side peaks parallel to the main diagonal at $(e,e')=(e_2,e_3)$. The remaining two pairs of side peaks at $(e,e')=(e_1,e_2)$ and $(e,e')=(e_1,e_3)$ are too weak to be seen. Figure 18(d) depicts the signal obtained using entangled photons where we observe two additional strong side cross-peak pairs with $(e,e')=(e_1,e_3)$ and $(e,e')=(e_1,e_2)$. The weak peak at $(e,e')=(e_2,e_3)$ is significantly enhanced as well.

As shown in Fig. 17 the LAP signal displayed vs $(\tilde\Omega_1,\tilde\Omega_3)$ does not effectively reveal intraband dephasing. This can, however, be done by the LAP signal displayed vs $(\tilde\Omega_2,\tilde\Omega_3)$. Figure 18(c) reveals several $\tilde\Omega_3=\omega_{fe}$ peaks that overlap in $\tilde\Omega_3$ axes due to large dephasing γ_{fe}. With entangled light, the LAP protocol yields some enhancement in several peaks around ±0.01 eV but overall the LOP yields a much cleaner result. The pathways for the density matrix (LAP) and the wave function (LOP) are different and may result in different types of resonances.

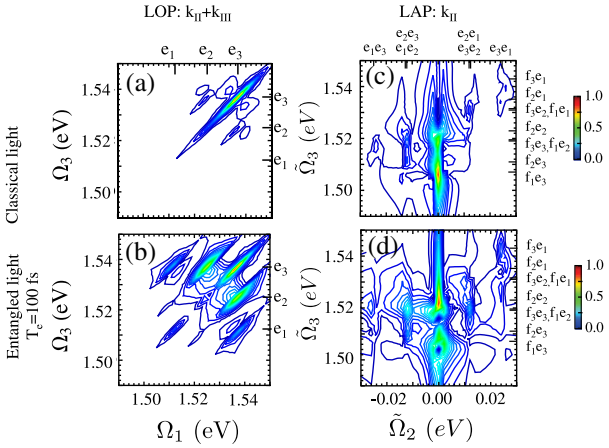

FIG. 18. Left column: LOP signal $S_{\mathbf{k}_{\rm II}+\mathbf{k}_{\rm III}}(\Omega_1,\tau_2=0,\Omega_3)$ for a molecular trimer with classical light Eqs. (123) and (124) (a), entangled light (125) with $T_e=100$ fs (b). Right column: LAP signal $S_{\mathbf{k}_{\rm II}}(\tilde\Omega_1,t_2=0,\tilde\Omega_3)$ using classical light Eq. (119) (c), entangled light with $T_e=100$ fs, Eq. (128) (d). Intraband dephasing $\gamma_{ee'}=1$ meV. All other parameters are given in Sec. 5 of Dorfman and Mukamel (2014b).

C. Heterodyne-detected nonlinear signals

In Sec. III.B we have considered fluorescence (homodyne) detection. Homodyne and heterodyne are two complementary detection schemes for nonlinear optical signals. For classical fields, if the sample radiation is detected for different modes than the incident radiation, the signal is proportional to $|E|^2$. This is known as homodyne detection whereby the intensity is the square modulus of the emitted field itself. If the emitted field coincides with a frequency of the incident radiation $E_{\rm in}$, then the signal intensity is proportional to $|E+E_{\rm in}|^2$. Consequently, the detected intensity contains a mixed interference term, i.e., $E^*E_{\rm in}+$ c.c. This is defined as the heterodyne signal, since the emitted field is mixed with another field. In terms of quantized fields, the signal is denoted homodyne if detected at a field mode that is initially vacant and heterodyne when detected at a field mode that is already occupied. Note that the nomenclature which is commonly used in nonlinear multidimensional spectroscopy is different from the definition used in quantum optics and optical engineering where homodyne and heterodyne refer to mixing with a field with the same or different frequency of the signal. In this review, we use the spectroscopy terminology (Potma and Mukamel, 2013). Fluorescence detection is often more sensitive than heterodyne detection as the latter is limited by the pulse duration so there are fewer constraints on the laser system. In addition the low intensity requirements for biological samples limit the range of heterodyne detection setups. This was demonstrated by Fu *et al.* (2007), Tekavec, Lott, and Marcus (2007), and Ye, Fu, and Warren (2009) even in single-molecule spectroscopy (Brinks *et al.*, 2010). Historically, Ramsey fringes constitute the first example of incoherent detection (Ramsey, 1950; Cohen-Tannoudji and Guéry-Odelin, 2011; Schlawin *et al.*, 2013). Information similar to coherent spectroscopy can be extracted from the parametric dependence on various pulse sequences applied prior to the incoherent detection (Rahav and Mukamel, 2010; Mukamel

and Richter, 2011). Possible incoherent detection modes include fluorescence (Elf, Li, and Xie, 2007; Barkai, 2008), photoaccoustic (Patel and Tam, 1981), atomic force microscope (AFM) (Mamin *et al.*, 2005; Poggio *et al.*, 2009; Rajapaksa, Uenal, and Wickramasinghe, 2010; Rajapaksa and Wickramasinghe, 2011), or photocurrent detection (Cheng and Xie, 2012; Nardin *et al.*, 2013).

1. Heterodyne intensity measurements: Raman versus TPA pathways

With $A(t) = E^\dagger(t)E(t)$, Eq. (111) yields the rate of change of the transmitted photon number,

$$S_1(t;\Gamma) = \frac{2}{\hbar}\Im\langle E_+^\dagger(t)V_+(t)\rangle_{\text{final}}. \tag{131}$$

The semiclassical signal may be obtained from Eq. (131) by simply replacing the field operator $E^\dagger(t)$ by a classical field amplitude $A^*(t)$. Similarly, by spectrally dispersing the time-integrated intensity, which amounts to measuring $A(\omega) = E^\dagger(\omega)E(\omega)$, we obtain

$$S(\omega;\Gamma) = \frac{2}{\hbar}\Im\langle E^\dagger(\omega)V(\omega)\rangle_{\text{final}}. \tag{132}$$

The third-order contribution of the time-integrated absorption signal (131) is given by the four loop diagrams in Fig. 19,

$$S_{1,(\mathrm{I})}(\Gamma) = -\frac{1}{\hbar}\Im\left[\left(-\frac{i}{\hbar}\right)^3\int_{-\infty}^{\infty}dt\int_{-\infty}^{t}d\tau_2\int_{-\infty}^{\tau_2}d\tau_1\int_{-\infty}^{t}d\tau_1'\right.$$
$$\times\langle V(\tau_1')V(t)V^\dagger(\tau_2)V^\dagger(\tau_1)\rangle$$
$$\left.\times\langle E^\dagger(\tau_1')E^\dagger(t)E(\tau_2)E(\tau_1)\rangle\right], \tag{133}$$

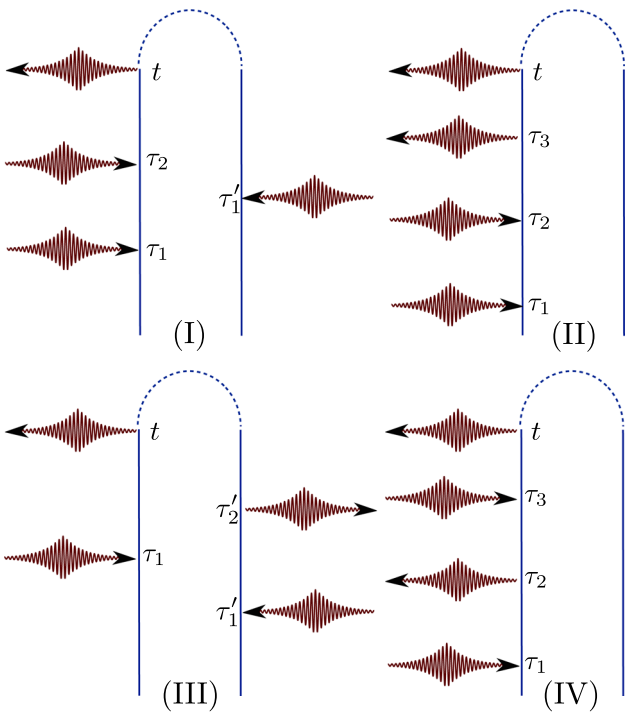

FIG. 19. Diagrams representing the third-order contributions to Eq. (131).

$$S_{1,(\mathrm{II})}(\Gamma) = \frac{1}{\hbar}\Im\left[\left(-\frac{i}{\hbar}\right)^3\int_{-\infty}^{\infty}dt\int_{-\infty}^{t}d\tau_3\int_{-\infty}^{\tau_3}d\tau_2\int_{-\infty}^{\tau_2}d\tau_1\right.$$
$$\times\langle V(t)V(\tau_3)V^\dagger(\tau_2)V^\dagger(\tau_1)\rangle$$
$$\left.\times\langle E^\dagger(t)E^\dagger(\tau_3)E(\tau_2)E(\tau_1)\rangle\right], \tag{134}$$

$$S_{1,(\mathrm{III})}(\Gamma) = \frac{1}{\hbar}\Im\left[\left(-\frac{i}{\hbar}\right)^3\int_{-\infty}^{\infty}dt\int_{-\infty}^{t}d\tau_1\int_{-\infty}^{t}d\tau_2'\int_{-\infty}^{\tau_2'}d\tau_1'\right.$$
$$\times\langle V(\tau_1')V^\dagger(\tau_2')V(t)V^\dagger(\tau_1)\rangle$$
$$\left.\times\langle E^\dagger(\tau_1')E(\tau_2')E^\dagger(t)E(\tau_1)\rangle\right], \tag{135}$$

$$S_{1,(\mathrm{IV})}(\Gamma) = \frac{1}{\hbar}\Im\left[\left(-\frac{i}{\hbar}\right)^3\int_{-\infty}^{\infty}dt\int_{-\infty}^{t}d\tau_3\int_{-\infty}^{\tau_3}d\tau_2\int_{-\infty}^{\tau_2}d\tau_1\right.$$
$$\times\langle V(t)V^\dagger(\tau_3)V(\tau_2)V^\dagger(\tau_1)\rangle$$
$$\left.\times\langle E^\dagger(t)E(\tau_3)E^\dagger(\tau_2)E(\tau_1)\rangle\right]. \tag{136}$$

An identical expansion of Eq. (132) yields the frequency-resolved third-order signal (its sum-over-state expansion is shown in Appendix D)

$$S_{1,(\mathrm{I})}(\omega;\Gamma) = -\frac{1}{\hbar}\Im\left[\left(-\frac{i}{\hbar}\right)^3\int_{-\infty}^{\infty}dt\int_{-\infty}^{t}d\tau_2\int_{-\infty}^{\tau_2}d\tau_1\int_{-\infty}^{t}d\tau_1'\right.$$
$$\times e^{i\omega t}\langle V(\tau_1')V(t)V^\dagger(\tau_2)V^\dagger(\tau_1)\rangle$$
$$\left.\times\langle E^\dagger(\tau_1')E^\dagger(\omega)E(\tau_2)E(\tau_1)\rangle\right], \tag{137}$$

$$S_{1,(\mathrm{II})}(\omega;\Gamma) = \frac{1}{\hbar}\Im\left[\left(-\frac{i}{\hbar}\right)^3\int_{-\infty}^{\infty}dt\int_{-\infty}^{t}d\tau_3\int_{-\infty}^{\tau_3}d\tau_2\int_{-\infty}^{\tau_2}d\tau_1\right.$$
$$\times e^{i\omega t}\langle V(t)V(\tau_3)V^\dagger(\tau_2)V^\dagger(\tau_1)\rangle$$
$$\left.\times\langle E^\dagger(\omega)E^\dagger(\tau_3)E(\tau_2)E(\tau_1)\rangle\right], \tag{138}$$

$$S_{1,(\mathrm{III})}(\omega;\Gamma) = \frac{1}{\hbar}\Im\left[\left(-\frac{i}{\hbar}\right)^3\int_{-\infty}^{\infty}dt\int_{-\infty}^{t}d\tau_1\int_{-\infty}^{t}d\tau_2'\int_{-\infty}^{\tau_2'}d\tau_1'\right.$$
$$\times e^{i\omega t}\langle V(\tau_1')V^\dagger(\tau_2')V(t)V^\dagger(\tau_1)\rangle$$
$$\left.\times\langle E^\dagger(\tau_1')E(\tau_2')E^\dagger(\omega)E(\tau_1)\rangle\right], \tag{139}$$

$$S_{1,(\mathrm{IV})}(\omega;\Gamma) = \frac{1}{\hbar}\Im\left[\left(-\frac{i}{\hbar}\right)^3\int_{-\infty}^{\infty}dt\int_{-\infty}^{t}d\tau_3\int_{-\infty}^{\tau_3}d\tau_2\int_{-\infty}^{\tau_2}d\tau_1\right.$$
$$\times e^{i\omega t}\langle V(t)V^\dagger(\tau_3)V(\tau_2)V^\dagger(\tau_1)\rangle$$
$$\left.\times\langle E^\dagger(\omega)E(\tau_3)E^\dagger(\tau_2)E(\tau_1)\rangle\right]. \tag{140}$$

It is instructive to relate the four diagrams corresponding to Eqs. (D1)–(D4) to the transition amplitudes between the initial and final matter states to gain some intuition for this signal. This is possible only for the total photon counting signal $\int d\omega S(\omega;\Gamma)/(2\pi)$, which represents the full energy exchanged between the light field and the matter system.

We now define the *transition amplitude operators*

$$T^{(1)}_{e'g}(\omega) = \frac{\mu_{e'g}}{\hbar}E(\omega), \tag{141}$$

$$T^{(2)}_{fg}(\omega_{\rm sum}) = \frac{1}{\hbar^2}\sum_e \int \frac{d\omega_a}{2\pi}\frac{\mu_{ge}\mu_{ef}E(\omega_{\rm sum}-\omega_a)E(\omega_a)}{\omega_a-\omega_e+i\gamma_e}, \tag{142}$$

$$T^{(2)}_{g'g}(\omega) = \frac{1}{\hbar^2}\sum_e \int \frac{d\omega_a}{2\pi}\frac{\mu_{ge}\mu_{eg'}E^\dagger(\omega_a-\omega)E(\omega_a)}{\omega_a-\omega_e+i\gamma_e}, \tag{143}$$

$$T^{(3)}_{e'g}(\omega) = \frac{1}{\hbar^3}\sum_{e,f}\int\frac{d\omega_a}{2\pi}\int\frac{d\omega_x}{2\pi}\frac{\mu_{ge}}{\omega_a-\omega_e+i\gamma_e}\frac{\mu_{ef}\mu_{fe'}}{\omega_x-\omega_f+i\gamma_f} \times E^\dagger(\omega_x-\omega)E(\omega_x-\omega_a)E(\omega_a), \tag{144}$$

$$T'^{(3)}_{e'g}(\omega) = \frac{1}{\hbar^3}\sum_{e,g'}\int\frac{d\omega_a}{2\pi}\int\frac{d\omega_-}{2\pi}\frac{\mu_{ge}}{\omega_a-\omega_e+i\gamma_e}\frac{\mu_{eg'}\mu_{g'e'}}{\omega_--\omega_{g'}+i\gamma_g} \times E(\omega-\omega_-)E^\dagger(\omega_a-\omega_-)E(\omega_a). \tag{145}$$

Assuming a unitary time evolution, we can replace the dephasing rates in Eqs. (D1)–(D4) by infinitesimal imaginary factors $\gamma \to \epsilon$. This allows us to use the identity $1/(\omega+i\epsilon) = \mathrm{PP}1/\omega + i\pi\delta(\omega)$ and carry out the remaining frequency integrals. We arrive at

$$\int\frac{d\omega}{2\pi}S_{1,(\mathrm{I})}(\omega;\Gamma) = \sum_f\langle T^{(2)\dagger}_{fg}(\omega_f)T^{(2)}_{fg}(\omega_f)\rangle, \tag{146}$$

$$\int\frac{d\omega}{2\pi}S_{1,(\mathrm{II})}(\omega;\Gamma) = \sum_e\langle T^{(1)\dagger}_{eg}(\omega_e)T^{(3)}_{eg}(\omega_e)\rangle, \tag{147}$$

$$\int\frac{d\omega}{2\pi}S_{1,(\mathrm{III})}(\omega;\Gamma) = \sum_{g'}\langle T^{(2)\dagger}_{g'g}(\omega_{g'})T^{(2)}_{g'g}(\omega_{g'})\rangle, \tag{148}$$

$$\int\frac{d\omega}{2\pi}S_{1,(\mathrm{IV})}(\omega;\Gamma) = \sum_e\langle T^{(1)\dagger}_{eg}(\omega_e)T'^{(3)}_{eg}(\omega_e)\rangle. \tag{149}$$

Details of the sum-over-state expansion are presented in Appendix D. These results clarify the statement we made at the end of Sec. III.B.1: The $\chi^{(3)}$-absorption signal comprises matter transitions from the ground to the f state, just like the TPIF signal, but it also contains transitions to e and g states. The absorption and the TPIF signals contain the same information, only when transitions between the e and g states can be neglected, as is the case when e is off resonant.

2. Heterodyne-detected four-wave mixing and the double-quantum-coherence technique

Time-domain two-dimensional (2D) spectroscopic techniques (Mukamel, 2000) provide a versatile tool for exploring the properties of molecular systems, such as photosynthetic aggregates (Engel *et al.*, 2007; Abramavicius, Voronine, and Mukamel, 2008) and coupled (hybrid) nanostructures to semiconductor quantum wells (Zhang *et al.*, 2007; Pasenow *et al.*, 2008; Yang *et al.*, 2008; Vogel *et al.*, 2009). These techniques use sequences of coherent pulses that are shorter than the dephasing times of the system.

Earlier we presented different delay scanning protocols (LOP and LAP) for multidimensional spectroscopy with entangled photons. These protocols can be experimentally realized using entangled-photon pulse shaping, using collinear geometry and precise control of the phase, via the phase cycling. These protocols allow one to extract interband and intraband dephasing with high resolution by exciting doubly excited-state distributions. We now present a different multidimensional time-domain signal that involves higher electronic states manifold, but does not require excited populations. This is known as double-quantum coherence (DQC) (Mukamel, Oszwaldowski, and Yang, 2007; Yang and Mukamel, 2008; Kim, Mukamel, and Scholes, 2009; Palmieri, Abramavicius, and Mukamel, 2009), which monitors the coherence between ground and doubly excited states $|f\rangle\langle g|$ rather than the population $|f\rangle\langle f|$. This technique reveals the energies of single and doubly excited-state energies as well as the correlations between single and doubly excited states. We show how pulsed entangled photons affect the two-photon resonances. Some bandwidth limitations of classical beams are removed and selectivity of quantum pathways is possible.

a. The DQC signal

In the following we use the LAP delay scanning protocol which monitors the density matrix. A pulse shaper creates a sequence of four well-separated chronologically ordered pulses described by field operator $E_j(t) = \int(d\omega/2\pi)E_j(\omega)e^{-i\omega(t-T_j)}$, $j = 1, 2, 3$, and 4. The control parameters are their central times $T_1 < T_2 < T_3 < T_4$ and phases ϕ_1, ϕ_2, ϕ_3, and ϕ_4 [see Fig. 20(a)]. The DQC signal selects those contributions with the phase signature $\phi_1+\phi_2-\phi_3-\phi_4$. The signal is defined as the change in the time-integrated transmitted intensity in component ϕ_4, which is given by

$$S = \frac{2}{\hbar}\int dt\langle E^\dagger_4(t)V(t)\rangle. \tag{150}$$

We thus have a configuration similar to an impulsive experiment with four short well-separated classical fields. Introducing the LAP delays $t_3 = T_4 - T_3$, $t_2 = T_3 - T_2$, and $t_1 = T_2 - T_1$. We can calculate Eq. (150) by expanding perturbatively in the dipole field-matter interaction Hamiltonian (7). The two contributions to the signal are represented by the ladder diagrams shown in Fig. 20(b). The corresponding signal (150) can be read off these diagrams and is given by $S^{(\mathrm{LAP})}_{\mathrm{DQC}}(\Gamma) = S^{(\mathrm{LAP})}_{\mathrm{DQC}i}(\Gamma) + S^{(\mathrm{LAP})}_{\mathrm{DQC}ii}(\Gamma)$, where

$$S^{(\mathrm{LAP})}_{\mathrm{DQC}i}(\Gamma) = \frac{1}{\hbar^3}\mathrm{Re}\int_{-\infty}^{\infty}dt\int_0^\infty ds_1\int_0^\infty ds_2\int_0^\infty ds_3\langle\Psi|E^\dagger_3(t-s_3)E^\dagger_4(t)E_2(t-s_3-s_2)E_1(t-s_3-s_2-s_1)|\Psi\rangle \times\sum_{ee'f}V_{e'f}V_{ge'}V^*_{ef}V^*_{ge}e^{-i\xi_{fe's_3}-i\xi_{fgs_2}-i\xi_{egs_1}}, \tag{151}$$

$$S^{(\mathrm{LAP})}_{\mathrm{DQC}ii}(\Gamma) = -\frac{1}{\hbar^3}\mathrm{Re}\int_{-\infty}^{\infty}dt\int_0^{\infty}ds_1\int_0^{\infty}ds_2\int_0^{\infty}ds_3\langle\Psi|E_4^{\dagger}(t)E_3^{\dagger}(t-s_3)E_2(t-s_3-s_2)E_1(t-s_3-s_2-s_1)|\Psi\rangle \times\sum_{ee'f}V_{e'f}V_{ge'}V^*_{ef}V^*_{ge}e^{-i\xi_{eg}s_3-i\xi_{fg}s_2-i\xi_{e'g}s_1}. \tag{152}$$

We introduced the complex frequency variables $\xi_{ij} = \omega_{ij} + i\gamma_{ij}$, where $\omega_{ij} = \varepsilon_i - \varepsilon_j$ are the transition frequencies and γ_{ij} are the dephasing rates. The signal may be depicted by its variation with various parameters of the field

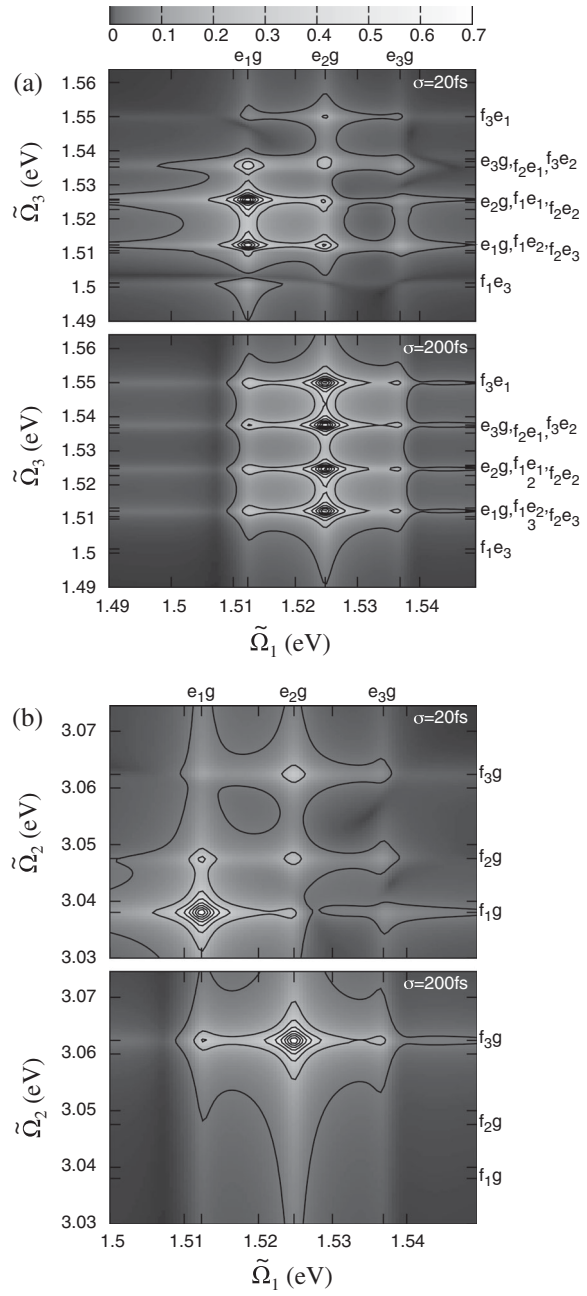

FIG. 20. (a) 2D signal $S^{(\mathrm{LAP})}_{\mathrm{DQC}}(\tilde{\Omega}_1,\tilde{\Omega}_3)$ Eq. (162) (absolute value), showing correlation plots with different pump bandwidths σ as indicated. The bottom panel is multiplied by 6. (b) Same as (a) but for the 2D signal $S^{(\mathrm{LAP})}_{\mathrm{DQC}}(\tilde{\Omega}_1,\tilde{\Omega}_2)$ Eq. (163). Parameters for simulations are given by Richter and Mukamel (2010).

wave function denoted collectively as Γ. Various choices of Γ lead to different types of 2D signals. These are specified in Eqs. (162) and (163).

b. The field correlation function for entangled-photon pairs

We consider the pulsed entangled-photon pairs described in Sec. II.F. We use the wave function introduced by Keller and Rubin (1997), where the two-photon wave function $\Phi(\boldsymbol{k}_i,\boldsymbol{k}_j)$ takes the form

$$\Phi(\boldsymbol{k}_i,\boldsymbol{k}_j) = g\hat{u}\{[\omega(\boldsymbol{k}_j)-\omega(\boldsymbol{k}_i)]/2\}e^{-i[\omega(\boldsymbol{k}_i)+\omega(\boldsymbol{k}_j)]\hat{\tau}_{ij}} \times e^{-i[\omega(\boldsymbol{k}_j)]\tau_{ij}}A_P(\omega(\boldsymbol{k}_i)+\omega(\boldsymbol{k}_j)-\Omega_P), \tag{153}$$

$$\hat{u}(\omega) = e^{\omega T_{ij}/2}\mathrm{sinc}(\omega T_{ij}/2), \tag{154}$$

where $A_P(\cdots)$ is the pulse envelope and Ω_p is the central frequency of the pump pulse used to generate the pairs.

The correlation function of the entangled fields reads (Keller and Rubin, 1997)

$$\langle 0|E_1(s_1-T_1)E_2(s_2-T_2)|\Psi\rangle = V_0e^{-\Omega_p/2(s_1+s_2-t_1)}\mathrm{rect}(s_2-s_1-t_1)A_p\left(\frac{s_1+s_2-t_1}{2}\right), \tag{155}$$

$$\mathrm{rect}(t) = \begin{cases}\frac{1}{T} & 0<t<T,\\ 0 & \text{otherwise},\end{cases} \qquad A_p(t) = \exp[-t^2/(2\sigma^2)], \tag{156}$$

which describes the pulsed counterpart of the cw-correlation function (52) we had described earlier, where the step function $\mathrm{rect}(t)$ is replaced by the finite pulse amplitude A_p.

c. Simulated 2D signals

Next we present a simulated DQC signal for a model trimer system with parameters given by Richter and Mukamel (2010). By inserting Eq. (155) into Eqs. (151) and (152) and carrying out all integrations, assuming that $\gamma \ll \sigma$, we arrive at the final expression for the two contributions to the signal:

$$S^{(\mathrm{LAP}e)}_{\mathrm{DQC}i}(\Gamma) = \frac{1}{\hbar^3}\mathrm{Re}\sum_{ee'f}V_{e'f}V_{ge'}V^*_{ef}V^*_{ge}|V_0|^2|A_p(\omega_{fg}-\Omega_p)|^2 \times e^{-i\xi_{eg}t_1}e^{-i\xi_{fe'}t_3}e^{-i\xi_{fg}t_2}\frac{(e^{i(\omega_{fg}/2-\xi_{eg})T}-1)e^{-i\xi_{fg}T/2}}{i(\omega_{fg}/2-\xi_{eg})T} \times\frac{(e^{i(\omega_{fg}/2-\xi_{fe'})T}-1)e^{-i\xi_{fg}T/2}}{i(\omega_{fg}/2-\xi_{fe'})T}, \tag{157}$$

$$S^{(\mathrm{LAP}e)}_{\mathrm{DQC}ii}(\Gamma)=\frac{1}{\hbar^3}\mathrm{Re}\sum_{ee'f}V_{ge'}V_{e'f}V^*_{ef}V^*_{ge}|V_0|^2|A_p(\omega_{fg}-\Omega_p)|^2 \times e^{-i\xi_{eg}t_1}e^{-i\xi_{e'g}t_3}e^{-i\xi_{fg}t_2} \times\frac{(e^{i(\omega_{fg}/2-\xi_{eg})T}-1)e^{-i\xi_{fg}T/2}}{i(\omega_{fg}/2-\xi_{eg})T} \times\frac{(e^{i(\omega_{fg}/2-\xi_{e'g})T}-1)e^{-i\xi_{fg}T/2}}{i(\omega_{fg}/2-\xi_{e'g})T}, \quad (158)$$

$$|A_p(\omega)|^2=\exp(-\sigma^2\omega^2). \quad (159)$$

The control parameters Γ now include the delay times (t_1,t_2,t_3) and the entanglement time T.

For comparison, we present the same signal obtained with four impulsive classical pulses with envelopes $E_j(\cdot)$, $j=1,\ldots,4$, $E_2(\cdot)$, $E_3(\cdot)$, and $E_4(\cdot)$ and carrier frequency Ω_p^0 (Abramavicius *et al.*, 2009):

$$S^{(\mathrm{LAP}c)}_{\mathrm{DQC}i}=\frac{1}{\hbar^3}\mathrm{Re}\sum_{ee'f}V_{e'f}V_{ge'}V^*_{ef}V^*_{ge} \times E_4^*(\omega_{fe'}-\Omega_p^0)E_3^*(\omega_{e'g}-\Omega_p^0) \times E_2(\omega_{fe}-\Omega_p^0)E_1(\omega_{eg}-\Omega_p^0) \times e^{-i\xi_{eg}\tau_{12}}e^{-i\xi_{fe'}\tau_{34}}e^{-i\xi_{fg}\tau_d}, \quad (160)$$

$$S^{(\mathrm{LAP}c)}_{\mathrm{DQC}ii}=\frac{1}{\hbar^3}\mathrm{Re}\sum_{ee'f}V_{ge'}V_{e'f}V^*_{ef}V^*_{ge} \times E_4^*(\omega_{e'g}-\Omega_p^0)E_3^*(\omega_{fe'}-\Omega_p^0) \times E_2(\omega_{fe}-\Omega_p^0)E_1(\omega_{eg}-\Omega_p^0) \times e^{-i\xi_{eg}\tau_{12}}e^{-i\xi_{e'g}\tau_{34}}e^{-i\xi_{fg}\tau_d}. \quad (161)$$

With the help of Eqs. (157) and (158), we can compare the entangled-photon and classical DQC signals. We first note that Eq. (157) is linear in the intensity of the generating pump pulse, in contrast with the intensity square scaling of the classical case Eq. (160). In the classical case the signal is limited by the bandwidths of the four pulses [cf. Eqs. (160) and (161)], which control the four transitions (ω_{eg}, ω_{fe}, $\omega_{e'g}$, and $\omega_{fe'}$) in the two-photon transitions inside the pulse bandwidth (Abramavicius *et al.*, 2009). In Eq. (157) envelope bandwidth limitations are imposed only through the bandwidth of entangled-photon pair $A_p(\cdot)$ and the limitation is imposed only on the two-photon transition ω_{fg}, leading to a much broader bandwidth for the ω_{eg} and ω_{fe} transitions, if the ω_{fg} transition is within the generating pump pulse bandwidth.

This effect is illustrated in Fig. 20(a) for the following 2D signal:

$$S^{(\mathrm{LAP})}_{\mathrm{DQC}}(\tilde\Omega_1,\tilde\Omega_3)=\int_0^\infty dt_1\int_0^\infty dt_3 S(t_1,t_3)e^{it_1\tilde\Omega_1+it_3\tilde\Omega_3}, \quad (162)$$

ω_{eg} resonances are seen along $\tilde\Omega_1$ and ω_{eg} and ω_{fe} on axis $\tilde\Omega_3$. As the bandwidth is reduced, we get contributions only from the doubly excited-state resonant to the generating pump pulse. This results in four identical patterns along the Ω_1 axis. All peaks are connected to the same doubly excited states. More precisely we get four contributions along the $\tilde\Omega_1$ axis connected to the transitions $\omega_{f_3e_1}$, $\omega_{f_3e_2}$ overlapping with ω_{e_3g}, ω_{e_2g} overlapping with $\omega_{f_3e_3}$ and ω_{e_1g}. The remaining transitions are not affected by the reduced pump bandwidth. Here the narrow bandwidth of the pump can be used to select contributions in the spectra connected to a specific doubly excited state. In Fig. 20(b) we display a different signal:

$$S^{(\mathrm{LAP})}_{\mathrm{DQC}}(\tilde\Omega_1,\tilde\Omega_2)=\int_0^\infty dt_1\int_0^\infty dt_2 S(t_1,t_2)e^{it_1\tilde\Omega_1+it_2\tilde\Omega_2}, \quad (163)$$

ω_{eg} resonances are now seen along $\tilde\Omega_1$ and ω_{fg} in $\tilde\Omega_2$. This is similar to Fig. 20(a) except that here we see the singly excited-state contributions ω_{e_1g}, ω_{e_2g}, and ω_{e_3g} to the selected doubly excited state f_3 along a single row.

Bandwidth limitations on the singly excited-state transitions ω_{eg} and ω_{fe} are imposed only indirectly by the factors in Eqs. (157) and (158) which depend on the entanglement time T. These become largest for $\omega_{fg}=2\omega_{fe}$.

The factors in Eq. (157) and (158) which depend on the entanglement time T contain an interference term of the form $e^{i(\omega-\gamma)T}-1$, where ω is a material frequency (see Secs. II.J and III.B.2). If we now vary the entanglement time, some resonances will interfere destructively for values of the entanglement time which match the period of ω. One can therefore use the entanglement times to control selected resonances. This holds only as long as the entanglement times are not much longer than the dephasing time, since in this case the signal will be weak. The frequencies ω can be in the contributing diagrams $\omega_{fg}/2-\omega_{eg}$ or $\omega_{fg}/2-\omega_{fe}$ (which differs from the first frequency only by a sign) for a different combination of the states e, e', and f. By varying T, we expect an oscillation of the magnitudes of resonances with different frequencies. The details of manipulation of the entanglement time as a control parameter have been studied by Richter and Mukamel (2010) and Schlawin *et al.* (2013).

In an earlier study we used two pulsed entangled-photon pairs (Richter and Mukamel, 2010) $(\boldsymbol{k}_1,\boldsymbol{k}_2)$ and $(\boldsymbol{k}_3,\boldsymbol{k}_4)$. With the pulse shaping described in Sec. II.G, a single shaped entangled-photon pair is sufficient to realize any time-domain four-wave-mixing signal.

D. Multiple photon counting detection

A different class of multidimensional signals is possible by detecting sequences of individual photons emitted by an optically driven system. With proper gating, each photon j can be characterized by frequency ω_j and time t_j. By detecting N photons we thus obtain a $2N$-dimensional signal parametrized by $\omega_1,t_1,...,\omega_N,t_N$. Unlike coherent multidimensional heterodyne signals which are parametrized by delays of the incoming fields, these incoherent signals are parametrized by the emitted photons. The photon time t_j and frequency ω_j are not independent and can be detected only to within a Fourier uncertainty $\Delta\omega_j\Delta t_j>1$. This poses a fundamental limitation on the joint temporal and spectral resolution. We derive these signals and connect them to multipoint $2N$ dipole correlation functions of matter. The Fourier uncertainty is naturally built in by a proper description of photon gating and need not be imposed in an *ad hoc* matter as is commonly done.

A semiclassical photon counting formalism was first derived by Mandel (1958, 1959). The full quantum-mechanical description of the field and photon detection was developed by Glauber (2007). The theory of the electromagnetic field measurement through photoionization and the resulting photoelectron counting was developed by Kelley and Kleiner (1964). The experimental application to normal and time-ordered intensity correlation measurements was given in the seminal work of Kimble, Dagenais, and Mandel (1977). According to these treatments free-field operators, in general, do not commute with source-quantity operators. This is the origin of the fact that the normal and time ordering of the measured field correlations, according to the Kelley-Kleiner theory (Kelley and Kleiner, 1964), are transformed into normal and time-ordered source quantities occurring inside the integral representations of the filtered source-field operators. This constitutes the backreaction of the detector on the field state (Cohen-Tannoudji *et al.*, 1992). An ideal photon detector is a device that measures the radiation field intensity at a single point in space. The detector size should be much smaller than spatial variations of the field. The response of an ideal time-domain photon detector is independent of the frequency of the radiation.

The resolution of simultaneous frequency and time-domain measurements is limited by the Fourier uncertainty $\Delta\omega\Delta t > 1$. A naive calculation of signals without proper time-and-frequency gating can work for slowly varying spectrally broad optical fields where the above inequality is satisfied but otherwise it may yield unphysical and even negative signals (Eberly and Wodkiewicz, 1977). Mukamel, Ciordas-Ciurdariu, and Khidekel (1996) calculated the mixed time-frequency representation for the coherent optical measurements with interferometric or autocorrelation detection in terms of a mixed material response functions and a Wigner distribution for the incoming pulses, the detected field, and the gating device. Multidimensional gated fluorescence signals for single-molecule spectroscopy were calculated by Mukamel and Richter (2011).

The standard Glauber theory of photon counting and correlation measurements (Mollow, 1972; Scully and Zubairy, 1997; Glauber, 2007) was formulated solely in the radiation field space (matter is not considered explicitly). Signals are related to the multipoint normally ordered field correlation function, convoluted with time-and-frequency gating spectrograms of the corresponding detectors. This approach assumes that the detected field is given. Thus, it does not address the matter information and the way this field has been generated. Temporally and spectrally resolved measurements can reveal important matter information. Single-photon spectroscopy of single molecules (Fleury *et al.*, 2000; Lettow *et al.*, 2010; Rezus *et al.*, 2012) calls for an adequate microscopic foundation where joint matter and field information could be retrieved by a proper description of the detection process.

A microscopic diagrammatic approach may be used for calculating time-and-frequency-gated photon counting measurements (Dorfman and Mukamel, 2012a). The observed signal can be represented by a convolution of the bare signal and a detector spectrogram that contains the time-and-frequency gate functions. The bare signal is given by the product of two transition amplitude superoperators (Mukamel and Rahav, 2010) (one for bra and one for ket of the matter plus field joint density matrix), each creating a coherence in the field between states with zero and one photon. By combining the transition amplitude superoperators from both branches of the loop diagram we obtain the photon occupation number that can be detected. The detection process is described in the joint field and matter space by a sum over pathways each involving a pair of quantum modes with different time orderings. The signal is recast using time-ordered superoperator products of matter and field. In contrast to the Glauber theory that uses normally ordered ordinary field operators, the microscopic approach of Dorfman and Mukamel (2012a) is based on time-ordered superoperators. Ideal frequency-domain detection requires only a single mode (Mukamel and Richter, 2011). However, maintaining any time resolution requires a superposition of several field modes that contain the pathway information. This information is not directly accessible in the standard detection theory that operates in the field space alone (Glauber, 2007).

1. Photon correlation measurements using gated photon number operators

A time-and-frequency-gated Nth order photon correlation measurement performed at N detectors characterized by central time t_j and central frequency ω_j, $j = 1, \ldots, N$ is defined as

$$g^{(N)}(t_1, \omega_1, \Gamma_1; \ldots, t_N; \omega_N, \Gamma_N) = \frac{\langle \mathcal{T} \hat{n}_{t_1,\omega_1} \cdots \hat{n}_{t_N,\omega_N} \rangle_T}{\langle \mathcal{T} \hat{n}_{t_1,\omega_1} \rangle_T \cdots \langle \mathcal{T} \hat{n}_{t_N,\omega_N} \rangle_T}, \tag{164}$$

where $\langle \cdots \rangle_T = \mathrm{Tr}[\cdots \rho_T(t)]$ and $\rho_T(t)$ represents the total density matrix of the entire system in joint field plus matter space and contains information about the system evolution prior to the detection (e.g., the photon generation process, etc.). Γ_j, $j = 1, \ldots, N$ represents other parameters of the detectors such as bandwidth (σ_T^j and σ_ω^j are the time gate and frequency gate bandwidths, respectively). The time-and-frequency-gated photon number superoperator is given by

$$\hat{n}_{t,\omega} = \int dt' \int d\tau D(t, \omega; t', \tau) \hat{n}(t', \tau). \tag{165}$$

Here $D(t, \omega, t', \tau)$ is a detector time-domain spectrogram (the ordinary function, not an operator) which takes into account the detector's parameters and is given by

$$D(t, \omega, t', \tau) = \int \frac{d\omega''}{2\pi} e^{-i\omega''\tau} |F_f(\omega'', \omega)|^2 F_t^*(t' + \tau, t) F_t(t', t), \tag{166}$$

where F_t and F_f are time and frequency gating functions that are characterized by central time t and frequency ω and detection bandwidths σ_T and σ_ω, respectively. Note that in Eq. (166) the time gate is applied first, followed by the frequency gate. A similar expression can be written when the order in gating is reversed. $\hat{n}(t, t')$ is a bare photon number superoperator defined in terms of the bare field operators as

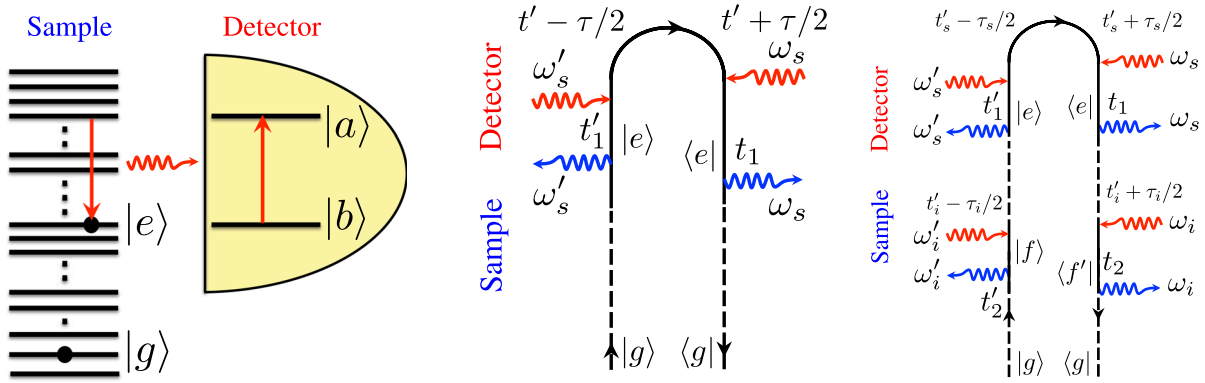

FIG. 21. (a) Schematic of time-and-frequency-resolved photon coincidence measurement. (b) Loop diagram for the bare signal Eq. (E15) in a gated measurement. (c) Loop diagram for correlated two photon measurement Eq. (E26). Dashed lines represent the dynamics of the system driven by the field modes. τ_i and τ_s can be either positive or negative.

$$\hat{n}(t',\tau)=\sum_{s,s'}\hat{E}^{\dagger}_{sR}(t'+\tau)\hat{E}_{s'L}(t')\rho(t'). \tag{167}$$

Details are found in Appendix E.

2. Photon counting connected to matter dipole correlation functions

To connect the photon coincidence counting (PCC) signals to matter properties one needs to expand the density operator in Eq. (167) in perturbative series over field-matter interactions. We first calculate the time-and-frequency-resolved emission spectra

$$n_{t,\omega}=\int dt'\int d\tau D(t,\omega;t',\tau)n(t',\tau), \tag{168}$$

where the bare photon number $n(t',\tau)\equiv\langle\mathcal{T}\hat{n}(t',\tau)\rangle_T$ is an expectation value of the bare photon number operator with respect to the total density matrix. The leading contribution is coming from the second order in field-matter interactions with vacuum modes [see Fig. 21(b)]

$$\begin{aligned}n(t',\tau)=&\frac{1}{\hbar^2}\int_{-\infty}^{t'}dt_1\int_{-\infty}^{t'+\tau}dt_2\langle V^{\dagger}(t_2)V(t_1)\rangle\\&\times\sum_{s,s'}\langle\hat{E}_{s'}(t_2)\hat{E}^{\dagger}_{s'}(t'+\tau)\hat{E}_s(t')\hat{E}^{\dagger}_s(t_1)\rangle_v,\end{aligned} \tag{169}$$

where we had utilized superoperator time ordering and $\langle\cdots\rangle=\mathrm{Tr}[\cdots\rho(t)]$, where $\rho(t)$ is the density operator that excludes vacuum modes and $\langle\cdots\rangle_v=\mathrm{Tr}[\cdots\rho_v(t)]$ with $\rho_v(t)=|0\rangle\langle 0|$ is the density matrix of the vacuum modes. Using the bosonic commutation relations introduced in Sec. I.A [see Eq. (6)] and moving to the continuous density of states, one can obtain

$$n(t',\tau)=\mathcal{D}^2(\omega)\langle V^{\dagger}(t'+\tau)V(t')\rangle, \tag{170}$$

where $\mathcal{D}(\omega)=(1/2\pi)\tilde{\mathcal{D}}(\omega)$ is a combined density of states evaluated at the central frequency of the detector ω for smooth enough distribution of modes. The detected signal (165) is given by

$$\begin{aligned}S^{(1)}(t,\omega)\equiv n_{t,\omega}=&\int dt'\int d\tau D(t,\omega;t',\tau)\mathcal{D}^2(\omega)\\&\times\langle V^{\dagger}(t'+\tau)V(t')\rangle.\end{aligned} \tag{171}$$

One can similarly calculate the second-order bare correlation function

$$\begin{aligned}\langle\mathcal{T}\hat{n}_{t_1,\omega_1}\hat{n}_{t_2,\omega_2}\rangle_T=&\int dt_1'\int d\tau_1 D^{(1)}(t_1\omega_1;t_1',\tau_1)\\&\times\int dt_2'\int d\tau_2 D^{(2)}(t_2,\omega_2;t_2',\tau_2)\\&\times\langle\mathcal{T}\hat{n}(t_1',\tau_1)\hat{n}(t_2',\tau_2')\rangle_T.\end{aligned} \tag{172}$$

The bare PCC rate $\langle\mathcal{T}\hat{n}(t_1',\tau_1)\hat{n}(t_2',\tau_2')\rangle_T$ can be read off the diagram shown in Fig. 21(c). The leading contribution requires a fourth-order expansion in field-matter interactions

$$\begin{aligned}&\langle\mathcal{T}\hat{n}(t_1',\tau_1)\hat{n}(t_2',\tau_2')\rangle_T\\&=\frac{1}{\hbar^4}\int_{-\infty}^{t_1'}dt_1\int_{-\infty}^{t_1'+\tau_1}dt_3\\&\times\int_{-\infty}^{t_2'}dt_2\int_{-\infty}^{t_2'+\tau_2}dt_4\langle V^{\dagger}(t_4)V^{\dagger}(t_3)V(t_1)V(t_2)\rangle\\&\times\sum_{s,s'}\sum_{r,r'}\langle E_{r'}(t_4)E_{s'}(t_3)E^{\dagger}_{r'}(t_2'+\tau_2)E^{\dagger}_{s'}(t_1'+\tau_1)\\&\times E_s(t_1')E_r(t_2')E^{\dagger}_s(t_1)E^{\dagger}_r(t_2)\rangle_v.\end{aligned} \tag{173}$$

After tracing over the vacuum modes we obtain

$$\begin{aligned}&\langle\mathcal{T}\hat{n}(t_1',\tau_1)\hat{n}(t_2',\tau_2')\rangle_T\\&=\mathcal{D}^2(\omega_1)\mathcal{D}^2(\omega_2)\langle V^{\dagger}(t_2'+\tau_2)V^{\dagger}(t_1'+\tau_1)V(t_1')V(t_2')\rangle.\end{aligned} \tag{174}$$

The gated coincidence signal (172) is finally given by

$$\begin{aligned}&S^{(2)}(t_1,\omega_1;t_2,\omega_2)\\&\equiv\langle\mathcal{T}\hat{n}_{t_1,\omega_1}\hat{n}_{t_2,\omega_2}\rangle_T\\&=\mathcal{D}^2(\omega_1)\mathcal{D}^2(\omega_2)\int dt_1'\int d\tau_1 D^{(1)}(t_1\omega_1;t_1',\tau_1)\\&\times\int dt_2'\int d\tau_2 D^{(2)}(t_2,\omega_2;t_2',\tau_2)\\&\times\langle V^{\dagger}(t_2'+\tau_2)V^{\dagger}(t_1'+\tau_1)V(t_1')V(t_2')\rangle.\end{aligned} \tag{175}$$

Therefore, the fundamental material quantity that yields the emission spectra (171) is a two-point dipole correlation function given by Eq. (170), and for the coincidence $g^{(2)}$ measurement (175) it is the four-point dipole correlation function in Eq. (174). Sum-over-state expansions of these expressions are given in Appendix E.

3. Connection to the physical spectrum

Eberly and Wodkiewicz (1977) had pointed out that detector gating with a finite bandwidth must be added to describe the real detector. Recently del Valle *et al.* (2012) and González-Tudela, del Valle, and Laussy (2015) used a two-level model detector with a single parameter Γ that characterizes both time-and-frequency detection. This was denoted the physical spectrum (178) which can be recovered from our model by removing the time gate $F_t = 1$ and using a Lorentzian frequency gate

$$F_f(\omega, \omega') = \frac{i}{\omega' + \omega + i\Gamma/2}. \tag{176}$$

Using the physical spectrum, the time-and-frequency-resolved photon coincidence signal is given by

$$g^{(2)}_{\Gamma_1\Gamma_2}(\omega_1, \omega_2; \tau) = \lim_{t\to\infty} \frac{\langle \hat{A}^\dagger_{\omega_1,\Gamma_1}(t)\hat{A}^\dagger_{\omega_2,\Gamma_2}(t+\tau)A_{\omega_2,\Gamma_2}(t+\tau)\hat{A}_{\omega_1,\Gamma_1}(t)\rangle}{\langle \hat{A}^\dagger_{\omega_1,\Gamma_1}(t)\hat{A}_{\omega_1,\Gamma_1}(t)\rangle\langle \hat{A}^\dagger_{\omega_2,\Gamma_2}(t+\tau)\hat{A}_{\omega_2,\Gamma_2}(t+\tau)\rangle}, \tag{177}$$

where

$$\hat{A}_{\omega,\Gamma}(t) = \int_{-\infty}^{t} dt_1 e^{(i\omega-\Gamma/2)(t-t_1)}\hat{E}(t_1) \tag{178}$$

is the gated field. This model provides a simple benchmark for finite-band detection, which has several limitations. First, the time-and-frequency gating parameters are not independent, unlike the actual experimental setup, where frequency filters and avalanche photodiodes are two independent devices. Second, this method does not address the generation and photon bandwidth coming from the emitter, as the analysis is performed solely in the field space. Finally, the multiphoton correlation function presented by González-Tudela, del Valle, and Laussy (2015) is stationary. For instance, the four-point bare correlation function

$$A_B(\omega_1, \omega_2, t_1, t_2) = \langle E^\dagger_{\omega_1}(t_1)E^\dagger_{\omega_2}(t_2)E_{\omega_2}(t_2)E_{\omega_1}(t_1)\rangle \tag{179}$$

depends on four times and four frequencies. After gating suggested by del Valle *et al.* (2012) and González-Tudela, del Valle, and Laussy (2015) the correlation function (179) is recast using $C_B(\omega_1, \omega_2, t_2 - t_1)$, which depends only on the time difference $t_2 - t_1$, which is an approximation for stationary fields. This model also works if $t \gg \Gamma^{-1}$, which means that Γ cannot approach zero (a perfect reflection in the Fabry-Pérot cavity). It also works when $\Gamma\tau_0 \ll 1$, where τ_0 is the scale of change in the field envelope. For comparison, the PCC (164) for $N = 2$ reads

$$g^{(2)}(t_1, \omega_1, \Gamma_1; t_2; \omega_2, \Gamma_2)\frac{\langle \mathcal{T}\hat{n}_{t_1,\omega_1}\hat{n}_{t_2,\omega_2}\rangle}{\langle \mathcal{T}\hat{n}_{t_1,\omega_1}\rangle\langle \mathcal{T}\hat{n}_{t_2,\omega_2}\rangle}, \tag{180}$$

which depends on two time t_1, t_2 and two frequency ω_1, ω_2 arguments. The presented theory which gives rise to Eq. (180) has several merits compared to the physical spectrum (del Valle *et al.*, 2012; González-Tudela, del Valle, and Laussy, 2015). First, independent control of time-and-frequency gates (with guaranteed Fourier uncertainty for the time-and-frequency resolution) along with the fact that the bare photon number operator depends on two time variables $\hat{n}(t, \tau)$ allows one to capture any dynamical process down to the very short scale dynamics in ultrafast spectroscopy applications. Second, the gating (165) provides a unique tool that can capture nonequlibrium and nonstationary states of matter which can be controlled by gating bandwidths. In this case a series of frequency ω_1, ω_2 correlation plots (using the central frequencies of the spectral gates as variables) for different time delays $t_1 - t_2$ yields a 2D spectroscopy tool capable of measuring ultrafast dynamics. Third, the superoperator algebra allows one to connect the gated field correlation function

$$A_G(\bar{\omega}_1, \bar{\omega}_2, \bar{t}_1, \bar{t}_2) = \langle E^{(tf)\dagger}_{\bar{\omega}_1}(\bar{t}_1)E^{(tf)\dagger}_{\bar{\omega}_2}(\bar{t}_2)E^{(tf)}_{\bar{\omega}_2}(\bar{t}_2)E^{(tf)}_{\bar{\omega}_1}(\bar{t}_1)\rangle \tag{181}$$

with the bare correlation function (179), with time-and-frequency gates (arbitrary, not necessarily Lorentzian) as well as a material response that precedes the emission and detection of photons. The superoperator expressions require time ordering and can be generalized to correlation functions of field operators that are not normally ordered. Superoperators provide an effective bookkeeping tool for field-matter interactions prior to the spontaneous emission of photons. We shall apply it to the detection of photon correlations as shown in Sec. IV.I, PCC can be recast in terms of matter correlation functions by expanding the total density matrix operator in a perturbation series and tracing the vacuum modes. This way photon counting measurements can be related to the matter response functions which are the standard building blocks of nonlinear spectroscopy.

E. Interferometric detection of photon coincidence signals

The simultaneous detection of entangled photon pairs has long been employed for imaging applications (Strekalov *et al.*, 1995; Pittman *et al.*, 1995). The transverse spatial entanglement of photon pairs allows one to detect to resolve the image of a sample by the detection of an entangled partner that never interacted with it. This approach is denoted ghost imaging, and could enable atomic resolution with optical photons that are entangled with x-ray photons (Li *et al.*, 2015). Photon coincidence signals also known as biphoton signals (Scarcelli *et al.*, 2003; Yabushita and Kobayashi, 2004; Kalachev *et al.*, 2007; Slattery *et al.*, 2013) became recently available as a tool for nonlinear spectroscopy. In a typical setup, a pair of entangled photons denoted E_s and E_r generated by PDC are separated on a beam splitter [see Fig. 22(a)]. One photon E_s is transmitted through the molecular sample and then detected in coincidence with E_r. In order to use it as a spectroscopic tool, a frequency filter can be placed in front of

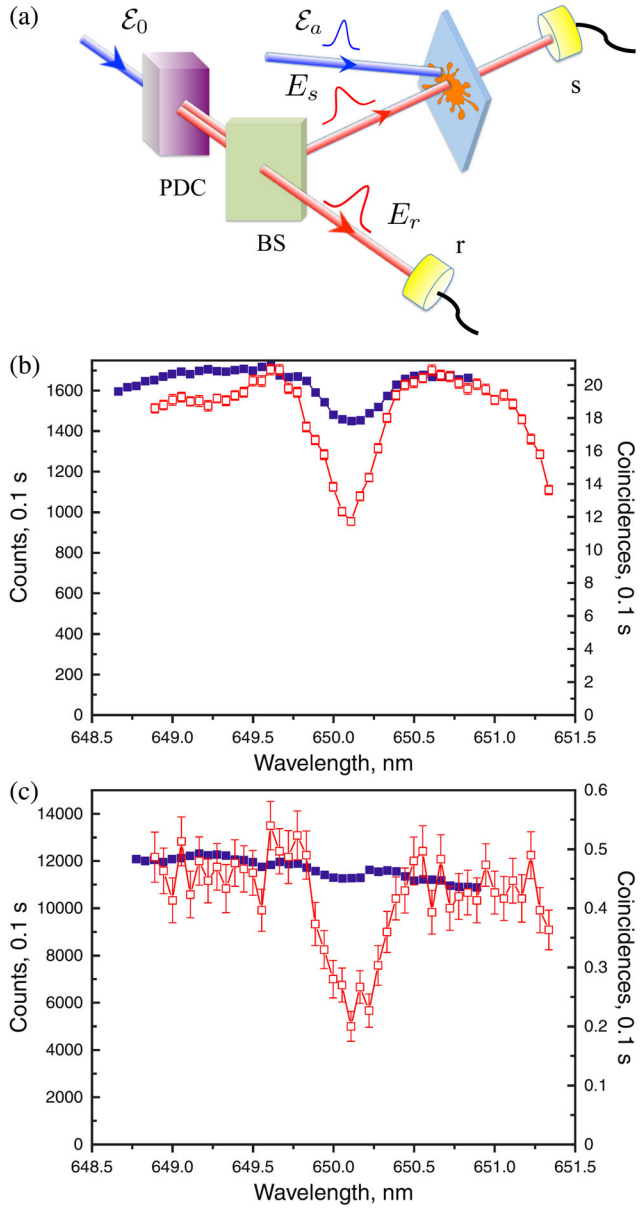

FIG. 22. Linear absorption experiment of Kalachev *et al.* (2007) with coincidence detection. (a) The entangled-photon pairs in beams E_s and E_r are split on a beam splitter. E_s is employed as a probe transmitted through the sample, while E_r is detected in coincidence.The absorption spectrum of the Er^{3+} ion in a yttrium aluminum garnet (YAG) crystal around 650 nm obtained by single-photon counting (blue filled squares, left Y axis) and coincidence counting (red open squares, right Y axis) at various values of signal-to-noise ratios in the channel with the sample: (b) 1/2 and (c) 1/30.

one of the detectors which measures the spectrum. This type of signal shows a number of interesting features: First, coincidence detection improves the signal-to-noise ratio (Kalashnikov *et al.*, 2014). Second, the two detectors may operate in very different spectral regions and at different spatial locations (Kalachev *et al.*, 2007). For example, to measure the spectroscopic properties of a sample in the vacuum ultraviolet (VUV) range, it is not necessary to set and control a spectrometer in a vacuum chamber. Instead, using a VUV and a visible entangled-photon pair only the latter should be resolved by a spectrometer. Similarly a visible photon detection can replace an infrared detection with improved signal-to-noise ratio. The power of the light source must often be very low to prevent possible damage of a sample, but an infrared photodetector is usually noisy. Photon coincidence measurements involve the lowest intensities of light, single photons, and can overcome the noise.

In the following, we present photon coincidence versions of three signals: linear absorption, pump-probe, and femtosecond stimulated Raman signals (FSRS).

1. Coincidence detection of linear absorption

Linear absorption is the most elementary spectroscopic measurement. Photon coincidence detection can improve the signal-to-noise ratio. We now present the simplest intuitive phenomenological approach. In Secs. II and III we present more rigorous microscopic derivations for pump-probe and Raman signals.

In the case of the linear signal, the joint detection of two entangled photons provides linear absorption information provided one of the photons is transmitted through a molecular sample. If the coincidence gate window accepts counts for a time T, then the joint detection counting rate R_c of detectors r and s is

$$R_c \propto \int_0^T dt_1 \int_0^T dt_2 |\langle 0|a_s^\dagger(t_1)a_r^\dagger(t_2)|\psi\rangle|^2, \quad (182)$$

where ψ is a two-photon entangled state (33). The gating window T is typically much larger than the reciprocal bandwidth of the light or the expected dispersive broadening

$$R_c \propto \int d\omega_1 \int d\omega_2 |\langle 0|a_s(\omega_1)a_r(\omega_2)|\psi\rangle|^2. \quad (183)$$

Denote the spectral transfer functions of the sample and monochromator $H_S(\omega)$ and $H_M(\omega)$, respectively. In this case,

$$a_s(\omega_1) = \frac{1}{\sqrt{2}}\tilde{a}_s(\omega_1)H_S(\omega_1) \quad (184)$$

and

$$a_r(\omega_2) = \frac{i}{\sqrt{2}}\tilde{a}_r(\omega_2)H_M(\omega_2) \quad (185)$$

provided that the signal and idler photons are separated by a 50/50 beam splitter. For narrow-band classical pump, the two-photon amplitude reads

$$\Phi(\omega_1,\omega_2) = F\left(\frac{\omega_1-\omega_2}{2}\right)\delta(\omega_1+\omega_2-2\omega_0).$$

The corresponding coincidence counting rate is then given by

$$R_c \propto \int d\Omega |H_S(\omega_0+\Omega)H_M(\omega_0-\Omega)F(\Omega)|^2. \quad (186)$$

Now assume that $H_M(\omega)$ is much narrower than $H_S(\omega)$ and $\tilde{\Phi}(\omega_1,\omega_2)$, so that we can set $H_M(\omega)=\delta(\omega-\omega_M)$, and the frequency ω_M does not exceed the frequency range in which function $F(\omega)$ is essentially nonzero. Dividing the coincidence counting rate with a sample $R_{c,\text{sample}}$ by one without the sample R_c, we obtain the absorption spectrum

$$S_{ILA}(\omega_M) = \frac{R_{c,\text{sample}}}{R_c} \propto |H_S(2\omega_0 - \omega_M)|^2, \quad (187)$$

where the subscript *ILA* marks the interferometric nature of the photon coincidence detection combined with the linear absorption measurement. Thus, the joint detection counting rate reproduces the spectral function of the sample, provided that the linewidth of the pumping field as well as the bandwidth of the monochromator is narrow enough for resolving the absorption spectrum features.

Kalachev *et al.* (2007) used the coincidence signals to measure the spectroscopic properties of the YAG : Er^{3+} crystal in order to demonstrate the advantage of the coincidence detection in the presence of an enhanced background noise. Figures 22(b) and 22(c) show the central part of the absorption spectrum measured in two ways: using the coincidence counting as described previously and using the single-photon counting, when the sample was placed above the monochromator in the idler channel. The signal-to-noise ratio in the channel was changed from 1/2 to 1/30. It is evident from these experimental data that the standard classical method which suffers from a high noise level does not allow one to obtain any spectroscopic information, but in contrast the coincidence counting measurement does not undergo the reduction in resolution and is robust to noise. This scheme was later extended to plasmonic nanostructures (Kalashnikov *et al.*, 2014).

2. Coincidence detection of pump-probe signals

Consider the setup depicted in Fig. 23(a). Unlike the linear absorption, here the probe photon is sent through the sample, which has previously been excited by a classical ultrafast laser pulse and then detected.

The interferometric pump-probe (IPP) signal with photon coincidence detection is dispersed spectrally by placing spectral filters in front of both detectors, and our signal is given by the change to this two-photon counting rate that is governed by a four-point correlation function of the field (Mosley *et al.*, 2008; Cho *et al.*, 2014)

$$\langle E_r^\dagger(\omega_r) E_s^\dagger(\omega) E_s(\omega) E_r(\omega_r)\rangle. \quad (188)$$

Here ω/ω_r denotes the detected frequency of the respective spectral filter, and the brackets $\langle\cdots\rangle$ represent the expectation value with respect to the transmitted fields. To obtain the desired pump-probe signal in a three-level system, we used a third-order perturbation theory (Schlawin, Dorfman, and Mukamel, 2016). The first two interactions are with the classical pump pulse, which is taken to be impulsive $\mathcal{E}_a(t) = \mathcal{E}_a\delta(t)$, and the third is with the probe centered at $t = t_0$. Assuming E_s to be far off resonant from the $e-g$ transition, we obtain only the single diagram shown in Fig. 23(c), which reads

$$S_{\text{IPP}}(\omega,\omega_r;t_0) = -\frac{2}{\hbar}\Im\left(-\frac{i}{\hbar}\right)^3 |\mathcal{E}_a|^2 \int_0^\infty dt e^{i\omega(t-t_0)} \times \int_0^t d\tau F(t-\tau,\tau)\langle E_r^\dagger(\omega_r) E_s^\dagger(\omega) E_s(\tau) E_r(\omega_r)\rangle. \quad (189)$$

We defined the matter correlation function,

$$F(t-\tau,\tau) = \langle|\mu_{ge}|^2|\mu_{ef}|^2 G_{fe}(t-\tau) G_{ee}(\tau)\rangle_{\text{env}}, \quad (190)$$

where μ_{ge} and μ_{ef} denote the dipole moments which connect the ground state with the singly excited-state manifold, as well as the single with the doubly excited-state manifold, respectively. $\langle\cdots\rangle_{\text{env}}$ denotes the average with respect to environmental degrees of freedom, obtained from tracing out the bath. Here we employ a stochastic Liouville equation (Tanimura, 2006) which represents the TSJ model: A ground state g is dipole coupled to an electronic excited state e, which is connected to two spin states $\uparrow$ and $\downarrow$ undergoing relaxation (Šanda and Mukamel, 2006). We additionally consider a doubly excited state f, which is dipole coupled to both $|e,\uparrow\rangle$ and $|e,\downarrow\rangle$ [see Fig. 23(b)]. The electronic states are damped by a dephasing rate γ. We assume the low-temperature limit, where only the decay from $\uparrow$ to $\downarrow$ is allowed (Dorfman, Fingerhut, and Mukamel, 2013b). The decay is entirely incoherent, such that the description may be restricted to the two spin populations $|\uparrow\rangle\langle\uparrow| = (1,0)^T$ and $|\downarrow\rangle\langle\downarrow| = (0,1)^T$. The field correlation function (190) is then given by

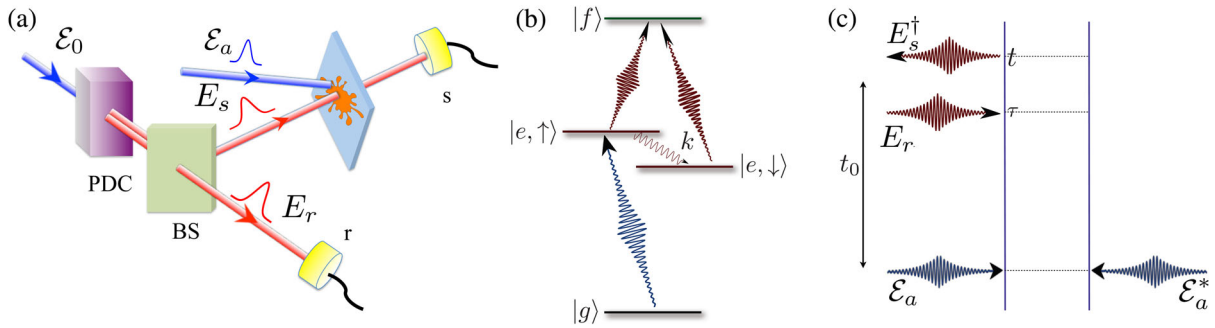

FIG. 23. (a) The IPP setup: the entangled-photon pair in beams E_s and E_r are split on a beam splitter. A classical, actinic, ultrafast pulse $\mathcal{E}_a$ excites the sample, and E_s is employed as a probe in a pump-probe measurement, while E_r is detected in coincidence. (b) The level scheme for the two-state jump (TSJ) model considered in this work. The $g-e$ transition is far off resonant from the spectral range of the entangled-photon wave packet, which couples only to the $e-f$ transition. (c) Diagram representing the pump-probe measurement. From Schlawin, Dorfman, and Mukamel, 2016.

$$F(t_2,t_1)=|\mu_{ge}|^2|\mu_{ef}|^2e^{-\gamma(t_1+2t_2)}\times\left(e^{-i\omega_+t_2}+\frac{2i\delta}{k+2i\delta}e^{-kt_1}[e^{-(k+i\omega_-)t_2}-e^{-i\omega_+t_2}]\right),\tag{191}$$

where δ is the energy difference between the two spin states, and $\omega_\pm=\omega_{fe}\pm\delta$. Note that, since we monitor the $f-e$ transition, the detected frequency will increase in time from ω_- to ω_+.

We shall use these results to first simulate the classical pump-probe signal and then the two-photon counting signal with entangled photons. For the pump-probe technique we use a classical Gaussian probe pulse

$$E_{pr}(\omega)=\frac{1}{\sqrt{2\pi\sigma^2}}\exp\left[-(\omega-\omega_0)^2/2\sigma^2\right].\tag{192}$$

We chose the following system parameters: $\omega_{fe}=11\,000$, $\delta=200$, $k=120$, and $\gamma=100$ cm^{-1}.

The peak frequency ω_0 is fixed at the transition frequency ω_{fe}, and we vary the probe bandwidth. Figure 23(a) shows the signal for $\sigma=1000$ cm^{-1}. The two peaks at $\omega_{fe}\pm\delta$ correspond to the detected frequency, when the system is either in the upper state (at $\omega_{fe}-\delta$) or in the lower state ($\omega_{fe}+\delta$). Because of the spectrally dispersed detection of the signal, the resonance widths are given by the linewidth γ and not the much broader probe pulse bandwidth σ. For very short time delays t_0, both resonances increase, until the probe pulse has

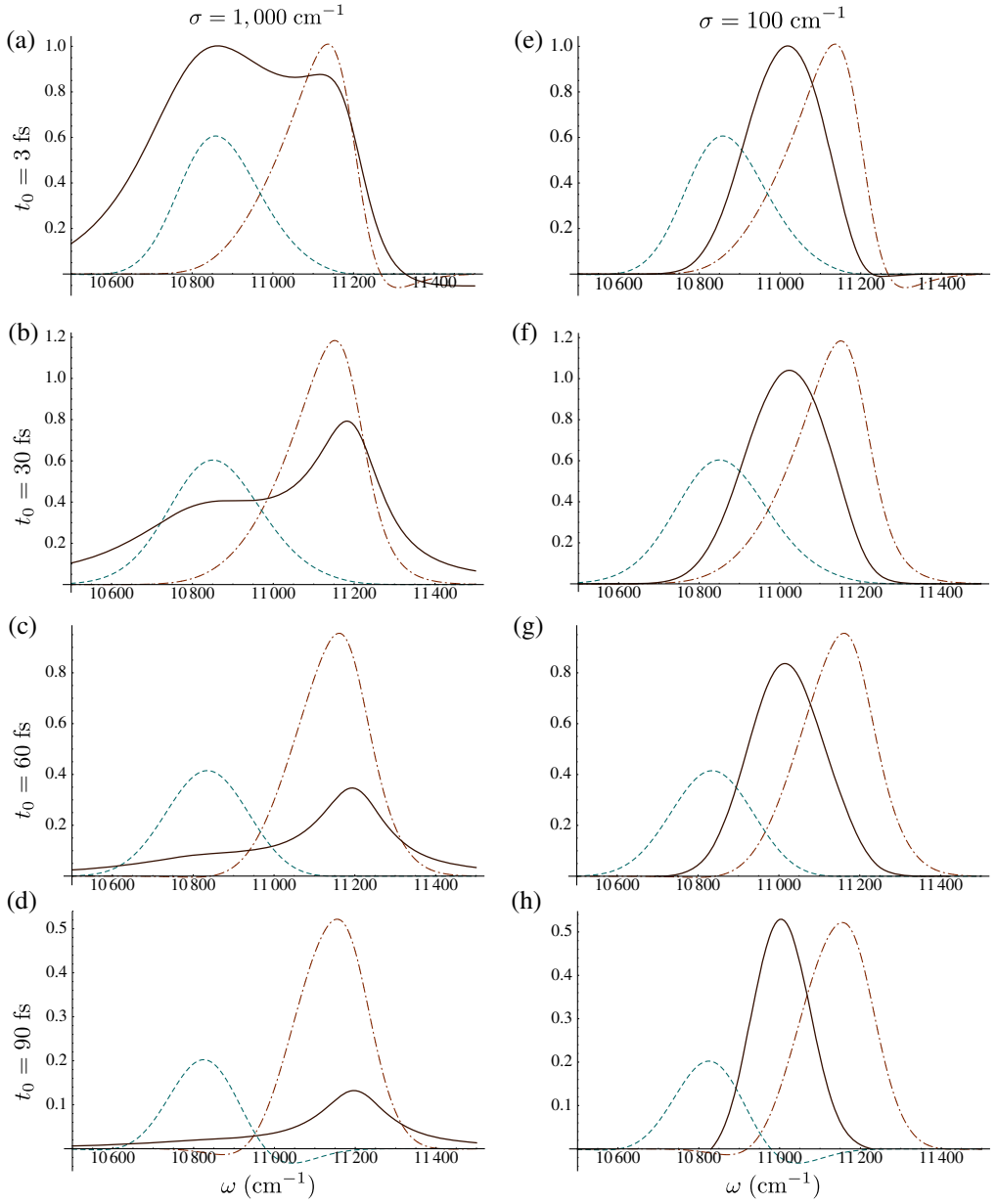

FIG. 24. (a) TPC signals with $\sigma_p=2000$ cm^{-1} and $T=90$ fs, $\omega_r=10\,400$ cm^{-1} (blue, dashed) and $11\,400$ cm^{-1} (red, dot-dashed) as well as the classical pump-probe signal (black, solid) with $\sigma=1000$ cm^{-1} are plotted vs the dispersed frequency ω with a time delay set to $t_0=3$ fs. (b) Same for $t_0=30$, (c) 60, and (d) 90 fs. (e)–(h) Same as (a)–(d), but with classical bandwidth $\sigma=100$ cm^{-1}. The classical signal is normalized, such that its maximum value at $t_0=0$ is equal to 1. Similarly, the TPC signals are normalized to the maximum value of the signal with $\omega_r=11\,400$ cm^{-1} at $t_0=0$. From Schlawin, Dorfman, and Mukamel, 2016.

fully passed through the sample. Then the resonance at 10 800 cm^{-1}, i.e., the state $|e,\uparrow\rangle$, starts to decay rapidly, while the 11 200 cm^{-1} resonance peaks at longer delay times due to its initial population by the upper state. For longer delays, both resonances decay due to the additional dephasing.

The two-photon counting signal with entangled photons offers novel control parameters: The dispersed frequency ω of beam 1, the pump frequency ω_p, and its bandwidth σ_p loosely correspond to the classical control parameters, i.e., the central frequency ω_0 and bandwidth σ. In addition, we may vary the entanglement time T and the detected frequency of the reference beam ω_r.

Figure 24 depicts the signal (189) obtained with entangled photons with $T = 90$ fs for different time delays t_0. For comparison, we show the classical pump probe with bandwidth $\sigma = 1000$ cm^{-1} in the left column and with 100 cm^{-1} in the right column. The two-photon coincidence (TPC) signals are normalized with respect to the maximum value of the signal at $t_0 = 3$ fs and $\omega_r = 11\,400$ cm^{-1}. The classical signal is normalized to its peak value at zero time delay, and the TPC signals to the signal with $\omega_r = 11\,400$ cm^{-1} at zero delay. As becomes apparent from the figure, a broadband classical probe pulse (left column) cannot excite specific states, such that the two resonances merge into one band. A narrow-band probe (right column), on the other hand, cannot resolve the fast relaxation at all and shows only the unperturbed resonance at ω_{fe}. Interferometric signals, however, can target the relaxation dynamics of individual states.

3. Coincidence detection of femtosecond stimulated Raman signals

So far we have demonstrated how coincidence detection can enhance linear absorption and pump-probe signals. We now demonstrate the power of this interferometric detection for stimulated Raman signals commonly used to probe molecular vibrations. Applications include probing time-resolved photophysical and photochemical processes (Kukura, McCamant, and Mathies, 2007; Schreier *et al.*, 2007; Adamczyk *et al.*, 2009; Kuramochi, Takeuchi, and Tahara, 2012), chemically specific biomedical imaging (Cheng *et al.*, 2002), and remote sensing (Pestov *et al.*, 2008; Arora *et al.*, 2012). Considerable effort has been devoted to increasing the sensitivity and eliminating off-resonant background, thus improving the signal-to-noise ratio and enabling the detection of small samples and even single molecules. Pulse shaping (Oron *et al.*, 2002; Pestov *et al.*, 2007) and the combination of broadband and narrow-band pulses (FSRS) (Dietze and Mathies, 2016) have been employed. Here we present an interferometric FSRS (IFSRS) technique that combines quantum entangled light with interferometric detection (Scarcelli *et al.*, 2003; Yabushita and Kobayashi, 2004; Kalachev *et al.*, 2007; Slattery *et al.*, 2013) in order to enhance the resolution and selectivity of Raman signals (Dorfman, Schlawin, and Mukamel, 2014). The measurement uses a pair of entangled photons, one (signal) photon interacts with the molecule and acts as the broadband probe, while the other (idler) provides a reference for the coincidence measurement. By counting photons, IFSRS can separately measure the gain and loss contributions to the Raman signal (Harbola, Umapathy, and Mukamel, 2013) which is not possible with classical FSRS signals that report only their sum (i.e., the net gain or loss). We had previously shown how the entangled twin photon state may be used to manipulate two-photon absorption $(\omega_1 + \omega_2)$-type resonances in aggregates (Saleh *et al.*, 1998; Lee and Goodson, 2006; Schlawin *et al.*, 2013; Dorfman and Mukamel, 2014b) but these ideas do not apply to Raman $\omega_1 - \omega_2$ resonances.

In FSRS, an actinic resonant pulse $\mathcal{E}_a$ first creates a vibrational superposition state in an electronically excited state [see

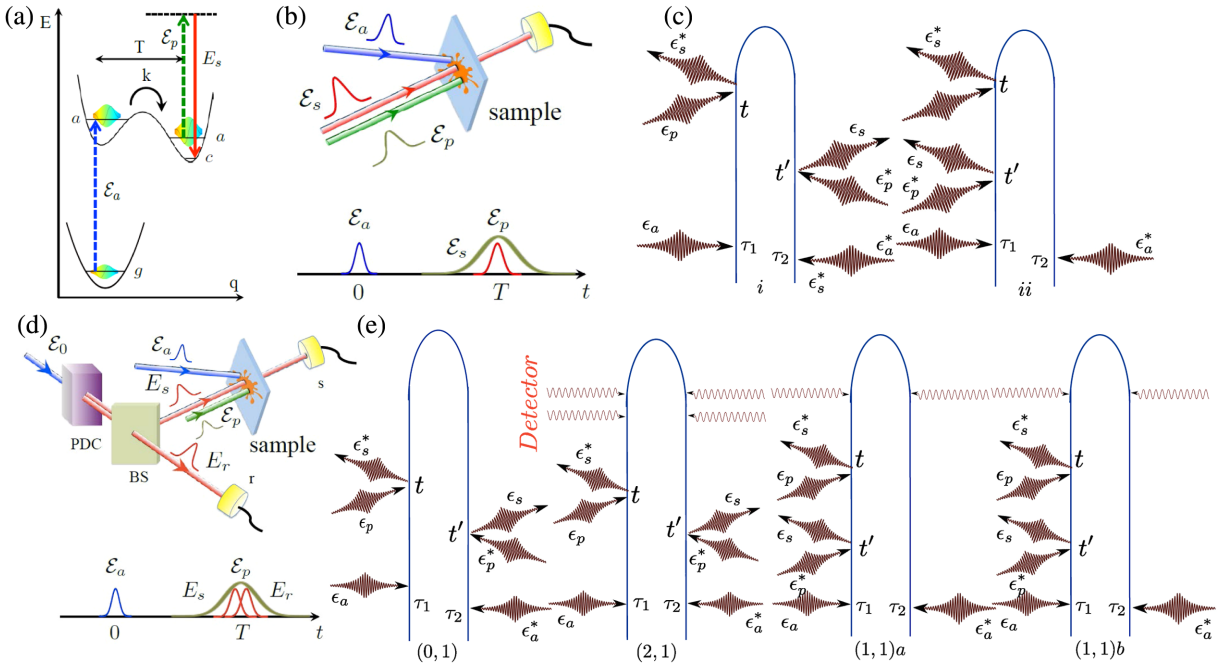

FIG. 25. Top row: (a) FSRS level scheme for the tunneling model, (b) pulse configuration, and (c) loop diagrams (for diagram rules see Appendix A). (d), (e) The same as (b) and (c) but for IFSRS. The pairs of indices (0,1), etc., indicate the number of photons registered by detectors s and r in each photon counting signal (N_s, N_r)

Figs. 25(a) and 25(b)]. After a variable delay τ, the frequency-resolved transmission of a broadband (femtosecond) probe E_s in the presence of a narrow-band (picosecond) pump $\mathcal{E}_p$ shows excited-state vibrational resonances generated by an off-resonant stimulated Raman process. The FSRS signal is given by (Dorfman, Fingerhut, and Mukamel, 2013a)

$$S_{\mathrm{FSRS}}(\omega,\tau) = \frac{2}{\hbar}\mathcal{I}\int_{-\infty}^{\infty} dt e^{i\omega(t-\tau)}\langle \mathcal{T}\mathcal{E}_s^*(\omega)\mathcal{E}_p(t)\alpha(t)e^{-i/\hbar\int H'_-(\tau)d\tau}\rangle, \tag{193}$$

where α is the electronic polarizability, $\mathcal{I}$ denotes the imaginary part, and $\mathcal{E}_s = \langle E_s\rangle$ is the expectation value of the probe field operator with respect to the classical state of light (hereafter $\mathcal{E}$ denotes classical fields and E stands for quantum fields). H'_- is the Hamiltonian superoperator in the interaction picture which, for off-resonance Raman processes, can be written as

$$H'(t) = \alpha E_s^\dagger(t)\mathcal{E}_p(t) + \mathcal{E}_a^*(t)V + \mathrm{H.c.}, \tag{194}$$

where V is the dipole moment and α is the off-resonant polarizability. Formally, this is a six-wave-mixing process. Expanding the signal (193) to sixth order in the fields $\sim\mathcal{E}_s^2\mathcal{E}_p^2\mathcal{E}_a^2$ we obtain the classical FSRS signal

$$\begin{aligned} S_{\mathrm{FSRS}}^{(i)}(\omega,\tau) = \frac{2}{\hbar}\mathcal{I}\int_{-\infty}^{\infty} dt\int_{-\infty}^{t} d\tau_1\int_{-\infty}^{t} dt'\int_{-\infty}^{t'} d\tau_2 \\ \times e^{i\omega(t-\tau)}\mathcal{E}_p(t)\mathcal{E}_p^*(t')\mathcal{E}_a^*(\tau_2)\mathcal{E}_a(\tau_1)\mathcal{E}_s^*(\omega)\mathcal{E}_s(t') \\ \times F_i(t'-\tau_2, t-t', t-\tau_1), \end{aligned} \tag{195}$$

$$\begin{aligned} S_{\mathrm{FSRS}}^{(ii)}(\omega,\tau) = \frac{2}{\hbar}\mathcal{I}\int_{-\infty}^{\infty} dt\int_{-\infty}^{t} d\tau_2\int_{-\infty}^{t} dt'\int_{-\infty}^{t'} d\tau_1 \\ \times e^{i\omega(t-\tau)}\mathcal{E}_p(t)\mathcal{E}_p^*(t')\mathcal{E}_a(\tau_1)\mathcal{E}_a^*(\tau_2)\mathcal{E}_s^*(\omega)\mathcal{E}_s(t') \\ \times F_{ii}(t-\tau_2, t-t', t'-\tau_1). \end{aligned} \tag{196}$$

The two terms correspond to the two diagrams in Fig. 25(c). All relevant information is contained in the two four-point correlation functions

$$F_i(t_1,t_2,t_3) = \langle VG^\dagger(t_1)\alpha G^\dagger(t_2)\alpha G(t_3)V^\dagger\rangle, \tag{197}$$

$$F_{ii}(t_1,t_2,t_3) = \langle VG^\dagger(t_1)\alpha G(t_2)\alpha G(t_3)V^\dagger\rangle, \tag{198}$$

where the retarded Green's function $G(t) = (-i/\hbar)\theta(t)e^{-iHt}$ represents forward time evolution with the free-molecule Hamiltonian H [diagrams $(1,1)a$, $(1,1)b$] and $G^\dagger$ represents backward evolution. F_i involves one forward and two backward evolution periods and F_{ii} contains two forward followed by one backward propagation. F_i and F_{ii} differ by the final state of matter (at the top of each diagram). In F_i (F_{ii}) it is different (the same) as the state immediately after the actinic pulse.

a. Photon correlation measurements

In IFSRS, the probe pulse E_s belongs to a pair of entangled beams generated in degenerate type-II PDC. The polarizing beam splitter (BS) in Fig. 25(d) then separates the orthogonally polarized photons. The horizontally polarized beam E_s propagates in the s arm of the interferometer and interacts with the molecule. The vertically polarized beam E_r propagates freely in the r arm and serves as a reference. IFSRS has the following control knobs: the time-and-frequency parameters of the single-photon detectors, the frequency of the narrow-band classical pump pulse ω_p, and the time delay T between the actinic pulse $\mathcal{E}_a$ and the probe E_s.

As discussed in Sec. III.D.1, the joint time-and-frequency-gated detection rate of N_s photons ($N_s = 0, 1, 2$) in detector s and a single photon in r when both detectors have narrow spectral gating are given by

$$S_{\mathrm{IFSRS}}^{(N_s,1)}(\bar\omega_{s_1},\ldots,\bar\omega_{s_{N_s}},\bar\omega_r,\Gamma_i) = \left\langle \mathcal{T}E_r^\dagger(\bar\omega_r)E_r(\bar\omega_r)\prod_{j=1}^{N_s}E_s^\dagger(\bar\omega_{s_j})E_s(\bar\omega_{s_j})e^{-\frac{i}{\hbar}\int_{-\infty}^{\infty}H'_-(\tau)d\tau}\right\rangle, \tag{199}$$

where Γ_i stands for the incoming light beam parameters. In the standard Glauber approach (Glauber, 2007), the correlation function is calculated in the field space using normally ordered field operators. The present expressions, in contrast, are given in the joint field and matter degrees of freedom, and the bookkeeping of the fields is instead solely based on the time ordering of superoperators. Normal ordering is never used.

Expansion of Eq. (199) in the number of the field-matter interactions depicted by loop diagrams in Fig. 25(e) yields for $N_s = 0$—Raman loss (no photon in the molecular arm)

$$S_{\mathrm{IFSRS}}^{(0,1)}(\bar\omega_r;\tau) = \mathcal{I}\frac{1}{\hbar}\int_{-\infty}^{\infty}dt\int_{-\infty}^{\infty}dt'\int_{-\infty}^{t}d\tau_1\int_{-\infty}^{t'}d\tau_2\mathcal{E}_p(t')\mathcal{E}_p^*(t)\mathcal{E}_a(\tau_1)\mathcal{E}_a^*(\tau_2)\langle\mathcal{T}E_s^\dagger(t')\tilde E_r^\dagger(\bar\omega_r)\tilde E_r(\bar\omega_r)E_s(t)\rangle F_i(t'-\tau_2,t-t',t-\tau_1). \tag{200}$$

To make sure that there is no photon at detector s we integrated over its entire bandwidth, thus eliminating the dependence on detector parameters.

For the Raman gain $N_s = 2$ signal (i.e., two photons in the s arm, and one photon in the r arm), when both s and r detectors have narrow frequency gates, we get

$$\begin{aligned} S_{\mathrm{IFSRS}}^{(2,1)}(\bar\omega_{s_1},\bar\omega_{s_2},\bar\omega_r;\tau) = \mathcal{I}\frac{1}{\hbar}\int_{-\infty}^{\infty}d\bar t_{s_1}e^{i\bar\omega_{s_1}(\bar t_{s_1}-\tau)}\int_{-\infty}^{\bar t_{s_1}}dt\int_{-\infty}^{t}dt'\int_{-\infty}^{t'}d\tau_1\int_{-\infty}^{t'}d\tau_2\mathcal{E}_p(t)\mathcal{E}_p^*(t')\mathcal{E}_a(\tau_1)\mathcal{E}_a^*(\tau_2) \\ \times\langle\mathcal{T}E_s(t')\tilde E_s^\dagger(\bar\omega_{s_1})\tilde E_s^\dagger(\bar\omega_{s_2})\tilde E_r^\dagger(\bar\omega_r)\tilde E_r(\bar\omega_r)\tilde E_s(\bar\omega_{s_2})\tilde E_s(\bar t_{s_1})E_s^\dagger(t)\rangle F_i(t'-\tau_2,t-t',t-\tau_1). \end{aligned} \tag{201}$$

Finally, the $N_s = 1$ signal (single photon in each arm) is given by

$$S^{(1,1)a}_{\mathrm{IFSRS}}(\bar{\omega}_s,\bar{\omega}_r;\tau)=-\mathcal{I}\frac{1}{\hbar}\int_{-\infty}^{\infty}dt_s' e^{i\bar{\omega}_s(t_s'-\tau)}\int_{-\infty}^{t_s'}dt\int_{-\infty}^{t}dt'\int_{-\infty}^{t'}d\tau_1\int_{-\infty}^{t_s'}d\tau_2\mathcal{E}_p(t)\mathcal{E}_p^*(t')\mathcal{E}_a(\tau_1)\mathcal{E}_a^*(\tau_2)$$
$$\times\langle\mathcal{T}\tilde{E}_s^\dagger(\bar{\omega}_s)\tilde{E}_r^\dagger(\bar{\omega}_r)\tilde{E}_r(\bar{\omega}_r)\tilde{E}_s(t_s')E_s^\dagger(t)E_s(t')\rangle F_{ii}(t-\tau_2,t-t',t'-\tau_1), \tag{202}$$

$$S^{(1,1)b}_{\mathrm{IFSRS}}(\bar{\omega}_s,\bar{\omega}_r;\tau)=-\mathcal{I}\frac{1}{\hbar}\int_{-\infty}^{\infty}dt_s' e^{i\bar{\omega}_s(t_s'-\tau)}\int_{-\infty}^{t_s'}dt\int_{-\infty}^{t}dt'\int_{-\infty}^{t'}d\tau_1\int_{-\infty}^{t_s'}d\tau_2\mathcal{E}_p(t')\mathcal{E}_p^*(t)\mathcal{E}_a(\tau_1)\mathcal{E}_a^*(\tau_2)$$
$$\times\langle\mathcal{T}\tilde{E}_s^\dagger(\bar{\omega}_s)\tilde{E}_r^\dagger(\bar{\omega}_r)\tilde{E}_r(\bar{\omega}_r)\tilde{E}_s(t_s')E_s(t)E_s^\dagger(t')\rangle F_{ii}(t-\tau_2,t-t',t'-\tau_1). \tag{203}$$

b. Photon counting detection window for the molecular response

The input two-photon state has a single photon in each of the s mode and single photon in the r mode and is described by [compare to Eq. (33)]

$$|\psi\rangle=|0\rangle+\int_{-\infty}^{\infty}d\omega_s\int_{-\infty}^{\infty}d\omega_r\Phi(\omega_s,\omega_r)a^\dagger_{\omega_s}a^\dagger_{\omega_r}|0\rangle, \tag{204}$$

where $a^\dagger_{\omega_s}$ ($a^\dagger_{\omega_r}$) is the creation operator of a horizontally (vertically) polarized photon and the two-photon amplitude is given by

$$\Phi(\omega_s,\omega_r)=\sum_{i\neq j=1}^{2}\mathrm{sinc}(\omega_{s0}T_i/2+\omega_{r0}T_j/2)$$
$$\times A_p(\omega_s+\omega_r)e^{i\omega_{s0}T_i/2+i\omega_{r0}T_j/2}, \tag{205}$$

where $\omega_{k0}=\omega_k-\omega_0$, $k=s,r$, $A_p(\omega)=A_0/[\omega-\omega_0+i\sigma_0]$ is the classical pump $T_j=(1/v_p-1/v_j)L$, with $j=1,2$, is the time delay between the jth entangled and the classical pump beam after propagation through the PDC crystal. $T=T_2-T_1$ is the entanglement time. In $A_p(\omega)$, the sum frequency $\omega_s+\omega_r$ is

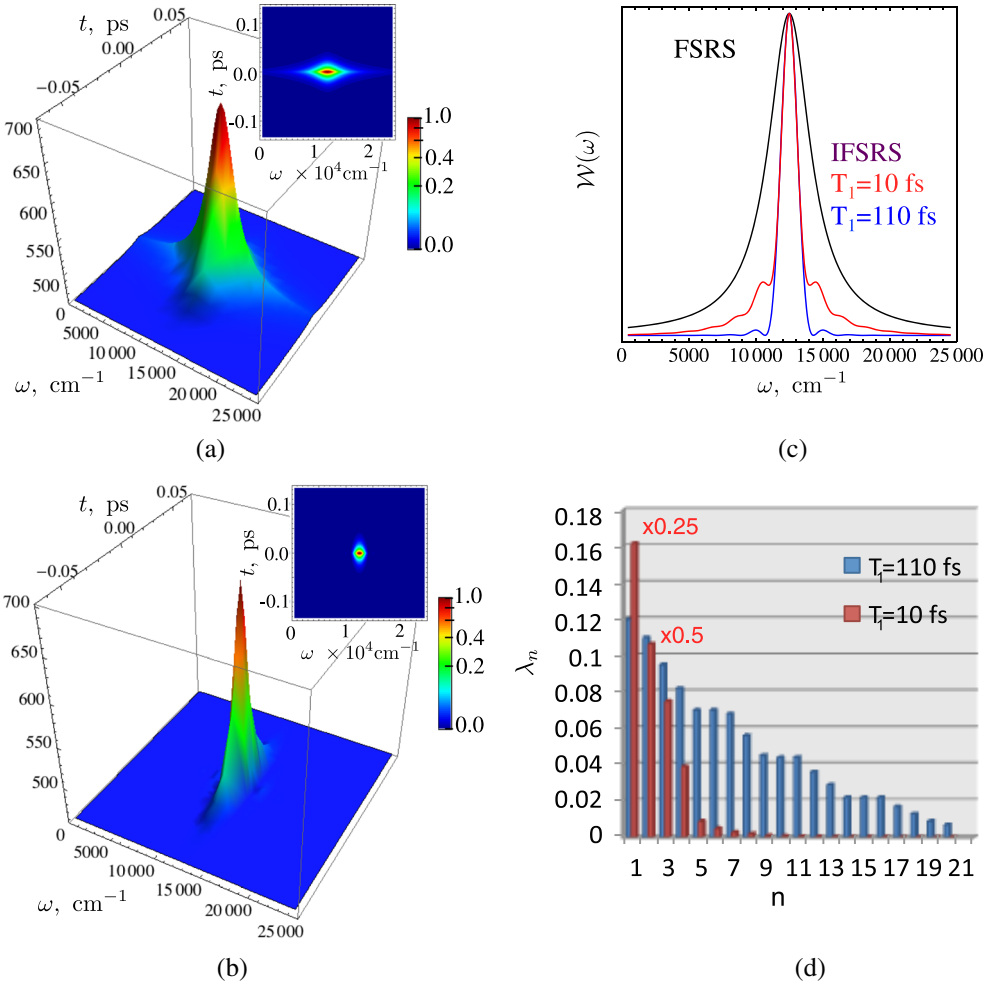

FIG. 26. (a) Time-frequency Wigner spectrogram for classical light, (b) the same as (a) but for an entangled twin state given by Eq. (205). The insets depict a 2D projection. (c) A window function for FSRS $\mathcal{E}_s^*(\omega)\mathcal{E}_s(\omega+i\gamma_a)$ (black), and IFSRS $\Phi^*(\omega,\bar{\omega}_r)\times\Phi(\omega+i\gamma_a,\bar{\omega}_r)$ different values of T_1. (d) Spectrum of the eigenvalues λ_n in the Schmidt decomposition (34) for entangled state with amplitude (205). Parameters for the simulations are listed in Dorfman, Schlawin, and Mukamel (2014).

centered around $2\omega_0$ with bandwidth σ_0. For a broadband classical pump, the frequency difference $\omega_s-\omega_0$ becomes narrow with bandwidth T_j^{-1}, $j=1, 2$. The output state of light in mode s may contain a varying number of photons, depending on the order of the field-matter interaction.

As discussed in Sec. II.C, the twin photon state Eq. (204) is not necessarily entangled. This depends on the two-photon amplitude. Using the Schmidt decomposition (34), we obtain the two-photon amplitude Eq. (205). The rich spectrum of eigenvalues shown in Fig. 26(d) shows that the state is highly entangled with up to 20 modes making significant contributions. As shown in Eq. (208), this entanglement is reflected in the violation of the Fourier uncertainty $\Delta\omega\Delta t \geq 1$ in two-photon transitions.

We next discuss how entanglement affects the Raman resonances. Both FSRS and IFSRS signals are governed by a four-point matter correlation function (two polarizabilities α_{ac} and two dipole moments V_{ag}) as depicted by the loop diagrams shown in Figs. 25(c) and 25(e), respectively. Depending on the number of photons detected, this four-point matter correlation function is convoluted with different field correlation functions. For $N_s = 0$ and $N_r = 1$ Eq. (200) is given by the four-point correlation function for a quantum field [red arrows in Fig. 25(e)]. For a twin photon state, we recall from Eq. (50) that the field correlation function can be factorized as

$$\langle\psi|E_s^\dagger(\omega_a)E_r^\dagger(\omega_b)E_r(\omega_c)E_s(\omega_d)|\psi\rangle = \Phi^*(\omega_a,\omega_b)\Phi(\omega_c,\omega_d). \tag{206}$$

The $N_s = 2$ signal is given by an eight-point field correlation function [see Eq. (201)], and for $N_s = 1$ it is governed by a six-point field correlation function as shown in Eqs. (202) and (203). The detailed derivation and explicit closed form expressions for multipoint correlation functions of the field are presented by Dorfman, Schlawin, and Mukamel (2014). All three IFSRS signals with $N_s = 0, 1, 2$ eventually scale linearly with the classical pump intensity $S_{\mathrm{IFSRS}} \propto |A_0|^2$, similar to classical FSRS even though a different number of fields contribute to the detection.

We now compare different field spectrograms which represent the temporal and spectral windows created by the fields. Figure 26(a) depicts the Wigner time-frequency spectrogram for the classical probe field $\mathcal{E}_s$:

$$W_s(\omega,t) = \int_{-\infty}^{\infty}\frac{d\Delta}{2\pi}\mathcal{E}_s^*(\omega)\mathcal{E}_s(\omega+\Delta)e^{-i\Delta t}. \tag{207}$$

The Fourier uncertainty $\Delta\omega\Delta t \geq 1$ limits the frequency resolution for a given time resolution. The corresponding Wigner two-photon spectrogram for the entangled twin photon state

$$W_q(\omega,t;\bar{\omega}_r) = \int_{-\infty}^{\infty}\frac{d\Delta}{2\pi}\Phi^*(\omega,\bar{\omega}_r)\Phi(\omega+\Delta,\bar{\omega}_r)e^{-i\Delta t} \tag{208}$$

is depicted in Fig. 26(b). For the same temporal resolution of the FSRS, the spectral resolution of IFSRS can be significantly improved since the time-and-frequency variables for entangled light are not Fourier conjugate variables (Schlawin *et al.*, 2013). The high spectral resolution in the entangled case is governed by T_j^{-1}, $j = 1, 2$ which is narrower than the broadband probe pulse such that $\Delta\omega\Delta t \simeq 0.3$. Figure 26(c) demonstrates that entangled window function $R_q^{(N_s,1)}$ for $N_s = 1, 2$ [see Eqs. (212) and (213)] that enters the IFSRS signal (210) yields a much higher spectral resolution than the classical R_c shown in Eq. (215).

The molecular information required for all three possible measurement outcomes ($N_s = 0, 1, 2$) is given by two correlation functions F_i and F_{ii} [see Figs. 25(c) and 25(e) and Eqs. (197) and (198)], which are then convoluted with a different detection window for FSRS and IFSRS. The correlation functions F_i and F_{ii} may not be separately detected by FSRS. However, in IFSRS the loss $S_{\mathrm{IFSRS}}^{(0,1)}$ and the gain $S_{\mathrm{IFSRS}}^{(2,1)}$ Raman signals probe F_i (the final state c may be different from initial state a) whereas the coincidence counting signal $S_{\mathrm{IFSRS}}^{(1,1)}$ depends on F_{ii} (initial and final states are identical). Interferometric signals can thus separately measure the two matter correlation functions.

c. IFSRS for a vibrational mode in a tunneling system

To demonstrate the effect of entanglement in interferometric measurements, we show the calculated signals for the three-level model system depicted in Fig. 25(a). Once excited by the actinic pulse, the initial state with vibrational frequency $\omega_+ = \omega_{ac} + \delta$ can tunnel through a barrier at a rate k and assume a different vibrational frequency $\omega_- = \omega_{ac} - \delta$ (Dorfman, Fingerhut, and Mukamel, 2013b). The probability to remain in the initial state with ω_+ decreases exponentially $P_+(t) = e^{-kt}$, whereas for ω_- it grows as $P_-(t) = 1 - e^{-kt}$. This model corresponds to Kubo's two-state jump model in the low-temperature limit (Kubo, 1963; Dorfman, Fingerhut, and Mukamel, 2013b) which we discussed in Sec. III.E.2. The absorption line shape is given by

$$S_l(\omega) = -\mathcal{I}\frac{4}{\hbar^2}|\mathcal{E}(\omega)|^2\frac{|\mu_{ac}|^2}{k+2i\delta} \times\left(\frac{k+i\delta}{\omega-\omega_-+i\gamma_a}+\frac{i\delta}{\omega-\omega_++i(\gamma_a+k)}\right). \tag{209}$$

This shows two peaks with combined width governed by dephasing γ_a and tunneling rates k. The corresponding IFSRS signal $S_{\mathrm{IFSRS}}^{(N_s,1)}$ with $N_s = 0, 1, 2$ is given by

$$\begin{aligned}S_{\mathrm{IFSRS}}^{(N_s,1)}&(\bar{\omega}_s,\bar{\omega}_r;\omega_p,\tau)\\ &= \mathcal{I}\frac{\mu}{\hbar^4}|\mathcal{E}_p|^2|\mathcal{E}_a|^2\sum_{a,c}\alpha_{ac}^2|\mu_{ag}|^2\\ &\quad\times e^{-2\gamma_a\tau}\Big(R_q^{(N_s,1)}(\bar{\omega}_s,\bar{\omega}_r,2\gamma_a,\bar{\nu}\omega_\nu-i\gamma_a)-\frac{2i\delta e^{-k\tau}}{k+2i\delta}\\ &\quad\times[R_q^{(N_s,1)}(\bar{\omega}_s,\bar{\omega}_r,2\gamma_a+k,\bar{\nu}\omega_\nu-i\gamma_a)\\ &\quad-R_q^{(N_s,1)}(\bar{\omega}_s,\bar{\omega}_r,2\gamma_a+k,\bar{\nu}\omega_{\bar{\nu}}-i(\gamma_a+k))]\Big),\end{aligned} \tag{210}$$

where $\nu = -$ for $N_s = 0, 2$ and $\nu = +$ for $N_s = 1$, $\mu = -$ for $N_s = 1, 2$, and $\mu = +$ for $N_s = 0$. The Raman response $R_q^{(N_s,1)}$ which depends on the window created by the quantum field for different photon numbers N_s is given by

$$R_q^{(0,1)}(\bar{\omega}_s,\bar{\omega}_r,\gamma,\Omega)=\int_{-\infty}^{\infty}\frac{d\omega}{2\pi}\frac{\Phi^*(\omega,\bar{\omega}_r)\Phi(\omega+i\gamma,\bar{\omega}_r)}{\omega-\omega_p-\Omega}, \tag{211}$$

$$R_q^{(1,1)}(\bar{\omega}_s,\bar{\omega}_r,\gamma,\Omega)=\frac{\Phi^*(\bar{\omega}_s,\bar{\omega}_r)\Phi(\omega_p+\Omega-i\gamma,\bar{\omega}_r)}{\bar{\omega}_s-\omega_p-\Omega}, \tag{212}$$

$$R_q^{(2,1)}(\bar{\omega}_s,\bar{\omega}_r,\gamma,\Omega)=\frac{\Phi^*(\bar{\omega}_s,\bar{\omega}_r)\Phi(\bar{\omega}_s+i\gamma,\bar{\omega}_r)}{\bar{\omega}_s-\omega_p-\Omega}. \tag{213}$$

For comparison, we give the classical FSRS signal (193)

$$\begin{aligned}S_{\mathrm{FSRS}}^{(c)}(\omega,\tau)=&-\mathcal{I}\frac{2}{\hbar^4}|\mathcal{E}_p|^2|\mathcal{E}_a|^2\sum_{a,c}\alpha_{ac}^2|\mu_{ag}|^2e^{-2\gamma_a\tau}\\&\times\Big[R_c(\omega,2\gamma_a,\omega_--i\gamma_a)\\&-\frac{2i\delta e^{-k\tau}}{k+2i\delta}[R_c(\omega,2\gamma_a+k,\omega_--i\gamma_a)\\&-R_c(\omega,2\gamma_a+k,\omega_+-i(\gamma_a+k))]\\&-(\omega_\pm\leftrightarrow-\omega_\mp)\Big],\end{aligned} \tag{214}$$

where

$$R_c(\omega,\gamma,\Omega)=\frac{\mathcal{E}_s^*(\omega)\mathcal{E}_s(\omega+i\gamma)}{\omega-\omega_p-\Omega} \tag{215}$$

is the Raman response gated by the classical field.

Figures 27(a)–27(h) compare the classical FSRS signal [Eq. (214)] with the IFSRS signals $S_{\mathrm{IFSRS}}^{(1,1)}$ and $S_{\mathrm{IFSRS}}^{(2,1)}$ [Eq. (210)]. For slow modulation and long dephasing time $k,\gamma_a\ll\delta$ the absorption spectrum [Fig. 27(a)] has two well-resolved peaks at $\omega_\pm$. The classical FSRS shown in Fig. 27(b) has one dominant resonance at ω_+ which decays with the increase of delay T, whereas the ω_- peak slowly builds up and dominates at longer T. This signal contains both blue-shifted and redshifted Raman resonances relative to the narrow-band pump frequency $\omega-\omega_p=\pm\omega_\pm$. If the modulation and dephasing rates are comparable to the level splitting $k,\gamma_a\sim\delta$, then the $\omega_\pm$ resonances in the absorption [Fig. 27(e)] and the classical FSRS [Fig. 27(f)] broaden and become less resolved.

We next compare this with the IFSRS signal. For small modulation and long dephasing, $S_{\mathrm{IFSRS}}^{(1,1)}$ is similar to the classical FSRS [see Fig. 27(c)]. However, both temporal and spectral resolutions remain high, even when the modulation is fast and the dephasing width is large as seen in Fig. 27(g). The same applies to the $S_{\mathrm{IFSRS}}^{(2,1)}$ signal depicted for slow[Fig. 27(d)] and fast [Fig. 27(h)] tunneling.

Apart from the different detection windows, there is another important distinction between IFSRS [Eq. (210)] and the classical FSRS (214) signals. In the latter, both the gain and loss contributions contain redshifted and blue-shifted features relative to the narrow pump. The FSRS signal can contain both Stokes and anti-Stokes components. FSRS can distinguish only between red and blue

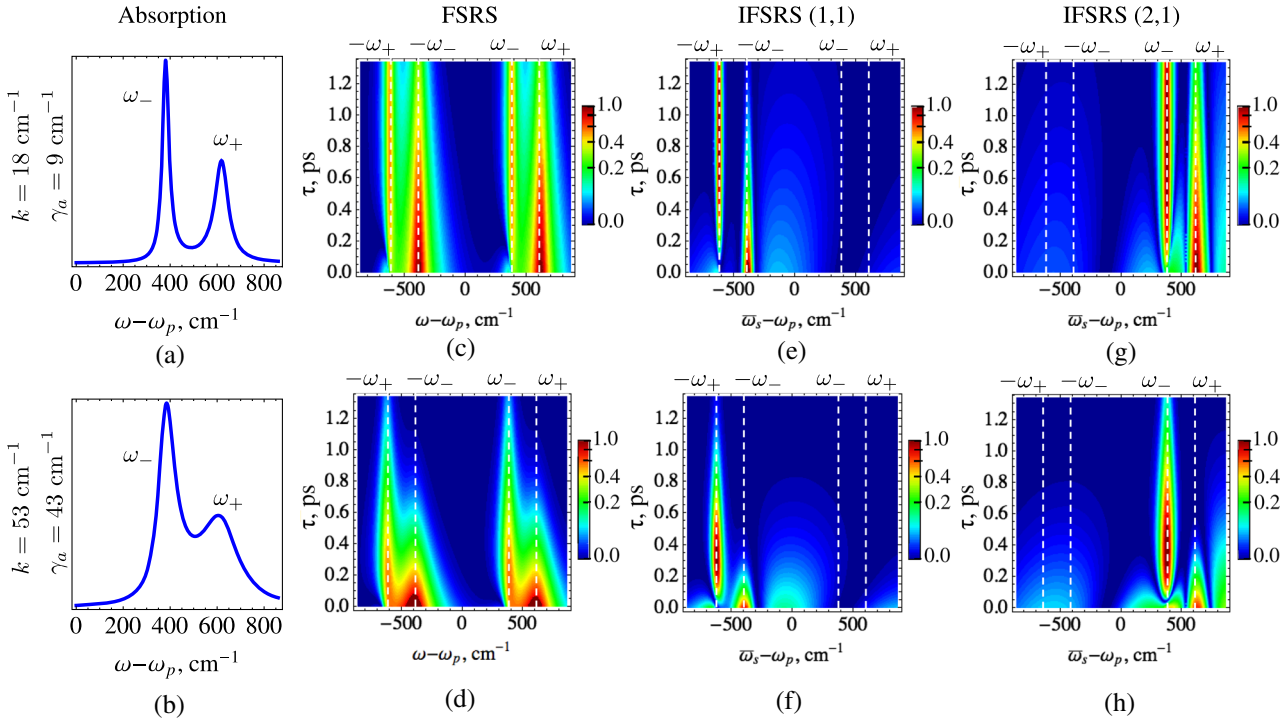

FIG. 27. (a) Absorption for a time evolving vibrational mode i vs $\omega-\omega_p$ for slow tunneling rate $k=18\ \mathrm{cm}^{-1}$ and narrow dephasing $\gamma_a=9\ \mathrm{cm}^{-1}$, (b) same as (a) but for fast tunneling rate $k=53\ \mathrm{cm}^{-1}$ and broad dephasing $\gamma_a=43\ \mathrm{cm}^{-1}$. (c), (d) The same as (a), (b) but for the classical FSRS signal. (e), (f) The same as (a), (b) but for $S_{\mathrm{IFSRS}}^{(1,1)}$. (g), (h) The same as (a), (b) but for $S_{\mathrm{IFSRS}}^{(2,1)}$ vs $\bar{\omega}_s-\omega_p$. Parameters for the simulations are listed in Dorfman, Schlawin, and Mukamel (2014).

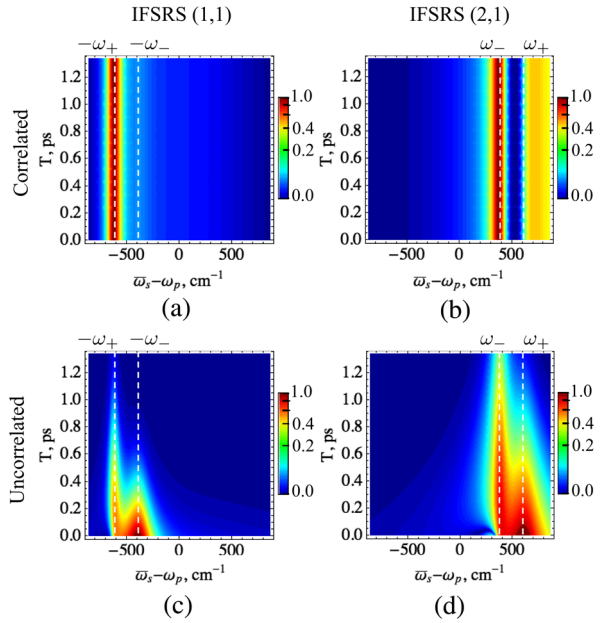

FIG. 28. Left column: $S^{(1,1)}_{\mathrm{IFSRS}}$ signal vs $\bar{\omega}_s-\omega_p$ for (a) entangled state (205), (b) correlated, and (c) uncorrelated separable states. (d)–(f) The same as (a)–(c) but for the $S^{(2,1)}_{\mathrm{IFSRS}}$ signal. Parameters for the simulations are listed in Dorfman, Schlawin, and Mukamel (2014).

contributions. In contrast, the interferometric signal can separately measure the gain $S^{(2,1)}_{\mathrm{IFSRS}}$ and the loss contributions $S^{(0,1)}_{\mathrm{IFSRS}}$.

d. The role of entanglement

We now show that the achieved enhanced resolution of Raman resonances may not be achieved by classically shaped light and that entanglement is essential. To this end, we calculate the IFSRS signals (210) for the correlated-separable state of the field (Zheng *et al.*, 2013) described by the density matrix

$$\rho_{\mathrm{cor}}=\int_{-\infty}^{\infty}d\omega_s d\omega_r|\Phi(\omega_s,\omega_r)|^2|1_{\omega_s},1_{\omega_r}\rangle\langle 1_{\omega_s},1_{\omega_r}|. \tag{216}$$

This is a diagonal part of the density matrix corresponding to state Eq. (204) with amplitude Eq. (205), which can be generated by the disentanglement of the twin state. This state yields the same single-photon spectrum and shows strong frequency correlations similar to the entangled case and is typically used as a benchmark to quantify entanglement in quantum information processing (Law, Walmsley, and Eberly, 2000). We further compare this with signals from the fully separable uncorrelated Fock state given by Eq. (204) with

$$\Phi_{\mathrm{uncor}}(\omega_s,\omega_r)=\Phi_s(\omega_s)\Phi_r(\omega_r), \tag{217}$$

where $\Phi_k(\omega_k)=\Phi_0/[\omega_k-\omega_0+i\sigma_0]$, $k=s,\ r$ with parameters matching the classical probe pulse used in FSRS.

Figures 28(a)–28(d) illustrate $S^{(1,1)}_{\mathrm{IFSRS}}$ for these two states of light. The separable correlated state shown in Fig. 26(a) has high spectral and no temporal resolution, as expected from a cw time-averaged state in which the photons arrive at any time (Zheng *et al.*, 2013). The separable uncorrelated state [see Fig. 26(c)] yields slightly better resolution than in the classical FSRS signal in Fig. 27(f). Similar results can be obtained for the $S^{(2,1)}_{\mathrm{IFSRS}}$ [see Figs. 28(b) and 28(d), respectively).

IV. ENTANGLED LIGHT GENERATION VIA NONLINEAR LIGHT-MATTER INTERACTIONS AND NONCLASSICAL RESPONSE FUNCTIONS

The generation process of quantum light is usually described by an effective Hamiltonian in the field space. The material quantities that assist the light conversion are typically set to be constant parameters governed by nonlinear semiclassical susceptibilities.

Superoperator nonequilibrium Green's functions are useful for calculating nonlinear optical processes involving any combination of classical and quantum-optical modes. Closed correlation-function expressions based on superoperator time ordering may be derived for the combined effects of causal (response) and noncausal (spontaneous

TABLE I. SNGFs of three wave-mixing techniques: heterodyne-detected SFG and DFG with all classical (c) modes; incoherent TPIF with two classical and one quantum (q) mode and corresponding coherent homodyne-detected SFG; incoherent TPEF with one classical and two quantum modes and type-I PDC; type-II PDC SNGF with one classical and four quantum modes.

	Three wave processes					
	Heterodyne		Homodyne			
			Incoherent		Coherent	
Technique	SFG	DFG	TPIF	TPEF	SFG	PDC
Modes	c/c/c	c/c/c	c/c/q	c/q/q	c/c/q	c/q/q
ω_3	$\omega_1+\omega_2$	$\omega_1-\omega_2$	⋯	⋯	$\approx\omega_1+\omega_2$	$\approx\omega_1-\omega_2$
SNGFs	$\chi^{(2)}_{+--}$	$\chi^{(2)}_{+--}$	$(\chi^{(5)}_{++----}$ $\chi^{(5)}_{++----})/2$	$(\chi^{(5)}_{++----}+2\chi^{(5)}_{+++---}$ $+\chi^{(5)}_{+++--})/4$	$\lvert\chi^{(2)}_{+--}\rvert^2$	$\lvert\chi^{(2)}_{+--}+\chi^{(2)}_{+++-}\rvert^2$
Expression	Eq. (235)	Eq. (233)	Eq. (240)	Eq. (251)	Eq. (235)	Type-I Eq. (253), Type-II Eqs. (256), (258)

fluctuations) correlation functions (Roslyak and Mukamel, 2009b).

Next we survey several wave-mixing schemes for generating quantum light by using a combination of classical and quantum modes of the radiation field. Homodyne-detected sum-frequency generation (SFG) (Shen, 1989) and difference-frequency generation (DFG) (Dick and Hochstrasser, 1983; Mukamel, 1995) involve two classical and one quantum mode. PDC (Louisell, Yariv, and Siegman, 1961; Hong and Mandel, 1985; Klyshko, 1988; Mandel and Wolf, 1995) involves one classical and two quantum modes and is one of the primary sources of entangled-photon pairs (Gerry and Knight, 2005; U'Ren *et al.*, 2006; Edamatsu, 2007). All of these are coherent measurements and scale as $N(N-1)$ for N active molecules of the signals (Marx, Harbola, and Mukamel, 2008).

We further consider incoherent $\sim N$-scaling signals. These include heterodyne-detected SFG and DFG, which involve three classical modes and two types of two-photon fluorescence (Denk, Strickler, and Webb, 1990): two-photon-induced fluorescence with one classical and two quantum modes (Callis, 1993; Rehms and Callis, 1993; Xu and Webb, 1996) and two-photon-emitted fluorescence (TPEF) with two classical and one quantum mode. The list of the different measurement is summarized in Table I.

Finally we present a more detailed microscopic theory of entangled light generation in two schemes, which describe light-matter interactions that involve a quantum field. The first is based on type-I PDC in a cascade three-level scheme, and in the second scheme an entangled-photon pair is generated by two remote molecules assisted by an ideal 50:50 beam splitter.

A. Superoperator description of *n*-wave mixing

So far we mostly used the L and R superoperator representation for describing signals. Here we consider various nonlinear signals which involve two-photon resonances (Roslyak and Mukamel, 2009b) (see Fig. 29) and describe them using $\pm$ representation. For coherent optical states, all field SNGFs in the L, R representation are identical $E'_L = E'_R$ (the superoperator index makes no difference since all operations commute). In the $\pm$ representation the "minus" field indices are not allowed, since $E'_- = 0$. The general m wave-mixing signals are given by 2^m products of material and corresponding optical field SNGFs of mth order:

$$S_\alpha^{(m)} = \Im \frac{i^m \delta_{m+1,\alpha}}{\pi m! \hbar^{m+1}} \sum_{\nu_m} \cdots \sum_{\nu_1} \int_{-\infty}^{\infty} dt_{m+1} dt_m \cdots dt_1 \Theta(t_{m+1}) \mathbb{V}^{(m)}_{\nu_{m+1}\nu_m\cdots\nu_1}(t_{m+1}, t_m, \ldots, t_1) \times \mathbb{E}^{(m)}_{\nu_{m+1}\bar{\nu}_m\cdots\bar{\nu}_1}(t_{m+1}, t_m, \ldots, t_1), \tag{218}$$

where $t_{m+1}, t_m, \ldots, t_1$ are the light-matter interaction times. The factor $\Theta(t_{m+1}) = \prod_{i=1}^m \theta(t_{m+1} - t_i)$ ensures that the t_{m+1} is the last light-matter interaction. The indices $\bar{\nu}_j$ are the conjugates to ν_j and defined as follows: the conjugate of $+$ is $-$ and vice versa. Equation (218) implies that the excitations in the material are caused by fluctuations in the optical field and vice versa. Equation (218) also holds in the L, R representation. Here we have $\nu_{m+1} = L$ and $\nu_j \in \{L, R\}$, $j = m, \ldots, 1$, $\bar{\nu}_j$. In the L, R representation the conjugate of "left" is "left" and the conjugate of "right" is "right": $\bar{L} = L$, $\bar{R} = R$. The material SNGF $\mathbb{V}^{(m)}_{L\underbrace{L\cdots L}_{n}\underbrace{R\cdots R}_{m-n}}$ represents a *Liouville space pathway* with $n+1$ interactions from the left (i.e., with the ket) and $m-n$ interactions from the right (i.e., with the bra).

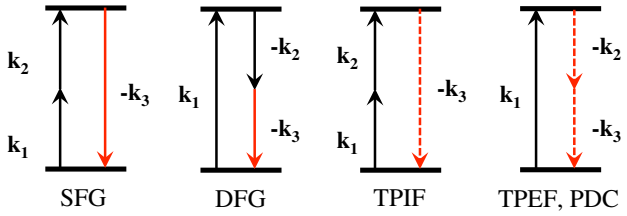

FIG. 29. Three-wave process involuting classical (solid line) and quantum (dashed line) modes. Black lines represent incoming fields, and red lines correspond to generated light.

The field SNGF in Eq. (218) is defined in Eq. (14), and the material SNGF is defined by Eq. (15). The latter in the form of $\mathbb{V}^{(m)}_{+\underbrace{-\cdots-}_{m}}$ gives a causal ordinary response function of mth order. The material SNGF of the form $\mathbb{V}^{(m)}_{+\underbrace{+\cdots+}_{m}}$ represents the mth moment of molecular fluctuations. The material SNGF of the form $\mathbb{V}^{(m)}_{+\underbrace{+\cdots+}_{n}\underbrace{-\cdots-}_{m-n}}$ indicates changes in the nth moment of molecular fluctuations up by $m-n$ perturbations. We next recast the material SNGF (15) in the frequency domain by performing a multiple Fourier transform:

$$\chi^{(m)}_{\nu_{m+1}\nu_m\cdots\nu_1}(-\omega_{m+1}; \omega_m, \ldots, \omega_1) = \int_{-\infty}^{\infty} dt_{m+1}\cdots dt_1 \Theta(t_{m+1}) e^{i(\omega_m t_m + \cdots + \omega_1 t_1)} \times \delta(-\omega_{m+1} + \omega_m + \cdots + \omega_1) \mathbb{V}^{(m)}_{\nu_{m+1}\nu_m\cdots\nu_1}(t_{m+1}, t_m, \ldots, t_1). \tag{219}$$

The SNGF $\chi^{(m)}_{+\underbrace{-\cdots-}_{m}}(-\omega_{m+1}; \omega_m, \ldots, \omega_1)$ (with one $+$ and the rest $-$ indices) is the mth order nonlinear susceptibility or causal response function. The rest of the SNGFs in the frequency domain can be interpreted similarly to their time-domain counterparts (15).

B. Connection to nonlinear fluctuation-dissipation relations

Spontaneous fluctuations and response functions are uniquely related in the linear regime (Hashitsume *et al.*, 1991) by the fluctuation-dissipation theorem, but not when they are nonlinear. Some nonlinear fluctuation-dissipation relations have been proposed for specific models under limited conditions (Bochkov and Kuzovlev, 1981; Bertini

et al., 2001; Lippiello *et al.*, 2008) but there is no universal relation of this type (Kryvohuz and Mukamel, 2012).

Quantum spectroscopy signals may be described by the Glauber-Sudarshan P representation which expresses the field density matrix as an integral over coherent state density matrices $|\beta\rangle\langle\beta|$ weighted by a quasiprobability distribution $P(\beta)$:

$$\hat{\rho} = \int d^2\beta P(\beta)|\beta\rangle\langle\beta|. \tag{220}$$

It was suggested (Kira *et al.*, 2011; Almand-Hunter *et al.*, 2014; Mootz *et al.*, 2014) that, since the response of a material system to a field initially prepared in a coherent state $|\beta\rangle$ is given by the classical response function CRF, the quantum response R_{QM} may be recast as an average of the classical response $R_{|\beta\rangle}$ with respect to this quasiprobability

$$R_{QM} = \int d^2\beta P(\beta) R_{|\beta\rangle}. \tag{221}$$

By transforming to the response of a nonclassical state given by $P(\beta)$, in which the fluctuations along one quadrature are squeezed below the classical limit, this form of data processing can uncover otherwise hidden features in the signal. For instance, Almand-Hunter *et al.* (2014) revealed the "dropleton," a new kind of quasiparticle excitation in semiconductors.

While this analysis has proven successful, it misses the multimode nature of the entangled states, which lies at the heart of time-energy entanglement presented here. Based on our analysis of the entangled light state (33), it can be shown that optical signals induced by such entangled states cannot be reduced to a simple sum over the signal of each quantum mode: The quantum correlations depicted in Fig. 3 require a multimode model. For instance, the transition amplitude (99) may be written as a sum over the Schmidt modes,

$$T_{fg}(t) \sim \sum_k \int d\omega_a \int d\omega_b R_t(\omega_a, \omega_b)\psi_k(\omega_a)\phi_k(\omega_b), \tag{222}$$

where R_t denotes the material response. Hence, the TPIF signal $\sim|T_{fg}|^2$ cannot be reduced to the signal of the indivdual Schmidt modes $|T_{fg}|^2 \sim \sum_{k,k'}\cdots \neq \sum_k \cdots$, and the above transformation fails to capture such a signal.

The Glauber-Sudarshan quasiprobability (Kira *et al.*, 2011; Almand-Hunter *et al.*, 2014; Mootz *et al.*, 2014) suggests that classical light can be identified with coherent states. This is not necessarily the case. For instance, the effect of the revival of Rabi oscillations demonstrated by Rempe, Walther, and Klein (1987) which is observed when a coherent state is treated quantum mechanically clearly shows that a coherent state is generally a quantum state of light. Therefore, Eq. (220) merely represents a transformation between two different basis sets for the quantum state. Of course, in the nonlinear response case, if the operators are normally ordered as in Eq. (74) the signal generated by a coherent state is equivalent to the classical case. In Rempe's example, the nonclassical contributions arise due to commutator terms in Eq. (87) and the higher the order in perturbative expansion, the larger the contribution of the commutator terms. Therefore, in the strong field limit one can observe the revival of Rabi oscillations.

We now use the superoperator formalism to show more broadly why the quantum response is different from the classical one so that Eq. (221) is violated. In Liouville space, the time-dependent density matrix is given by Eq. (69). We now make use of the superoperator algebraic relation (Marx, Harbola, and Mukamel, 2008):

$$H_{\text{int}-} = E_+V_- + E_-V_+. \tag{223}$$

Let us first assume that the electric field operators commute and set $E_- = 0$. We then calculate the expectation value of a system A operator O_A:

$$\mathrm{tr}[O_A\rho(t)] = \mathrm{tr}\left[O_A\mathcal{T}\exp\left(-\frac{i}{\hbar}\int_{t_0}^{t} E_+(t')V_-^A(t')dt'\right)\right.$$
$$\left.\times\exp\left(-\frac{i}{\hbar}\int_{t_0}^{t} E_+(t')V_-^B(t')dt'\right)\rho_{A,0}\rho_{B,0}\rho_{ph,0}\right]. \tag{224}$$

Since the trace of a commutator vanishes, and since there are only V_-^B operators for system B, all correlation functions of the form $\langle V_-^BV_-^B\cdots V_-^B\rangle = 0$. The nonlinear response function is thus additive. The time evolution of two coupled quantum systems and the field is generally given by a sum over Feynman paths in their joint phase space. Order by order in the coupling, dynamical observables can be factorized into products of correlation functions defined in the individual spaces of the subsystems. These correlation functions represent both *causal* response and *noncausal* spontaneous fluctuations (Cohen and Mukamel, 2003; Roslyak and Mukamel, 2010).

The linear response contains several possible combinations of field superoperators $\langle V_\pm V_\pm\rangle$. $\langle V_-V_-\rangle$ represents a commutator and thus vanishes since its trace is zero. Therefore $\langle V_+V_+\rangle$ (two anticommutators) and $\langle V_+V_-\rangle$ (commutator followed by anticommutator) are the only two quantities that contribute to the linear response. These two quantities are related by the universal fluctuation-dissipation relation (Hashitsume *et al.*, 1991),

$$C_{++} = \tfrac{1}{2}\coth(\beta\hbar\omega/2)C_{+-}(\omega). \tag{225}$$

Here

$$C_{+-}(\omega) = \int d\tau\langle V_+(\tau)V_-(0)\rangle e^{i\omega\tau} \tag{226}$$

is the response function, whereas

$$C_{++}(\omega) = \int d\tau\langle V_+(\tau)V_+(0)\rangle e^{i\omega\tau} \tag{227}$$

denotes spontaneous fluctuations.

The classical response function $C_{+-}(\omega)$ thus carries all relevant information about linear radiation-matter coupling, including the quantum response. In the nonlinear regime the CRF is a specific causal combination of matter correlation functions given by one $+$ and several $-$ operators, e.g., $\langle V_+V_-V_-V_-\rangle$ for the third-order response. However, the quantum response may also depend on the other

combinations. To nth order in the external field the CRF $\langle V_+(\omega_{n+1})V_-(\omega_n)\cdots V_-(\omega_2)V_-(\omega_1)\rangle$ is one member of a larger family of 2^n quantities $\langle V_+(\omega_{n+1})V_\pm(\omega_n)\cdots V_\pm(\omega_2)V_\pm(\omega_1)\rangle$ representing various combinations of spontaneous fluctuations (represented by V_+) and impulsive excitations (represented by V_-). For example, an "all +" quantity such as $\langle V_+V_+V_+V_+\rangle$ represents purely spontaneous fluctuations. The CRF does not carry enough information to reproduce all 2^n possible quantities which are accessible by quantum spectroscopy. The reason why the CRF and the quantum response function (QRF) are not simply related in is the lack of a fluctuation-dissipation relation in the nonlinear regime (Bochkov and Kuzovlev, 1981; Bertini *et al.*, 2001; Lippiello *et al.*, 2008; Kryvohuz and Mukamel, 2012).

The field commutator E_- corresponds to vacuum modes of the field which may induce coupling between noninteracting parts of the system. One example where such an effect arising from E_- is combined with the appearance of collective resonances, which occur for E_+, was recently investigated for harmonic systems (Glenn *et al.*, 2015). The response of classical or quantum harmonic oscillators coupled linearly to a classical field is strictly linear; all nonlinear response functions vanish identically. However quantum modes of the radiation field that mediate interactions between the harmonic oscillator resulted in nonlinear susceptibilities. A third-order nonlinear transmission of the optical field yields collective resonances that involve pairs of oscillators and are missed by the conventional quantum master equation treatment (Dorfman and Mukamel, 2013).

C. Heterodyne-detected sum and difference-frequency generation with classical light

We first compare two experiments which involve three classical modes. The third mode is singled out by the heterodyne detection which measures its time-averaged photon flux (photons per unit time). Both techniques represent second-order nonlinear signals $S_3^{(2)}$. The initial state of the field is given by a direct product of coherent states $|\psi(t=-\infty)\rangle = |\beta\rangle_1|\beta\rangle_2|\beta\rangle_3$, where $|\beta\rangle_\alpha$ are eigenfunctions of the mode α annihilation operator $a_\alpha|\beta\rangle_\alpha = \beta_\alpha|\beta\rangle_\alpha$. Coherent states are the most classical states of quantum light; hence we refer to them as classical optical fields (Glauber, 2007).

Only one type of optical SNGF contributes to the classical third-order signal:

$$\mathbb{E}^{(2)}_{+++}(t_3,t_2,t_1) = \mathcal{E}'(t_3)\mathcal{E}'(t_2)\mathcal{E}'(t_1),$$

where $\mathcal{E}'(t) = \langle E'_L(t)\rangle = \langle E'_R(t)\rangle = \beta_\alpha\sqrt{2\pi\hbar\omega_\alpha/\Omega}$ is the classical field amplitude.

The conjugate material SNGFs become

$$\mathbb{V}^{(2)}_{+--}(t_3,t_2,t_1) = \mathbb{V}^{(2)}_{LLL}(t_3,t_2,t_1) + \mathbb{V}^{(2)}_{LRL}(t_3,t_2,t_1), \tag{228}$$

where we assumed that initially the material system is in the ground state, which implies that $\mathbb{V}^{(2)}_{LRR}(t_3,t_2,t_1)\equiv 0$.

We assume the same three-level system used earlier. The L, R representation plus RWA allows the material SNGFs (228) to be represented by the loop diagrams shown in Figs. 30(c) and 31(c). The rules for constructing these partially time-ordered diagrams are summarized in Appendix A (Roslyak, Marx, and Mukamel, 2009a). The signal is given by the causal $\chi^{(2)}_{+--}(-\omega_3,\pm\omega_2,\pm\omega_1)$ response function. This result is not new and can be obtained by using various combinations of a classical field from the outset. To calculate Eq. (228) we have to specify the phase-matching conditions (frequencies and wave vectors of the optical modes). This is done later.

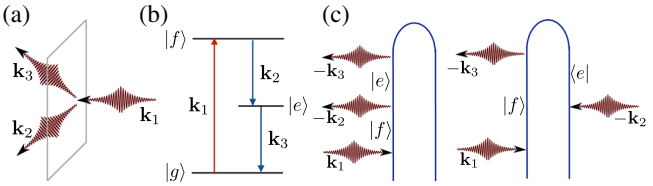

FIG. 30. Heterodyne-detected DFG: (a) phase-matching condition $\mathbf{k}_3 = \mathbf{k}_1 - \mathbf{k}_2$, (b) molecular level scheme, and (c) loop diagrams.

D. Difference-frequency generation

In DFG the first mode $\mathbf{k}_1$ promotes the system from its ground state $|g\rangle$ into state $|f\rangle$. The second mode $\mathbf{k}_2$ induces stimulated emission from $|f\rangle$ to an intermediate $|e\rangle$, and the third mode $\mathbf{k}_3$ stimulates the emission from $|e\rangle$ to $|g\rangle$, as sketched in Fig. 31(b). The signal is measured in the phase-matching direction $\mathbf{k}_3 = \mathbf{k}_1 - \mathbf{k}_2$ [see Fig. 30(a)].

The corresponding loop diagrams are shown in Fig. 30(c). The optical field SNGF yields

$$\mathbb{E}^{(2)}_{+++}(t_3,t_2,t_1) = \mathcal{E}^*_3(t)\mathcal{E}^*_2(t_2)\mathcal{E}_1(t_1). \tag{229}$$

The material SNGFs are

$$\mathbb{V}^{(2)}_{+--}(t_3,t_2,t_1) = \langle \mathcal{T}V^3_L(t)V^{2,\dagger}_L(t_2)V^{1,\dagger}_L(t_1) + \langle \mathcal{T}V^3_L(t)V^{2,\dagger}_R(t_2)V^{1,\dagger}_L(t_1)\rangle. \tag{230}$$

The DFG signal in the frequency domain can be written as

$$S_{\mathrm{DFG}}(-\omega_3,\omega_2,\omega_1) = \frac{1}{\pi\hbar}\Im\delta(\omega_1-\omega_2-\omega_3)\chi^{(2)}_{+--}(-\omega_3;-\omega_2,\omega_1)\mathcal{E}^*_3\mathcal{E}^*_2\mathcal{E}_1. \tag{231}$$

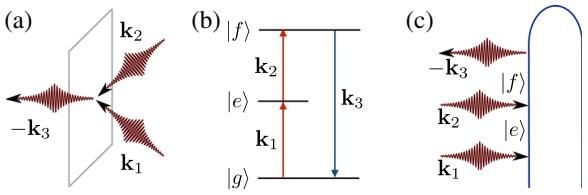

FIG. 31. Heterodyne-detected SFG: (a) phase-matching condition $\mathbf{k}_3 = \mathbf{k}_1 + \mathbf{k}_2$, (b) level scheme, and (c) loop diagrams.

Utilizing the rules given in Appendix A and the diagrams shown in Fig. 30(c) we obtain

$$\chi^{(2)}_{+--}(-(\omega_1-\omega_2);-\omega_2,\omega_1) = \frac{1}{2!\hbar^2}(\langle g|V_3G(\omega_g+\omega_1-\omega_2)V_2G(\omega_g+\omega_1)V_1^\dagger|g\rangle - \langle g|V_2G^\dagger(\omega_g+\omega_1-\omega_2)V_3G(\omega_g+\omega_1)V_1^\dagger|g\rangle). \tag{232}$$

A SOS expansion then yields

$$\chi^{(2)}_{+--}(-(\omega_1-\omega_2);-\omega_2,\omega_1) = \frac{1}{2!\hbar^2}\frac{\mu^x_{gf}\mu^x_{fe}\mu^x_{eg}}{(\omega_1-\omega_{gf}+i\hbar\gamma_{gf})(\omega_1-\omega_2-\omega_{eg}+i\hbar\gamma_{eg})} - \frac{1}{2!\hbar^2}\frac{\mu^x_{gf}\mu^x_{fe}\mu^x_{eg}}{(\omega_1-\omega_{gf}+i\hbar\gamma_{gf})(\omega_2-\omega_{eg}-i\hbar\gamma_{eg})}. \tag{233}$$

Equation (233) indicates that the signal induced by classical optical fields is given by the second-order CRF.

E. Sum-frequency generation

In SFG the first two modes promote the molecule from its ground state $|g\rangle$ through intermediate state $|e\rangle$ into the state $|f\rangle$. The third mode induces stimulated emission from $|f\rangle$ to the ground state $|g\rangle$ as sketched in Fig. 31(b). The signal is generated in the direction $\mathbf{k}_3=\mathbf{k}_1+\mathbf{k}_2$ [see Fig. 31(a)].

The heterodyne-detected SFG signal can be obtained in an analogous manner to the DFG by utilizing the diagrams shown in Fig. 31(c):

$$S_{\mathrm{SFG}}(\omega_1,\omega_2) = \frac{1}{\pi\hbar}\Im\delta(\omega_1+\omega_2-\omega_3)\chi^{(2)}_{+--}(-\omega_3;\omega_2,\omega_1)\mathcal{E}_3^*\mathcal{E}_2\mathcal{E}_1, \tag{234}$$

where the CRF is given by

$$\chi^{(2)}_{+--}(-(\omega_1+\omega_2);\omega_2,\omega_1) = \frac{1}{2!\hbar^2}\langle g|V_3G(\omega_g+\omega_1+\omega_2)V_2^\dagger G(\omega_g+\omega_1)V_1^\dagger|g\rangle = \frac{1}{2!\hbar^2}\frac{\mu^x_{ge}\mu^x_{fe}\mu^x_{eg}}{(\omega_1-\omega_{eg}+i\hbar\gamma_{eg})(\omega_1+\omega_2-\omega_{gf}+i\hbar\gamma_{gf})}. \tag{235}$$

In the coming sections Eqs. (233) and (235) will be compared with other techniques involving various combinations of quantum and classical optical fields. These include homodyne-detected SFG, DFG, and PDC where one or more optical modes are spontaneously generated, and must be treated quantum mechanically.

F. Two-photon-induced fluorescence versus homodyne-detected SFG

We now turn to techniques involving two classical and one quantum mode where the initial state of the optical field is $|\psi(t=-\infty)\rangle=|\beta_1\rangle_1|\beta_2\rangle_2|0\rangle_3$. The modes interact with the three-level material system [Fig. 32(b)]. We assume that $\omega_{eg}\neq\omega_{ef}$. This allows one to focus on the resonant SNGFs and reduce the number of diagrams.

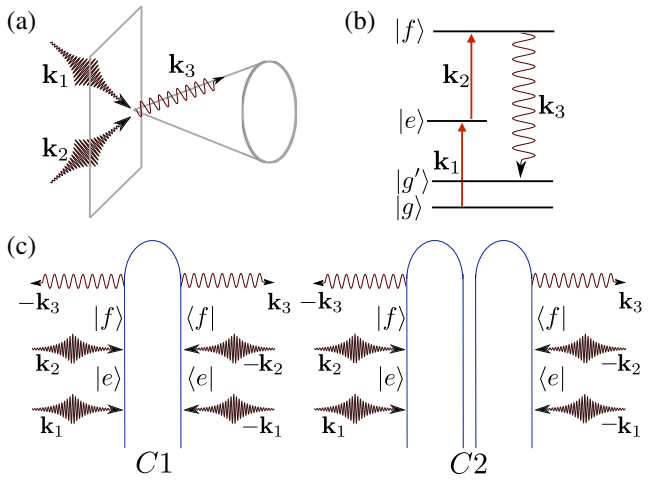

FIG. 32. Three-wave process with two classical and one quantum mode: (a) phase-matching condition, (b) molecular level scheme, and (c) loop for the incoherent TPIF (C1) and coherent homodyne SFG (C2).

The two classical modes $\mathbf{k}_1$ and $\mathbf{k}_2$ promote the molecule from its ground state $|g\rangle$ into the intermediate state $|e\rangle$ and to the final state $|f\rangle$. The system then spontaneously decays back into one of the ground state manifold $|g'\rangle$ emitting a photon into the third mode $\mathbf{k}_3$ which is initially in the vacuum state [see Fig. 32(b)]. The phase-matching condition $\mathbf{k}_1-\mathbf{k}_1+\mathbf{k}_2-\mathbf{k}_2+\mathbf{k}_3-\mathbf{k}_3=0$ is automatically satisfied for any $\mathbf{k}_3$. Therefore the spontaneous photons are emitted into a cone [see Fig. 32(a)].

We calculate the photon flux in the $\mathbf{k}_3$ mode, since the process involves three different modes and six light-matter interactions. The signal (218) must by expanded to fifth order in H_{int}. The fifth-order signal $S^{(5)}_{\mathrm{CCQ}}$ (CCQ implies two classical and one quantum mode) may be written as a sum of 2^5 terms each given by a product of molecule and field six-point SNGFs. Only the corresponding diagrams are shown in Fig. 32(c). These satisfy the following conditions:

(1) The creation operator of the quantum mode $a_3^\dagger$ must be accompanied by the corresponding annihilation operator a_3.
(2) The quantum modes deexcite the molecule, which implies that the annihilation operators must act on the bra and the creation operators act on the ket.
(3) The coherent optical fields are tuned off resonance with respect to the $\omega_{fg'}$ transition. Hence, the signal is not masked by stimulated emission.

To address the collective properties of three wave mixing, we consider a collection of N noninteracting molecules positioned at $\mathbf{r}_i$ so that $V=\sum_i V_i\delta(\mathbf{r}-\mathbf{r}_i)$. The optical field can interact with different systems at different times. Figure 32(c) shows processes involving three different molecules and six light-matter interactions. These modes can interact with either the same system [incoherent process, Fig. 32(C1)] or two different

systems [coherent process, Fig. 32(C2)] (Marx, Harbola, and Mukamel, 2008).

1. Two-photon-induced fluorescence

This is an incoherent three-wave process. Using the identity $\sum_{i=1}^{N}\exp i(\mathbf{k}_1-\mathbf{k}_1+\mathbf{k}_2-\mathbf{k}_2+\mathbf{k}_3-\mathbf{k}_3)(\mathbf{r}-\mathbf{r}_i)=N$ the optical field SNGF yields

$$\mathbb{E}^{(5)}_{LR++++}(t_6,t_5,\ldots,t_1) = N\mathcal{E}_1(t_1)\mathcal{E}_1^*(t_2)\mathcal{E}_2(t_3)\mathcal{E}_2^*(t_4)\frac{2\pi\hbar\omega_3}{\Omega}\exp\left[i\omega_3(t_6-t_5)\right]. \tag{236}$$

The relevant material SNGF is

$$\mathbb{V}^{(5)}_{LR++++}(t_6,t_5,\ldots,t_1) = \langle\mathcal{T}V_L^3(t_6)V_R^{3,\dagger}(t_5)V_-^2(t_4)V_-^{2,\dagger}(t_3)V_-^1(t_2)V_-^{1,\dagger}(t_1)\rangle. \tag{237}$$

Utilizing Eqs. (236) and (237) the frequency-domain signal can be written as

$$S_{\mathrm{TPIF}}(\omega_1,\omega_2) = \frac{N}{\pi\hbar}\sum_{\mathbf{k}_3}|\mathcal{E}_1|^2|\mathcal{E}_2|^2\frac{2\pi\hbar\omega_3}{\Omega} \times\Im\chi^{(5)}_{LR----}(-\omega_3;\omega_3,-\omega_2,\omega_2,-\omega_1,\omega_1). \tag{238}$$

Note that Eq. (238) is given in the mixed $(L/R,+/-)$ representation. It can be recast into the $+,-$ representation using $\chi^{(5)}_{LR----}=(\chi^{(5)}_{+-----}+\chi^{(5)}_{++----})/2$. The second term (two "plus" four "minus" indices) arises since one of the modes is nonclassical. The frequency-domain material SNGF can be calculated from the diagram of Fig. 32 (C1):

$$\begin{aligned}\chi^{(5)}_{LR----}(-\omega_3;\omega_3,-\omega_2,\omega_2,-\omega_1,\omega_1) &= \frac{1}{5!\hbar^5}\langle g|V_1G^\dagger(\omega_g+\omega_1)V_2G^\dagger(\omega_g+\omega_1+\omega_2)\\ &\times V_3^\dagger G^\dagger(\omega_g+\omega_1+\omega_2-\omega_3)V_3\\ &\times G(\omega_g+\omega_1+\omega_2)V_2^\dagger G(\omega_g+\omega_1)V_1^\dagger|g\rangle.\end{aligned} \tag{239}$$

Expanding Eq. (239) in molecular states gives

$$\begin{aligned}\chi^{(5)}_{LR----}(-(\omega_1+\omega_2);\omega_2,\omega_1) &= \sum_{gg'}|\mu^x_{g'f}\mu^x_{fe}\mu^x_{eg}|^2\\ &\times\frac{1}{5!\hbar^5}\frac{1}{[(\omega_1-\omega_{eg})^2+\gamma_{eg}^2][\omega_1+\omega_2-\omega_{fg}+i\gamma_{fg}]}\\ &\times\frac{1}{[\omega_1+\omega_2-\omega_{fg'}-i\gamma_{fg'}][\omega_1+\omega_2-\omega_3-\omega_{gg'}-i\gamma_{gg'}]}.\end{aligned} \tag{240}$$

Provided the energy splitting within the ground state manifold is small comparing to the optical transitions the signal can be recast in the following form:

$$S_{\mathrm{TPIF}}(\omega_1,\omega_2) = \frac{2N\omega_3}{5!\hbar^5\Omega}|\mathcal{E}_1|^2|\mathcal{E}_2|^2|T_{fg}(\omega_1,\omega_2)|^2\delta(\omega_1+\omega_2-\omega_3-\omega_{gg'}), \tag{241}$$

where

$$T_{fg}(\omega_1,\omega_2)=\frac{\mu_{gf}\mu_{fe}\mu_{eg}}{(\omega_1-\omega_{eg}+i\gamma_{eg})(\omega_1+\omega_2-\omega_{fg}+i\gamma_{fg})}$$

is the transition amplitude. This is similar to the Kramers-Heisenberg form of ordinary (single-photon) fluorescence (Marx, Harbola, and Mukamel, 2008). As in single-photon fluorescence, for a correct description of the TPIF the ground state must not be degenerate. Otherwise, $\gamma_{gg}=0$ (the degenerate ground state of the system has an infinite lifetime) and the signal vanishes.

The SNGF in Eq. (239) is commonly called the fluorescence quantum efficiency (Xu and Webb, 1996) or the two-photon tensor (Callis, 1993). Our result is identical to that of Callis, apart from the $\delta(\omega_1+\omega_2-\omega_3-\omega_{gg'})$ factor.

When the two classical coherent modes are degenerate $(\omega_1=\omega_2)$ the signal given by Eq. (241) describes nonresonant hyper-Raman scattering $(\omega_{gg'}\neq 0)$ also known as incoherent second harmonic inelastic scattering (Callis, 1993; Andrews and Allcock, 2002). When $\omega_1=\omega_2$ and $\omega_{gg'}\to 0$ (but not equal to) Eq. (241) describes nonresonant hyper-Rayleigh scattering also known as incoherent second harmonic elastic scattering. Off-resonant hyperscattering is a major complicating factor for TPIF microscopy (Xu, Shear, and Webb, 1997).

2. Homodyne-detected SFG

Here the optical field SNGF is given by Eq. (236), but instead of a factor N it contains the factor

$$\sum_{i=1}^{N}\sum_{j\neq i}^{N-1}e^{i\Delta\mathbf{k}\cdot(\mathbf{r}-\mathbf{r}_i)}e^{-i\Delta\mathbf{k}\cdot(\mathbf{r}-\mathbf{r}_j)}\approx N(N-1), \tag{242}$$

where $\Delta\mathbf{k}\approx\mathbf{k}_1+\mathbf{k}_2-\mathbf{k}_3$. The approximate sign reflects phase uncertainty given by the reciprocal of the molecular collection length which effectively narrows the optical cone. For large N, the coherent part $\propto N(N-1)$ dominates over the incoherent $\propto N$ response. For a small sample size, the exact calculation of the optical field part of the SNGF is rather lengthy, but it can be performed in the same fashion as done by Hong and Mandel (1985) for the probability of photon detection.

To calculate the matter SNGF, we must work in the joint space of two molecules $|\rangle_{1,2}=|\rangle_1|\rangle_2$ interacting with the same field mode. The matter SNGF of the joint system can be factorized into a product of each molecule SNGFs:

$$\begin{aligned}\mathbb{V}^{(5)}_{LR++++}(t_6,t_5,\ldots,t_1) &= \langle\mathcal{T}V_+^3(t)V_+^{3,\dagger}(t_5)V_-^2(t_4)V_-^{2,\dagger}(t_3)V_-^1(t_2)V_-^{1,\dagger}(t_1)\rangle_{1,2}\\ &= \langle\mathcal{T}V_+^3(t)V_-^{2,\dagger}(t_3)V_-^{1,\dagger}(t_1)\rangle_1\langle\mathcal{T}V_+^{3,\dagger}(t_5)V_-^2(t_4)V_-^1(t_2)\rangle_2,\end{aligned} \tag{243}$$

where we used the fact that the last interaction must be a plus.

Since the two molecules are identical, the following identity holds:

$$\langle \mathcal{T} V_+^{3,\dagger}(t_5) V_-^2(t_4) V_-^1(t_2)\rangle = [\langle \mathcal{T} V_+^3(t+\Delta t) V_-^{2,\dagger}(t_3+\Delta t) V_-^{1,\dagger}(t_1+\Delta t)\rangle]^*, \quad (244)$$

where $v_g \Delta t$ is the optical path length connecting molecules situated at $\mathbf{r}_i$ and $\mathbf{r}_j$. Using this identity and Eq. (243) the matter SNGF in the frequency domain can be factorized into the square of an ordinary (causal) response function (one + and several −):

$$\Im\chi^{(5)}_{++----}(-\omega_3;\omega_3,-\omega_2,\omega_2,-\omega_1,\omega_1) = |\chi^{(2)}_{+--}(-(\omega_1+\omega_2);\omega_2,\omega_1)|^2.$$

The unique factorization of the coherent matter SNGFs can also be obtained in the L, R representation using the diagrammatic technique as shown in Fig. 32(C2). The classical modes have to excite the molecules and the quantum mode has to deexcite them. Hence, the interactions with the first molecule ket (L) are accompanied by the conjugate interactions with the second molecule bra (R). We obtain that the ordinary, causal response function is given by Eq. (235) as $\chi^{(2)}_{+--}(-(\omega_1+\omega_2);\omega_2,\omega_1) = \chi^{(2)}_{LLL}(-(\omega_1+\omega_2);\omega_2,\omega_1)$.

The homodyne-detected SFG signal is finally given by

$$S_{\mathrm{SFG}} = N(N-1)|\mathcal{E}_1|^2|\mathcal{E}_2|^2 \frac{2(\omega_1+\omega_2)}{\Omega} \times |\chi^{(2)}_{+--}(-(\omega_1+\omega_2);\omega_2,\omega_1)|^2. \quad (245)$$

Both homodyne and heterodyne SFG are given by the same causal response function $\chi^{(2)}_{+--}$. The main difference is that the latter satisfies perfect phase matching, while for the former this condition is only approximate. For sufficiently large samples the two techniques are identical.

To conclude, we present the total signal for the three-wave process involving CCQ which includes both an incoherent and a coherent component:

$$S^{(5)}_{\mathrm{CCQ}}(\omega_2,\omega_1) = |\mathcal{E}_1|^2|\mathcal{E}_2|^2\frac{2\omega_3}{\Omega} \times [N\Im\chi^{(5)}_{++----}(-\omega_3;\omega_3,-\omega_2,\omega_2,-\omega_1,\omega_1) + N(N-1)|\chi^{(2)}_{+--}(-(\omega_1+\omega_2);\omega_2,\omega_1)|^2]. \quad (246)$$

G. Two-photon-emitted fluorescence versus type-I parametric downconversion

1. TPEF

We now turn to three wave processes involving one classical and two quantum modes. We start with the incoherent response of N identical molecules initially in their ground state. The initial state of the optical field is $|\psi(t=-\infty)\rangle = |\beta_1\rangle_1|0\rangle_2|0\rangle_3$. The classical field $\mathbf{k}_1$ pumps the molecule from its ground state $|g\rangle$ into the excited state $|f\rangle$. The system then spontaneously emits two photons into modes $\mathbf{k}_2$ and $\mathbf{k}_3$ [see Fig. 33(b)] which are initially in the vacuum state. Such an incoherent process which involves one classical and two quantum modes will be denoted as TPEF. To our knowledge there is neither theoretical nor experimental work concerning this process.

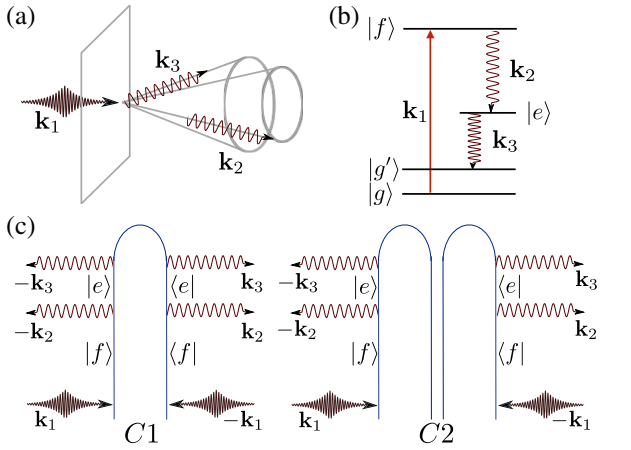

FIG. 33. Three wave processes involuting two quantum and one classical mode: (a) phase-matching condition, (b) molecular level scheme, and (c) loop diagrams for the incoherent TPEF (C1) and coherent type-I PDC (C2).

This process is not phase sensitive since the phase-matching condition $\mathbf{k}_1 - \mathbf{k}_1 + \mathbf{k}_2 - \mathbf{k}_2 + \mathbf{k}_3 - \mathbf{k}_3 = 0$ is automatically satisfied for any $\mathbf{k}_3$. Therefore spontaneously generated modes are emitted into two spatial cones [see Fig. 33(a)]. For a single molecule the cones are collinear, as in type-I PDC. Because of this similarity we chose beam polarizations as is usually done for PDC of this type: the spontaneously generated photons have the same polarization along the x axis and orthogonal to that of the classical mode polarized along the y axis.

The time-averaged photon flux in the $\mathbf{k}_3$ mode is our TPEF signal. We again make use of the loop diagrams to identify the relevant SNGF contributing to the signal. Using the initial state of the field the diagrams must satisfy the following conditions:

(1) The creation operators of spontaneously generated modes $a_3^\dagger$, $a_2^\dagger$ acting on the ket must be accompanied by the corresponding annihilation operators a_3, a_2 acting on the bra.
(2) The first mode $\omega_1(\mathbf{k}_1)$ is off resonant with both ω_{eg} and ω_{fe} transitions to avoid stimulated emission contributions.

Figure 33(C1) satisfies these conditions. The nonresonant diagrams have been omitted. Using this diagram the optical field SNGF yields

$$\mathbb{E}^{(5)}_{LLRR++}(t_6,t_5,\ldots,t_1) = N\mathcal{E}_1(t_1)\mathcal{E}_1^*(t_2)\frac{2\pi\hbar\omega_3}{\Omega}\frac{2\pi\hbar\omega_2}{\Omega} \times \exp[i\omega_3(t_6-t_5)]\exp[i\omega_3(t_4-t_3)]. \quad (247)$$

The matter SNGF assumes the following form:

$$\mathbb{V}^{(5)}_{LLRR--}(t_6,t_5,\ldots,t_1) = \langle \mathcal{T} V^3_L(t) V^{3,\dagger}_R(t_5) V^{2,\dagger}_R(t_4) V^2_L(t_3) V^1_-(t_2) V^{1,\dagger}_-(t_1)\rangle. \quad (248)$$

Using Eqs. (247) and (248) the incoherent part of the frequency-domain signal is given by

$$S_{\mathrm{TPEF}}(\omega_1) = \frac{N}{\pi\hbar}|\mathcal{E}_1|^2 \frac{2\pi\hbar(\omega_2)}{\Omega}\frac{2\pi\hbar\omega_3}{\Omega} \times \Im\chi^{(5)}_{LLRR--}(-\omega_3;\omega_3,\omega_2,-\omega_2,-\omega_1,\omega_1). \quad (249)$$

The corresponding SNGF can be calculated from the diagram in Fig. 33(C1):

$$\chi^{(5)}_{LLRR--}(-\omega_3;\omega_3,\omega_2,-\omega_2,-\omega_1,\omega_1) = \frac{1}{5!\hbar^5}\langle g|V_1^\dagger G^\dagger(\omega_g+\omega_1)V_2^\dagger G^\dagger(\omega_g+\omega_1-\omega_2) \times V_3 G^\dagger(\omega_g+\omega_1-\omega_2-\omega_3)V_3 \times G(\omega_g+\omega_1-\omega_2)V_2 G(\omega_g+\omega_1)V_1^\dagger|g\rangle. \quad (250)$$

Expansion in the molecular eigenstates brings the response function into the following Kramers-Heisenberg form:

$$\chi^{(5)}_{LLRR--}(-\omega_3;\omega_3,\omega_2,-\omega_2,-\omega_1,\omega_1) = \frac{1}{5!\hbar^5}\sum_{gg'}|\mu^x_{g'e}\mu^x_{ef}\mu^y_{fg}|^2\delta(\omega_1-\omega_2-\omega_3) \times \frac{1}{(\omega_1-\omega_{fg})^2+\gamma_{fg}^2}\left|\frac{1}{\omega_1-\omega_2-\omega_{eg}+i\gamma_{eg}}\right|^2. \quad (251)$$

Note that unlike TPIF, the TPEF signal depends on the SNGF other than the causal response function $\chi^{(5)}_{+-----}$.

2. Type-I PDC

We now turn to the coherent response of a collection of identical molecules which interact with one classical pumping mode and two spontaneously generated quantum modes [see Figs. 33(a) and 33(b)]. This is known as type-I PDC, which is widely used for producing entangled-photon pairs. Hereafter we assume perfect phase matching $\Delta\mathbf{k} = \mathbf{k}_1 - \mathbf{k}_2 - \mathbf{k}_3$ which is the case for a sufficiently large sample (Gerry and Knight, 2005).

The initial conditions for PDC are the same as for TPEF and most PDC experiments and are well described by the causal response function $\chi^{(2)}_{+--}$. Therefore one would expect a connection between TPEF and PDC, similar to that of TPIF and homodyne-detected SFG. However, as we are about to demonstrate, for a complete description of the PDC process the causal second-order response function is not enough.

To establish the corrections to the second-order CRF caused by the quantum origin of the spontaneous modes. We again resort to the close-time-path loops (CTPL) diagrams [see Fig. 33(C2)]. For the coherent response the optical field SNGF is given by Eq. (247) with the factor N replaced by $N(N-1)$. The material SNGF (248) can be factorized as

$$\mathbb{V}^{(5)}_{LLRR--}(t_6,t_5,\ldots,t_1) = \langle \mathcal{T} V^3_L(t_6) V^2_L(t_3) V^{1,\dagger}_L(t_1)\rangle\langle \mathcal{T} V^{3,\dagger}_R(t_5) V^{2,\dagger}_R(t_4) V^1_R(t_2)\rangle. \quad (252)$$

Note that this factorization is unique as $\langle \mathcal{T} V^3_L(t) V^{2,\dagger}_R(t_4) \times V^{1,\dagger}_L(t_1)\rangle = 0$ due to the material initially being in its ground state. The coherent PDC signal in the frequency domain can then be written as

$$S_{\mathrm{PDC}}(\omega_1) = \frac{N(N-1)}{4\pi\hbar}|\mathcal{E}_1|^2\frac{2\pi\hbar\omega_2}{\Omega}\frac{2\pi\hbar(\omega_1-\omega_2)}{\Omega} \times |\chi^{(2)}_{LL-}(-(\omega_1-\omega_2);\omega_2,\omega_1)|^2. \quad (253)$$

Here the generalized response function expanded in the eigenstates has the form

$$\chi^{(2)}_{LL-}(-(\omega_1-\omega_2);\omega_2,\omega_1) = \frac{1}{2!\hbar^2}\frac{\mu^y_{gf}\mu^x_{fe}\mu^x_{eg}}{(\omega_1-\omega_{gf}+i\hbar\gamma_{gf})(\omega_1-\omega_2-\omega_{eg}+i\hbar\gamma_{eg})}.$$

This mixed representation can be recast in $+,-$ and L, R representations:

$$\chi^{(2)}_{LL-} = \chi^{(2)}_{LLL} = \tfrac{1}{2}(\chi^{(2)}_{+--} + \chi^{(2)}_{++-}). \quad (254)$$

Comparing the CRF for heterodyne-detected DFG (233) and the SNGFs for type-I PDC (254) we see that the latter is described not only by causal response function $\chi^{(2)}_{+--}$ but also by the second moment of material fluctuations $\chi^{(2)}_{++-}$. On the other hand, in the L, R representation it singles out one Liouville pathway $\chi^{(2)}_{LLL}$, while the classical optical fields drive the material system along all possible pathways.

Interesting effects arise in type-I PDC if the detection process is included explicitly. These effects are discussed in Sec. IV.I.

In summary we give the signal for the three-wave process involving one classical and two quantum fields (CQQ). This contains both an incoherent and a coherent component:

$$S^{(5)}_{\mathrm{CQQ}}(\omega_2,\omega_1) = \frac{1}{\pi\hbar}|\mathcal{E}_1|^2\frac{2\pi\hbar\omega_2}{\Omega}\frac{2\pi\hbar\omega_3}{\Omega}N\Im\Big[\chi^{(5)}_{++----}(-\omega_3;\omega_3,-\omega_2,\omega_2,-\omega_1,\omega_1) + \chi^{(5)}_{+++---}(-\omega_3;\omega_3,-\omega_2,\omega_2,-\omega_1,\omega_1) + \chi^{(5)}_{++++--}(-\omega_3;\omega_3,-\omega_2,\omega_2,-\omega_1,\omega_1)\Big] + N(N-1)|\chi^{(2)}_{+--}(-(\omega_1-\omega_2);\omega_2,\omega_1) + \chi^{(2)}_{++-}(-(\omega_1-\omega_2);\omega_2,\omega_1)|^2. \quad (255)$$

H. Type-II PDC and polarization entanglement

In type-II parametric downconversion, the two spontaneously generated signals have orthogonal polarizations. Because of birefringence, the generated photons are emitted along two noncollinear spatial cones known as ordinary and extraordinary beams [see Fig. 34(a)]. Polarization-entangled light (Gerry and Knight, 2005) is generated at the intersections of the cones. An x polarization filter and a detector are placed at one of the cones intersections. The detector cannot tell from which beam a photon is obtained. To describe the process we need five optical modes: one classical $|1\rangle|y\rangle$ and four quantum modes $\{|2\rangle|x\rangle, |2\rangle|y\rangle, |3\rangle|x\rangle, |3\rangle|y\rangle\}$.

A polarization-entangled signal is described by CTPL diagrams shown in Fig. 34(c). The type-II PDC signal consist of two parts $S^{(5)}_{\mathrm{PDCII}} = S^{(5)}_{3x} + S^{(5)}_{2x}$. The signal $S^{(5)}_{3x}$ assumes the form of Eq. (253), with the material pathway depicted in Fig. 34(C1):

$$\begin{aligned}\chi^{(2)}_{LL-}&(-(\omega_1-\omega_2);-\omega_2,\omega_1)\\ &=\frac{1}{2}\Big[\chi^{(2)}_{+--}(-(\omega_1-\omega_2);-\omega_2,\omega_1)\\ &\quad+\chi^{(2)}_{++-}(-(\omega_1-\omega_2);\omega_2,-\omega_1)\Big]\\ &=\frac{1}{2!\hbar^2}\frac{C}{(\omega_1-\omega_{gf}+i\hbar\gamma_{gf})(\omega_1-\omega_2-\omega_{eg}+i\hbar\gamma_{eg})},\end{aligned} \tag{256}$$

where the coefficient C is given by

$$\begin{aligned}C^2=|\mu^y_{gf}|^2(|\mu^x_{fe}|^2|\mu^x_{eg}|^2+2\mu^x_{fe}\mu^x_{eg}\mu^y_{fe}\mu^y_{eg}\\ +\mu^x_{fe}\mu^x_{eg}\mu^x_{fe}\mu^y_{eg}+\mu^y_{fe}\mu^y_{eg}\mu^y_{fe}\mu^x_{eg}).\end{aligned} \tag{257}$$

The signal $S^{(5)}_{3x}$ is described by the diagram in Fig. 34(C2):

$$\begin{aligned}\chi^{(2)}_{LL-}&(-\omega_2;-(\omega_1-\omega_2),\omega_1)\\ &=\frac{1}{2}\Big[\chi^{(2)}_{+--}(-\omega_2;-(\omega_1-\omega_2),\omega_1)\\ &\quad+\chi^{(2)}_{++-}(-\omega_2;-(\omega_1-\omega_2),\omega_1)\Big]\\ &=\frac{1}{2!\hbar^2}\frac{C}{(\omega_1-\omega_{gf}+i\hbar\gamma_{gf})(\omega_2-\omega_{eg}+i\hbar\gamma_{eg})}.\end{aligned} \tag{258}$$

The net type-II PDC signal is

$$\begin{aligned}S_{\mathrm{PDCII}}&(\omega_1)\\ &=\frac{N(N-1)}{4\pi\hbar}|\mathcal{E}_1|^2\frac{2\pi\hbar\omega_2}{\Omega}\frac{2\pi\hbar(\omega_1-\omega_2)}{\Omega}\\ &\quad\times|\chi^{(2)}_{LL-}(-(\omega_1-\omega_2);-\omega_2,\omega_1)|^2\\ &\quad+|\chi^{(2)}_{LL-}(-\omega_2;-(\omega_1-\omega_2),\omega_1)|^2.\end{aligned} \tag{259}$$

I. Time-and-frequency-resolved type-I PDC

Previously we had surveyed various wave-mixing signals using a simple model without addressing the detection process in detail. In the following we include the photon counting detection described in Sec. III.D and demonstrate how the actual generation process in type-I PDC relates to nonlinear response and how different it is compared to semiclassical theory.

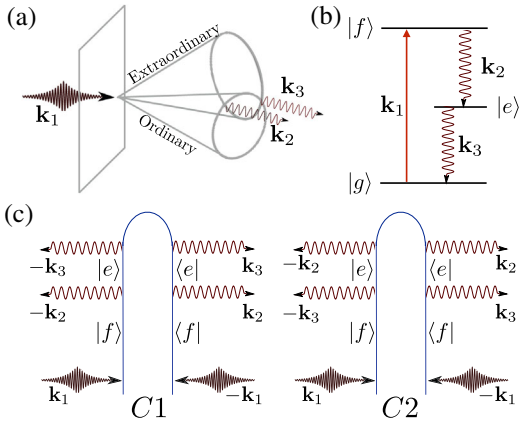

FIG. 34. Type-II PDC: (a) phase matching, (b) molecular level scheme, and (c) CTPL diagrams for the signal from $\mathbf{k}_3$ (C1) and $\mathbf{k}_2$ (C2) modes polarized along the x direction.

The standard calculation of nonlinear wave mixing assumes that all relevant field frequencies are off resonant with matter. It is then possible to adiabatically eliminate all matter degrees of freedom and describe the process by an effective Hamiltonian for the field that contains a nonlinear cubic coupling of three radiation modes (Mandel and Wolf, 1995). For SFG this reads

$$H_{\mathrm{eff}}=-\int d\mathbf{r}\chi^{(2)}E^\dagger_3(\omega_1-\omega_2)E^\dagger_2(\omega_2)E_1(\omega_1) \tag{260}$$

and for DFG and PDC

$$H_{\mathrm{eff}}=-\int d\mathbf{r}\chi^{(2)}E^\dagger_3(\omega_1+\omega_2)E_2(\omega_2)E_1(\omega_1). \tag{261}$$

All matter information is embedded into a coefficient that is proportional to $\chi^{(2)}$ (Gerry and Knight, 2005) which is defined by the semiclassical theory of radiation-matter coupling. Langevin quantum noise is added to represent vacuum fluctuations caused by other field modes (Scully and Zubairy, 1997; Glauber, 2007; Avenhaus *et al.*, 2008) and account for photon statistics.

The microscopic theory of type-I PDC presented next holds if the cascade of two photons in a three-level system is generated in both on and off resonance. The resonant case is especially important for potential spectroscopic applications (Mukamel, 1995), where unique information about entangled matter (Lettow *et al.*, 2010) can be revealed. Other examples are molecular aggregates and photosynthetic complexes or biological imaging (Saleh *et al.*, 1998). Second, it properly takes into account the quantum nature of the generated modes through a generalized susceptibility that has a very different behavior near resonance than the semiclassical $\chi^{(2)}$. $\chi^{(2)}$ is derived for two classical fields and a single quantum field. While this is true for the reverse process (sum-frequency generation) it does not apply for PDC, which couples a single classical and two quantum modes. Third, macroscopic

propagation effects are not required for the basic generation of the signal. Fourth, gated detection (Dorfman and Mukamel, 2012a) yields the finite temporal and spectral resolution of the coincident photons limited by a Wigner spectrogram. For either time- or frequency-resolved measurement of the generated field, the signal can be expressed as a modulus square of the transition amplitude that depends on three field modes. This is not the case for photon counting. Shwartz *et al.* (2012) recently reported PDC in diamond, where a 18 keV pump field generates two x-ray photons. Dorfman and Mukamel (2012b) reproduced experimental data in the entire frequency range without adding Langevin noise.

The nature of entangled light can be revealed by photon correlation measurements that are governed by energy, momentum, and/or angular momentum conservation. In PDC, a nonlinear medium is pumped by the electromagnetic field of frequency ω_p and some of the pump photons are converted into pairs of signal and idler photons with frequencies ω_s and ω_i, respectively [see Fig. 35(a)] satisfying $\omega_p = \omega_s + \omega_i$.

For a more detailed description of the wave-mixing process in PDC we recast an effective semiclassical Hamiltonian in Eq. (261) as follows:

$$H_{\rm int}(t) = i\hbar \sum_j \int \frac{d\omega_s}{2\pi}\frac{d\omega_i}{2\pi}\frac{d\omega_p}{2\pi}\chi^{(2)}_{+--}(\omega_s,\omega_i,\omega_p) \times \hat{a}^{(s)\dagger}\hat{a}^{(i)\dagger}\beta^{(p)} e^{i\Delta\mathbf{k}\cdot(\mathbf{r}-\mathbf{r}_j)} e^{-i(\omega_p-\omega_s-\omega_i)t}] + \text{H.c.}, \quad (262)$$

where $\hat{a}^{\dagger(s)}$ and $\hat{a}^{(i)\dagger}$ are creation operators for signal and idler modes, $\beta^{(p)}$ is the expectation value of the classical pump field, $\Delta\mathbf{k} = \mathbf{k}_p - \mathbf{k}_s - \mathbf{k}_i$, j runs over molecules, and $\chi^{(2)}_{+--}$ [normally denoted as $\chi^{(2)}(-\omega_s;-\omega_i,\omega_p)$] is the second-order nonlinear susceptibility

$$\chi^{(2)}_{+--}(\omega_s = \omega_p - \omega_i, \omega_i, \omega_p) = \left(\frac{i}{\hbar}\right)^2 \int_0^\infty \int_0^\infty dt_2 dt_1 \times e^{i\omega_i(t_2+t_1)+i\omega_p t_1}\langle[[V(t_2+t_1),V(t_1)],V(0)]\rangle + (i \leftrightarrow p). \quad (263)$$

The $+--$ indices in Eq. (263) signify two commutators followed by an anticommutator. The bottom line of the semiclassical approach is that PDC is represented by a three-point matter-field interaction via the second-order susceptibility $\chi^{(2)}_{+--}$ that couples the signal, idler, and pump modes. However, it was realized that other field modes are needed to yield the correct photon statistics. Electromagnetic field fluctuations are then added as quantum noise (Langevin forces) (Scully and Zubairy, 1997).

Next we summarize a microscopic calculation of the PCC rate in type-I PDC (Roslyak, Marx, and Mukamel, 2009a). We show that PDC is governed by a quantity that resembles but is different from Eq. (263). In contrast with the semiclassical

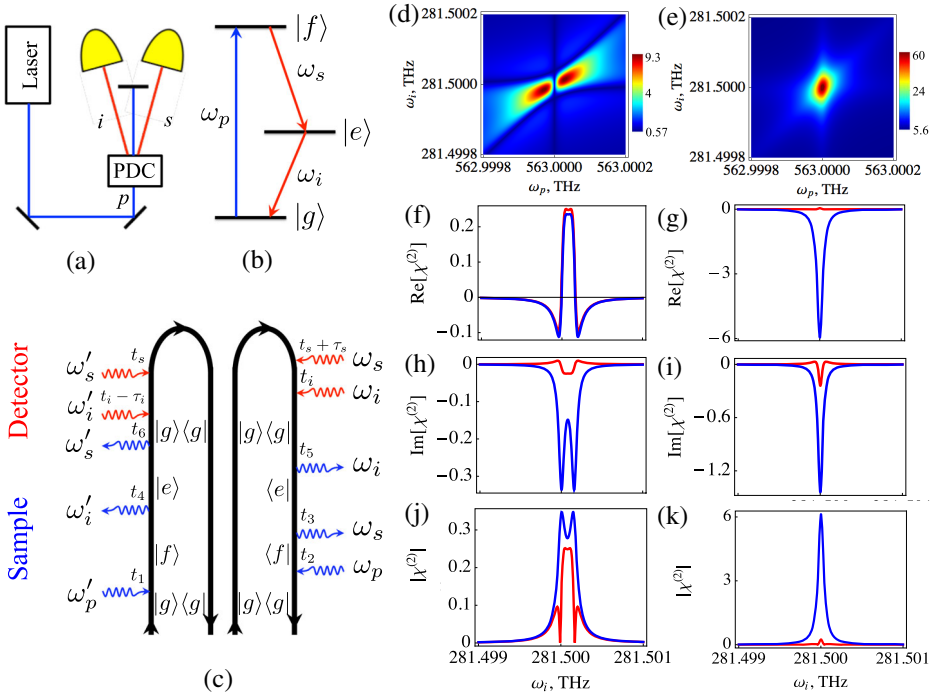

FIG. 35. (a) Schematic of the PDC experiment and (b) the three-level model system used in our simulations. (c) One out of four loop diagrams [the remaining three diagrams are presented by Dorfman and Mukamel (2012b)] for the PCC rate of signal and idler photons generated in type-I PDC [Eq. (265)]. The left and right diagrams represent a pair of molecules. Blue (red) arrows represent field-matter interaction with the sample (detectors). There are four possible permutations (s/i and s'/i') which leads to four terms when Eq. (267) is substituted into Eq. (266). (d) Absolute value of semiclassical susceptibility $|\chi^{(2)}_{+--}(-(\omega_p-\omega_i),-\omega_i,\omega_p)|$ (arb. units) Eq. (268), and (e) the susceptibility $|\chi^{(2)}_{LL-}(-(\omega_p-\omega_i),-\omega_i,\omega_p)|$ Eq. (267) vs pump ω_p and idler frequency ω_i. We used the standard potassium titanyl phosphate (KTP) crystal parameters outlined in the text. (f) Real and (h) imaginary parts and (j) absolute value of $\chi^{(2)}_{+--}$ (red lines) and $\chi^{(2)}_{LL-}$ (blue lines) for off-resonant pump $\omega_p - \omega_{gf} = 10\gamma_{gf}$. (g), (i), and (k) The same as (f), (h), and (j) but for resonant pump $\omega_p \simeq \omega_{gf}$.

approach, PDC emerges as a six-mode two-molecule rather than a three-mode matter-field interaction process and is represented by convolution of two quantum susceptibilities $\chi^{(2)}_{LL-}(\omega_s,\omega_i,\omega_p)$ and $\chi^{(2)*}_{LL-}(\omega'_s,\omega'_i,\omega'_p)$ that represent a pair of molecules in the sample interacting with many vacuum modes of the signal (s, s') and the idler (i, i'). Field fluctuations are included self-consistently at the microscopic level. Furthermore, the relevant nonlinear susceptibility is different from the semiclassical one $\chi^{(2)}_{+--}$ and is given by

$$\chi^{(2)}_{LL-}(\omega_s=\omega_p-\omega_i,\omega_i,\omega_p)=\left(\frac{i}{\hbar}\right)\int_0^\infty\int_0^\infty dt_2dt_1\times e^{i\omega_i(t_2+t_1)+i\omega_p t_1}\langle[V(t_2+t_1)V(t_1),V(0)]\rangle+(i\leftrightarrow s). \tag{264}$$

Equation (264) has a single commutator and is symmetric to a permutation of ω_i and $\omega_s=\omega_p-\omega_i$ as it should. Equation (263) has two commutators and lacks this symmetry.

1. The bare PCC rate

The measured PCC rate of signal and idler photons starts with the definition (175). The basis for the bare signal in Eq. (174) is given by the time-ordered product of Green's functions of superoperators in the interaction picture (Dorfman and Mukamel, 2012b)

$$\langle\mathcal{T}E_R^{\dagger(i)}(t'_i)E_R^{\dagger(s)}(t'_s+\tau_s)E_L^{(s')}(t'_s)E_L^{(i')}(t'_i-\tau_i)\times e^{-(i/\hbar)\int_{-\infty}^{\infty}H'_-(\tau)d\tau}\rho(-\infty)\rangle, \tag{265}$$

which represents four spectral modes arriving at the detectors, where modes s, s', i, and i' are defined by their frequencies ω_s, ω'_i, $\omega_i=\omega_p-\omega_s$, and $\omega'_s=\omega'_p-\omega'_i$.

In type-I PDC the sample is composed of N identical molecules initially in their ground state. They interact with one classical pump mode and emit two spontaneously generated quantum modes with the same polarization into two collinear cones. The initial state of the optical field is given by $|0\rangle_s|0\rangle_i|\beta\rangle_p$. A classical pump field promotes the molecule from its ground state $|g\rangle$ to the doubly excited state $|f\rangle$ [see Fig. 35(b)].

Because of the quantum nature of the signal and idler fields, the interaction of each of these fields with matter must be at least second order to yield a nonvanishing signal. The leading contribution to Eq. (265) comes from the four diagrams, one of which is shown in Fig. 35(c) [for rules see Appendix A (Roslyak, Marx, and Mukamel, 2009a)]. The coherent part of the signal represented by the interaction of two spontaneously generated quantum and one classical modes is proportional to the number of pairs of sites in the sample $\sim N(N-1)$, which dominates the other, incoherent, $\sim N$ response for large N. Details of the calculation of the correlation function (265) are presented by Dorfman and Mukamel (2012b). We obtain for the "bare" frequency-domain PCC rate $R_c^{(B)}(\omega_s,\omega'_i,\omega_p,\omega'_p)\equiv\int dt'_s dt'_i\langle\mathcal{T}\hat{n}_s(t'_s,\omega'_s)\hat{n}_i(t'_i,\omega'_i)\rangle_T e^{-i(\omega_s+\omega'_i-\omega'_p)t'_s+(\omega_s+\omega'_i-\omega_p)t'_i}$,

$$R_c^{(B)}(\omega_s,\omega'_i,\omega_p,\omega'_p)=N(N-1)\left(\frac{2\pi\hbar}{V}\right)^4\times\mathcal{E}^{*(p)}(\omega_p)\mathcal{E}^{(p)}(\omega'_p)\mathcal{D}(\omega_s)\mathcal{D}(\omega_p-\omega_s)\mathcal{D}(\omega'_i)\mathcal{D}(\omega'_p-\omega'_i)\times\chi^{(2)}_{LL-}[-(\omega'_p-\omega'_i),-\omega'_i,\omega'_p]\chi^{(2)*}_{LL-}[-\omega_s,-(\omega_p-\omega_s),\omega_p], \tag{266}$$

where $\mathcal{E}^{(p)}(\omega)\equiv E^{(p)}(\omega)\beta^{(p)}$ is a classical field amplitude, $E^{(p)}(\omega)$ is the pump pulse envelope, and $\mathcal{D}(\omega)=\omega\tilde{\mathcal{D}}(\omega)$, with $\tilde{\mathcal{D}}(\omega)=V\omega^2/\pi^2c^3$ the density of radiation modes. For our level scheme [Fig. 35(b)] the nonlinear susceptibility $\chi^{(2)}_{LL-}$ [see Eq. (264)] is given by

$$\chi^{(2)}_{LL-}[-(\omega'_p-\omega'_i),-\omega'_i,\omega'_p]=\frac{1}{2\hbar}\frac{\mu^*_{gf}\mu_{fe}\mu_{eg}}{\omega'_p-\omega_{gf}+i\gamma_{gf}}\times\frac{1}{(\omega'_p-\omega'_i-\omega_{eg}+i\gamma_{eg})}+(\omega'_i\leftrightarrow\omega'_p-\omega'_i). \tag{267}$$

Equation (266) represents a six-mode $(\omega_p,\omega_i,\omega_s,\omega'_p,\omega'_i,\omega'_s)$ field-matter correlation function factorized into two generalized susceptibilities each representing the interaction of two quantum and one classical mode with a different molecule. Because of two constraints $\omega_p=\omega_s+\omega_i$, $\omega'_p=\omega'_s+\omega'_i$ which originate from time translation invariance on each of the two molecules that generate the nonlinear response, Eq. (266) depends only on four field modes. Each molecule creates a coherence in the field between states with zero and one photon. By combining the susceptibilities from a pair of molecules we obtain a photon occupation number that can be detected. Thus, the detection process must be described in the joint space of the two molecules and involves the interference of four quantum pathways (two with bra and two with ket) with different time orderings. Note that this pathway information is not explicit in the Langevin approach.

For comparison, if all three fields (signal, idler, and pump) are classical, the number of material-field interactions is reduced to three—one for each field. Then the leading contribution to the field correlation function yields the semiclassical nonlinear susceptibility $\chi^{(2)}_{+--}$:

$$\begin{aligned}\chi^{(2)}_{+--}[-(\omega'_p-\omega'_i),-\omega'_i,\omega'_p]&=\frac{1}{2\hbar^2}\langle g|\mathcal{T}V_L\mathcal{G}(\omega'_p-\omega'_i)V_L\mathcal{G}(\omega'_p)V_L^\dagger|g\rangle+\frac{1}{\hbar^2}\langle g|\mathcal{T}V_L\mathcal{G}^\dagger(\omega'_i)V_L\mathcal{G}(\omega'_p)V_L^\dagger|g\rangle\\&=\frac{1}{\hbar^2}\frac{\mu^*_{gf}\mu_{fe}\mu_{eg}}{\omega_p-\omega_{gf}+i\gamma_{gf}}\left[\frac{1}{\omega_p-\omega'_i-\omega_{eg}+i\gamma_{eg}}+\frac{1}{\omega'_i-\omega_{eg}-i\gamma_{eg}}\right]+(\omega'_i\leftrightarrow\omega_p-\omega'_i),\end{aligned} \tag{268}$$

where $\mathcal{G}(\omega)=1/(\omega-H_{0-}/\hbar+i\gamma)$ is the retarded Liouville Green's function and γ is lifetime broadening. $\chi^{(2)}_{LL-}$ possesses a permutation symmetry with respect to $s\leftrightarrow i$ (both have L

index). In contrast the semiclassical calculation via $\chi^{(2)}_{++-}$ is nonsymmetric with respect to $s \leftrightarrow i$ (one $+$ and one $-$ index), which results in a PCC rate that depends upon whether the signal or idler detector clicks first (Shwartz *et al.*, 2012).

2. Simulations of typical PDC signals

Figures 35(d)–35(k) compare both susceptibilities calculated for a typical KTP crystal represented by a degenerate three-level system with parameters from Wu *et al.* (1986) and D'auria *et al.* (2008). Figures 35(f), 35(h), and 35(j) show that far from resonances ($\omega_i \neq \omega_{eg}$, $\omega_p \neq \omega_{gf}$) the semiclassical and quantum susceptibilities coincide and depend weakly on the frequencies ω_p and ω_i. This is the regime covered by the semiclassical theory, where the susceptibility is assumed to be a constant. Similar agreement between classical and quantum susceptibilities can be observed if the pump is resonant with two-photon transition $\omega_p \simeq \omega_{gf}$ but the idler is off resonance $\omega_i \neq \omega_{eg}$ [Figs. 35(g), 35(h), and 35(k)]. However, close to resonance [Figs. 35(d) and 35(e)] the two susceptibilities are very different. The semiclassical susceptibility $\chi^{(2)}_{+--}$ vanishes at resonance, where the quantum susceptibility $\chi^{(2)}_{LL-}$ reaches its maximum.

To put the present ideas into a more practical perspective we show in Fig. 36 the PCC rate for a monochromatic pump ω_p and mean signal detector frequency $\bar{\omega}_s$. The quantum theory yields one strong resonant peak at $\bar{\omega}_s = \omega_p - \omega_{eg}$ and two weak peaks at $\omega_p = \omega_{gf}$ and $\bar{\omega}_s = \omega_{eg}$ if the idler detector is resonant with the intermediate state $|e\rangle$: $\bar{\omega}_i = \omega_{eg}$ [Fig. 36(a)]. However, if we tune the idler detector to a different frequency, for instance $\omega_{eg} - \bar{\omega}_i = 2$ GHz, there is an additional peak at $\bar{\omega}_s = \omega_p - \bar{\omega}_i$ [Fig. 36(b)]. Similarly, when the pump consists of two monochromatic beams $\omega_p \neq \omega'_p$ [Figs. 36(c) and 36(d)] the number of peaks are doubled compare to a single monochromatic pump. Clearly, one can reproduce the exact same peaks for ω'_p as for ω_p.

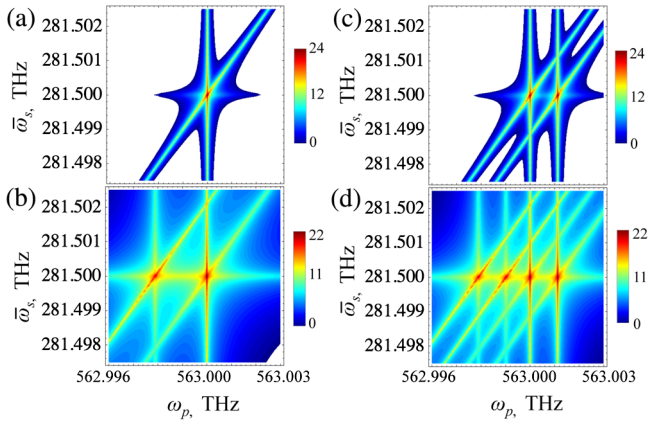

FIG. 36. Left column: Two-dimensional PCC rate (log scale in arb. units) calculated using quantum theory Eq. (175) assuming a single monochromatic pump with frequency ω_p. (a) Idler detector resonant with intermediate level $\bar{\omega}_i = \omega_{eg} = 282$ THz, while (b) $\omega_{eg} - \bar{\omega}_i = 2$ GHz. Right column: The same as the left but for a pump made out of two monochromatic beams with frequencies $\omega_p - \omega'_p = 2 \times 10^{-6}\omega_p$.

3. Spectral diffusion

Spectral diffusion (SD) which results from the stochastic modulation of frequencies can manifest itself either as discrete random jumps of the emission frequency (Siyushev *et al.*, 2009; Santori *et al.*, 2010; Walden-Newman, Sarpkaya, and Strauf, 2012) or as a broadening of a hole burned in the spectrum by a narrow-band pulse (Xie and Trautman, 1998; Wagie and Geissinger, 2012). We focus on the latter case assuming that the electronic states of molecule $\alpha = a, b$ are coupled to a harmonic bath described by the Hamiltonian $\hat{H}^\alpha_B = \sum_k \hbar\omega_k(\hat{a}^{\dagger\alpha}_k \hat{a}^\alpha_k + 1/2)$ [see Fig. 38(b)]. The bath perturbs the energy of state ν. This is represented by the Hamiltonian

$$\hat{H}^\alpha_\nu = \hbar^{-1}\langle\nu_\alpha|\hat{H}|\nu_\alpha\rangle = \epsilon_{\nu_\alpha} + \hat{q}_{\nu\alpha} + \hat{H}^\alpha_B, \tag{269}$$

where $\hat{q}_\nu$ is a collective bath coordinate

$$\hat{q}_{\nu\alpha} = \hbar^{-1}\langle\nu_\alpha|\hat{H}_{SB}|\nu_\alpha\rangle = \sum_k d_{\nu_\alpha\nu_\alpha,k}(\hat{a}^\dagger_k + \hat{a}_k), \tag{270}$$

$d_{mn,k}$ represents bath-induced fluctuations of the transition energies ($m = n$) and the intermolecular coupling ($m \neq n$). We define the line-shape function

$$\begin{aligned} g_\alpha(t) &\equiv g_{\nu_\alpha\nu'_\alpha}(t) \\ &= \int \frac{d\omega}{2\pi}\frac{C''_{\nu_\alpha\nu'_\alpha}(\omega)}{\omega^2} \\ &\quad\times\left[\coth\left(\frac{\beta\hbar\omega}{2}\right)(1-\cos\omega t) + i\sin\omega t - i\omega t\right], \end{aligned} \tag{271}$$

where the bath spectral density is given by

$$C''_{\nu_\alpha\nu'_\alpha}(\omega) = \frac{1}{2}\int_0^\infty dt e^{i\omega t}\langle[\hat{q}_{\nu\alpha}(t), \hat{q}_{\nu'\alpha}(0)]\rangle, \tag{272}$$

$\beta = k_B T$ with k_B being the Boltzmann constant and T is the ambient temperature. We use the overdamped Brownian oscillator model for the spectral density, assuming a single nuclear coordinate ($\nu_\alpha = \nu'_\alpha$)

$$C''_{\nu_\alpha\nu_\alpha}(\omega) = 2\lambda_\alpha\frac{\omega\Lambda_\alpha}{\omega^2 + \Lambda^2_\alpha}, \tag{273}$$

where Λ_α is the fluctuation relaxation rate and λ_α is the system-bath coupling strength. The corresponding line-shape function then depends on two parameters: the reorganization energy λ_α denoting the strength of the coupling to the bath and the fluctuation relaxation rate $\Lambda_\alpha = \sqrt{2\lambda_\alpha k_B T/\hbar}$. In the high-temperature limit $k_B T \gg \hbar\Lambda_\alpha$ we have

$$g_\alpha(t) = \left(\frac{\Delta^2_\alpha}{\Lambda^2_\alpha} - i\frac{\lambda_\alpha}{\Lambda_\alpha}\right)(e^{-\Lambda_\alpha t} + \Lambda_\alpha t - 1). \tag{274}$$

For a given magnitude of fluctuations Δ_α, $\alpha = a, b$ the FWHM of the absorption linewidth reads (Mukamel, 1995)

$$\Gamma_\alpha = \frac{2.355 + 1.76(\Lambda_\alpha/\Delta_\alpha)}{1 + 0.85(\Lambda_\alpha/\Delta_\alpha) + 0.88(\Lambda_\alpha/\Delta_\alpha)^2}\Delta_\alpha. \tag{275}$$

The absorption and emission line-shape functions for a pair of molecules obtained in the slow nuclear dynamics limit $\Lambda_\alpha \ll \Delta_\alpha$ are given by (Mukamel, 1995)

$$\sigma_A(\omega) = \sum_{\alpha=a,b} (2\pi\Delta_\alpha)^{-1/2} e^{-(\omega-\omega_\alpha^0-\lambda_\alpha)^2/2\Delta_\alpha^2}, \quad (276)$$

$$\sigma_F(\omega) = \sum_{\alpha=a,b} (2\pi\Delta_\alpha)^{-1/2} e^{-(\omega-\omega_\alpha^0+\lambda_\alpha)^2/2\Delta_\alpha^2}, \quad (277)$$

where $2\lambda_\alpha$ is the Stokes shift and $\Delta_\alpha = \sqrt{2\lambda_\alpha k_B T/\hbar}$ is a linewidth parameter. Together with the relaxation rate Λ_α [see Eq. (274)] these parameters completely describe the SD model and govern the evolution of the emission linewidth between the initial time given by Eq. (276) [see Fig. 37(a)] and the long time given by Eq. (277) [see Fig. 37(b)].

The corresponding four-point matter correlation function may be obtained by the second-order cumulant expansion (Mukamel, 1995)

$$F_\alpha(t_1,t_2,t_3,t_4) = |\mu_\alpha|^4 e^{-i\omega_\alpha(t_1-t_2+t_3-t_4)} e^{\Phi_\alpha(t_1,t_2,t_3,t_4)}, \quad (278)$$

where $\omega_\alpha \equiv \omega_{e_\alpha} - \omega_{g_\alpha}$ is the absorption frequency and $\Phi_\alpha(t_1,t_2,t_3,t_4)$ is the four-point line-shape function $\Phi_\alpha(t_1,t_2,t_3,t_4) = -g_\alpha(t_1-t_2) - g_\alpha(t_3-t_4) + g_\alpha(t_1-t_3) - g_\alpha(t_2-t_3) + g_\alpha(t_2-t_4) - g_\alpha(t_1-t_4)$.

We focus on the SD in the "hole burning" limit (HBL) which holds under two conditions: First, the dephasing is much faster than the fluctuation time scale, i.e., $t_k' \ll \Lambda_\alpha^{-1}$, $k = 1, 2, 3, 4$. Second, if excitation pulse duration σ_p^{-1} and the inverse spectral $(\sigma_\omega^j)^{-1}$, and temporal $(\sigma_T^j)^{-1}$, $j = r, s$ gate bandwidths are much shorter than the fluctuation time scales, one may neglect the dynamics during the delay between population evolution and its detection. This parameter regime is relevant to crystals which store information in the form of reversible notches that are created in their optical absorption spectra at specific frequencies. Long storage times (Longdell *et al.*, 2005), high efficiencies (Hedges *et al.*, 2010), and many photon qubits in each crystal (Shahriar *et al.*, 2002) can be achieved in this limit. The HBL limit is natural for long-term quantum memories where entanglement is achieved with telecom photons, proving the possibility of quantum internet (Clausen *et al.*, 2011; Saglamyurek *et al.*, 2011).

Time-and-frequency-resolved fluorescence is the simplest way to observe SD. The molecular transition frequency is coupled linearly to an overdamped Brownian oscillator that represents the bath [see Fig. 38(b)]. This fluorescence signal given by Eq. (284) is depicted as a series of the snapshot spectra at different times for molecule a in Fig. 37(c). It shows a time-dependent frequency redshift $\tilde{\omega}_a(t)$ and time-dependent spectral broadening given by $\tilde{\sigma}_{a0}(t)$. Initially $\tilde{\omega}_a(0) = \omega_a^0 + \lambda_a$, whereas at long times $\tilde{\omega}_a(\infty) = \omega_a^0 - \lambda_a$, where $2\lambda_\alpha$ is the Stokes shift. The same for molecule b is shown in Fig. 37(d). Because of the different reorganization energies λ_a, λ_b and relaxation rates Λ_a, Λ_b the Stokes shift dynamics and dispersion are different. Even when the absorption frequencies are the same $\omega_a = \omega_b$, the fluorescence can show a different profile due to SD. This affects the distinguishability of the emitted photons as demonstrated later.

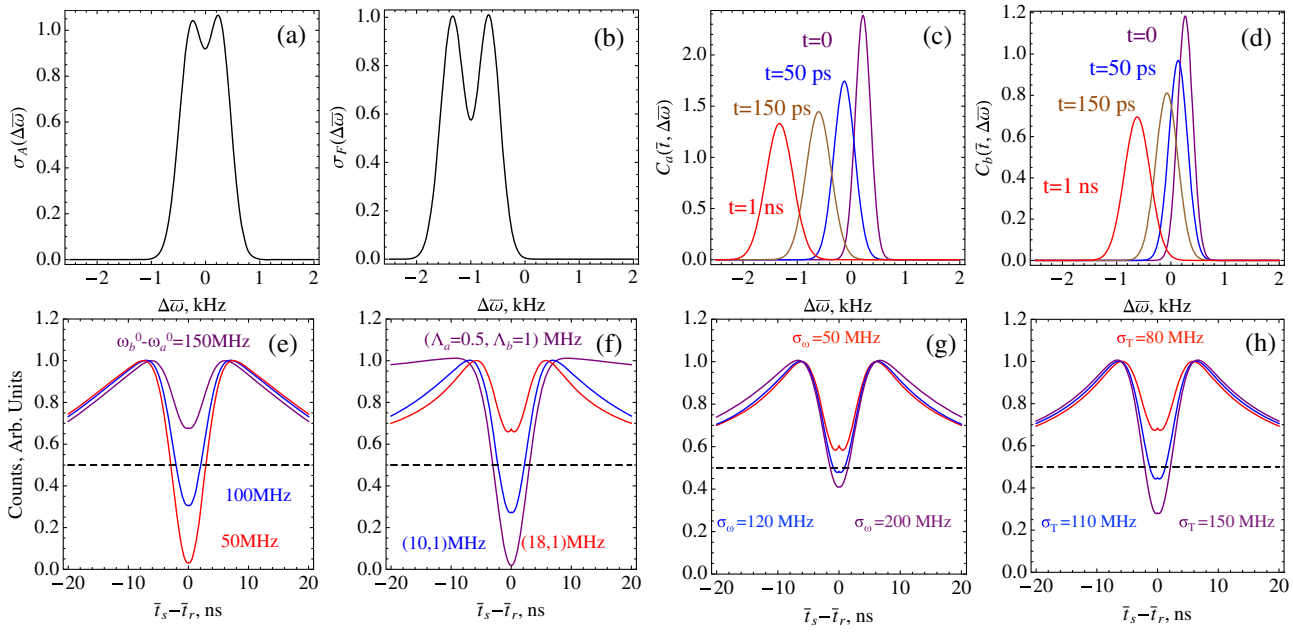

FIG. 37. Top row: (a) Absorption (276) and (b) fluorescence (277) line shapes vs displaced frequency $\Delta\bar{\omega} = \omega - \frac{1}{2}(\omega_a + \omega_b)$. Frequency dispersed time-resolved fluorescence (284) displayed as a snapshot spectra for molecule (c) (a) and (d) (b). Bottom row: (e) PCC for different transition energies of molecules excited at $\omega_p = \omega_b^0 + \lambda_b$, (f) PCC for different values of the SD time scale Λ_a and Λ_b and fixed linewidth Γ_a, Γ_b according to Eq. (275), PCC for different frequency gate bandwidths at (g) fixed time gate bandwidth $\sigma_T = 100$ MHz and for (h) different time gate bandwidths at fixed frequency gate bandwidth $\sigma_\omega = 100$ MHz. Molecules have distinct SD time scales $\Lambda_a = 15$ MHz, $\Lambda_b = 1$ MHz, and $\omega_b^0 - \omega_a^0 = 1$ MHz.

J. Generation and entanglement control of photons produced by two independent molecules by time-and-frequency-gated photon coincidence counting

As discussed in Sec. II, entangled photons can be produced by a large variety of $\chi^{(2)}$ processes. Alternatively, photons can be entangled by simultaneous excitation of two remote molecules and mixing the spontaneously emitted photons on the beam splitter. This entangled-photon generation scheme is suitable, e.g., for spectroscopic studies of single molecules by single photons discussed next. The manipulation of single-photon interference by appropriate time-and-frequency gating discussed next is presented in detail in Dorfman and Mukamel (2014a). The generated entangled-photon pair can be used in logical operations based on optical measurements that utilize interference between indistinguishable photons.

We examine photon interference in the setup shown in Fig. 38(a). A pair of photons is generated by two remote two-level molecules a and b with ground g_α and excited state e_α, $\alpha = a, b$. These photons then enter a beam splitter and are subsequently registered by time-and-frequency-gated detectors s and r. There are three possible outcomes: two photons registered in detector s, two photons registered in r, or coincidence where one photon is detected in each. The ratios of these outcomes reflect the photon Bose statistics and depend on their degree of indistinguishability. If the two photons incident on the beam splitter are indistinguishable, the PCC signal vanishes. This causes the Hong-Ou-Mandel (HOM) dip when varying the position of the beam splitter which causes delay T between the two photons. The normalized PCC rate varies between 1 for completely distinguishable photons (large T) and 0 when they are totally indistinguishable ($T = 0$). For classical fields and 50:50 beam splitter the PCC rate may not be lower than $1/2$. We denote the photons as indistinguishable (distinguishable) if the PCC rate is smaller (larger) than $1/2$.

PCC is typically measured by time-resolved detection (Gerry and Knight, 2005; Glauber, 2007). Originally performed with entangled photons generated by PDC (Hong, Ou, and Mandel, 1987) the shape of the dip versus delay is usually related to the two-photon state envelope which is governed by an effective PDC Hamiltonian (Dorfman and Mukamel, 2012b). Bath effects can become important for remote emitters, and have been introduced phenomenologically (Lettow *et al.*, 2010). We present a microscopic description of PCC with bath fluctuations by formulating the signal in the joint field-matter space measured by simultaneous time-and-frequency-resolved detection. This complex measurement can be achieved using a high-speed photodiode which converts a fast optical signal into a fast electric current, fast oscilloscopes to observe the waveform, wide bandwidth spectrum analyzers, and other elements. Short pulse characterization using a time-frequency map such as frequency-resolved optical gating (FROG) (Trebino, 2000) and spectral phase interferometry for direct-field reconstruction (SPIDER) (Dorrer *et al.*, 1999) are well established tools for ultrafast metrology (Wollenhaupt, Assion, and Baumert, 2007; Walmsley and Dorrer, 2009). Extending these techniques to a single-photon time-and-frequency-resolved detection is challenging and may be achieved if combined with on-chip tunable detectors (Gustavsson *et al.*, 2007) or upconversion processes (Gu *et al.*, 2010; Ma *et al.*, 2011).

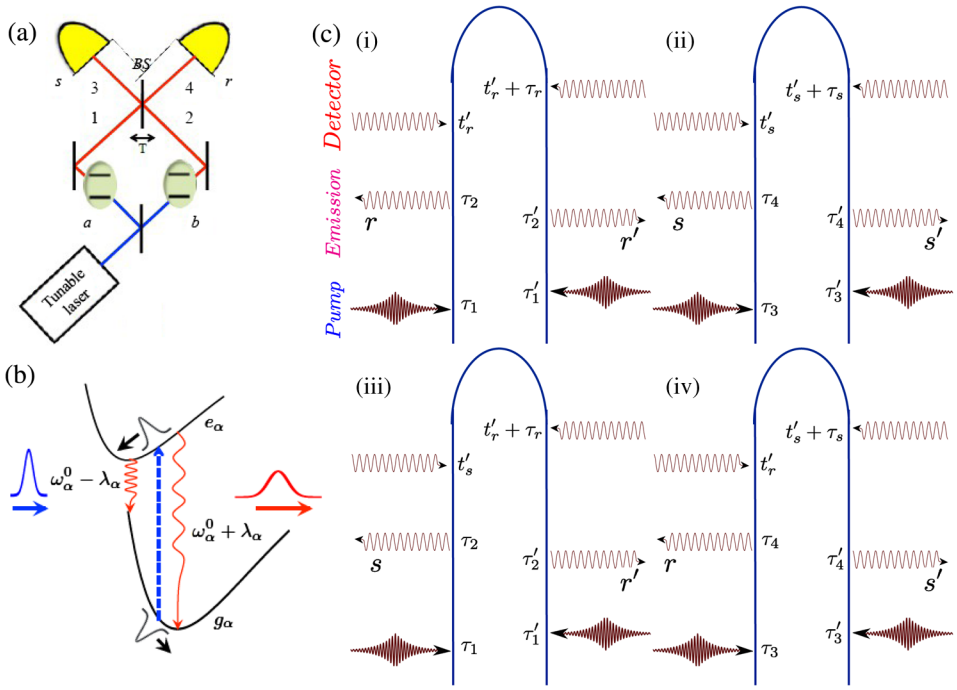

FIG. 38. Time-and-frequency-resolved measurement of PCC with spectral diffusion. (a) Schematic of the PCC experiment with two indistinguishable source molecules, and (b) the two-level model of the molecule with SD used in our simulations. (c) Loop diagrams for the PCC rate of emitted photons from two molecules (for diagram rules see Appendix A). The left and right branches of each diagram represent interactions with ket and bra of the density matrix, respectively. Field-matter interactions with the pump pulses p_1 and p_2 (blue), spontaneously emitted s, s', r, and r' photons (red) and detectors (brown).

1. PCC of single photons generated by two remote emitters

The time-and-frequency-gated PCC signal is described by the two pairs of loop diagrams shown in Fig. 38(c). Each loop represents one molecule (a or b) which undergoes four field-matter interactions and each detector interacts twice with the field. Figure 38(c) shows that after interacting with the pump (with its ket) at time t_2 molecule a evolves in the coherence $\rho_{e_a g_a}$ during time interval t_2'. The second interaction of the pump with the bra then brings the molecule into a population state $\rho_{e_a e_a}$ which evolves during interval t_1 until the first interaction with spontaneous emission mode occurs with the ket. The molecule then evolves into the coherence $\rho_{g_a e_a}$ during t_1' until the second bra interaction of spontaneous mode. During population and coherence periods, the characteristic time scale of the dynamics is governed by population relaxation and dephasing, respectively.

The relevant single-particle information for molecule α is given by the four-point dipole correlation function $F_\alpha(t_1,t_2,t_3,t_4)=\langle V_{ge}(t_1)V_{eg}^\dagger(t_2)V_{ge}(t_3)V_{eg}^\dagger(t_4)\rangle_\alpha$, where V and $V^\dagger$ are the lowering and raising dipole transition operators, respectively. Diagrams i, ii (two upper diagrams), and iii and iv (bottom diagrams) in Fig. 38(c) represent non-interfering terms given by a product of two independent fluorescence contributions of the individual molecules. Diagrams ii represent an interference in the joint space of the two molecules and involve the interference of eight quantum pathways (four with the bra and four with the ket) with different time orderings. Each molecule creates a coherence in the field between states with zero and one photon $|0\rangle\langle 1|$ and $|1\rangle\langle 0|$. By combining the contributions from a pair of molecules we obtain a photon population $|1\rangle\langle 1|$ that can be detected (Dorfman and Mukamel, 2012a, 2012b). For a pair of identical molecules, the beam splitter destroys the pathway information making the molecules indistinguishable and giving rise to quantum interference.

The PCC signal (175) (Dorfman and Mukamel, 2014a) has been calculated for the output fields E_3 and E_4 ($i=3$, $s=4$) of the beam splitter [see Fig. 38(a)]. The fields in the output 3,4 and input 1,2 ports of the 50:50 beam splitter are related by

$$E_3(t)=\frac{E_1(t)-iE_2(t+T)}{\sqrt{2}},\quad E_4(t)=\frac{E_2(t)-iE_1(t-T)}{\sqrt{2}}, \tag{279}$$

where $\pm cT$ is a small difference of path length in the two arms. Taking into account that Eq. (175) should be modified to include the beam splitter position and absorb it into the gating spectrograms, the time-and-frequency-resolved PCC in this case is given by

$$\begin{aligned}R_c^{34}&(\Gamma_r,\Gamma_s;T)\\&=\frac{1}{(2\pi)^2}\int_{-\infty}^{\infty}d^2\Gamma_r'd^2\Gamma_s'\\&\quad\times[W_D^{(r)}(\Gamma_r,\Gamma_r';0)W_D^{(s)}(\Gamma_s,\Gamma_s',0)R_B^{(i)}(\Gamma_r',\Gamma_s')\\&\quad+W_D^{(r)}(\Gamma_r,\Gamma_r';-T)W_D^{(s)}(\Gamma_s,\Gamma_s',T)R_B^{(ii)}(\Gamma_r',\Gamma_s')]\\&\quad+(s\leftrightarrow r,T\leftrightarrow -T).\end{aligned} \tag{280}$$

Here $\Gamma_j'=\{t_j',\omega_j'\}$ represents the set of parameters of the matter plus field incident on the detector $j=r,\ s$. Equation (280) is given by the spectral and temporal overlaps of the Wigner spectrograms of detectors $W_D^{(s)}$, $W_D^{(r)}$ and bare signal pathways $R_B^{(i)}$ and $R_B^{(ii)}$ given by

$$\begin{aligned}R_B^{(i)}(t_s',\omega_s';t_r',\omega_r')&=\sum_{u,u'}\sum_{v,v'}\int_{-\infty}^{\infty}d\tau_s d\tau_r e^{-i\omega_s'\tau_s-i\omega_r'\tau_r}\\&\quad\times\langle\mathcal{T}\hat{E}_{u'R}^\dagger(t_s'+\tau_s,r_b)\\&\quad\times\hat{E}_{v'R}^\dagger(t_r'+\tau_r,r_a)\hat{E}_{vL}(t_r',r_a)\\&\quad\times\hat{E}_{uL}(t_s',r_b)e^{-i/\hbar\int_{-\infty}^{\infty}\hat{H}_-'(T)dT}\rangle,\end{aligned} \tag{281}$$

$$\begin{aligned}R_B^{(ii)}(t_s',\omega_s';t_r',\omega_r')&=-\sum_{u,u'}\sum_{v,v'}\int_{-\infty}^{\infty}d\tau_s d\tau_r e^{-i\omega_s'\tau_s-i\omega_r'\tau_r}\\&\quad\times\langle\mathcal{T}\hat{E}_{u'R}^\dagger(t_s'+\tau_s,r_b)\\&\quad\times\hat{E}_{v'R}^\dagger(t_r'+\tau_r,r_a)\hat{E}_{uL}(t_s',r_a)\\&\quad\times\hat{E}_{vL}(t_r',r_b)e^{-(i/\hbar)\int_{-\infty}^{\infty}\hat{H}_-'(T)dT}\rangle.\end{aligned} \tag{282}$$

Equations (281) and (282) contain all relevant field-matter interactions. The modified expressions for the gating spectrograms that include delay T are given by Dorfman and Mukamel (2014a).

2. Time-and-frequency-gated PCC

Under SD and HBL conditions the PCC signal (175) is given by

$$\begin{aligned}R_c^{34}&(\Gamma_r,\Gamma_s;T)\\&=R_0C_a^r(\Gamma_r)C_b^s(\Gamma_s)\\&\quad\times\left[1-\frac{I_a^r(\Gamma_r,\bar{t}_s,-T)I_b^s(\bar{t}_r,\Gamma_s,T)}{C_a^r(\Gamma_r)C_b^s(\Gamma_s)}\right.\\&\quad\left.\times\cos[U(\Gamma_r,\Gamma_s;T)]e^{-\tilde{\Gamma}(\bar{t}_s-\bar{t}_r)}\right]\\&\quad+(a\leftrightarrow b,T\leftrightarrow -T),\end{aligned} \tag{283}$$

where expressions in the last line represent permutation of the molecules a and b and $\Gamma_j=\{\bar{t}_j,\bar{\omega}_j\}$ represents a set of gating parameters for the detector $j=r,\ s$. $C_\alpha(\Gamma=\{t,\omega\})$ is the time-and-frequency-resolved fluorescence of molecule $\alpha=a$, b corresponding to diagram i in Fig. 38(c):

$$C_\alpha^j(t,\omega)=C_{\alpha 0}^j(t)e^{-(\omega_p-\omega_\alpha^0-\lambda_a)^2/2\tilde{\sigma}_{p\alpha}^2[\omega-\tilde{\omega}_\alpha(t)]^2/2\tilde{\sigma}_\alpha^{j2}(t)}, \tag{284}$$

where $\omega_\alpha^0=\omega_\alpha-\lambda_\alpha$ is the mean absorption and fluorescence frequency. $I_\alpha^j(\Gamma_1,t_2,\tau)$ and $I_\alpha^j(t_1,\Gamma_2,\tau)$ with $t_1<t_2$ is the interference contribution $\alpha=a$, b, $j=r$, s corresponding to diagram ii in Fig. 38(c)

$$\begin{aligned}I_\alpha^j(\Gamma_1,t_2,\tau)&=I_{\alpha 0}^j(t_1,t_2)e^{-\omega_{ab}^2/4\sigma_T^{j2}-(1/4)\sigma_{\tau a}^j(t_1,t_2)^2\tau^2}\\&\quad\times e^{-[\omega_p-\omega_{p\alpha}^j(t_1,t_2)]^2/2\sigma_{p\alpha}^{j2}(t_1,t_2)}e^{-[\omega_1-\omega_\alpha^j(t_1,t_2)]^2/2\sigma_\alpha^{j2}(t_1,t_2)},\end{aligned} \tag{285}$$

$U(\Gamma_r,\Gamma_s;\tau)=\omega_a(\bar{t}_s-\bar{t}_r)+\omega_{\tau a}^r(\bar{t}_r,\bar{t}_s,\bar{\omega}_r)\tau+(\lambda_a/\Lambda_a)\{2[F_a(\bar{t}_r)-F_a(\bar{t}_s)]+F_a(\bar{t}_s-\bar{t}_r)\}-(a\leftrightarrow b,r\leftrightarrow s)$, $\tilde{\Gamma}(t)=\sum_{\alpha=a,b}(\Delta_\alpha^2/\Lambda_\alpha^2)\times F_\alpha(t)$ with $F_\alpha(t)=e^{-\Lambda_\alpha t}+\Lambda_\alpha t-1$, $\alpha=a$, b and all the

remaining parameters are listed in Dorfman and Mukamel (2014a). The contribution of Eq. (284) is represented by an amplitude square coming from each molecule in the presence of fluctuations. The interference term (285) generally cannot be recast as a product of two amplitudes (Mukamel and Rahav, 2010). Equations (283)–(285) are simulated below using the typical parameters of the two-photon interference experiments (Santori *et al.*, 2002; Coolen *et al.*, 2008; Lettow *et al.*, 2010; Patel *et al.*, 2010; Trebbia, Tamarat, and Lounis, 2010; Ates *et al.*, 2012; Bernien *et al.*, 2012; Sanaka *et al.*, 2012; Sipahigil *et al.*, 2012; Wolters *et al.*, 2013).

3. Signatures of gating and spectral diffusion in the HOM dip

Photon indistinguishability depends on the molecular transition frequencies. Figure 37(e) shows that for fixed time-and-frequency gate bandwidths σ_ω^j and σ_T^j, $j = r,\ s$ the photons are distinguishabe as long as the transition energy offset $\omega_b^0 - \omega_a^0$ is larger than the gate bandwidth and are indistinguishable otherwise. The SD time scale is a key parameter affecting the degree of indistinguishability. Using Eq. (275) we fixed the absorption linewidth Γ_α and varied Λ_α and Δ_α. The PCC signal (283) depicted in Fig. 37(f) shows that, if the molecules have nearly degenerate transition energy offset for slower fluctuations, the photons are indistinguishable. Increasing the SD rate of one of the molecules increases the photon distinguishability when both time-and-frequency gates are broader than the difference in transition frequencies.

We further illustrate the effect of frequency-and-time gating on spectral diffusion. Figure 37(g) shows that if two molecules have different SD time scales and the frequency gate bandwidth is narrow the photons are rendered distinguishable and the HOM dip is 0.6. By increasing the σ_ω the photons become indistinguishable and the HOM dip is 0.48 for $\sigma_\omega = 120$ MHz and 0.35 for $\sigma_\omega = 200$ MHz. In all three cases we kept the time gate fixed. Alternatively we changed the time gate bandwidth while keeping the frequency gate fixed. Figure 37(h) shows that initially indistinguishable photons at $\sigma_T = 80$ MHz with the HOM dip 0.675 become indistinguishable at $\sigma_T = 110$ MHz with the HOM dip 0.45 and at $\sigma_T = 150$ MHz with the HOM dip 0.275. Thus, if the presence of the bath erodes the HOM dip the manipulation of the detection gating allows one to preserve the quantum interference.

V. SUMMARY AND OUTLOOK

The term quantum spectroscopy broadly refers to spectroscopy techniques that make use of the quantum nature of light. Photon counting studies obviously belong to this category. Studies that detect the signal field such as heterodyne detection or fluorescence are obtained by expanding the signals in powers of the field operators. These depend on multipoint correlation functions of the incoming fields. Spectroscopy is classical if all fields are in a coherent state and the observable is given by normally ordered products of field amplitudes. The appearance of field correlation functions rather than products field amplitudes may arise from stochastic classical fields (Asaka *et al.*, 1984; Beach and Hartmann, 1984; Morita and Yajima, 1984; Turner *et al.*, 2013) or may reflect genuine quantum field effects. These should be sorted out.

Another important aspect of quantum spectroscopy, which we had touched on only briefly in Sec. IV.B, concerns the nonclassical fluctuations of quantum light and their exploitation as spectroscopic tools (Benatti, Floreanini, and Marzolino, 2010; Giovannetti, Lloyd, and Maccone, 2011). These may also lead to novel features in nonlinear optical signals (López Carreño *et al.*, 2015).

We now briefly survey the main features of quantum spectroscopy. First, the unusual time and frequency windows for homodyne, heterodyne, and fluorescence detection arising due to the quantum nature of the light generation resulting in the enhanced resolution of the signals not accessible by classical light. Second, photon counting and interferometric detection schemes constitute a class of multidimensional signals that are based on detection and manipulation of single photons and are parametrized by the emitted photons rather than by the incoming fields. Third, the quantum nature of light manifests in collective effects in many-body systems by projecting entanglement of the field to matter. This allows one to prepare and control higher excited states in molecular aggregates, access dark multiparticle states, etc. Fourth, due to the lack of nonlinear fluctuation-dissipation relations, quantum light can manifest new combinations of field and corresponding matter correlation functions not governed by semiclassical response functions such as in parametric down-conversion, sum- or difference-frequency generation, two-photon-induced fluorescence, etc. Finally, pulse shaping techniques that have been recently scaled down to single-photon level provide an additional tool for multidimensional measurements using delay scanning protocols not available for classical laser experiments.

The potential merits of quantum spectroscopy may be traced back to the strong time-frequency correlations inherent to quantum light and the backaction of the interaction events onto the quantum field's state. Combination of the two effects leads to the excitation of distinct wave packets, which can be designed to enhance or suppress selected features of the resulting optical signals.

We have described nonlinear optical signals in terms of convolutions of multitime correlation functions of the field and the matter. This approach naturally connects to the established framework of quantum optics, where field correlation functions are analyzed (Glauber, 1963) with nonlinear laser spectroscopy, which investigates the information content of matter correlation functions. As such, it provides a flexible platform to explore quantum light interaction with complex systems well beyond spectroscopic applications. This could include coherent control with quantum light (Schlawin and Buchleitner, 2015; Wu *et al.*, 2015), or the manipulation of ultracold atoms with light (Mekhov and Ritsch, 2012). Entangled quantum states with higher photon numbers (Shalm *et al.*, 2013) promise access to the $\chi^{(5)}$ susceptibility and its additional information content. The combination of quantum light with strong coupling to intense fields in optical cavities (Hutchison *et al.*, 2012; Schwartz *et al.*, 2013; Herrera *et al.*, 2014) may result in new coherent control techniques of chemical reactions.

ACKNOWLEDGMENTS

We gratefully acknowledge the support of the National Science Foundation through Grant No. CHE-1361516, the Chemical Sciences, Geosciences and Biosciences Division, Office of Basic Energy Sciences, Office of Science, U.S. Department of Energy. K. D. was supported by a DOE grant. We also thank the support and stimulating environment at FRIAS (Freiburg Institute for Advanced Studies). F. S. thanks the German National Academic Foundation and European Research Council under the European Unions Seventh Framework Programme (FP7/2007-2013)/ERC Grant Agreement No. 319286 Q-MAC.

APPENDIX A: DIAGRAM CONSTRUCTION

In leading (fourth-)order perturbation theory, the population of a two-excitation state f is given by

$$p_{\mathrm{f}}(t;\Gamma) = \left(-\frac{i}{\hbar}\right)^4 \int_{t_0}^{t} d\tau_4 \int_{t_0}^{\tau_4} d\tau_3 \int_{t_0}^{\tau_3} d\tau_2 \int_{t_0}^{\tau_2} d\tau_1 \times \langle P_f(t) H_{\mathrm{int},-}(\tau_4) H_{\mathrm{int},-}(\tau_3) \times H_{\mathrm{int},-}(\tau_2) H_{\mathrm{int},-}(\tau_1) \varrho(t_0)\rangle, \tag{A1}$$

where $P_f(t) = |f(t)\rangle\langle f(t)|$ is the projector onto the final state, the interaction Hamiltonian H_{int} is as given in Eq. (7), and Γ denotes the set of control parameters in the light field.

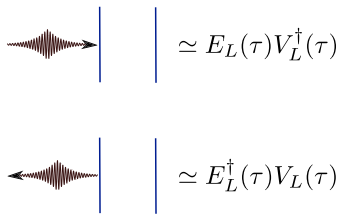

FIG. 39. Diagram construction in a quantum electrodynamics (QED) formulation: The vertical blue lines indicate the evolution of the matter density matrix. An arrow pointing toward (away from) it corresponds to a matter excitation $V^\dagger(\tau)$ [deexcitation $V(\tau)$], which is accompanied by a photon annihilation $E(\tau)$ [creation $E^\dagger(\tau)$]. In the Liouville space formulation, interactions on the left side represent left superoperators (1), and interactions on the right side represent right superoperators (2).

Equation (A1) contains $4^4 = 256$ terms, of which only very few contribute to the signal. These contributions can be conveniently found using a diagrammatic representation. Its basic building blocks are shown in Fig. 39: The evolution of both the bra and the ket sides of the density matrix in Eq. (10) [$\langle\psi|$ and $|\psi\rangle$ in Eq. (17)] are represented by vertical blue lines, and sample excitations (deexcitations) are represented by arrows pointing toward (away from) the density matrix.

1. Loop diagrams

The following rules are used to construct the field and matter correlation function from the diagrams (see Fig. 40) (Marx, Harbola, and Mukamel, 2008):

(1) Time runs along the loop clockwise from bottom left to bottom right.
(2) The left branch of the loop represents the ket, and the right represents the bra.
(3) Each interaction with a field mode is represented by an arrow line on either the right (R operators) or the left (L operators).
(4) The field is marked by dressing the lines with arrows, where an arrow pointing to the right (left) represents the field annihilation (creation) operator $E_\alpha(t)$ [$E_\alpha^\dagger(t)$].
(5) Within the RWA, each interaction with the field annihilates the photon $E_\alpha(t)$ and is accompanied by applying the operator $V_\alpha^\dagger(t)$, which leads to excitation of the state represented by the ket and deexcitation of the state represented by the bra, respectively. Arrows pointing inward (i.e., pointing to the right on the ket and to the left on the bra) consequently cause absorption of a photon by exciting the system, whereas arrows pointing outward (i.e., pointing to the left on the bra and to the right on the ket) represent deexcitation of the system by photon emission.
(6) The observation time t is fixed and is always the last. As a convention, it is chosen to occur from the left. This can always be achieved by a reflection of all interactions through the center line between the ket and the bra, which corresponds to taking the complex conjugate of the original correlation function.
(7) The loop translates into an alternating product of interactions (arrows) and periods of free evolutions (vertical solid lines) along the loop.

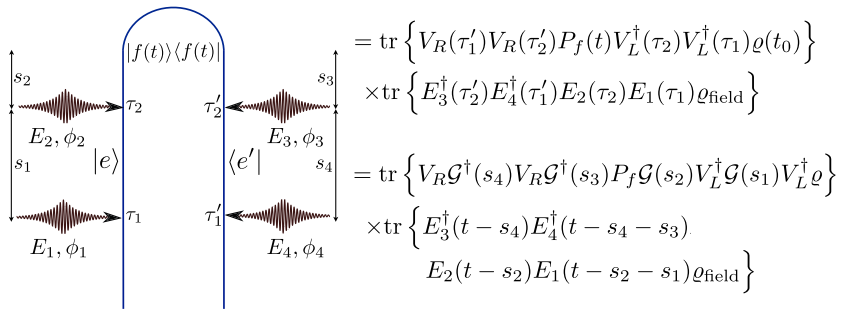

FIG. 40. Loop diagram construction in a QED formulation: Using the diagram rules given in the text, the diagram translates into the Heisenberg picture expression (top) or the Schrödinger picture expression (bottom). The corresponding field correlation functions are reordered as in the loop diagram.

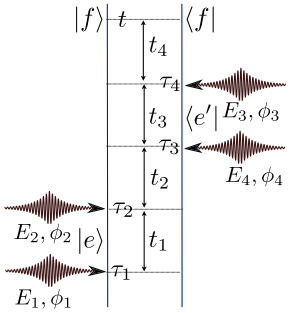

$$= \mathrm{tr}\left\{P_f(t)V_R(\tau_4)V_R(\tau_3)V_L^\dagger(\tau_2)V_L^\dagger(\tau_1)\varrho(t_0)\right\}$$
$$\times \mathrm{tr}\left\{E_3^\dagger(\tau_4)E_4^\dagger(\tau_3)E_2(\tau_2)E_1(\tau_1)\varrho_{\mathrm{field}}(t_0)\right\}$$
$$= \mathrm{tr}\left\{P_f\mathcal{G}(t_4)V_R\mathcal{G}(t_3)V_R\mathcal{G}(t_2)V_L^\dagger\mathcal{G}(t_1)V_L^\dagger\varrho\right\}$$
$$\times \mathrm{tr}\left\{E_3^\dagger(t-t_4)E_4^\dagger(t-t_4-t_3)\right.$$
$$\left.E_2(t-t_4-t_3-t_2)E_1(t-t_4-t_3-t_2-t_1)\varrho_{\mathrm{field}}\right\}$$

FIG. 41. Ladder diagram construction in a QED formulation: Using the diagram rules given in the text, the diagram translates into the Heisenberg picture expression (top) or the Schrödinger picture expression (bottom). The corresponding field correlation functions are reordered as in the loop diagram.

(8) Since the loop time goes clockwise along the loop, periods of free evolution on the left branch amount to propagating forward in real time with the propagator given by the retarded Green's function G, whereas evolution on the right branch corresponds to backward propagation (advanced Green's function $G^\dagger$).
(9) The frequency arguments of the various propagators are cumulative, i.e., they are given by the sum of all "earlier" interactions along the loop. Additionally, the ground state frequency is added to all arguments of the propagators.
(10) The Fourier transform of the time-domain propagators adds an additional factor of $i(-i)$ for each retarded (advanced) propagator.
(11) The overall sign of the SNGF is given by $(-1)^{N_R}$, where N_R stands for the number of R superoperators.

2. Ladder diagrams

The same rules may be applied to evaluate ladder diagrams, with the exception of rule 1, which reads (see Fig. 41)
(1) Time runs from bottom to top.

APPENDIX B: ANALYTICAL EXPRESSIONS FOR THE SCHMIDT DECOMPOSITION

Here we point out how the Schmidt decomposition (34) may be carried out analytically. To this end, we approximate the phase-matching function by a Gaussian,

$$\mathrm{sinc}\left(\frac{\Delta k(\omega_a,\omega_b)L}{2}\right) \approx \exp\left\{-\gamma\left[\Delta k(\omega_a,\omega_b)L\right]^2\right\}, \tag{B1}$$

where the factor $\gamma = 0.048\,22$ is chosen, such that the Gaussian reproduces the central peak of the sinc function. In combination with the Gaussian pump envelope (53), this enables us to use the relation for the decomposition of a bipartite Gaussian (Grice, U'Ren, and Walmsley, 2001; U'Ren, Banaszek, and Walmsley, 2003)

$$-\frac{i\alpha}{\hbar\sqrt{2\pi\sigma_p^2}}\exp\left[-ax^2-2bxy-cy^2\right] = \sum_{n=0}^{\infty} r_n H_n(k_1 x)H_n^*(k_2 y), \tag{B2}$$

where we defined the Hermite functions H_n. Here we have $a = 1/(2\sigma_p^2)+\gamma T_1^2$, $b = 1/(2\sigma_p^2)+\gamma T_1 T_2$, and $c = 1/(2\sigma_p^2)+\gamma T_2^2$. The Hermite functions are then given by

$$H_n(k_i x) = \sqrt{\frac{k}{\sqrt{\pi}2^n n!}}e^{i(3\pi/8)-(k_i x)^2}h_n(k_i x), \tag{B3}$$

with the Hermite polynomials h_n, and we further defined the parameters

$$\mu = \frac{-\sqrt{ac}+\sqrt{ac-b^2}}{b}, \tag{B4}$$

and

$$r_n = \frac{\alpha}{\hbar}\sqrt{\frac{1+\mu^2}{4ac\sigma_p^2}}\mu^n, \tag{B5}$$
$$k_1 = \sqrt{\frac{2a(1-\mu^2)}{1+\mu^2}}, \tag{B6}$$
$$k_2 = \sqrt{\frac{2c(1-\mu^2)}{1+\mu^2}}. \tag{B7}$$

APPENDIX C: GREEN'S FUNCTIONS OF MATTER

In the case of the model system described in Sec. II.J.1, the superoperator correlation functions in Eqs. (102)–(104) may be rewritten as sum-over-state expressions,

$$p_{f,(\mathrm{I})}(t;\Gamma) = \left(-\frac{i}{\hbar}\right)^4\int_0^\infty dt_4\int_0^\infty dt_3\int_0^\infty dt_2\int_0^\infty dt_1 \times\sum_{e,e'}\mathcal{G}_{ff}(t_4)\mu_{e'f}\mathcal{G}_{fe'}(t_3)\mu_{ge'}\mathcal{G}_{fg}(t_2)\mu_{ef}\mathcal{G}_{eg}(t_1)\mu_{ge} \times\langle E^\dagger(t-t_4-t_3)E^\dagger(t-t_4)E(t-t_4-t_3-t_2) \times E(t-t_4-t_3-t_2-t_1)\rangle, \tag{C1}$$

$$p_{f,(\mathrm{II})}(t;\Gamma)=\left(-\frac{i}{\hbar}\right)^4\int_0^\infty dt_4\int_0^\infty dt_3\int_0^\infty dt_2\int_0^\infty dt_1 \times\sum_{e,e',e''}\mathcal{G}_{ff}(t_4)\mu_{e''f}\mathcal{G}_{fe''}(t_3)\mu_{e''f}\mathcal{G}_{ee';e''e''}(t_2)\mu_{ge'}\mathcal{G}_{eg}(t_1)\mu_{ge} \times\langle E^\dagger(t-t_4-t_3)E^\dagger(t-t_4)E(t-t_4-t_3-t_2)E(t-t_4-t_3-t_2-t_1)\rangle, \tag{C2}$$

$$p_{f,(\mathrm{III})}(t;\Gamma)=\left(-\frac{i}{\hbar}\right)^4\int_0^\infty dt_4\int_0^\infty dt_3\int_0^\infty dt_2\int_0^\infty dt_1 \times\sum_{e,e',e''}\mathcal{G}_{ff}(t_4)\mu_{e''f}\mathcal{G}_{e''f}(t_3)\mu_{e''f}\mathcal{G}_{ee';e''e'''}(t_2)\mu_{ge'}\mathcal{G}_{eg}(t_1)\mu_{ge} \times\langle E^\dagger(t-t_4-t_3)E^\dagger(t-t_4)E(t-t_4-t_3-t_2)E(t-t_4-t_3-t_2-t_1)\rangle. \tag{C3}$$

Here we have changed to the time delay variables $t_1,\ldots,t_4$. The various propagators are given by

$$\mathcal{G}_{eg}(t)=\Theta(t)e^{-i(\omega_{eg}-i\gamma_{eg})t}, \tag{C4}$$

$$\mathcal{G}_{fe}(t)=\Theta(t)e^{-i(\omega_{fe}-i\gamma_{fe})t}, \tag{C5}$$

$$\mathcal{G}_{fg}(t)=\Theta(t)e^{-i(\omega_{fg}-i\gamma_{fg})t}, \tag{C6}$$

and the single-excitation propagator

$$\mathcal{G}_{ee';e''e'''}(t)=\Theta(t)\left\{(1-\delta_{ee'})\delta_{ee''}\delta_{e'e'''}e^{-i(\omega_{ee'}-i\gamma_{ee'})t}+\delta_{ee'}\delta_{e''e'''}\exp\left[Kt\right]_{ee''}\right\}, \tag{C7}$$

with the transport matrix

$$K=\frac{2\pi}{T_0}\begin{pmatrix}-1/20 & 1\\ 1/20 & -1\end{pmatrix}, \tag{C8}$$

which transfers the single excited-state populations to the equilibrium state (with $p_{e_1}=5\%$ and $p_{e_2}=95\%$) with the rate $2\pi/T_0$.

In the frequency domain, the sum-over-state expressions read

$$p_{f,(\mathrm{I})}(t;\Gamma)=\left(-\frac{i}{\hbar}\right)^4\int\frac{d\omega_a}{2\pi}\int\frac{d\omega_b}{2\pi}\int\frac{d\omega_a'}{2\pi}\int\frac{d\omega_b'}{2\pi}\langle E^\dagger(\omega_a')E^\dagger(\omega_b')E(\omega_b)E(\omega_a)\rangle e^{i(\omega_a'+\omega_b'-\omega_b-\omega_a)t} \times\sum_{e,e'}\mathcal{G}_{ff}(\omega_a+\omega_b-\omega_a'-\omega_b')\mu_{e'f}\mathcal{G}_{fe'}(\omega_a+\omega_b-\omega_a')\mu_{ge'}\mathcal{G}_{fg}(\omega_a+\omega_b)\mu_{ef}\mathcal{G}_{eg}(\omega_a)\mu_{ge}, \tag{C9}$$

$$p_{f,(\mathrm{II})}(t;\Gamma)=\left(-\frac{i}{\hbar}\right)^4\int\frac{d\omega_a}{2\pi}\int\frac{d\omega_b}{2\pi}\int\frac{d\omega_a'}{2\pi}\int\frac{d\omega_b'}{2\pi}\langle E^\dagger(\omega_a')E^\dagger(\omega_b')E(\omega_b)E(\omega_a)\rangle e^{i(\omega_a'+\omega_b'-\omega_b-\omega_a)t} \times\sum_{e,e',e''}\mathcal{G}_{ff}(\omega_a+\omega_b-\omega_a'-\omega_b')\mu_{e''f}\mathcal{G}_{fe''}(\omega_a+\omega_b-\omega_a')\mu_{e''f}\mathcal{G}_{ee';e''e''}(\omega_a-\omega_a')\mu_{ge'}\mathcal{G}_{eg}(\omega_a)\mu_{ge}, \tag{C10}$$

$$p_{f,(\mathrm{III})}(t;\Gamma)=\left(-\frac{i}{\hbar}\right)^4\int\frac{d\omega_a}{2\pi}\int\frac{d\omega_b}{2\pi}\int\frac{d\omega_a'}{2\pi}\int\frac{d\omega_b'}{2\pi}\langle E^\dagger(\omega_a')E^\dagger(\omega_b')E(\omega_b)E(\omega_a)\rangle e^{i(\omega_a'+\omega_b'-\omega_b-\omega_a)t} \times\sum_{e,e',e''}\mathcal{G}_{ff}(\omega_a+\omega_b-\omega_a'-\omega_b')\mu_{e''f}\mathcal{G}_{e''f}(\omega_a-\omega_a'-\omega_b')\mu_{e''f}\mathcal{G}_{ee';e''e'''}(\omega_a-\omega_a')\mu_{ge'}\mathcal{G}_{eg}(\omega_a)\mu_{ge}. \tag{C11}$$

APPENDIX D: INTENSITY MEASUREMENTS: TPA VERSUS RAMAN

Expanding the frequency domain signal (137)–(140) (Roslyak and Mukamel, 2009a) in eigenstates we obtain

$$S_{1,(\mathrm{I})}(\omega;\Gamma)=\frac{2}{\hbar^4}\Im\int\frac{d\omega_a}{2\pi}\int\frac{d\omega_{\mathrm{sum}}}{2\pi}\langle E^\dagger(\omega_{\mathrm{sum}}-\omega)E^\dagger(\omega)E(\omega_{\mathrm{sum}}-\omega_a)E(\omega_a)\rangle \times\sum_{e,e',f}\frac{\mu_{ge}}{\omega_a-\omega_e+i\gamma_e}\frac{\mu_{ef}}{\omega_{\mathrm{sum}}-\omega_f+i\gamma_f}\frac{\mu_{fe'}}{\omega_{\mathrm{sum}}-\omega-\omega_{e'}-i\gamma_{e'}}\mu_{e'g}, \tag{D1}$$

$$S_{1,(\mathrm{II})}(\omega;\Gamma)=\frac{2}{\hbar^4}\Im\int\frac{d\omega_a}{2\pi}\int\frac{d\omega_{\mathrm{sum}}}{2\pi}\langle E^\dagger(\omega)E^\dagger(\omega_{\mathrm{sum}}-\omega)E(\omega_{\mathrm{sum}}-\omega_a)E(\omega_a)\rangle \times\sum_{e,e',f}\frac{\mu_{ge}}{\omega_a-\omega_e+i\gamma_e}\frac{\mu_{ef}}{\omega_{\mathrm{sum}}-\omega_f+i\gamma_f}\frac{\mu_{fe'}}{\omega-\omega_{e'}+i\gamma_{e'}}\mu_{e'g}, \tag{D2}$$

$$S_{1,(\mathrm{III})}(\omega;\Gamma)=\frac{2}{\hbar^4}\Im\int\frac{d\omega_a}{2\pi}\int\frac{d\omega_b}{2\pi}\langle E^\dagger(\omega_a+\omega_b-\omega)E(\omega_b)E^\dagger(\omega)E(\omega_a)\rangle \times\sum_{e,e',g'}\frac{\mu_{ge}}{\omega_a-\omega_e+i\gamma_e}\frac{\mu_{eg'}}{\omega_a-\omega-\omega_{g'}-i\gamma_g}\frac{\mu_{g'e'}}{\omega_a+\omega_b-\omega-\omega_{e'}-i\gamma_e}\mu_{e'g}, \tag{D3}$$

$$S_{1,(\mathrm{IV})}(\omega;\Gamma)=\frac{2}{\hbar^4}\Im\int\frac{d\omega_a}{2\pi}\int\frac{d\omega_b}{2\pi}\langle E^\dagger(\omega)E(\omega_b)E^\dagger(\omega_a+\omega_b-\omega)E(\omega_a)\rangle \times\sum_{e,e',g'}\frac{\mu_{ge}}{\omega_a-\omega_e+i\gamma_e}\frac{\mu_{eg'}}{\omega-\omega_b-\omega_{g'}+i\gamma_g}\frac{\mu_{g'e'}}{\omega-\omega_{e'}+i\gamma_e}\mu_{e'g}. \tag{D4}$$

Using the definitions of transition operators (141)–(145) we recast the signal as

$$\int\frac{d\omega}{2\pi}S_{1,(\mathrm{I})}(\omega;\Gamma)=\Im\int\frac{d\omega_{\mathrm{sum}}}{\pi}\sum_f\frac{\langle T^{(2)\dagger}_{fg}(\omega_{\mathrm{sum}})T^{(2)}_{fg}(\omega_{\mathrm{sum}})\rangle}{\omega_{\mathrm{sum}}-\omega_f+i\gamma_f}, \tag{D5}$$

$$\int\frac{d\omega}{2\pi}S_{1,(\mathrm{II})}(\omega;\Gamma)=\Im\int\frac{d\omega}{\pi}\sum_e\frac{\langle T^{(1)\dagger}_{eg}(\omega)T^{(3)}_{eg}(\omega)\rangle}{\omega-\omega_e+i\gamma_e}, \tag{D6}$$

$$\int\frac{d\omega}{2\pi}S_{1,(\mathrm{III})}(\omega;\Gamma)=\Im\int\frac{d\omega_-}{\pi}\sum_{g'}\frac{\langle T^{(2)\dagger}_{g'g}(\omega_-)T^{(2)}_{g'g}(\omega_-)\rangle}{\omega_--\omega_{g'}-i\gamma_g}, \tag{D7}$$

$$\int\frac{d\omega}{2\pi}S_{1,(\mathrm{IV})}(\omega;\Gamma)=\Im\int\frac{d\omega}{\pi}\sum_e\frac{\langle T^{(1)\dagger}_{eg}(\omega)T'^{(3)}_{eg}(\omega)\rangle}{\omega-\omega_e+i\gamma_e}. \tag{D8}$$

APPENDIX E: TIME-AND-FREQUENCY GATING

1. Simultaneous time-and-frequency gating

To a good approximation we can represent an ideal detector by a two-level atom that is initially in the ground state b and is promoted to the excited state a by the absorption of a photon [see Fig. 21(a)]. The detection of a photon brings the field from its initial state ψ_i to a final state ψ_f. The probability amplitude for photon absorption at time t can be calculated in first-order perturbation theory, which yields (Glauber, 2007)

$$\langle\psi_f|\mathbf{E}(t)|\psi_i\rangle\cdot\langle a|\mathbf{d}|b\rangle, \tag{E1}$$

where $\mathbf{d}$ is the dipole moment of the atom and $\mathbf{E}(t)=E^\dagger(t)+E(t)$ is the electric field operator (we omit the spatial dependence). Clearly, only the annihilation part of the electric field contributes to the photon absorption process. The transition probability to find the field in state ψ_f at time t is given by the modulus square of the transition amplitude

$$\sum_{\psi_f}|\langle\psi_f|E(t)|\psi_i\rangle|^2=\langle\psi_i|E^\dagger(t)\sum_{\psi_f}|\psi_f\rangle\langle\psi_f|E(t)|\psi_i\rangle =\langle\psi_i|E^\dagger(t)E(t)|\psi_i\rangle. \tag{E2}$$

Since the initial state of the field ψ_i is rarely known with certainty, we must trace over all possible initial states as determined by a density operator ρ. Thus, the output of the idealized detector is more generally given by $\mathrm{tr}[\rho E^\dagger(t)E(t)]$.

Simultaneous time-and-frequency-resolved measurement must involve a frequency (spectral) gate combined with a time gate—a shutter that opens up for a very short interval of time. The combined detector with input located at r_G is represented by a time gate F_t centered at $\bar{t}$ followed by a frequency gate F_f centered at $\bar{\omega}$ (Stolz, 1994). First the time gate transforms the electric field $E(r_G,t)=\sum_s\hat{E}_s(r_G,t)$ with $\hat{E}_s(r_G,t)=E(r_G,\omega_s)e^{-i\omega_s t}$ as follows:

$$E^{(t)}(\bar{t};r_G,t)=F_t(t,\bar{t})E(r_G,t). \tag{E3}$$

Then the frequency gate is applied $E^{(tf)}(\bar{t},\bar{\omega};r_G,\omega)=F_f(\omega,\bar{\omega})E^{(t)}(\bar{t};r_G,\omega)$ to obtain the time-and-frequency-gated field. We assume that the time gate is applied first. Therefore, the combined detected field at the position r_D can be written as

$$E^{(tf)}(\bar{t},\bar{\omega};r_D,t)=\int_{-\infty}^{\infty}dt'F_f(t-t',\bar{\omega})F_t(t',\bar{t})E(r_G,t'), \tag{E4}$$

where $E(t)$ is the electric field operator (8) in the Heisenberg picture. Similarly, one can apply the frequency gate first and obtain the frequency-and-time-gated field $E^{(ft)}$,

$$E^{(ft)}(\bar{t},\bar{\omega};r_D,t)=\int_{-\infty}^{\infty}dt'F_t(t,\bar{t})F_f(t-t',\bar{\omega})E(r_G,t'). \tag{E5}$$

The following discussion is based on Eq. (E4). Equation (E5) can be handled similarly.

For Gaussian gates

$$F_t(t',t)=e^{-(1/2)\sigma_T^2(t'-t)^2},\qquad F_f(\omega',\omega)=e^{-(\omega'-\omega)^2/4\sigma_\omega^2},\tag{E6}$$

the detector time domain and Wigner spectrograms are given by

$$D(t,\omega,t',\tau)=\frac{\sigma_\omega}{\sqrt{2\pi}}e^{-(1/2)\sigma_T^2(t'-t)^2-(1/2)\tilde{\sigma}_\omega^2\tau^2-[\sigma_T^2(t'-t)+i\omega]\tau},\tag{E7}$$

$$W_D(t,\omega;t',\omega')=N_De^{-(1/2)\tilde{\sigma}_T^2(t'-t)^2-(\omega'-\omega)^2/2\tilde{\sigma}_\omega^2-iA(\omega'-\omega)(t'-t)},\tag{E8}$$

where

$$\tilde{\sigma}_\omega^2=\sigma_T^2+\sigma_\omega^2,\qquad \tilde{\sigma}_T^2=\sigma_T^2+\frac{1}{\sigma_\omega^{-2}+\sigma_T^{-2}},$$
$$N_D=\frac{1}{\sigma^T[\sigma_\omega^2+\sigma_T^2]^{1/2}},\qquad A=\frac{\sigma_T^2}{\sigma_T^2+\sigma_\omega^2}.\tag{E9}$$

Note that σ_T and σ_ω can be controlled independently, but the actual time and frequency resolution is controlled by $\tilde{\sigma}_T$ and $\tilde{\sigma}_\omega$, respectively, which always satisfy Fourier uncertainty $\tilde{\sigma}_\omega/\tilde{\sigma}_T>1$. For Lorentzian gates

$$F_t(t',t)=\theta(t-t')e^{-\sigma_T(t-t')},\qquad F_f(\omega',\omega)=\frac{i}{\omega'-\omega+i\sigma_\omega},\tag{E10}$$

the detector time domain and Wigner spectrograms are given by

$$D(t,\omega,t',\tau)=\frac{i}{2\sigma_\omega}\theta(\tau)\theta(t'-t)e^{-(i\omega+\sigma_\omega+\sigma_T)\tau-2\sigma_T(t'-t)},\tag{E11}$$

$$W_D(t,\omega;t',\omega')=-\frac{1}{2\sigma_\omega}\theta(t-t')\frac{e^{-2\sigma_T(t'-t)}}{\omega'-\omega+i(\sigma_T+\sigma_\omega)}.\tag{E12}$$

The gated signal is given by

$$n_{\bar{t},\bar{\omega}}=\int_{-\infty}^{\infty}dt\sum_{s,s'}\langle\hat{E}_{sR}^{(tf)\dagger}(\bar{t},\bar{\omega};r_D,t)\hat{E}_{s'L}^{(tf)}(\bar{t},\bar{\omega};r_D,t)\rangle,\tag{E13}$$

where the angular brackets denote $\langle\cdots\rangle\equiv\mathrm{Tr}[\rho(t)\cdots]$. The density operator $\rho(t)$ is defined in the joint field-matter space of the entire system. Note that Eq. (E13) represents the observable signal, which is always positive since it can be recast as a modulus square of an amplitude [Eq. (E2)]. For clarity we hereafter omit the position dependence in the fields assuming that propagation between r_G and r_D is included in the spectral gate function.

2. The bare signal

The bare signal assumes infinite spectral and temporal resolution. It is unphysical but carries all necessary information for calculating the photon counting measurement. It is given by the closed path time-loop diagram shown in Fig. 21 (Harbola and Mukamel, 2008). We assume an arbitrary field-matter evolution starting from the matter ground state g that promotes the system up to some excited state. The system then emits a photon with frequency ω_s that leaves the matter in the state e. This photon is later absorbed by the detector.

In the absence of dissipation (unitary evolution) the matter correlation function can be further factorized into a product of two amplitudes that correspond to the unitary evolution of the bra and ket. This transition amplitude can be recast in Hilbert space without using superoperators and is given by

$$T_{eg}(t)=-\frac{i}{\hbar}\sum_s\frac{2\pi\hbar\omega_s}{\Omega}\int_{-\infty}^{t}dt_1'e^{-i\omega_s(t-t_1')-i\omega_{eg}t}\times\langle e(t)|V(t_1')\mathcal{T}\exp\left(-\frac{i}{\hbar}\int_{-\infty}^{t_1'}H'(T)dT\right)|g\rangle.\tag{E14}$$

This gives for the bare Wigner spectrogram

$$n(t',\omega')=\sum_e\int_0^\infty d\tau e^{-i\omega'\tau}\times T_{eg}(t'-\tau/2)T_{eg}^*(t'+\tau/2).\tag{E15}$$

3. Spectrogram-overlap representation for detected signal

In the standard theory (Stolz, 1994), the detected signal is given by a convolution of the spectrograms of the detector and bare signal. The detector spectrogram is an ordinary function of the gating parameters whereas the bare signal is related to the field prior to detection. We now show that when the process is described in the joint matter plus field space the signal can be brought to the same form, except that now the bare signal is given by a correlation function of matter that further includes a sum over the detected modes. We denote this as the spectrogram-overlap (SO) representation of the signal. Alternatively one can introduce a spectrogram-superoperator-overlap representation where field modes that interact with the detector are included in the detector spectrogram, which becomes a superoperator in the field space. Details of this representation are presented by Dorfman and Mukamel (2012a). Next we present the signals in the time domain, which can be directly read off the diagram [Fig. 21(b)]. We then recast them using Wigner spectrograms, which simultaneously depict temporal and spectral profiles of the signal. We now define the detector Wigner spectrogram

$$W_D(\bar{t},\bar{\omega};t',\omega')=\int_{-\infty}^{\infty}d\tau\int_{-\infty}^{\infty}\frac{d\omega}{2\pi}e^{i(\omega'-\omega)\tau}\times|F_f(\omega,\bar{\omega})|^2F_t^*(t'+\tau/2,\bar{t})F_t(t'-\tau/2,\bar{t}),\tag{E16}$$

if the spectral gate applied first, using Eq. (E5). The detector spectrogram is alternatively given by

$$W_D(\bar{t},\bar{\omega};t',\omega) = \int_{-\infty}^{\infty} d\tau e^{i\omega'\tau}\int_{-\infty}^{\infty} dt \times |F_t(t,\bar{t})|^2 F_f^*(t-t'-\tau/2,\bar{\omega})F_f(t-t'+\tau/2,\bar{\omega}). \tag{E17}$$

Combining Eqs. (E4)–(E16) we find that the gated signal is given by the temporal overlap of the bare signal and detector Wigner spectrogram

$$n_{\bar{t},\bar{\omega}} = \int_{-\infty}^{\infty} dt' \frac{d\omega'}{2\pi} W_D(\bar{t},\bar{\omega};t',\omega')n(t',\omega'). \tag{E18}$$

Equation (165) can be alternatively recast in terms of Wigner spectrograms

$$\hat{n}_{t,\omega} = \int dt' \int \frac{d\omega'}{2\pi} W_D(t,\omega;t',\omega')\hat{n}(t',\omega'), \tag{E19}$$

where $W_D(t,\omega,t',\omega')$ is a detector Wigner spectrogram given by

$$W_D(t,\omega,t',\omega') = \int d\tau D(t,\omega,t',\tau)e^{i\omega'\tau} \tag{E20}$$

and the Wigner spectrogram for the bare photon number operator is given by

$$\hat{n}(t',\omega') = \int d\tau e^{-i\omega'\tau}\hat{n}(t',\tau). \tag{E21}$$

This is the conventional form (Stolz, 1994) introduced originally for the field space alone. Equation (E15) explicitly contains the multiple pairs of radiation modes s and s' that can be revealed only in the joint field plus matter space. Eventually this takes into account all the field-matter interactions that lead to the emission of the detected field modes. All parameters of F_f and F_t can be freely varied. The spectrogram will always satisfy the Fourier uncertainty $\Delta t\Delta\omega > 1$.

Together with the gated spectrogram (E16) the bare signal (E15) represents the time-and-frequency-resolved-gated signal. Note that in the presence of a bath, the signal (E15) is no longer given by a product of two amplitudes. $\hat{T}_{eg}(t)$ is then an operator in the space of the bath degrees of freedom. Therefore, one has to replace the product of amplitudes in Eq. (E15) by $\langle \hat{T}_{eg}(t'-\tau/2)\hat{T}_{eg}^*(t'+\tau/2)\rangle$, where $\langle\cdots\rangle$ corresponds to averaging over the bath degrees of freedom. The convolution of two operators $\hat{T}_{eg}$ reveals the multiple pathways between these initial and final states of matter that allow one to observe them through the simultaneous time and frequency resolution.

We now consider two limiting cases. In the absence of a frequency gate, then $F_f(\omega,\bar{\omega}) = 1$ we get $W_D(\bar{\omega},\bar{t};t,\tau) = \delta(\tau)F_t^*(t+\tau/2,\bar{t})F_t(t-\tau/2,\bar{t})$. For the narrow time gate $|F_t(t,\bar{t})|^2 = \delta(t-\bar{t})$ we then obtain the time-resolved measurement

$$n_{\bar{t}} = \sum_e |T_{eg}(\bar{t})|^2. \tag{E22}$$

In the opposite limit, where there is no time gate, i.e., $F_t(t,\bar{t}) = 1$, and the frequency gate is very narrow, such that $F_f(t,\bar{\omega}) = (\sqrt{\gamma}/\pi)e^{-i\bar{\omega}t-\gamma t}\theta(t)$ at $\gamma\to 0$, then $W_D(\bar{\omega},\bar{t};t,\tau) = e^{-i\bar{\omega}\tau}$. In this case we obtain the frequency-resolved measurement

$$n_{\bar{\omega}} = \sum_e |T_{eg}(\bar{\omega})|^2, \tag{E23}$$

where $T_{eg}(\omega) = \int_{-\infty}^{\infty} dt e^{i\omega t}T_{eg}(t)$. Equations (E22) and (E23) indicate that if the measurement is either purely time or purely frequency resolved, the signal can be expressed in terms of the modulus square of a transition amplitude. Interference can then occur only within T_{eg} in Hilbert space but not between the two amplitudes. Simultaneous time and frequency gating also involves interference between the two amplitudes; the pathway is in the joint ket plus bra density matrix space. In the presence of a bath, the signal can be written as a correlation function in the space of bath coordinates $\langle \hat{T}_{eg}^*(\bar{t})\hat{T}_{eg}(\bar{t})\rangle$ for Eq. (E22) and $\langle \hat{T}_{eg}^*(\bar{\omega})\hat{T}_{eg}(\bar{\omega})\rangle$ for Eq. (E23).

4. Multiple detections

The present formalism is modular and may be easily extended to any number of detection events. To that end it is more convenient to use the time domain, rather than Wigner representation. For coincidence counting of two photons measured by a first detector with parameters $\bar{\omega}_i,\bar{t}_i$ followed by a second detector characterized by $\bar{\omega}_s,\bar{t}_s$ the time-and-frequency-resolved measurement in SO representation is given by

$$S(\bar{t}_s,\bar{\omega}_s;\bar{t}_i,\bar{\omega}_i) = \int_{-\infty}^{\infty} dt_s' d\tau_s \int_{-\infty}^{\infty} dt_i' d\tau_i \times D^{(s)}(\bar{t}_s,\bar{\omega}_s;t_s',\tau_s)D^{(i)}(\bar{t}_i,\bar{\omega}_i;t_i',\tau_i')B(t_s',\tau_s;t_i',\tau_i'), \tag{E24}$$

where the detector spectrogram for mode $\nu = i,\ s$ reads

$$D(\bar{t}_\nu,\bar{\omega}_\nu;t_\nu',\tau_\nu) = \int_{-\infty}^{\infty}\frac{d\omega_\nu}{2\pi}e^{-i\omega_\nu\tau_\nu} \times |F_f(\omega_\nu,\bar{\omega}_\nu)|^2 F_t^*(t_\nu'+\tau_\nu/2,\bar{t}_\nu)F_t(t_\nu'-\tau_\nu/2,\bar{t}_\nu). \tag{E25}$$

The bare signal is given by the loop diagram in Fig. 21(c) which reads

$$B(t_s',\tau_s;t_i',\tau_i) = -\sum_e T_{eg}(t_s'-\tau_s/2,t_i'-\tau_i/2)T_{eg}^*(t_s'+\tau_s/2,t_i'+\tau_i/2). \tag{E26}$$

The transition amplitude for the ket reads

$$T_{eg}(t_s,t_i)=\left(-\frac{i}{\hbar}\right)^2\int_{-\infty}^{t_s}dt_1'\int_{-\infty}^{t_i}dt_2'e^{-i\omega_{eg}t_s}\times\langle\langle e(t_s)g|\hat{V}_L(t_1')\hat{V}_L(t_2')\times\mathcal{T}\exp\left(-\frac{i}{\hbar}\int_{-\infty}^{\max[t_1',t_2']}\hat{H}_L{}'(T)dT\right)|gg\rangle\rangle, \tag{E27}$$

and for the bra

$$T_{eg}^*(t_s,t_i)=\left(\frac{i}{\hbar}\right)^2\int_{-\infty}^{t_s}dt_1\int_{-\infty}^{t_i}dt_2e^{i\omega_{eg}t_s}\times\langle\langle gg|\hat{V}_R^\dagger(t_1)\hat{V}_R^\dagger(t_2)\times\mathcal{T}\exp\left(\frac{i}{\hbar}\int_{-\infty}^{\max[t_1,t_2]}\hat{H}_R{}'(T)dT\right)|e(t_s)g\rangle\rangle. \tag{E28}$$

REFERENCES

Abolghasem, P., J. Han, B. J. Bijlani, and A. S. Helmy, 2010, Opt. Express **18**, 12681.

Abouraddy, A. F., M. B. Nasr, B. E. A. Saleh, A. V. Sergienko, and M. C. Teich, 2002, Phys. Rev. A **65**, 053817.

Abramavicius, D., B. Palmieri, D. V. Voronine, F. Šanda, and S. Mukamel, 2009, Chem. Rev. **109**, 2350.

Abramavicius, D., D. V. Voronine, and S. Mukamel, 2008, Proc. Natl. Acad. Sci. U.S.A. **105**, 8525.

Adamczyk, K., M. Prémont-Schwarz, D. Pines, E. Pines, and E. T. J. Nibbering, 2009, Science **326**, 1690.

Akiba, K., D. Akamatsu, and M. Kozuma, 2006, Opt. Commun. **259**, 789.

Almand-Hunter, A. E., H. Liu, S. T. Cundiff, M. Mootz, M. Kira, and S. W. Koch, 2014, Nature (London) **506**, 471.

Andrews, D. L., and P. Allcock, 2002, *Optical harmonics in molecular systems: quantum electrodynamical theory* (Wiley-VCH, Weinheim, Germany), Vol. 1.

Arora, R., G. I. Petrov, V. V. Yakovlev, and M. O. Scully, 2012, Proc. Natl. Acad. Sci. U.S.A. **109**, 1151.

Asaka, S., H. Nakatsuka, M. Fujiwara, and M. Matsuoka, 1984, Phys. Rev. A **29**, 2286.

Aspect, A., J. Dalibard, and G. Roger, 1982, Phys. Rev. Lett. **49**, 1804.

Aspect, A., P. Grangier, and G. Roger, 1981, Phys. Rev. Lett. **47**, 460.

Aspect, A., P. Grangier, and G. Roger, 1982, Phys. Rev. Lett. **49**, 91.

Ates, S., I. Agha, A. Gulinatti, I. Rech, M. T. Rakher, A. Badolato, and K. Srinivasan, 2012, Phys. Rev. Lett. **109**, 147405.

Avenhaus, M., H. B. Coldenstrodt-Ronge, K. Laiho, W. Mauerer, I. A. Walmsley, and C. Silberhorn, 2008, Phys. Rev. Lett. **101**, 053601.

Balić, V., D. A. Braje, P. Kolchin, G. Y. Yin, and S. E. Harris, 2005, Phys. Rev. Lett. **94**, 183601.

Barkai, E., 2008, *Theory and Evaluation of Single-molecule Signals* (World Scientific Publishing Company, Singapore).

Beach, R., and S. R. Hartmann, 1984, Phys. Rev. Lett. **53**, 663.

Bellini, M., F. Marin, S. Viciani, A. Zavatta, and F. T. Arecchi, 2003, Phys. Rev. Lett. **90**, 043602.

Benatti, F., R. Floreanini, and U. Marzolino, 2010, Ann. Phys. (Amsterdam) **325**, 924.

Bennink, R. S., S. J. Bentley, R. W. Boyd, and J. C. Howell, 2004, Phys. Rev. Lett. **92**, 033601.

Bernien, H., L. Childress, L. Robledo, M. Markham, D. Twitchen, and R. Hanson, 2012, Phys. Rev. Lett. **108**, 043604.

Bertini, L., A. De Sole, D. Gabrielli, G. Jona-Lasinio, and C. Landim, 2001, Phys. Rev. Lett. **87**, 040601.

Bochkov, G., and Y. E. Kuzovlev, 1981, Physica A (Amsterdam) **106**, 443.

Boto, A. N., P. Kok, D. S. Abrams, S. L. Braunstein, C. P. Williams, and J. P. Dowling, 2000, Phys. Rev. Lett. **85**, 2733.

Boyd, R. W., 2003, *Nonlinear optics* (Academic Press, Waltham, USA).

Braunstein, S. L., and H. J. Kimble, 2000, Phys. Rev. A **61**, 042302.

Brinks, D., F. D. Stefani, F. Kulzer, R. Hildner, T. H. Taminiau, Y. Avlasevich, K. Mullen, and N. F. van Hulst, 2010, Nature (London) **465**, 905.

Brown, R. H., 1956, Nature (London) **178**, 1046.

Callis, P. R., 1993, J. Chem. Phys. **99**, 27.

Carrasco, S., A. V. Sergienko, B. E. A. Saleh, M. C. Teich, J. P. Torres, and L. Torner, 2006, Phys. Rev. A **73**, 063802.

Castet, F., V. Rodriguez, J.-L. Pozzo, L. Ducasse, A. Plaquet, and B. Champagne, 2013, Acc. Chem. Res. **46**, 2656.

Chen, W., K. M. Beck, R. Bücker, M. Gullans, M. D. Lukin, H. Tanji-Suzuki, and V. Vuletić, 2013, Science **341**, 768.

Cheng, J., and X. Xie, 2012, *Coherent Raman Scattering Microscopy*, Cellular and Clinical Imaging (Taylor & Francis, London).

Cheng, J.-x., A. Volkmer, L. D. Book, and X. S. Xie, 2002, J. Phys. Chem. B **106**, 8493.

Chernyak, V., N. Wang, and S. Mukamel, 1995, Phys. Rep. **263**, 213.

Cho, Y.-W., K.-K. Park, J.-C. Lee, and Y.-H. Kim, 2014, Phys. Rev. Lett. **113**, 063602.

Christ, A., B. Brecht, W. Mauerer, and C. Silberhorn, 2013, New J. Phys. **15**, 053038.

Christ, A., K. Laiho, A. Eckstein, K. N. Cassemiro, and C. Silberhorn, 2011, New J. Phys. **13**, 033027.

Clausen, C., I. Usmani, F. Bussières, N. Sangouard, M. Afzelius, H. de Riedmatten, and N. Gisin, 2011, Nature (London) **469**, 508.

Cohen, A. E., and S. Mukamel, 2003, Phys. Rev. Lett. **91**, 233202.

Cohen-Tannoudji, C., J. Dupont-Roc, G. Grynberg, and P. Thickstun, 1992, *Atom-photon interactions: Basic processes and applications* (Wiley Online Library).

Cohen-Tannoudji, C., and D. Guéry-Odelin, 2011, *Advances In Atomic Physics: An Overview* (World Scientific Publishing Company, Incorporated, Singapore).

Coolen, L., X. Brokmann, P. Spinicelli, and J.-P. Hermier, 2008, Phys. Rev. Lett. **100**, 027403.

Dalibard, J., Y. Castin, and K. Mølmer, 1992, Phys. Rev. Lett. **68**, 580.

D'Angelo, M., M. V. Chekhova, and Y. Shih, 2001, Phys. Rev. Lett. **87**, 013602.

Das, S., and G. S. Agarwal, 2008, J. Phys. B **41**, 225502.

Das, S., G. S. Agarwal, and M. O. Scully, 2008, Phys. Rev. Lett. **101**, 153601.

D'auria, V., S. Fornaro, A. Porzio, E. Sete, and S. Solimeno, 2008, Appl. Phys. B **91**, 309.

Dayan, B., A. Pe'er, A. A. Friesem, and Y. Silberberg, 2004, Phys. Rev. Lett. **93**, 023005.

Dayan, B., A. Pe'er, A. A. Friesem, and Y. Silberberg, 2005, Phys. Rev. Lett. **94**, 043602.

Defienne, H., M. Barbieri, I. A. Walmsley, B. J. Smith, and S. Gigan, 2016, Sci. Adv. **2**, e1501054.

de J Leon-Montiel, R., J. Svozilík, L. J. Salazar-Serrano, and J. P. Torres, 2013, New J. Phys. **15**, 053023
del Valle, E., A. Gonzalez-Tudela, F. P. Laussy, C. Tejedor, and M. J. Hartmann, 2012, Phys. Rev. Lett. **109**, 183601.
Denk, W., J. Strickler, and W. Webb, 1990, Science **248**, 73.
Dick, B., and R. Hochstrasser, 1983, Phys. Rev. Lett. **51**, 2221.
Dietze, D. R., and R. A. Mathies, 2016, ChemPhysChem **17**, 1224.
Dolde, F., I. Jakobi, B. Naydenov, N. Zhao, S. Pezzagna, C. Trautmann, J. Meijer, P. Neumann, F. Jelezko, and J. Wrachtrup, 2013, Nat. Phys. **9**, 139.
Dorfman, K. E., B. P. Fingerhut, and S. Mukamel, 2013a, Phys. Chem. Chem. Phys. **15**, 12348.
Dorfman, K. E., B. P. Fingerhut, and S. Mukamel, 2013b, J. Chem. Phys. **139**, 124113.
Dorfman, K. E., and S. Mukamel, 2012a, Phys. Rev. A **86**, 013810.
Dorfman, K. E., and S. Mukamel, 2012b, Phys. Rev. A **86**, 023805.
Dorfman, K. E., and S. Mukamel, 2013, Phys. Rev. A **87**, 063831.
Dorfman, K. E., and S. Mukamel, 2014a, Sci. Rep. **4**, 3996.
Dorfman, K. E., and S. Mukamel, 2014b, New J. Phys. **16**, 033013.
Dorfman, K. E., F. Schlawin, and S. Mukamel, 2014, J. Phys. Chem. Lett. **5**, 2843.
Dorrer, C., B. de Beauvoir, C. L. Blanc, S. Ranc, J.-P. Rousseau, P. Rousseau, J.-P. Chambaret, and F. Salin, 1999, Opt. Lett. **24**, 1644.
Duan, L.-M., G. Giedke, J. I. Cirac, and P. Zoller, 2000, Phys. Rev. Lett. **84**, 2722.
Eberly, J., and K. Wodkiewicz, 1977, J. Opt. Soc. Am. **67**, 1252.
Edamatsu, K., 2007, Jpn. J. Appl. Phys. **46**, 7175.
Edamatsu, K., G. Oohata, R. Shimizu, and T. Itoh, 2004, Nature (London) **431**, 167.
Elf, J., G.-W. Li, and X. S. Xie, 2007, Science **316**, 1191.
Engel, G. S., T. R. Calhoun, E. L. Read, T.-K. Ahn, T. Mancal, Y.-C. Cheng, R. E. Blankenship, and G. R. Fleming, 2007, Nature (London) **446**, 782.
Esposito, M., 2016, "A new spectroscopic approach to collective excitations in solids: Pump-probe quantum state tomography," Ph.D. thesis (University of Trieste).
Faez, S., P. Türschmann, H. R. Haakh, S. Götzinger, and V. Sandoghdar, 2014, Phys. Rev. Lett. **113**, 213601.
Fei, H.-B., B. M. Jost, S. Popescu, B. E. A. Saleh, and M. C. Teich, 1997, Phys. Rev. Lett. **78**, 1679.
Fleury, L., J.-M. Segura, G. Zumofen, B. Hecht, and U. P. Wild, 2000, Phys. Rev. Lett. **84**, 1148.
Franken, P. A., A. E. Hill, C. W. Peters, and G. Weinreich, 1961, Phys. Rev. Lett. **7**, 118.
Franson, J. D., 1989, Phys. Rev. Lett. **62**, 2205.
Franson, J. D., 1992, Phys. Rev. A **45**, 3126.
Friberg, S., C. Hong, and L. Mandel, 1985, Opt. Commun. **54**, 311.
Fu, D., T. Ye, G. Yurtsever, W. S. Warren, and T. E. Matthews, 2007, J. Biomed. Opt. **12**, 054004.
Garay-Palmett, K., H. J. McGuinness, O. Cohen, J. S. Lundeen, R. Rangel-Rojo, A. B. U'ren, M. G. Raymer, C. J. McKinstrie, S. Radic, and I. A. Walmsley, 2007, Opt. Express **15**, 14870.
Garay-Palmett, K., A. B. U'Ren, R. Rangel-Rojo, R. Evans, and S. Camacho-López, 2008, Phys. Rev. A **78**, 043827.
Gea-Banacloche, J., 1989, Phys. Rev. Lett. **62**, 1603.
Georgiades, N. P., E. Polzik, K. Edamatsu, H. Kimble, and A. Parkins, 1995, Phys. Rev. Lett. **75**, 3426.
Georgiades, N. P., E. S. Polzik, and H. J. Kimble, 1997, Phys. Rev. A **55**, R1605.
Gerry, C., and P. Knight, 2005, *Introductory Quantum Optics* (Cambridge University Press, Cambridge, UK).
Ginsberg, N. S., Y.-C. Cheng, and G. R. Fleming, 2009, Acc. Chem. Res. **42**, 1352.
Giovannetti, V., S. Lloyd, and L. Maccone, 2004, Science **306**, 1330.
Giovannetti, V., S. Lloyd, and L. Maccone, 2006, Phys. Rev. Lett. **96**, 010401.
Giovannetti, V., S. Lloyd, and L. Maccone, 2011, Nat. Photonics **5**, 222.
Glauber, R. J., 2007, *Quantum Theory of Optical Coherence* (Wiley, Hoboken).
Glauber, R. J., 1963, Phys. Rev. **130**, 2529.
Glenn, R., K. Bennett, K. E. Dorfman, and S. Mukamel, 2015, J. Phys. B **48**, 065401.
González-Tudela, A., E. del Valle, and F. P. Laussy, 2015, Phys. Rev. A **91**, 043807.
Gorniaczyk, H., C. Tresp, J. Schmidt, H. Fedder, and S. Hofferberth, 2014, Phys. Rev. Lett. **113**, 053601.
Grice, W. P., A. B. U'Ren, and I. A. Walmsley, 2001, Phys. Rev. A **64**, 063815.
Grice, W. P., and I. A. Walmsley, 1997, Phys. Rev. A **56**, 1627.
Gu, X., K. Huang, Y. Li, H. Pan, E. Wu, and H. Zeng, 2010, Appl. Phys. Lett. **96**, 131111.
Gustavsson, S., M. Studer, R. Leturcq, T. Ihn, K. Ensslin, D. C. Driscoll, and A. C. Gossard, 2007, Phys. Rev. Lett. **99**, 206804.
Guzman, A. R., M. R. Harpham, O. Suzer, M. M. Haley, and T. G. Goodson, 2010, J. Am. Chem. Soc. **132**, 7840.
Hamm, P., and M. Zanni, 2011, *Concepts and Methods of 2D Infrared Spectroscopy* (Cambridge University Press, Cambridge, UK).
Hansen, T., and T. Pullerits, 2012, J. Phys. B **45**, 154014.
Harbola, U., and S. Mukamel, 2008, Phys. Rep. **465**, 191.
Harbola, U., S. Umapathy, and S. Mukamel, 2013, Phys. Rev. A **88**, 011801.
Harpham, M. R., O. Suzer, C.-Q. Ma, P. Bäuerle, and T. Goodson, 2009, J. Am. Chem. Soc. **131**, 973.
Hashitsume, N., M. Toda, R. Kubo, and N. Saitō, 1991, *Statistical physics II: Nonequilibrium statistical mechanics*, Springer Science & Business Media (Springer-Verlag, Berlin), Vol. 30.
He, B., A. V. Sharypov, J. Sheng, C. Simon, and M. Xiao, 2014, Phys. Rev. Lett. **112**, 133606.
Hedges, M. P., J. J. Longdell, Y. Li, and M. J. Sellars, 2010, Nature (London) **465**, 1052.
Herrera, F., B. Peropadre, L. A. Pachon, S. K. Saikin, and A. Aspuru-Guzik, 2014, J. Phys. Chem. Lett. **5**, 3708.
Hong, C. K., and L. Mandel, 1985, Phys. Rev. A **31**, 2409.
Hong, C. K., Z. Y. Ou, and L. Mandel, 1987, Phys. Rev. Lett. **59**, 2044.
Howell, J. C., R. S. Bennink, S. J. Bentley, and R. Boyd, 2004, Phys. Rev. Lett. **92**, 210403.
Hutchison, J. A., T. Schwartz, C. Genet, E. Devaux, and T. W. Ebbesen, 2012, Angew. Chem., Int. Ed. Engl. **51**, 1592.
Javanainen, J., and P. L. Gould, 1990, Phys. Rev. A **41**, 5088.
Jennewein, T., C. Simon, G. Weihs, H. Weinfurter, and A. Zeilinger, 2000, Phys. Rev. Lett. **84**, 4729.
Joobeur, A., B. E. A. Saleh, and M. C. Teich, 1994, Phys. Rev. A **50**, 3349.
Kalachev, A., D. Kalashnikov, A. Kalinkin, T. Mitrofanova, A. Shkalikov, and V. Samartsev, 2007, Laser Phys. Lett. **4**, 722.
Kalachev, A., D. Kalashnikov, A. Kalinkin, T. Mitrofanova, A. Shkalikov, and V. Samartsev, 2008, Laser Phys. Lett. **5**, 600.
Kalashnikov, D. A., Z. Pan, A. I. Kuznetsov, and L. A. Krivitsky, 2014, Phys. Rev. X **4**, 011049.
Kaltenbaek, R., J. Lavoie, D. N. Biggerstaff, and K. J. Resch, 2008, Nat. Phys. **4**, 864.
Kaltenbaek, R., J. Lavoie, and K. J. Resch, 2009, Phys. Rev. Lett. **102**, 243601.

Keldysh, L., 1965, Sov. Phys. JETP **20**, 1018 [http://www.jetp.ac.ru/cgi-bin/e/index/e/20/4/p1018?a=list].
Keller, T. E., and M. H. Rubin, 1997, Phys. Rev. A **56**, 1534.
Kelley, P., and W. Kleiner, 1964, Phys. Rev. **136**, A316.
Keusters, D., H.-S. Tan, and Warren, 1999, J. Phys. Chem. A **103**, 10369.
Kim, J., S. Mukamel, and G. D. Scholes, 2009, Acc. Chem. Res. **42**, 1375.
Kim, Y.-H., and W. P. Grice, 2005, Opt. Lett. **30**, 908.
Kimble, H., M. Dagenais, and L. Mandel, 1977, Phys. Rev. Lett. **39**, 691.
Kira, M., S. W. Koch, R. P. Smith, A. E. Hunter, and S. T. Cundiff, 2011, Nat. Phys. **7**, 799.
Klyshko, D., 1988, *Photons and Nonlinear Optics* (Gordon and Breach, New York).
Knill, E., R. Laflamme, and G. Milburn, 2001, Nature (London) **409**, 46.
Kojima, J., and Q.-V. Nguyen, 2004, Chem. Phys. Lett. **396**, 323.
Kok, P., W. J. Munro, K. Nemoto, T. C. Ralph, J. P. Dowling, and G. J. Milburn, 2007, Rev. Mod. Phys. **79**, 135.
Krčmář, J., M. F. Gelin, and W. Domcke, 2013, Chem. Phys. **422**, 53.
Kryvohuz, M., and S. Mukamel, 2012, Phys. Rev. A **86**, 043818.
Kubo, R., 1963, J. Math. Phys. (N.Y.) **4**, 174.
Kukura, P., D. W. McCamant, and R. A. Mathies, 2007, Annu. Rev. Phys. Chem. **58**, 461.
Kuramochi, H., S. Takeuchi, and T. Tahara, 2012, J. Phys. Chem. Lett. **3**, 2025.
Kwiat, P. G., K. Mattle, H. Weinfurter, A. Zeilinger, A. V. Sergienko, and Y. Shih, 1995, Phys. Rev. Lett. **75**, 4337.
Larchuk, T. S., M. C. Teich, and B. E. A. Saleh, 1995, Phys. Rev. A **52**, 4145.
Lavoie, J., R. Kaltenbaek, and K. J. Resch, 2009, Opt. Express **17**, 3818.
Law, C. K., and J. H. Eberly, 2004, Phys. Rev. Lett. **92**, 127903.
Law, C. K., I. A. Walmsley, and J. H. Eberly, 2000, Phys. Rev. Lett. **84**, 5304.
Lee, D.-I., and T. Goodson, 2006, J. Phys. Chem. B **110**, 25582.
Lee, T. D., K. Huang, and C. N. Yang, 1957, Phys. Rev. **106**, 1135.
Lerch, S., B. Bessire, C. Bernhard, T. Feurer, and A. Stefanov, 2013, J. Opt. Soc. Am. B **30**, 953.
Lettow, R., Y. L. A. Rezus, A. Renn, G. Zumofen, E. Ikonen, S. Götzinger, and V. Sandoghdar, 2010, Phys. Rev. Lett. **104**, 123605.
Li, Z., N. Medvedev, H. Chapman, and Y. Shih, 2015, arXiv:1511.05068v2.
Lippiello, E., F. Corberi, A. Sarracino, and M. Zannetti, 2008, Phys. Rev. E **78**, 041120.
Longdell, J. J., E. Fraval, M. J. Sellars, and N. B. Manson, 2005, Phys. Rev. Lett. **95**, 063601.
Loo, V., C. Arnold, O. Gazzano, A. Lemaître, I. Sagnes, O. Krebs, P. Voisin, P. Senellart, and L. Lanco, 2012, Phys. Rev. Lett. **109**, 166806.
López Carreño, J. C., C. Sánchez Muñoz, D. Sanvitto, E. del Valle, and F. P. Laussy, 2015, Phys. Rev. Lett. **115**, 196402.
Loudon, R., 2000, *The Quantum Theory of Light* (Oxford University Press, Oxford, UK).
Louisell, W. H., A. Yariv, and A. E. Siegman, 1961, Phys. Rev. **124**, 1646.
Lvovsky, A. I., and M. G. Raymer, 2009, Rev. Mod. Phys. **81**, 299.
Ma, L., J. C. Bienfang, O. Slattery, and X. Tang, 2011, Opt. Express **19**, 5470.
Mamin, H. J., R. Budakian, B. W. Chui, and D. Rugar, 2005, Phys. Rev. B **72**, 024413.
Mandel, L., 1958, Proc. Phys. Soc. London **72**, 1037.
Mandel, L., 1959, Proc. Phys. Soc. London **74**, 233.
Mandel, L., and E. Wolf, 1995, *Optical Coherence and Quantum Optics* (Cambridge University Press, Cambridge, UK).
Marx, C. A., U. Harbola, and S. Mukamel, 2008, Phys. Rev. A **77**, 022110.
McKinstrie, C. J., and M. Karlsson, 2013, Opt. Express **21**, 1374.
McKinstrie, C. J., J. R. Ott, and M. Karlsson, 2013, Opt. Express **21**, 11009.
Mekhov, I. B., and H. Ritsch, 2012, J. Phys. B **45**, 102001.
Minaeva, O., C. Bonato, B. E. A. Saleh, D. S. Simon, and A. V. Sergienko, 2009, Phys. Rev. Lett. **102**, 100504.
Mitchell, M. W., J. S. Lundeen, and A. M. Steinberg, 2004, Nature (London) **429**, 161.
Mollow, B., 1972, Phys. Rev. A **5**, 2217.
Mollow, B. R., 1968, Phys. Rev. **175**, 1555.
Mootz, M., M. Kira, S. W. Koch, A. E. Almand-Hunter, and S. T. Cundiff, 2014, Phys. Rev. B **89**, 155301.
Morita, N., and T. Yajima, 1984, Phys. Rev. A **30**, 2525.
Mosley, P. J., J. S. Lundeen, B. J. Smith, P. Wasylczyk, A. B. URen, C. Silberhorn, and I. A. Walmsley, 2008, Phys. Rev. Lett. **100**, 133601.
Mukamel, S., 1995, *Principles of nonlinear optical spectroscopy* (Oxford University Press, Oxford, UK).
Mukamel, S., 2000, Annu. Rev. Phys. Chem. **51**, 691.
Mukamel, S., 2008, Phys. Rev. A **77**, 023801.
Mukamel, S., 2010, J. Chem. Phys. **132**, 241105.
Mukamel, S., C. Ciordas-Ciurdariu, and V. Khidekel, 1996, IEEE J. Quantum Electron. **32**, 1278.
Mukamel, S., and Y. Nagata, 2011, Procedia Chem. **3**, 132.
Mukamel, S., R. Oszwaldowski, and L. Yang, 2007, J. Chem. Phys. **127**, 221105.
Mukamel, S., and S. Rahav, 2010, in *Advances in Atomic, Molecular, and Optical Physics*, Vol. 59, edited by P. B. E. Arimondo and C. Lin (Academic Press, Waltham, USA), pp. 223–263.
Mukamel, S., and M. Richter, 2011, Phys. Rev. A **83**, 013815.
Muthukrishnan, A., G. S. Agarwal, and M. O. Scully, 2004, Phys. Rev. Lett. **93**, 093002.
Myers, J. A., K. L. Lewis, P. F. Tekavec, and J. P. Ogilvie, 2008, Opt. Express **16**, 17420.
Nardin, G., T. M. Autry, K. L. Silverman, and S. T. Cundiff, 2013, Opt. Express **21**, 28617.
Nasr, M. B., B. E. A. Saleh, A. V. Sergienko, and M. C. Teich, 2003, Phys. Rev. Lett. **91**, 083601.
O'Brien, J. L., G. J. Pryde, A. G. White, T. C. Ralph, and D. Branning, 2003, Nature (London) **426**, 264.
Oka, H., 2011a, J. Chem. Phys. **135**, 164304.
Oka, H., 2011b, J. Chem. Phys. **134**, 124313.
Oka, H., 2012, Phys. Rev. A **85**, 013403.
Oka, H., 2015, J. Phys. B **48**, 115503.
Oron, D., N. Dudovich, D. Yelin, and Y. Silberberg, 2002, Phys. Rev. Lett. **88**, 063004.
Ou, Z. Y., and L. Mandel, 1988, Phys. Rev. Lett. **61**, 50.
Palmieri, B., D. Abramavicius, and S. Mukamel, 2009, J. Chem. Phys. **130**, 204512.
Pan, J.-W., Z.-B. Chen, C.-Y. Lu, H. Weinfurter, A. Zeilinger, and M. Żukowski, 2012, Rev. Mod. Phys. **84**, 777.
Pasenow, B., H. Duc, T. Meier, and S. Koch, 2008, Solid State Commun. **145**, 61.
Patel, C. K. N., and A. C. Tam, 1981, Rev. Mod. Phys. **53**, 517.
Patel, R. B., A. J. Bennett, I. Farrer, C. A. Nicoll, D. A. Ritchie, and A. J. Shields, 2010, Nat. Photonics **4**, 632.
Pe'er, A., B. Dayan, A. A. Friesem, and Y. Silberberg, 2005, Phys. Rev. Lett. **94**, 073601.

Peřina, J., B. E. A. Saleh, and M. C. Teich, 1998, Phys. Rev. A **57**, 3972.
Pestov, D., V. V. Lozovoy, and M. Dantus, 2009, Opt. Express **17**, 14351.
Pestov, D., X. Wang, G. O. Ariunbold, R. K. Murawski, V. A. Sautenkov, A. Dogariu, A. V. Sokolov, and M. O. Scully, 2008, Proc. Natl. Acad. Sci. U.S.A. **105**, 422.
Pestov, D., *et al.*, 2007, Science **316**, 265.
Peyronel, T., O. Firstenberg, Q.-Y. Liang, S. Hofferberth, A. V. Gorshkov, T. Pohl, M. D. Lukin, and V. Vuletic, 2012, Nature (London) **488**, 57.
Pittman, T. B., Y. H. Shih, D. V. Strekalov, and A. V. Sergienko, 1995, Phys. Rev. A **52**, R3429.
Poggio, M., H. J. Mamin, C. L. Degen, M. H. Sherwood, and D. Rugar, 2009, Phys. Rev. Lett. **102**, 087604.
Potma, E., and S. Mukamel, 2013, in *Coherent Raman Scattering Microscopy*, edited by J. Cheng and X. Xie (CRC Press, Boca Raton), pp. 3–42.
Pototschnig, M., Y. Chassagneux, J. Hwang, G. Zumofen, A. Renn, and V. Sandoghdar, 2011, Phys. Rev. Lett. **107**, 063001.
Rahav, S., and S. Mukamel, 2010, Phys. Rev. A **81**, 063810.
Raimond, J. M., M. Brune, and S. Haroche, 2001, Rev. Mod. Phys. **73**, 565.
Rajapaksa, I., and H. Kumar Wickramasinghe, 2011, Appl. Phys. Lett. **99**, 161103.
Rajapaksa, I., K. Uenal, and H. K. Wickramasinghe, 2010, Appl. Phys. Lett. **97**, 073121.
Rammer, J., 2007, *Quantum Field Theory of Non-equilibrium States* (Cambridge University Press, Cambridge, UK).
Ramsey, N. F., 1950, Phys. Rev. **78**, 695.
Raymer, M. G., A. H. Marcus, J. R. Widom, and D. L. P. Vitullo, 2013, J. Phys. Chem. B **117**, 15559.
Rehms, A., and P. Callis, 1993, Chem. Phys. Lett. **208**, 276.
Rempe, G., H. Walther, and N. Klein, 1987, Phys. Rev. Lett. **58**, 353.
Rezus, Y. L. A., S. G. Walt, R. Lettow, A. Renn, G. Zumofen, S. Götzinger, and V. Sandoghdar, 2012, Phys. Rev. Lett. **108**, 093601.
Richter, M., and S. Mukamel, 2010, Phys. Rev. A **82**, 013820.
Richter, M., and S. Mukamel, 2011, Phys. Rev. A **83**, 063805.
Roslyak, O., C. A. Marx, and S. Mukamel, 2009a, Phys. Rev. A **79**, 063827.
Roslyak, O., C. A. Marx, and S. Mukamel, 2009b, Phys. Rev. A **79**, 033832.
Roslyak, O., and S. Mukamel, 2009a, Phys. Rev. A **79**, 063409.
Roslyak, O., and S. Mukamel, 2009b, Mol. Phys. **107**, 265.
Roslyak, O., and S. Mukamel, 2010, "A unified quantum field description of spontaneous and stimulated nonlinear wave mixing and hyper-Rayleigh scattering," Lectures of virtual university, Max-Born Institute.
Rubin, M. H., D. N. Klyshko, Y. H. Shih, and A. V. Sergienko, 1994, Phys. Rev. A **50**, 5122.
Saglamyurek, E., N. Sinclair, J. Jin, J. A. Slater, D. Oblak, F. Bussières, M. George, R. Ricken, W. Sohler, and W. Tittel, 2011, Nature (London) **469**, 512.
Salam, A., 2010, *Molecular Quantum Electrodynamics: Long-range Intermolecular Interactions* (John Wiley & Sons, New York).
Salazar, L. J., D. A. Guzmán, F. J. Rodríguez, and L. Quiroga, 2012, Opt. Express **20**, 4470.
Saleh, B. E. A., B. M. Jost, H.-B. Fei, and M. C. Teich, 1998, Phys. Rev. Lett. **80**, 3483.
Sanaka, K., A. Pawlis, T. D. Ladd, D. J. Sleiter, K. Lischka, and Y. Yamamoto, 2012, Nano Lett. **12**, 4611.
Šanda, F., and S. Mukamel, 2006, J. Chem. Phys. **125**, 014507.
Santori, C., P. E. Barclay, K.-M. C. Fu, R. G. Beausoleil, S. Spillane, and M. Fisch, 2010, Nanotechnology **21**, 274008.
Santori, C., D. Fattal, J. Vuckovic, G. S. Solomon, and Y. Yamamoto, 2002, Nature (London) **419**, 594.
Scarcelli, G., A. Valencia, S. Gompers, and Y. Shih, 2003, Appl. Phys. Lett. **83**, 5560.
Scheurer, C., and S. Mukamel, 2001, J. Chem. Phys. **115**, 4989.
Schlawin, F., 2016, *Quantum-enhanced nonlinear spectroscopy* (Springer, New York).
Schlawin, F., and A. Buchleitner, 2015, arXiv:1510.06726.
Schlawin, F., K. E. Dorfman, B. P. Fingerhut, and S. Mukamel, 2012, Phys. Rev. A **86**, 023851.
Schlawin, F., K. E. Dorfman, B. P. Fingerhut, and S. Mukamel, 2013, Nat. Commun. **4**, 1782.
Schlawin, F., K. E. Dorfman, and S. Mukamel, 2016, Phys. Rev. A **93**, 023807.
Schlawin, F., and S. Mukamel, 2013, J. Phys. B **46**, 175502.
Schreier, W. J., T. E. Schrader, F. O. Koller, P. Gilch, C. E. Crespo-Hernández, V. N. Swaminathan, T. Carell, W. Zinth, and B. Kohler, 2007, Science **315**, 625.
Schwartz, T., J. A. Hutchison, C. Genet, and T. W. Ebbesen, 2011, Phys. Rev. Lett. **106**, 196405.
Schwartz, T., J. A. Hutchison, J. Léonard, C. Genet, S. Haacke, and T. W. Ebbesen, 2013, ChemPhysChem **14**, 125.
Schwinger, J., 1961, J. Math. Phys. (N.Y.) **2**, 407.
Scully, M. O., and M. S. Zubairy, 1997, *Quantum Optics* (Cambridge University Press, Cambridge, UK).
Shahriar, M. S., P. R. Hemmer, S. Lloyd, P. S. Bhatia, and A. E. Craig, 2002, Phys. Rev. A **66**, 032301.
Shalm, L. K., D. R. Hamel, Z. Yan, C. Simon, K. J. Resch, and T. Jennewein, 2013, Nat. Phys. **9**, 19.
Shen, Y., 1989, Nature (London) **337**, 519.
Shih, Y., 2003, Rep. Prog. Phys. **66**, 1009.
Shih, Y. H., and C. O. Alley, 1988, Phys. Rev. Lett. **61**, 2921.
Shomroni, I., S. Rosenblum, Y. Lovsky, O. Bechler, G. Guendelman, and B. Dayan, 2014, Science **345**, 903.
Shwartz, S., R. Coffee, J. Feldkamp, Y. Feng, J. Hastings, G. Yin, and S. Harris, 2012, Phys. Rev. Lett. **109**, 013602.
Silberberg, Y., 2009, Annu. Rev. Phys. Chem. **60**, 277.
Sipahigil, A., M. L. Goldman, E. Togan, Y. Chu, M. Markham, D. J. Twitchen, A. S. Zibrov, A. Kubanek, and M. D. Lukin, 2012, Phys. Rev. Lett. **108**, 143601.
Siyushev, P., *et al.*, 2009, New J. Phys. **11**, 113029.
Slattery, O., L. Ma, P. Kuo, Y.-S. Kim, and X. Tang, 2013, Laser Phys. Lett. **10**, 075201.
Spano, F. C., and S. Mukamel, 1989, Phys. Rev. A **40**, 5783.
Steinberg, A. M., P. G. Kwiat, and R. Y. Chiao, 1992a, Phys. Rev. A **45**, 6659.
Steinberg, A. M., P. G. Kwiat, and R. Y. Chiao, 1992b, Phys. Rev. Lett. **68**, 2421.
Stevenson, R. M., A. J. Hudson, R. J. Young, P. Atkinson, K. Cooper, D. A. Ritchie, and A. J. Shields, 2007, Opt. Express **15**, 6507.
Stolz, H., 1994, *Time-Resolved Light Scattering from Excitons* (Springer-Verlag, Berlin).
Strekalov, D. V., *et al.*, 1995, Phys. Rev. Lett. **74**, 3600.
Tan, H.-S., 2008, J. Chem. Phys. **129**, 124501.
Tanimura, Y., 2006, J. Phys. Soc. Jpn. **75**, 082001.
Teich, M., and B. Saleh, 1998, U.S. Patent No. 5796477.
Tekavec, P. F., G. A. Lott, and A. H. Marcus, 2007, J. Chem. Phys. **127**, 214307.
Tian, P., D. Keusters, Y. Suzaki, and W. S. Warren, 2003, Science **300**, 1553.

Tittel, W., J. Brendel, N. Gisin, and H. Zbinden, 1999, Phys. Rev. A **59**, 4150.
Trebbia, J.-B., P. Tamarat, and B. Lounis, 2010, Phys. Rev. A **82**, 063803.
Trebino, R., 2000, *Frequency-resolved Optical Gating: The Measurement of Ultrashort Laser Pulses No. v. 1* (Springer, New York).
Turner, D. B., P. C. Arpin, S. D. McClure, D. J. Ulness, and G. D. Scholes, 2013, Nat. Commun. **4**, 3298.
Upton, L., M. Harpham, O. Suzer, M. Richter, S. Mukamel, and T. Goodson, 2013, J. Phys. Chem. Lett. **4**, 2046.
U'Ren, A. B., K. Banaszek, and I. A. Walmsley, 2003, Quantum Inf. Comput. **3**, 480 [http://dl.acm.org/citation.cfm?id=2011564.2011567].
U'Ren, A. B., R. K. Erdmann, M. de la Cruz-Gutierrez, and I. A. Walmsley, 2006, Phys. Rev. Lett. **97**, 223602.
Valencia, A., G. Scarcelli, M. D'Angelo, and Y. Shih, 2005, Phys. Rev. Lett. **94**, 063601.
Van Amerongen, H., L. Valkunas, and R. Van Grondelle, 2000, *Photosynthetic excitons* (World Scientific, Singapore).
Van Enk, S., 2005, Phys. Rev. A **72**, 064306.
Vogel, M., A. Vagov, V. M. Axt, A. Seilmeier, and T. Kuhn, 2009, Phys. Rev. B **80**, 155310.
Voronine, D., D. Abramavicius, and S. Mukamel, 2006, J. Chem. Phys. **124**, 034104.
Voronine, D. V., D. Abramavicius, and S. Mukamel, 2007, J. Chem. Phys. **126**, 044508.
Wagie, H. E., and P. Geissinger, 2012, Appl. Spectrosc. **66**, 609 [http://as.osa.org/abstract.cfm?URI=as-66-6-609].
Walborn, S., C. Monken, S. Pádua, and P. S. Ribeiro, 2010, Phys. Rep. **495**, 87.
Walden-Newman, W., I. Sarpkaya, and S. Strauf, 2012, Nano Lett. **12**, 1934.
Walmsley, I. A., 2015, Science **348**, 525.
Walmsley, I. A., and C. Dorrer, 2009, Adv. Opt. Photonics **1**, 308.
Walther, H., B. T. H. Varcoe, B.-G. Englert, and T. Becker, 2006, Rep. Prog. Phys. **69**, 1325.
Wasilewski, W., A. I. Lvovsky, K. Banaszek, and C. Radzewicz, 2006, Phys. Rev. A **73**, 063819.
Wollenhaupt, M., A. Assion, and T. Baumert, 2007, in *Springer Handbook of Lasers and Optics* (Springer, New York), pp. 937–983.
Wolters, J., N. Sadzak, A. W. Schell, T. Schröder, and O. Benson, 2013, Phys. Rev. Lett. **110**, 027401.
Wu, L.-A., H. J. Kimble, J. L. Hall, and H. Wu, 1986, Phys. Rev. Lett. **57**, 2520.
Wu, R.-B., C. Brif, M. R. James, and H. Rabitz, 2015, Phys. Rev. A **91**, 042327.
Xie, X. S., and J. K. Trautman, 1998, Annu. Rev. Phys. Chem. **49**, 441.
Xu, C., J. B. Shear, and W. W. Webb, 1997, Anal. Chem. **69**, 1285.
Xu, C., and W. Webb, 1996, J. Opt. Soc. Am. B **13**, 481.
Yabushita, A., and T. Kobayashi, 2004, Phys. Rev. A **69**, 013806.
Yan, S., and H.-S. Tan, 2009, Chem. Phys. **360**, 110.
Yang, L., and S. Mukamel, 2008, Phys. Rev. B **77**, 075335.
Yang, L., T. Zhang, A. D. Bristow, S. T. Cundiff, and S. Mukamel, 2008, J. Chem. Phys. **129**, 234711.
Ye, T., D. Fu, and W. S. Warren, 2009, Photochem. Photobiol. **85**, 631.
Zäh, F., M. Halder, and T. Feurer, 2008, Opt. Express **16**, 16452.
Zhang, T., I. Kuznetsova, T. Meier, X. Li, R. P. Mirin, P. Thomas, and S. T. Cundiff, 2007, Proc. Natl. Acad. Sci. U.S.A. **104**, 14227.
Zhang, Z., K. L. Wells, E. W. J. Hyland, and H.-S. Tan, 2012, Chem. Phys. Lett. **550**, 156.
Zhang, Z., K. L. Wells, and H.-S. Tan, 2012, Opt. Lett. **37**, 5058.
Zheng, Z., P. L. Saldanha, J. R. Rios Leite, and C. Fabre, 2013, Phys. Rev. A **88**, 033822.